JPL Publication 94–5

SCIENCE WITH HIGH SPATIAL RESOLUTION FAR-INFRARED DATA

Edited by S. Terebey and J. Mazzarella

1994 (Pasadena: JPL)

Proceedings of a Workshop held
14-16 June 1993 at the
Infrared Processing and Analysis Center
770 S. Wilson, Caltech, Pasadena, California 91125

PREFACE

Data at far-infrared wavelengths are difficult to obtain and usually have much lower spatial resolution than data which are routinely obtained at other wavelengths. However, the many astrophysical problems that can only be well addressed in the far-infrared have inspired efforts to extract high spatial resolution information from instruments including the Infrared Astronomical Satellite (IRAS) and the Kuiper Airborne Observatory (KAO). The IRAS data also provide a fundamental archive since IRAS produced a nearly complete survey of the infrared sky. Although the IRAS survey strategy was not designed with the specific purpose of constructing images of the sky, the ingenuity of software developers has recently resulted in innovative techniques which are allowing astronomers to push the limits of these and other far-infrared data.

The goal of this workshop was to discuss new science and techniques relevant to high spatial resolution processing of far-infrared data, with particular focus on high resolution processing of IRAS data. Users of the maximum correlation method, maximum entropy, and other resolution enhancement algorithms applicable to far-infrared data gathered at the Infrared Processing and Analysis Center (IPAC) on the Caltech campus in Pasadena for two days in June 1993 to compare techniques and discuss new results. During a special session on the third day, interested astronomers were introduced to IRAS HIRES processing, which is IPAC's implementation of the maximum correlation method to the IRAS data. Individuals who desire further information about IRAS or HIRES processing are encouraged to contact IPAC.

This workshop would not have been possible without the hard work of Donna Milton during all stages, from planning of the conference through formatting and editing of the proceedings. We also express our thanks to the Local Organizing Committee— Chas Beichman (IPAC), Zhong Wang (IPAC), and Tom Soifer (Caltech), and the Scientific Advisory Committee— Tj. Romke Bontekoe (ESA/ESTEC), John Hackwell (Aerospace Corp.), Dan Lester (U. Texas), and Erick Young (Steward Obs.). Thanks also go to Steve Lord, Pat McLane, Mary Ellen Barba, and David Stanley for help before and during the workshop. Some funding was provided by registration fees, but this conference would not have been possible without substantial financial assistance from the Jet Propulsion Laboratory, which is operated by the California Institute of Technology, under contract with the National Aeronautics and Space Administration.

S. Terebey and J. Mazzarella, Editors
May 1994, Pasadena, CA

TABLE OF CONTENTS

PART I: Introduction and Technical Overviews

PART II: Extragalactic Astronomy

PART III: Galactic and Solar System Astronomy

N95-21750

S1-82
40921
P 10

HIRES AND BEYOND

J. W. FOWLER AND H. H. AUMANN
Infrared Processing and Analysis Center, MS 100-22
California Institute of Technology, Jet Propulsion Laboratory
Pasadena, CA 91125

ABSTRACT The High-Resolution image construction program (HiRes) used at IPAC is based on the Maximum Correlation Method. After HiRes intensity images are constructed from IRAS data, additional images are needed to aid in scientific interpretation. Some of the images that are available for this purpose show the fitting noise, estimates of the achieved resolution, and detector track maps. Two methods have been developed for creating color maps without discarding any more spatial information than absolutely necessary: the "cross-band simulation" and "prior-knowledge" methods. These maps are demonstrated using the survey observations of a 2×2 degree field centered on M31. Prior knowledge may also be used to achieve super-resolution and to suppress ringing around bright point sources observed against background emission. Tools to suppress noise spikes and for accelerating convergence are also described.

1. INTRODUCTION

The high-resolution image construction program used at IPAC is based on the Maximum Correlation Method (MCM; see Aumann, Fowler, and Melnyk, 1990). This program uses IRAS survey and additional observation data to construct images in the four IRAS survey wavelength bands. These images are intensity maps covering typically one to four square degrees. The effective beam size varies significantly over these images because of the manner in which the IRAS telescope gathered infrared data. This makes interpreting the images and obtaining color ratios especially challenging. Complications are added by the nature of the celestial background (the varying zodiacal background) and the detectors. The more important effects caused by the detectors and the orbital environment are: hysteresis, residuals of radiation hits, saturation for bright sources, detectors of different noise amplitude, and baseline drift due to 1/f noise (*IRAS Explanatory Supplement 1988*).

In this paper we discuss additional tools and techniques that have been developed at IPAC over the last two years to address these difficulties. Some of these are byproducts of the intensity imaging (e.g., correction-factor variance and coverage maps), while others have been added recently to the default products (e.g., beam-sample maps and detector track maps). Some techniques that have been developed are now employed by default (e.g., automatic flux-bias pro-

S. Terebey and J. Mazzarella (eds.), *Science with High-Spatial Resolution Far Infrared Data*, 1–10, 1994, Jet Propulsion Laboratory, Pasadena, CA.

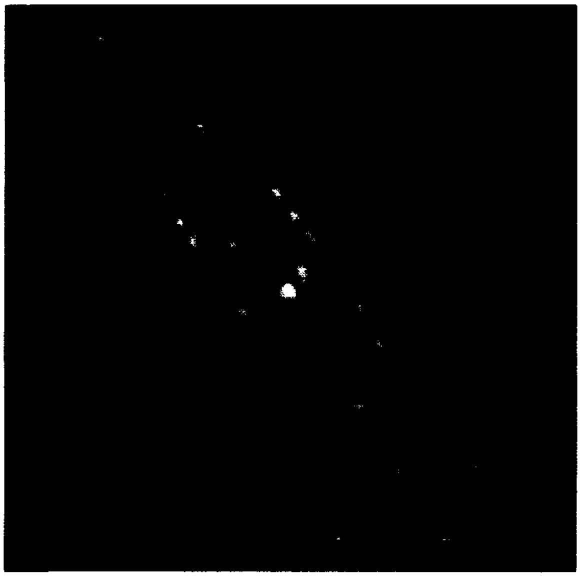

Fig. 1: Intensity image of M31 at 100 microns after 20 iterations

Fig. 2: Correction-factor variance map for Figure 1

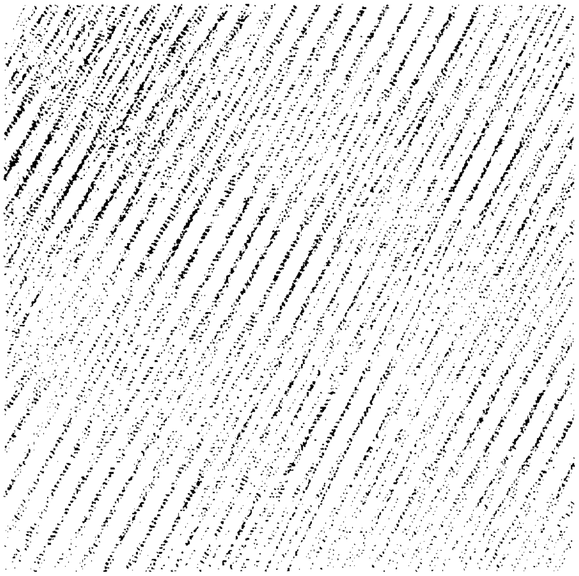

Fig. 3: Detector track map for Fig. 1

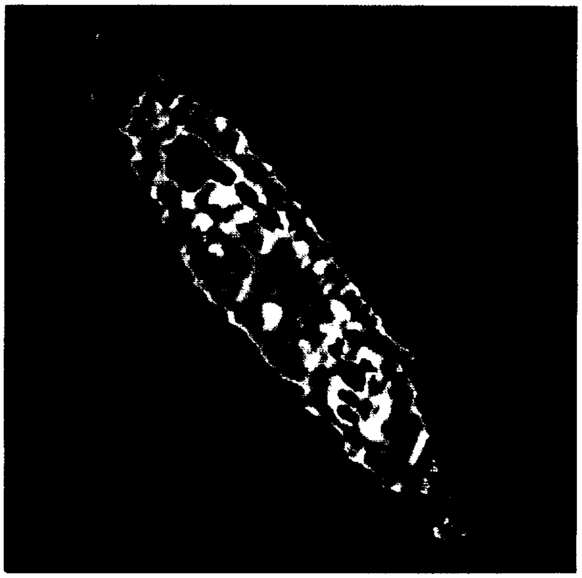

Fig. 4: Color-ratio map of M31 from cross-band simulation (100 micron/60 micron)

cessing), but most remain available by special-request only (e.g., point-source masking, scan-direction masking, spike median filtering, n-sigma data editing, point-source ringing suppression, color ratio and multi-band intensity maps). Some techniques require special preparation by the investigator (e.g., simulation and prior-knowledge input).

2. CORRECTION-FACTOR VARIANCE MAPS

The MCM iteratively constructs an image that reproduces the observed data to within the noise by computing mean correction factors for each pixel. This includes computing the variance of the correction factors, i.e., the fitting noise. After most of the resolvable structure has been obtained, the correction-factor variance (CFV) is essentially the *square* of the population *Noise-to-Signal* ratio for the corresponding pixel, and is typically much less than one. Since each pixel has a CFV value, the CFV information may be viewed in image form. Where there is no significant signal, the CFV is generally large (approaching unity). Where appreciable signal is present, particularly noisy measurements stand out noticeably (e.g., undeglitched particle radiation). It is important to know whether such measurements affect objects of interest in the image, and the methods discussed in sections 4 and 5 below can be used to eliminate individual detector samples that may be affecting the image adversely.

The CFV image is also useful for determining the consistency in measurements obtained at different epochs. By imaging data from two epochs both separately and combined in a single image, it is possible to see where the CFV is enhanced in the combined image. A useful exercise is to compute a CFV ratio image, where the combined CFV is in the numerator and the CFV from one of the separate epochs is in the denominator. The result is related to the F-statistic, and regions where the ratio is significantly greater than unity may be where systematic incompatibilities exist between the two epochs. This may result from photometric variability or proper motion, but most often is caused by such phenomena as zodiacal background variation or hysteresis affected by changes in scan angle.

Figure 1 shows the intensity map of M31 at 100 microns after 20 iterations. The corresponding CFV map is shown in Figure 2. Both figures employ logarithmic scaling, with that of the CFV map set to show an area of enhanced fitting noise near the nucleus. The CFV is generally small in the region of the galaxy, and all but one of the peaks inside the dark area are associated with low-brightness regions. The peak just southeast of the nucleus reveals the presence of a low-level data glitch that causes a slight brightening at that location which is removable with the methods discussed in sections 3 and 4 below.

3. COVERAGE AND DETECTOR TRACK MAPS

Since the correction factors used in the MCM are mean values computed with response-function weighting, an image of the sum of the weights in each pixel shows the depth of coverage. This must be adjusted if inverse-variance noise weighting is also employed (by special request), but relative coverage density is still obvious. The coverage maps are a useful diagnostic tool, since circumstances occasionally conspire to eliminate data unexpectedly.

Detector track maps are also now available. These are images which show the locations of the response-function centers of the detector samples used to construct the intensity map. Only the pixel containing the center is marked for each measurement. The marking is done by setting the pixel equal to the detector ID. This results in different detectors having different colors (or grey levels) when viewed with the IPAC image-processing program, SkyView (or similar program), with which one may "pick" specific pixels and thus learn the identity of the detector. Pixels not containing detector centers are zeroed out. Where two or more different detectors had measurements fall with centers in the same pixel, only the last is retained, but most images are sparse enough so that the trails of crossing detectors allow easy identification. The detector track map corresponding to Figure 1 is shown in Figure 3. The crossing of scans from the first two hours-confirmation coverages (HCONS) is obvious, and gives rise to large variations in the size and shape of the effective beam (see section 8 and Figure 8 below).

Since the MCM program allows selective exclusion of detectors by ID number, the detector track map is useful for determining such numbers. This may be for the purpose of eliminating a particularly noisy detector, for example. Another use currently being explored is to eliminate saturated point-source measurements; saturation is alleviated (there is hope that it can be essentially eliminated) without much loss of spatial information by this method. Generally some measurements see the bright object in the shoulders of the response functions, where the response functions are still fairly accurately known but the data are not saturated. If all measurements at higher response can be eliminated, the low-response measurements may construct the image correctly. When the saturation is not too severe, some relief is possible just by masking out measurements marked as associated with point sources by the data preparation program as part of its deglitching processing.

4. N-SIGMA DATA EDITING

In most iterative averaging processes, an effective way to eliminate "outliers" is to exclude samples that differ from the previous iteration's mean by more than some threshold in units of the previous iteration's standard deviation. This is available (applied to the correction factors) by special request in the MCM program and has been found to be quite powerful in some tests cases, but it has not yet been used extensively enough to build up a foundation of experience involving many varieties of image and settings of the n-sigma level and number of iterations to perform before beginning the editing. Furthermore, while it can eliminate practically all the flux associated with a feature caused by an outlier, it cannot generally remove all trace of the shape of the feature once it has been injected into an image, since the information contradicting the shape is usually not in the data. It may also have adverse effects on some parts of the image while fixing others. This method was used to eliminate the excess brightness of the data glitch that caused the enhanced CFV near the nucleus of M31 shown in Figure 2, as mentioned in section 2 above.

5. SCAN ANGLE AND SCAN DIRECTION EXCLUSION

Bright objects near each other in the scan direction can be affected by hysteresis, as well as other effects (e.g., "tails" in the response). The MCM program provides two ways to isolate scans. When using additional observation data, the user may specify that only scans in the survey direction be used, or alternatively, only scans in the antisurvey direction. Constructing images both ways and comparing them sheds considerable light on spurious interaction between sources. Another exclusion option is to accept only scans with angles within specified ranges. This is useful for survey data taken several months apart. These methods were used to establish that the bright object just northwest of the nucleus of M31 (see Figure 1) is real and not an artifact caused by hysteresis operating on the nucleus. Although hysteresis makes this object 7% brighter in the image in which it is downstream from the nucleus, this variation is expected and is much too small to damage the source's credibility.

6. SIMULATION

The IPAC image construction program works by simulating the scanning of a trial image and comparing the results to the observations. A natural extension was the addition of the capability to accept an arbitrary initial image and to output the simulated measurements obtained from it. The simulated CRDD (Calibrated Reconstructed Detector Data) is realistically aliased, noise can be added to it if desired (baseline error and sample-frequency noise with an arbitrary distribution), and certain types of response-function model error can be invoked.

This capability has been employed in four activities so far: (a.) it has provided CRDD from a known scene for testing destriping algorithms; (b.) it has been used to postulate scenes that were subsequently "scanned" and images constructed, with comparison between the simulated and actual images shedding light on subtle features; (c.) it is used in creating the "beam sample" maps discussed in section 8 below; (d.) it is used in the "cross-band simulation" method of registering spatial resolution for different wavelengths.

Cross-band simulation is one of two methods for matching the resolution in one wavelength to that in another (the other, "prior knowledge", is described in the next section and requires caution). Suppose, for example, that a color-ratio map involving 60 and 100 microns is desired. Simply computing color ratios in each pixel by employing the two intensity images typically yields fantastic artifacts because of the incompatible resolutions. The following method transforms each intensity image to obtain corresponding ones with compatible resolution without abandoning spatial information unnecessarily.

First, images are constructed in the two bands. Then the 60 micron image is "scanned" with the 100 micron detectors, using the same scan geometry and measurement locations as the real 100 micron image. The simulated CRDD is then used to construct an image. In the same way, the real 100 micron image is used to produce simulated 60 micron CRDD, which is used to construct an image. The two simulation images then have compatible resolution, and may be used to create a color-ratio map or a multi-band intensity image. Figure 4 shows a 100 micron/60 micron color ratio map for M31. In this image, brighter features have lower blackbody temperatures. Note the feature just southeast of the nucleus that is apparently very cold: this is the artifact caused by the data glitch discussed in section 2, and it does not appear when the data glitch is removed with the method of section 4.

7. PRIOR KNOWLEDGE INPUT

The IPAC MCM program actually works by modifying an initial image only at the spatial frequencies necessary to make it yield the observations to within the noise. Normally the initial image is flat, so that the final image retains as much of the initial flatness as is consistent with the data. If an arbitrary initial image is used, it too is modified only as needed to make it consistent with the observations, but the result is not generally a maximum-correlation image, because the pixels are not generally 100% correlated at the beginning. Most often it is the higher spatial frequencies that need the least modification and which therefore persist.

The use of a nonflat initial image is called "prior knowledge", since normally this is done only when one believes one has information consistent with the observational data but going beyond them. This term is used to describe the injection of external information into imaging calculations in a variety of ways. The IPAC MCM program employs prior knowledge in an extremely literal manner: it accepts a complete picture of what one believes to be the truth and proceeds to make it consistent with the IRAS data.

The prior knowledge technique has been used at IPAC as an alternative to cross-band simulation for obtaining color ratio maps. The example using 60 and 100 micron data discussed in the preceding section is handled as follows. The normal 60 micron image is used as the prior knowledge image for the 100 micron image construction, and vice versa. This amounts to assuming that if the structure in these two wavelengths could be perfectly resolved, it would be the same. Caution must be exercised because, for example, a star visible at 60 microns but not at 100 microns could lie in a region containing a cold cloud visible only at 100 microns. Using the 60 micron image as prior knowledge for the 100 micron image construction would cause the cold cloud emission to be concentrated as much as possible at the star position.

When used with care in applicable situations, this method can yield consistent resolution at two wavelengths with less overall loss of spatial information, since the resolution in the two resulting images is closer to the shorter-wavelength image, whereas cross-band simulation yields images slightly lower in resolution than the longer-wavelength image. The cross-band simulation method should always be used as a rough confirmation of the prior-knowledge method. Good results have been obtained in this way for M31; the corresponding color ratio map is very similar to Figure 4, which was produced with the cross-band simulation method discussed in the previous section.

Another use for the prior-knowledge technique is in producing super-resolved images, i.e., images with structure at spatial frequencies beyond the diffraction limit. For example, when one is certain that one is dealing with point sources (e.g., raster scans of the asteroid Egeria), the resolution is limited only by the pixel size. This capability has been demonstrated to work only via simulation at present.

Finally, employing prior knowledge input can be used to suppress ringing around bright point sources observed against background emission. The ringing occurs because such an image satisfies the measurements with higher pixel correlation (and higher entropy) than the intuitively expected image. It is possible via an iterative procedure to estimate the point source location and amplitude and employ this information as prior-knowledge input, refining the estimates until the ringing is suppressed. The ringing pattern itself contains information, and is determined primarily by the response function size, sample density and degree of uniformity, and the ratio of the point source flux to the extended emission. Overestimates of this ratio yield a ringing pattern that is distinctively different from that of underestimates (primarily in phase), and this information can be used in the iterative procedure. This typically also yields super-resolution. The resulting lower pixel correlation (and entropy) reflects the injection of external pixel decorrelation (or negative entropy) in the form of the prior knowledge. This has also been demonstrated via simulation and is ready for scientific application. Figure 5 shows a beam-sample map (see section 8 below) of M31 at 60 microns in which the imaged spikes ring noticeably against the smoothed background (a negative print is used to make the ringing more visible). Figure 6 shows the corresponding image with ringing suppressed.

8. BEAM SAMPLE MAPS

The effective beam size in typical high-resolution IRAS images varies by factors of three over distances of several arcminutes. In order to estimate the beam size at any given position and to see typical variation over the field, "beam sample maps" are provided. These are produced from simulated CRDD based on actual coverage geometry, with the simulation scene being a collection of spike sources against a smooth background. An image of the reconstructed spikes is generated with all the same processing options as the actual image.

Three types of spikes are available: uniformly spaced spikes (the default spacing is 12 arcminutes), spikes located where the deglitching algorithm found point sources, and spikes at user-defined locations (specified either in RA and Dec or in IRAF pixel coordinates). By default only the first type is used; the pattern is phased so that there is a spike at the center of the image, but the phase can be overridden. The spikes default to fluxes of 10 Jy, but can also be specified by the user or else an auto-scaling option is available which employs the pixel flux histogram of the actual image.

By default the background is flat and equal to the actual median background. By option, the actual background can be smoothed with obvious point sources removed. It is important to have a realistic background level, since the convergence rate for point sources is affected by background. Figure 7 shows automatically scaled spikes of the first two types and smoothed background for M31 at 100 microns. The simulated CRDD obtained from this scene were used to construct the beam sample map shown in Figure 8, in which the considerable variation of effective beam size and shape can be seen, as well as the higher state of convergence of spikes in the field relative to those embedded in the extended

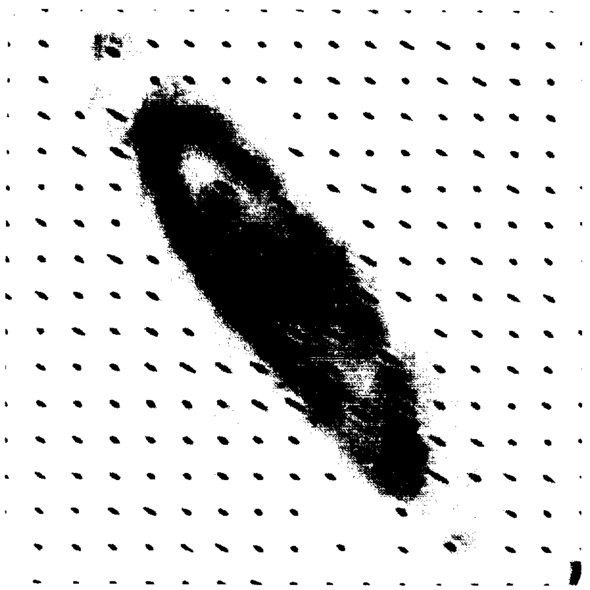

Fig. 5: Beam sample map in 60 microns, showing point-source ringing

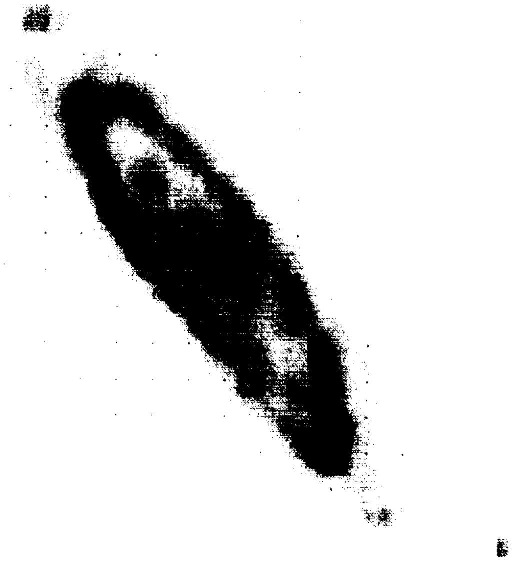

Fig. 6: Same as Figure 5 except with suppression of point-source ringing

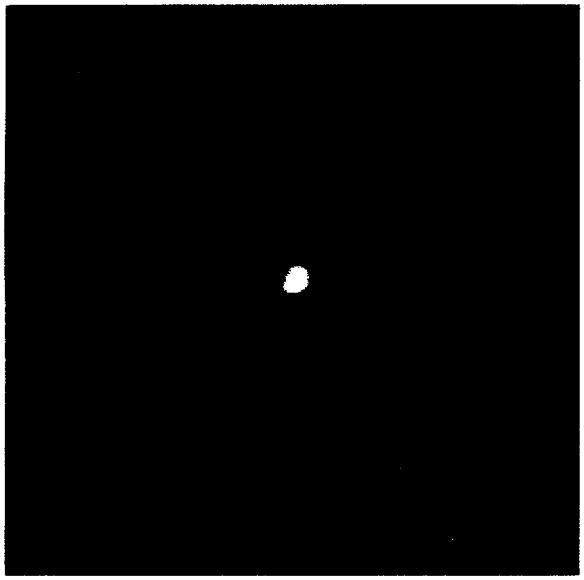

Fig. 7: Spike map with smoothed background for Figure 1

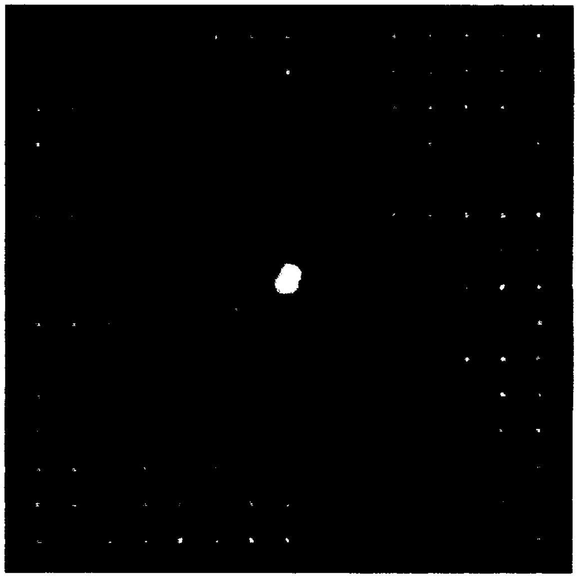

Fig. 8: Beam sample map constructed from simulation CRDD based on Figure 7

background.

An automatic analysis of the reconstructed spikes is provided in a text file. This includes the full width at half maximum on the principal axes of the beam shape, the twist angle, centroid error, and peak intensity, along with the pixel coordinates, RA and Dec, and simulated peak intensity and background.

9. IMAGING WITH A FLUX BIAS

Although the MCM program has no problem handling negative fluxes, there are reasons why positively constraining the image is desirable (e.g., reduced ringing and the inability of negative noise spikes to form), so this capability is included. On the other hand, simply excluding negative data (e.g., negative noise excursions after baseline removal) results in biased noise. The solution is to employ a flux bias, and this is now done by default.

The data preparation program informs the imaging program of the most negative intensity, and an appropriate bias is used. The bias is inserted by adding an intensity to each detector sample appropriate to the detector's response solid angle. The bias is removed from the final image by subtracting the appropriate flux from each pixel. Since the solid angle of the pixels is known exactly, but those of the detectors have estimation errors of a few percent, large flux biases cannot be used, because doing so would inject stripes into the image (in fact, this effect could be used to renormalize the detector solid angles). For most cases, this is not a problem, and the benefits of flux-bias processing far outweigh the cost. When baseline removal is used to prepare the data, a small positive flux bias is normally used. For destriping only, a negative flux bias with a larger amplitude is typical; this brings the action closer to the zero level, reducing ringing and accelerating convergence of higher spatial frequencies. Note that in the noise-to-signal interpretation of the CFV, the signal is that with the flux bias in effect.

10. SOME ADDITIONAL ENHANCEMENT TECHNIQUES

Two other techniques are worthy of mention. One of them improves the appearance of images, and one of them provides virtually instantaneous convergence at the expense of significant cosmetic degradation.

When image construction is carried to a high number of iterations, sample-frequency noise is typically driven into spikes. Since real features normally cannot be converged into spikes (with reasonable pixel sizes and typical measurement densities), and since noise features are usually accompanied by relatively high fitting variance, most of these noise spikes can be removed as follows: (a.) a spike filter (a 3×3 zero-sum filter with a central peak) is evaluated everywhere; (b.) when its output is above a threshold, the correction-factor variance of the central pixel is tested against another threshold; (c.) when both thresholds are surpassed, the pixel value is replaced with the median value of the surrounding nonspike pixels (i.e., pixels which did not also ring the spike filter). This has been found to improve image appearances and is available upon request.

Finally, an interesting technique has been found to accelerate convergence: instead of computing a mean correction factor for each pixel on the first iteration, the minimum factor from a measurement with response above a threshold at that pixel is used. This discards flux conservation at this point, but one more iteration rescales the image, so that flux is better conserved after two iterations than normally occurs (typically about ten iterations are needed to stabilize the total flux to better than 1%). The resulting image suffers from having fit all the model errors, just as images taken to 1000 iterations have been found to do.

ACKNOWLEDGMENTS

The authors would like to thank E. L. Kopan, M. Melnyk, S. Price, and G. Veeder for useful conversations that resulted in contributions to the work described herein. This work was carried out at the Jet Propulsion Laboratory, California Institute of Technology, under a contract with the National Aeronautics and Space Administration.

REFERENCES

Aumann, H. H., Fowler, J. W., and Melnyk, M. 1990, *AJ*, **99**, 1674

IRAS Catalogs and Atlases: Explanatory Supplement. 1988, ed. C.A. Beichman, G. Neugebauer, H.J. Habing, P.E. Clegg, and T.J. Chester (Washington, DC: GPO)

N95-21751

- 82
22
6

MEM APPLICATION TO IRAS CPC IMAGES

A. P. MARSTON
Dept. of Physics & Astronomy, Drake University, Des Moines, IA 50311

ABSTRACT A method for applying the Maximum Entropy Method (MEM) to Chopped Photometric Channel (CPC) IRAS additional observations is illustrated. The original CPC data suffered from problems with repeatability which MEM is able to cope with by use of a noise image, produced from the results of separate data scans of objects. The process produces images of small areas of sky with circular Gaussian beams of approximately $30''$ full width half maximum resolution at 50 and $100\mu m$. Comparison is made to previous reconstructions made in the far-infrared as well as morphologies of objects at other wavelengths. Some projects with this dataset are discussed.

INTRODUCTION

The Chopped Photometric Channel (CPC) instrument was part of the Dutch Auxiliary instrument package on IRAS. It produced simultaneous 50 and $100\mu m$ raster scan, pointed observations of small areas ($9'$ x $9'$) of the sky. Generally, objects covered by these scans were observed more than once. The original resolution of these images is $88''$ at $50\mu m$ and $100''$ at $100\mu m$ and beams were close to circular gaussians (Wesselius *et al.* 1986). They had the best "raw" resolution of any IRAS data set at these wavelengths. In all, approximately 3000 images of 1000 objects in the two wavebands were made including over 300 galaxies. There were a number of problems with images produced:

i) Major (and minor) glitching in the images. (These were removed in an off-line process performed in Groningen).

ii) Small sky coverage leading to problems in the calibration.

iii) Repeatability of (in particular) faint features was low.

In using a CPC image we are starting with a high resolution image and would therefore expect to recover the highest resolutions of any IRAS product after applying MEM. Keeping in mind the noise problems experienced by the CPC detectors, the fact that MEM reconstructs an image which is not an overinterpretation of the original data, i.e. that is reasonable given the noise across the image, is an important part of the image reconstruction.

METHOD OF APPLICATION

The flow chart shown in Figure 1 illustrates the procedure used in the MEM reconstruction of a CPC image. Only objects for which two or more CPC observations exist were used. Reconstructions were halted when the global χ^2 fit

S. Terebey and J. Mazzarella (eds.), *Science with High-Spatial Resolution Far Infrared Data*, 11–16, 1994, Jet Propulsion Laboratory, Pasadena, CA.

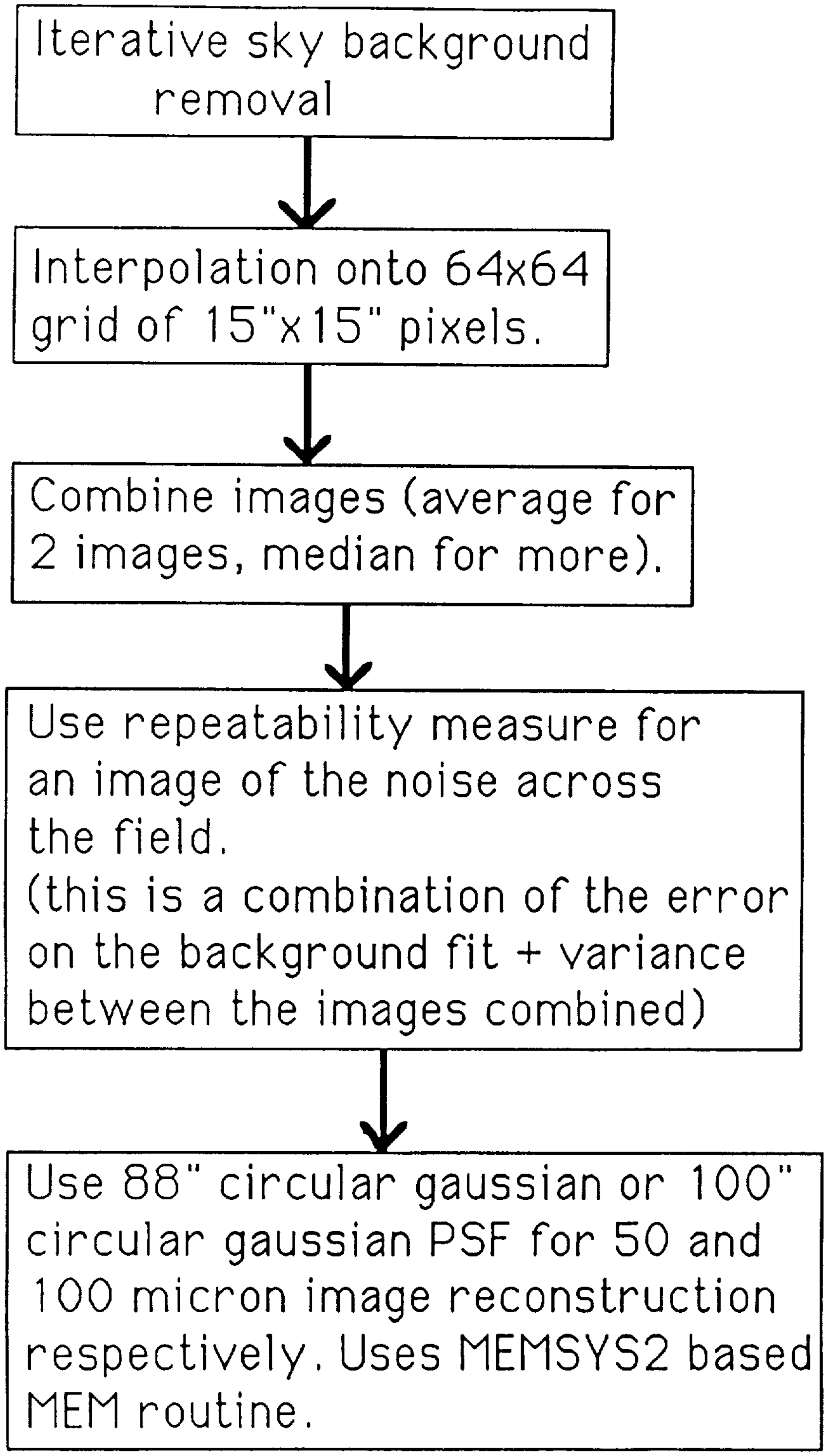

FIGURE 1 Flow chart outlining the procedure used in the MEM reconstructions of CPC images.

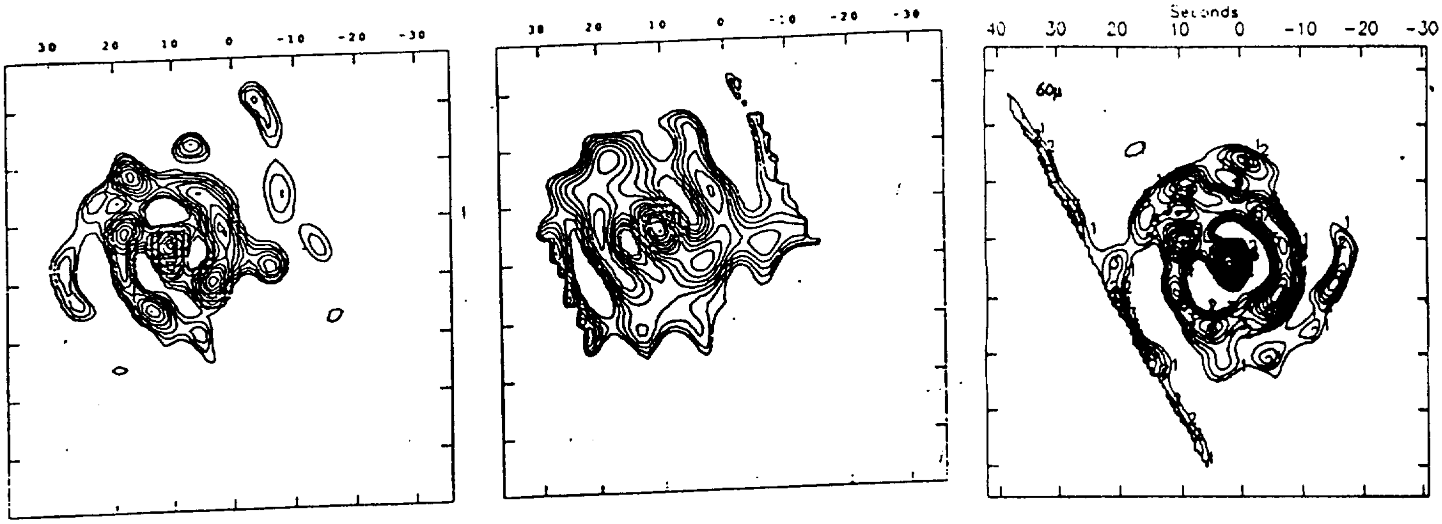

FIGURE 2 The 50 and 100μm MEM reconstruction images of M83 (left and center respectively) from the CPC data compared with the DSD 60μm reconstruction of Marston (1989) to the right.

of the image reconstruction compared to the original data equalled 1.0 per pixel or after 20 iterations of the MEM routine (for details on the background fitting and noise maps see Marston 1992a).

RESULTS AND COMPARISON TO PREVIOUS WORK

Morphological features produced in the reconstructions were compared to features seen in previous reconstructions for M83 and M51 (Marston 1989; Canterna *et al.* 1990). The M83 example is shown in Figure 2. The CPC reconstructions show very similar features to the reconstructed IRAS DSD AO produced by Marston (1989). Comparisons to features observed in other wavebands were also used as secondary indicators of the reliability of the reconstructed images (see Figure 6 of Marston 1989). A reconstruction of a point source image indicated a resolution of 24″ was typically achieved at both 50 and 100μm.

Limitations of the data

Some limitations exist on the reconstruction. Objects need to be smaller than 9′ across to fit within the raster scans of the CPC. Noise exists at the edge of the arrays where the individual raster scans, combined to create the final image of an object, do not precisely overlap. Features below 5MJy/sr (typically) are unreliable (this is a 3σ value for noise at the sky level on the combined maps).

DATA USES

A number of topics have been investigated or are under investigation using MEM processed CPC images.

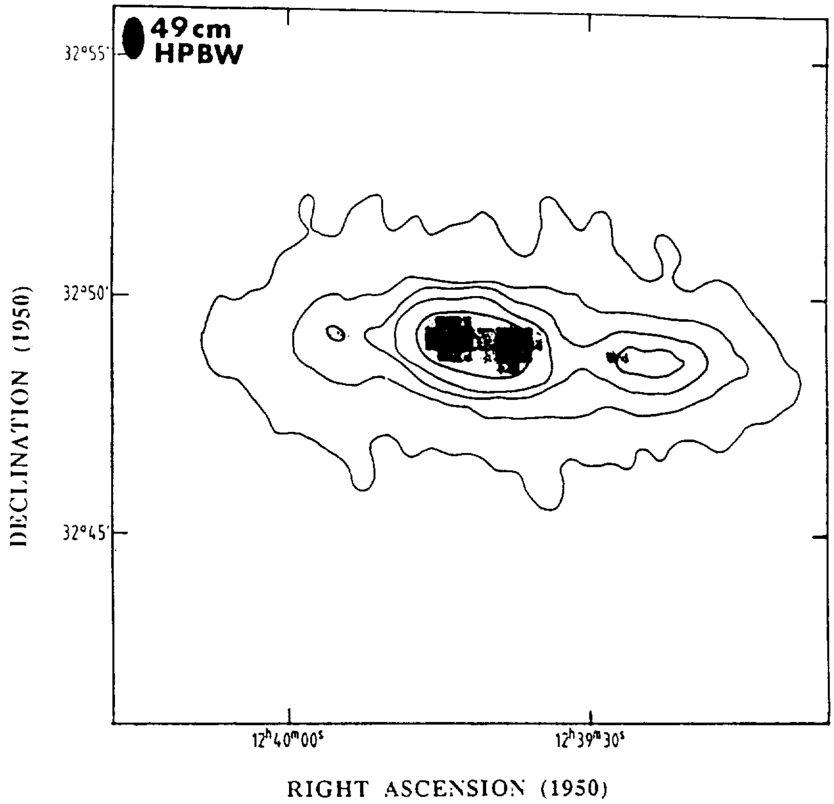

FIGURE 3 A greyscale image of the reconstructed 50μm image of the edge-on spiral NGC 4631 with contours of the 49cm non-thermal radio emission overlaid (Werner 1985). A distinct spatial correlation is evident between the features seen in both the radio and far-infrared.

Extended Far-Infrared Emission in Active Galaxies

The nearby radio galaxy, Centaurus A, shows a warped dust disk structure in reconstructed images (see Marston 1992b). Emission follows the Hα distribution shown in the TAURUS data of Bland et al. (1987). Regions of Hα line-splitting are coincident with peaks seen in the 50μm image. A sample of CPC images of Seyfert galaxies have been investigated in order to investigate the relation of the active nucleus in these galaxies to the far-infrared emission (Marston 1992a; Marston 1993). These show that many nearby Seyfert galaxies have extended regions of FIR emission which can often be resolved into RdiskS and RbulgeS components (e.g., NGC 7582).

Detailed correlation of far-infrared and radio features

Recent work by Bicay and Helou (1990) and Helou and Bicay (1993) have indicated that the strong non-thermal radio – far-infrared correlation shown in the global fluxes of galaxies also exists as a strong spatial correlation inside the galaxies. To investigate this further, the MEM processed images allow a more detailed comparison. An example of this is NGC 4631 (Figure 3). The spatial relation between features is excellent. However, the far-infrared peaks compared

FIGURE 4 Contours of the IRAS 50μm image overlaid on a greyscale production of an R band CCD frame of Arp 270. The extended far-infrared emission associated with each of the galaxies is evident and they are clearly separated. The apparent distance between the nuclei of the two galaxies is 80″.

to the far-infrared background are stronger by a factor of 3 than the corresponding radio peaks compared to the radio background in this galaxy. This would suggest these areas are the source of the fast charged particles needed for the radio emission, the charged particles having now leaked away from these sources.

Interacting galaxies

Preliminary investigations have so far been made into separating the far-infrared emission associated with pairs and groups of interacting galaxies (see the example of Arp 270 in Figure 4). This allows the determination of the effect that interactions have on the star formation processes in these interactions (see e.g. Surace *et al.* 1993). The example in Figure 4 shows how Arp 270 has been easily split into the two components associated with the galaxies NGC 3995 and NGC 3996.

Classification of edge-on spiral galaxies

The existence of the far-infrared knots seen in the reconstructed CPC image of NGC 4631, shown in Figure 3, suggest they are due to the perspective of viewing along the edge of a spiral arm of this edge-on disk galaxy. The spacing between the arms, indicated by the far-infrared peaks, should allow the arm class classification of this galaxy and may also be applied to reconstructions of other edge-on spirals.

CONCLUSION

A method of reconstructing far infrared images at 50 and 100μm at 30$''$ resolution from the IRAS CPC database has been illustrated. The reconstructed beams are circular Gaussians. Reliable reconstructions of objects $< 9'$ across have been obtained. The CPC database contains a number of galaxies, and these may be used for the study of distributed far-infrared emission from active galaxies, star formation in interacting galaxies and groups, the far-infrared/non-thermal radio correlation in galaxies and spiral arm classification of edge-on spirals.

REFERENCES

Bicay, M. D., and Helou, G. 1990, *ApJ*, **362**, 59

Bland, J., Taylor, K., and Atherton, P. D. 1987, *MNRAS*, **228**, 595

Canterna, R., Hackwell, J. A., and Grasdalen, G. L. 1990, In *Proceedings of the Second Wyoming Conference: The Interstellar Medium in External Galaxies, Summaries of Contributed Papers*, eds. D. J. Hollenbach and H. A. Thronson Jr., NASA Conference Publication 3084, p. 301

Helou, G., and Bicay, M. D. 1993, *ApJ*, **415**, 93

Marston, A. P. 1989, *AJ*, **98**, 1572

Marston, A. P. 1992a, In *Relationships Between Active Galactic Nuclei and Starburst Galaxies*, ed. A. V. Filippenko, ASP Conference Series, Vol. 31, p.117

Marston, A. P., 1992b, In *Relationships Between Active Galactic Nuclei and Starburst Galaxies*, ed. A. V. Filippenko, ASP Conference Series, **31**, p.123

Marston, A. P. 1993, in *Proceedings of the Workshop on Science with High Spatial Resolution Far-Infrared Data*, JPL, pp. 89-95

Surace, J. A., Mazzarella, J. M., Soifer, B. T., and Wehrle, A. E. 1993, *AJ*, **105**, 864

Werner, W. 1985, *A&A*, **144**, 502

Wesselius, P. R., Beitema, D. A., de Jonge, A. R. W., Jurriens, T. A, Kester, D. J. M., van Weerden, J. E., de Vries, J., and Perault, M. 1986, *IRAS-DAX Chopped Photometric Channel, Explanatory Supplement* (Groningen: Laboratory for Space Research)

N95- 21752

3
6

AN ASSESSMENT OF IMAGE RECONSTRUCTION FROM BALLOON-BORNE AND THE IRAS DATA

S.K. GHOSH, B. DAS, T.N. RENGARAJAN AND R.P. VERMA
Tata Institute of Fundamental Research, Homi Bhabha Road, Bombay 400005 INDIA

ABSTRACT Angular resolution and structural information from the far-infrared mapping of astronomical sources (Galactic star forming regions, spiral galaxies etc.) made using the TIFR 1 m balloon-borne telescope and the IRAS have been compared. The effective wavelengths of the TIFR two-band photometer are 58 and 150 μm. From IRAS, the survey COADD data, additional observations (AOs) made with the survey detectors with different Macros (DPS, DSD, DPM), as well as the chopped photometric channel (CPC) data have been considered here. The observed signals have been processed using different deconvolution strategies, either based on a maximum entropy method (MEM) developed at TIFR or the HiRes package developed at IPAC. Relative merits of each of these, under different conditions of signal to noise ratio, are highlighted. The following sources have been selected for illustration: Carina complex, W31 region, IRAS 10361–5830 (all Galactic), M101 and M81 (extragalactic). The main conclusions are: far-infrared maps from MEM deconvolution of balloon-borne data have the best angular resolution; MEM deconvolution of IRAS AOs gives resolution comparable to HiRes but with less amount of computation, though the dynamic range in MEM maps is less than in HiRes maps.

INTRODUCTION

At the far-infrared wavelengths, observations are made by telescopes aboard aircrafts, balloons, rockets and satellites. These telescopes are of moderate size ($\leq$ 1 m) and generally the field of view is several arcminutes (except in the case of Kuiper Airborne Observatory where the field of view is less than $1'$). Therefore, there is a need for increasing the resolution by signal processing. Many techniques have been used to improve the resolution of the maps. In this paper we compare three of these techniques – two based on the maximum entropy method (MEM) and the third one, HiRes, based on maximum correlation method (MCM).

OBSERVATIONS AND DATA ANALYSIS

The data used are taken from balloon flights made with the Tata Institute of Fundamental Research (TIFR) 1 m telescope and from the IRAS satellite. The

S. Terebey and J. Mazzarella (eds.), *Science with High-Spatial Resolution Far Infrared Data*, 17–22, 1994, Jet Propulsion Laboratory, Pasadena, CA.

TIFR balloon-borne telescope is an f/8 cassegrain telescope with metal mirrors. The field of view is 2$'\!.$4 diameter and the radiation is chopped along the cross-elevation (XEL) axis by vibrating the secondary mirror at a frequency of 20 Hz and with an amplitude of 3$'\!.$6. A one band photometer with an effective wavelength of 150 μm and a two band photometer with effective wavelengths of 58 and 150 μm have been used. Mapping is done by raster scanning an area of $\sim 30' \times 30'$ by scanning along the XEL axis at a typical rate of 0$'\!.$75 s^{-1} and steps of 1$'\!.$4 in elevation (EL). Far-infrared signals are passed through a digital filter to reduce the noise and then gridded in XEL-EL plane with pixel size of 0$'\!.$3 x 0$'\!.$3. Two dimensional deconvolution is performed on these signals using a MEM procedure based on Gull and Daniell (1978). The code for this MEM deconvolution has been developed at TIFR. The point spread profile (PSP) has been obtained using the observations of the planets. Hereafter, this procedure is referred to as MEM(a). The resolution in the deconvolved maps is $\sim$ 1$'\!.$2 and typical dynamic range for good signal to noise ratio is $\sim$ 100. The computing time for deconvolving a 1° x 1° field is $\sim$ 1 hour per band on a PC 486. Further details of the telescope and the data processing are given in Ghosh et al. (1988).

The sizes of the IRAS survey detectors along the cross-scan direction are $\geq$ 4$'\!.$5; along the in-scan direction the sizes are 0$'\!.$75 at 12 and 25 μm, 1$'\!.$5 at 60 μm and 3$'\!.$0 at 100 μm. There are a few edge detectors with smaller size along the cross-scan direction– 0$'\!.$75 at 12 and 25 μm, 1$'\!.$5 at 60 μm and 3$'\!.$0 at 100 μm (IRAS Catalogs and Atlases, Explanatory Supplement, 1988). In the CPC, the detectors have a circular field of view with a diameter of 1$'\!.$2 at 50 and 100 μm. Besides the survey data, there are additional observations (AOs) with smaller cross-scan steps and generally slower scan rate leading to higher signal to noise ratio (SNR). Data from the IRAS satellite are available in several forms. These are – Survey COADD grids, AO grids with different Macros, CPC data and calibrated reconstructed detector data (CRDD). For the first three of these sets, the signals from different detectors in the given band are mixed, therefore for the deconvolution one has to use an average PSP. In the CRDD, the signals from different detectors are kept separate, therefore the characteristics of individual detectors can be used.

We have deconvolved data from survey COADDs, AOs with different Macros and the CPC data, using a self adaptive scheme using MEM based on Skilling and Bryan (1984). The PSPs are derived from the observations of point sources (NGC 6543, asteroids). The resolution in the deconvolved map depends on the wavelength and the nature of the input grid. The FWHM size for the deconvolved map of a point source for some of the grids is given in Table 1. The dynamic range for a good SNR is $\sim$ 300. The computing time for deconvolving a 1° x 1° field is less than 30 minutes per band on a PC 486. The above procedure is referred to as MEM(b). Details of this procedure along with the deconvolved maps for 18 large galaxies based on data from the AOs and the CPC can be found in Ghosh et al. (1993).

The CRDD data are processed using the HiRes routine which is based on a maximum correlation method. Here the pixel size is much smaller, $15'' \times 15''$. The input image is "cleaned" and "flat fielded" before processing further to remove various artifacts. The digitized spatial response function, the detector sky position and the orientation for each detector are used to calculate the correction factors iteratively. The details of this technique are given by Aumann, Fowler

TABLE 1 FWHM size for a point source.

Grid	Processing	FWHM Size (in-scan x cross-scan)			
		12 μm	25 μm	50/60 μm	100 μm
AO DPS02B	MEM(b)	$\leq 0'.5 X 0'.7$	$\leq 0'.5 X 0'.7$	$0'.6 X 1'.0$	$1'.4 X 1'.7$
AO DSD01A	MEM(b)	$\leq 0'.5 X 0'.5$	$\leq 0'.5 X 0'.5$	$\leq 0'.5 X 0'.5$	$0'.9 X 1'.2$
CPC	MEM(b)	...	...	$\leq 0'.3 X 0'.4$	$\leq 0'.5 X 0'.4$
	HiRes [a]	$0'.4 X 0'.6$	$0'.4 X 0'.6$	$0'.7 X 1'.0$	$1'.3 X 1'.6$

---

[a] From Rice (1993)

and Melnyk (1990). The resolution in the processed maps after 20 iterations is given in Table 1. The processing time on a Sun Sparc2 (for 20 iterations) for a 1° x 1° field is more than 30 minutes for each band.

RESULTS

Some of the maps obtained using different procedures are presented here for illustration. First we consider Galactic HII/star-forming regions. In Figures 1, 2 and 3 we give the maps of a region in the Carina nebula, around IRAS 10361–5830 and W31 respectively generated from balloon-borne observations deconvolved with MEM(a) and compare these with the maps obtained from the IRAS data with HiRes processing (for Carina) and MEM(b). Most of the sources in the the two sets of maps are reproduced rather well. However the superior resolution of the maps from balloon-borne observations for these complex regions is quite clear.

Next we present some examples of the maps of large galaxies. In Figures 4 and 5 we give the maps for the galaxies M101 and M81 respectively, generated from AO data deconvolved with MEM(b) and compare these with the maps processed with HiRes routine. HiRes maps are taken from Rice (1993). One can see that the two sets of maps are remarkably similar. Specifically, in the case of M101 galaxy, the HII regions resolved in the HiRes maps are equally well resolved in the MEM(b) maps.

CONCLUSIONS

1. The angular resolution of maps obtained from TIFR balloon-borne measurements at 150 μm is better than or comparable to that from HiRes at 100 μm. This is mainly due to smaller field of view of the balloon-borne photometer. It may be mentioned that for our future balloon flights we will be using a new photometer with liquid ^3He cooled bolometer arrays. This two band photometer will have a field of view of $1'.6$ and effective wavelengths of $\sim$ 130 and 200 μm. This will give further improvement in angular resolution besides going to longer wavelengths and higher sensitivity.

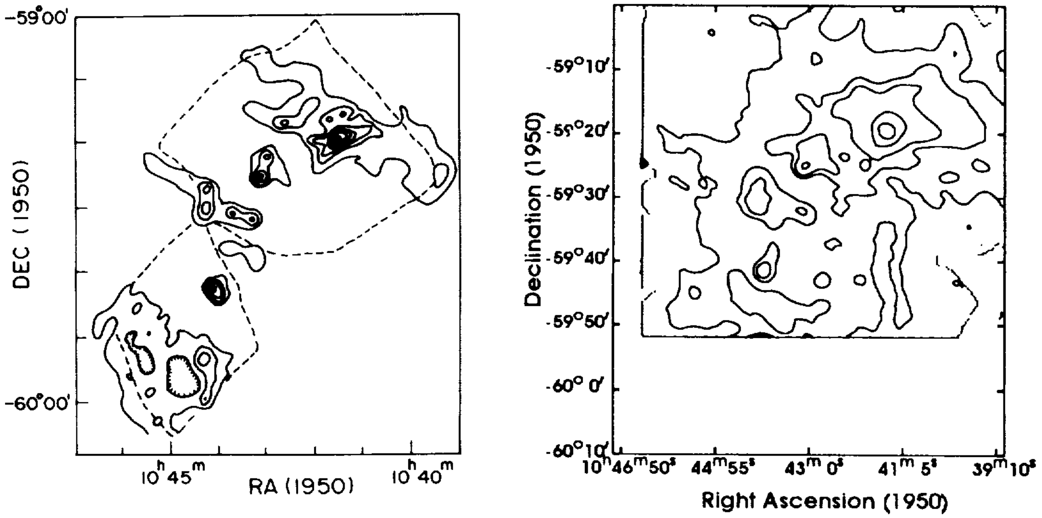

FIGURE 1 Intensity distribution for Carina nebula **a)** at 150 μm from balloon-borne observations deconvolved with MEM(a) **b)** at 100 μm from IRAS survey data with HiRes processing. The contour levels are 0.95, 0.5, 0.3, 0.1, 0.05 and 0.01 of the peak.

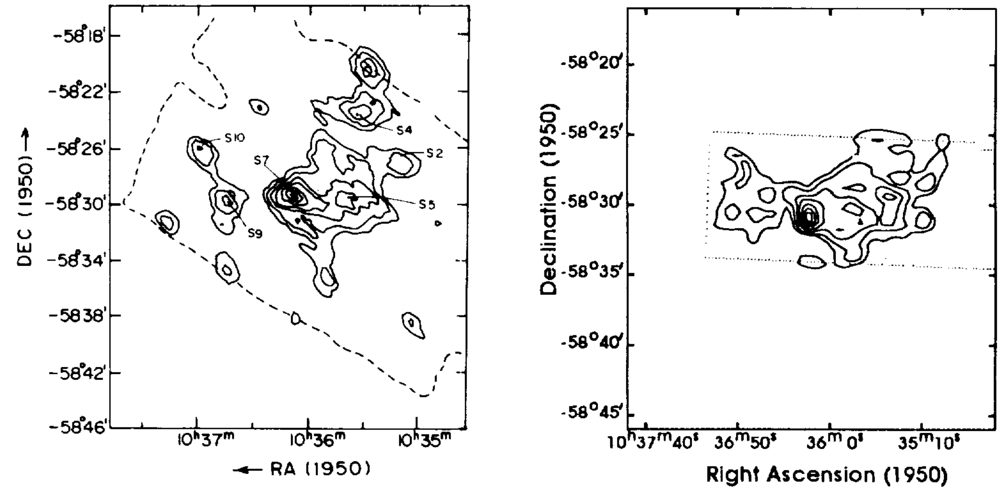

FIGURE 2 Intensity distribution for a region around IRAS 10361–5830 at 60 μm; **a)** from balloon-borne observations; and **b)** from AO data with DSD01A grid processed through MEM(b). The contour levels are 0.9, 0.7, 0.5, 0.3, 0.2, 0.1, and 0.05 of the peak.

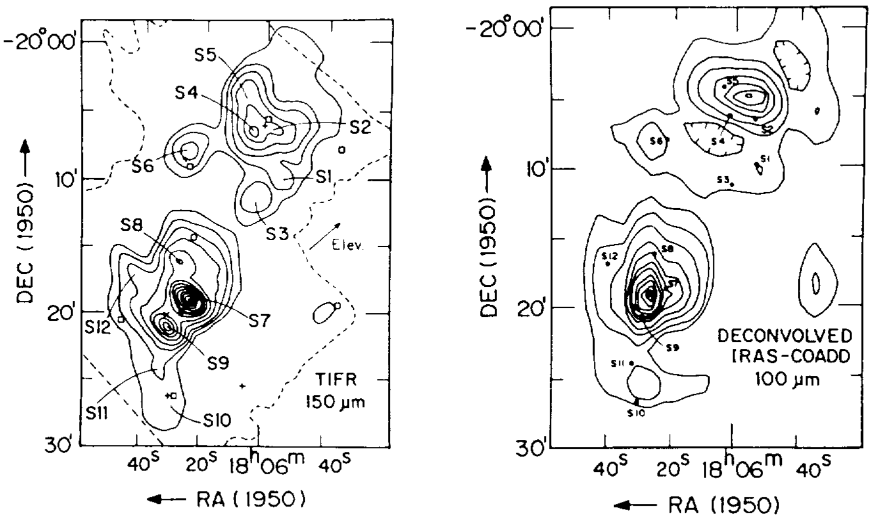

FIGURE 3 Intensity distribution of W31 region **a)** at 150 μm from balloon-borne observations with MEM(a); and **b)** at 100 μm from COADD data deconvolved with MEM(b). The contour levels are 0.95, 0.9, 0.8, 0.7, 0.6, 0.5, 0.4, 0.3, 0.2, 0.1, 0.05, 0.025 and 0.01 of the peak.

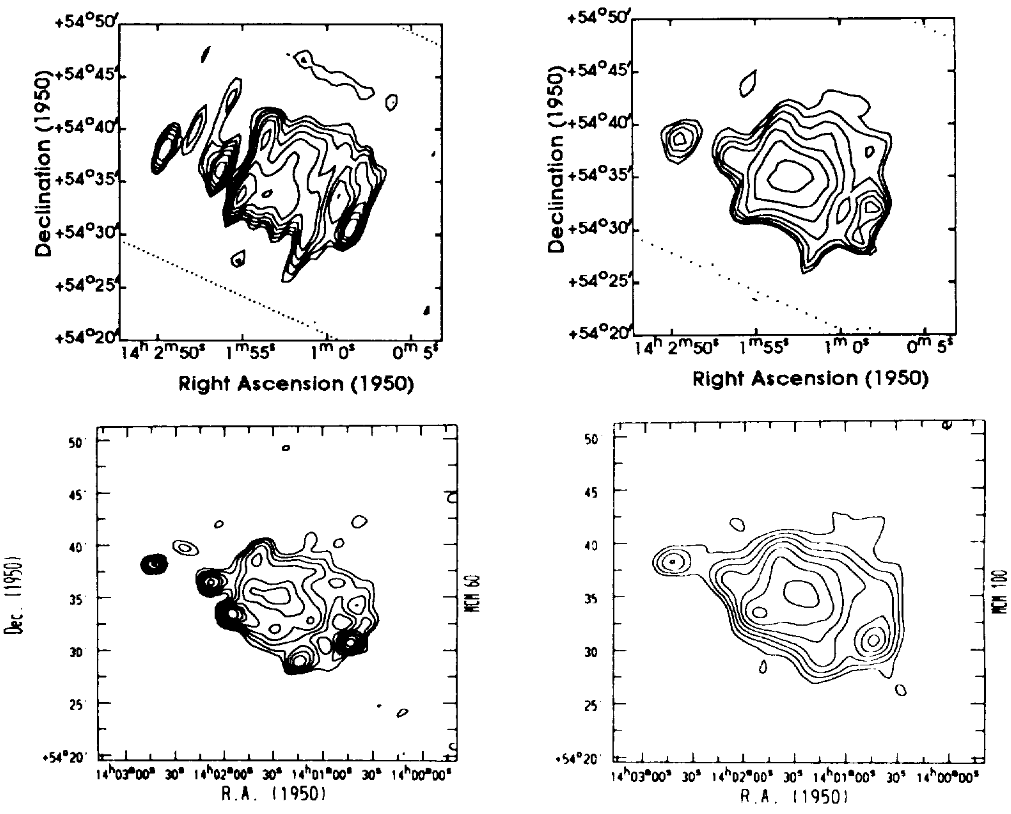

FIGURE 4 Intensity distribution for M101; **a)**, **b)** at 60 μm and 100 μm from AO MEM(b); **c)**, **d)** at 60 μm and 100 μm from HiRes. The contour levels are scaled by a factor of $\sqrt{3}$.

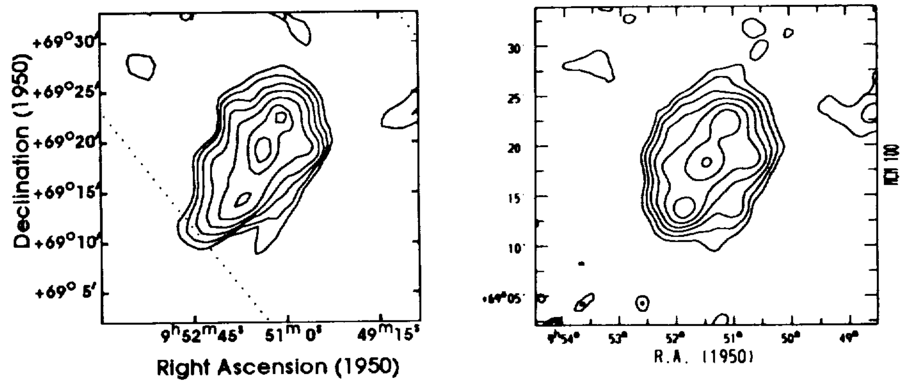

FIGURE 5 Intensity distribution at 100 μm for M81; **a)** from AO MEM; and **b)** from HiRes. The contour levels are scaled by a factor of $\sqrt{3}$.

2. MEM deconvolution of averaged IRAS data from AOs, MEM(b), gives a resolution comparable to that obtained from HiRes processing. However, the dynamic range in the HiRes processing is superior to that of the MEM maps. MEM processing is computationally inexpensive as compared to HiRes processing.

ACKNOWLEDGMENTS

We thank the Infrared Processing and Analysis Center (IPAC) for providing IRAS data and HiRes data processing.

REFERENCES

Aumann, H. H., Fowler, J. W. and Melnyk, M. 1990, *AJ*, **99**, 1674

Ghosh, S. K., Iyengar, K. V. K., Rengarajan, T. N., Tandon, S. N., Verma, R. P. and Daniel, R. R. 1988, *ApJ*, **330**, 928

Ghosh, S. K., Verma, R. P., Rengarajan, T. N., Das, B. and Saraiya, H.T. 1993, *ApJS*, **86**, 401

Gull, S. F. and Daniell, G. J. 1978, Nature, **272**, 686

IRAS Catalogs and Atlases: Explanatory Supplement 1988, ed. C.A. Beichman, G. Neugebauer, H.J. Habing, P.E. Clegg, and T.J. Chester (Washington, DC: GPO)

Rice, W. 1993, *AJ*, **105**, 67

Skilling, J. and Bryan, R. K. 1984, *MNRAS*, **211**, 111

N95-21753

IN SEARCH OF RANDOM NOISE

DO KESTER
Laboratory for Space Research
Postbus 800, 9700 AV Groningen, The Netherlands

TJ. ROMKE BONTEKOE[1]
Astrophysics Division of ESA, ESTEC, Postbus 299, 2200 AG Noordwijk, The Netherlands

ABSTRACT In order to make the best high resolution images of IRAS data it is necessary to incorporate any knowledge about the instrument into a model: the IRAS model. This is necessary since every remaining systematic effect will be amplified by any high resolution technique into spurious artifacts in the images. The search for random noise is in fact the never ending quest for better quality results, and can only be obtained by better models.

The Dutch high-resolution effort has resulted in HIRAS which drives the MEMSYS5[2] algorithm. It is specifically designed for IRAS image construction. A detailed description of HIRAS with many results is in preparation (Bontekoe, Koper & Kester 1993). In this paper we emphasize many of the instrumental effects incorporated in the IRAS model, including our improved 100 μm IRAS response functions.

INTRODUCTION

The InfraRed Astronomical Satellite (IRAS) All Sky Survey was designed and optimized for the detection of point sources. This allowed the survey to be conducted in the form of narrow strip scans with redundant coverage of the sky, but with non-uniform covering densities. The data show in addition to point sources many sources of extended emission, which are best analyzed from images. However, the non-uniform coverage now forms a significant obstacle in the image (re-)construction. Low resolution images, such as in the Infrared Sky Survey Atlas, yield spatial resolutions of five to ten times the IRAS telescope diffraction limit; HIRAS can improve on this by a factor of one to two times!

In HIRAS the imaging equation

$$d = R f \pm \sigma, \tag{1}$$

---

[1] Current address: Bontekoe Data Consultancy, Jaap Bergmanstraat 3, 2221 BM Katwijk ZH, The Netherlands

[2] MemSys5 is a software package of Maximum Entropy Data Consultants Ltd. Cambridge, UK.

S. Terebey and J. Mazzarella (eds.), *Science with High-Spatial Resolution Far Infrared Data*, 23–31, 1994, Jet Propulsion Laboratory, Pasadena, CA.

is solved. Here d is the data vector, f is the image vector, the matrix R describes the instrumental response, and σ is the estimated noise in the data. High demands are placed on the quality of the data and the response matrix R. Therefore, HIRAS utilizes the individual response functions of the focal plane detectors and rotates them according to the scan angle over the requested map (Bontekoe et al., 1991).

The spatial correlations in an image can be controlled via a new multichannel method, pyramid images, in which virtually all spatial frequencies are represented. In a pyramid image a 64×64 pixel image is the sum of a 64×64, a 32×32, ..., a 2×2, and a 1×1 pixel channel, all covering the same map area. The final result, of course, is a single map.

In image reconstruction there is an inevitable amplification of the noise in the data, due to the ill-conditioned nature of the inversion of the imaging equation. In HIRAS this amplification of the noise can be quantified by the computation of an error map, having identical dimensions to the requested map. The error map represents a full propagation of σ through the inversion of the imaging equation. Comparing the image with the error map gives indispensable information about the authenticity of detailed features. For example, the flux of point sources in the IRAS Point Source Catalog is usually within the error as determined by HIRAS.

In Groningen the complete IRAS database (survey, AOs, and LRS) has been written to a magneto-optical jukebox system, and is made accessible to the astronomical community. The extraction of IRAS data is performed by an automatic mail request server (for info: irasman@sron.rug.nl). The data are stored as integer numbers just as they were relayed from the satellite. The selected data are retrieved in the form of a IRAS Data Set (IRDS) (Roelfsema and Kester, 1992), which is a specialized version of a GIPSY data set. The Groningen Image Processing SYstem (GIPSY)[3] is a general purpose astronomical image processing package (van der Hulst et al., 1992). In GIPSY there are many software tools for processing IRAS data.

The IRDS is the basis of all our high-resolution processing, starting with calibration from integer data numbers to MJy/sr and adding pointing information.

The data d, still administered in the form of scans, are first flatfielded and destriped against a low-resolution map (CoAdd) by the IMAGE task in GIPSY. After a first convergence of HIRAS subsequent refinements in the calibration can be performed, now against the new high-resolution map. Corrections in the baseline, drift, and detector gain are applied and continuation of the HIRAS run shows a significant improvement in the result.

HIRAS is a highly interactive GIPSY task, although it can also be run with reasonable settings in an automatic mode. Being part of a larger image processing system opens venues for inspecting and investigating the data and moulding them to obtain the best possible solution. Since HIRAS uses proprietary software, it cannot be distributed without proper licensing.

For a full description of HIRAS we refer to Bontekoe, Koper & Kester (1993). Below we describe our IRAS model, which includes corrections for the

---

[3] GIPSY can be obtained, free of charge (for info: kgb@astro.rug.nl).

noise due to digitization and data compression, de-glitching and de-tailing of the data and the redetermination of the 100 μm detector response functions.

PREPROCESSING

After calibration to physical units and the subtraction of a zodiacal emission model from the data, the IMAGE task performs the local flatfielding and de-striping of the data. Generally one starts with a zero-valued template map. First order baseline corrections, zero points and drifts, are derived for each detector scan by fitting the scans to the template. The fit is a lower envelope fit. For detector response functions the nominal rectangular apertures are used as a first order approximation. The thus corrected scans are co-added into a new map, the CoAdd. In subsequent iterations the CoAdd of the previous iteration serves a template map (Wesselius et al. 1992). Typically, the procedure requires five iterations, after which, in general, no further improvement can be obtained. The de-striping works best when at least two sets of scans are present with an appreciable angle between them, but it does not exclude proper de-striping for areas with almost parallel scan only. Some more care is necessary in such cases. The derived correction parameters are stored at the appropriate levels in the IRDS. HIRAS uses this improved IRDS as input, not the CoAdd.

ZERO POINT OF DATA

As a consequence of the above improvement of the internal consistency of the data, our knowledge of the value of the absolute zero point of the data has eroded. Ideally, a black sky should give zero signal apart from instrumental noise, which can give positive as well as negative data values. An erroneous off-set in the zero point shifts the balance between noise and data. MEMSYS5 yields non-negative images, but accepts negative data values. Negative data values are regarded as noise, in full agreement with Gaussian statistics. Gross errors in the zero point of the data result in areas in the image devoid of any emission in the case when significant data are shifted below zero. Positive offsets are not very apparent in the results, but generally show up as unrealistically high backgrounds.

In a trade-off the fiducial zero point is taken such that typically five percent of the data become negative. 'Hard zeroes' in the resulting image are usually avoided in this way.

NOISE MODELING

The noise in the data is estimated by application of a zero-sum filter over a sufficiently long part of the detector scan, i.e. data from a single detector from a part of a single scan over the image area. The median value of the filter output is appropriately scaled to the correct standard deviation in the case of Gaussian noise (Bontekoe et al. 1991). This yields a noise estimate σ per detector scan; to this noise estimate two corrections for non-Gaussian effects are added.

First, a contribution is added which accounts for the lossy data compression scheme on board the satellite. The bulk of the data were transmitted as logarithmically compressed 8-bit differences, with every four seconds a 16-bit fiducial point (IRAS Explanatory Supplement 1988, App. II.1). These data were decompressed at the ground station into 16-bit integers. In the worst case, strong gradients were transmitted by only three significant bits plus a sign bit. To accommodate for this loss in precision we adjust σ as follows:

$$\sigma_n = \sqrt{\sigma^2 + a * |d_n - d_{n-1}|^2}. \tag{2}$$

($d_n \pm \sigma_n$ is the value of the n-th datum and its uncertainty.) The constant a is usually taken 0.03, corresponding to a precision loss of a few percent. MEMSYS5 allows each datum to have a different noise estimate. Subsequently, the values of consecutive noise estimates are smoothed a little to avoid too large variations.

Second, for samples which partly overlap the map boundary an additional correction for the noise estimate is made. Samples are included only if at least half of the 'volume' of the RF is inside the image area. The value of d_n is multiplied by the fraction of the volume inside the image area and the σ_n is divided by it, thus diminishing the relative influence of the 'unknown world outside'.

And finally, the minimum step in the sample values, after calibration, is identical to the (scaled) unit step as when the samples were represented by integers. This step size is quite large, either of the same size as the noise estimates σ. This means that the smallest deviation possible in the data is of the order of 1 σ. The assumption of Gaussian noise then tends to break down. This is similar to a Gaussian fit of a random series of $+1, -1, \cdots$, which has a standard deviation of $\sqrt{0.5} < 1$. Every deviation is at least a 'one-σ-detection'.

MEMSYS5, being designed for Gaussian noise, is quite sensitive to such systematic effects. A more fundamental approach, which transcends the Gaussian assumption, is not (yet) possible. We ameliorated the data by smoothing the least significant bit, from the 16-bit integer representation, with a cubic spline function.

TIME DOMAIN FILTERING

Thus far only global corrections on d are made in the preprocessing stage and instrumental effects are modeled in σ. However, glitches and memory effects in the data are short duration phenomena and have to be corrected in a few data samples. Glitches, originating from e.g., cosmic ray hits, are identified by application of a glitch filter and these samples are removed. Memory effects (also known as hysteresis), resulting in decaying offsets after passing over a strong compact source, are mainly present in 12 μm and 25 μm data.

A combination of filters and flags are implemented to signal their occurrence. Two zero-sum filters run over the data. One is mainly sensitive to point sources $\{-1, -1, -1, +2, +2, +2, -1, -1, -1\}$ and the other is more sensitive to glitches $\{-3, +6, -3\}$. (Glitches are of shorter duration that point sources.) If the point source filter output surpasses a given threshold and if it is also larger than the glitch filter output, then the source is flagged as a point source. Otherwise, it can be flagged as a glitch and the corresponding section of the data is subsequently ignored.

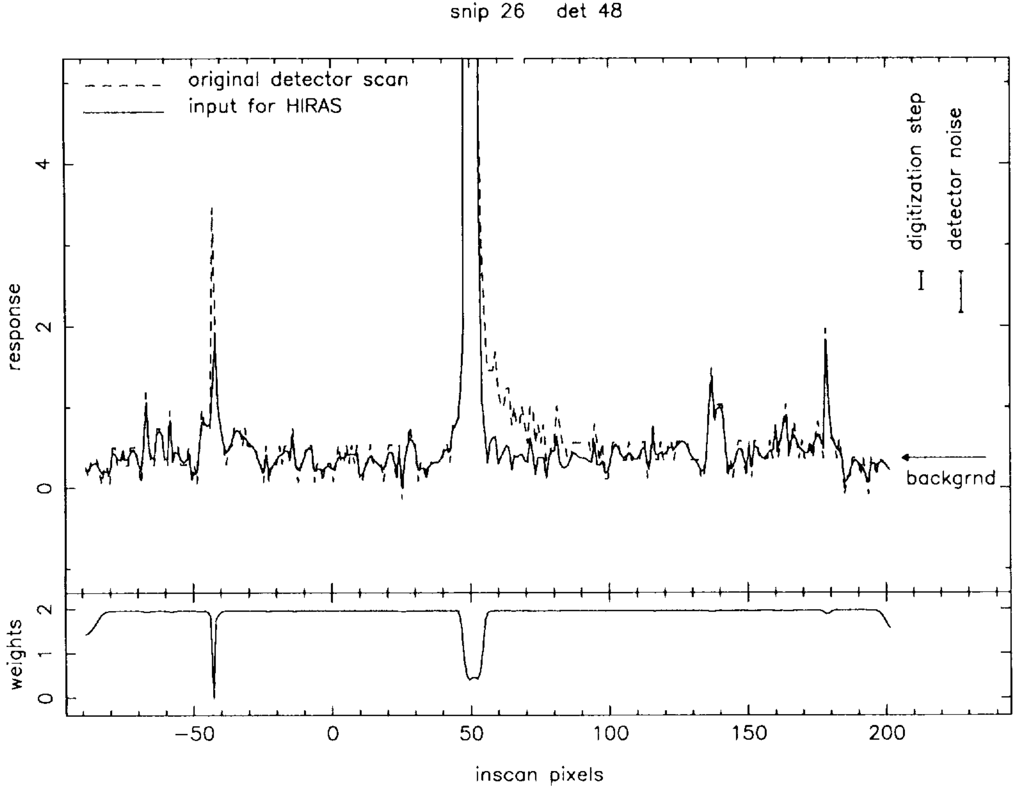

FIGURE 1 Sample values of one detector scan, running over a point source in the Chamaeleon region. In the upper panel the dashed line represents a calibrated and destriped detector scan; the full line represents the same detector scan after de-tailing, de-glitching, and digitization-smoothing, and will be input for HIRAS. In the lower panel the weights of the data are displayed, the weights are $1/\sigma_n$. A weight equal to zero indicates a sample which is rejected, e.g. a glitch.

It is well known that the IRAS detectors exhibit memory effects after having observed a bright source, especially at 12 and 25 μm. A number of data samples taken just after observing a strong point source can suffer from those nonlinearity effects, which are called 'tails'. Depending on the strength of the filter outputs a number of tail samples are flagged. These tail samples are either excluded or corrected via a de-tail filter. We implemented a version of Russ Walker's (priv. comm.) de-tailing algorithm, which assumes an exponential decay. We are studying a way to derive parameters of the memory effects within the MEMSYS5 context. Figure 1 summarizes the effects thus far described.

RESPONSE FUNCTIONS

The current IRAS Response Functions (RF) have been derived from a series of special raster observations on the planetary nebula NGC 6543 by Mehrdad Moshir (priv. comm.) in 1986. They were never intended for the construction of maps, though they served a good role in doing so. These observations were taken at half survey speed. In the cross-scan direction the wings are not defined below $\approx 15\%$ of the maximum (see Fig. 2). This can be improved somewhat extending the RFs with a linear roll-off in the cross-scan direction over $\approx 1'$. This made 12, 25, and 60 μm HIRAS results more acceptable when compared with, e.g., ground-based observations. Some 100 μm results, however, were inconsistent with their 60 μm counterparts. Although an exact correspondence cannot be expected, many of the physical processes are well understood; for example, the nearby edge-on galaxy NGC 55 had a significantly different morphology in the two bands. Detailed analysis of the 60 and 100 μm data led to the conclusion that the 100 μm RFs were suspect (Bontekoe, Koper & Kester, 1993).

We decided to rederive the RFs for the 100 μm detectors from survey data passing over NGC 6543. This would yield RFs at full survey speed. Since NGC 6543 is almost exactly in the pole of the IRAS orbit, it has been observed many times. ¿From the data server 107 scans in the neighborhood could be extracted, for which all the necessary calibration and position parameters are present, and in which the source is present. In this area of the sky the on-board calibration also took place, by illuminating the focal plane with two flashes of known intensity. These flash-data were later used for the calibration of the data. Almost all scans over NGC 6543 contain these flashes, and the useful parts had to be selected manually. (Under standard operation of the data server calibration flashes are removed.) However, the focal plane is very unevenly covered by passes of NGC 6543 (see Fig. II.D.9 of *IRAS Faint Source Survey Explanatory Suppl.*). Large gaps with no useful data, in one case almost $2'$ wide, occur in the cross-scan covering density.

A response function can be derived via the following method. The imaging equation (1) has a certain symmetry in R and f. The rows of the matrix R codify how the RF of a detector, at a single instant, overlies the sky. The RF, however, can also be regarded as an image of the detector response. The datum d_n thus is the vector product of the 'image' of the detector with f. In other words, the rows in R can be regarded as shifted and rotated images of the detectors. If we postulate that we know the scene f, we can de-shift and de-rotate the image f into the rows of a new matrix $\hat{R}$, and solve for the image of the detector RFs. In our case, we have to decide what NGC 6543 looks like at 100 μm.

Optically, NGC 6543 is a bright H II region of approximately $10''$ in radius, surrounded by a weak halo of $190''$ radius (Millikan, 1974). From many crossings over the Low Resolution Spectrograph (LRS) it could be established that in the wavelength range from 4 to 22 μm NGC 6543 is smaller than $5''$. However most of this is line emission from the central source. Moseley (1980) attempted to determine its size in 37μm continuum radiation, and found little flux outside a beam of $20''$. With the effective CPC beam of $88''$ and $100''$ for bands at, respectively, 50 μm and 100 μm, the nebula seems unresolved. In the CPC images there is no evidence that a halo is present (Wesselius et al. 1985). ¿From this we conclude that the nebula must be appreciably smaller than the effective CPC beam. NGC 6543 is extended at a wavelength of 6 cm with a FWHM of $15''$ (see Pottasch 1984), which is significantly less than the IRAS telescope diffraction limit of $100''$. Therefore and also for simplicity reasons, we assume NGC 6543 to be a point source at location ($17^h58^m33^s.9 + 66°38'6''$, eq1950). (Note that the IRAS PSC differs from this position by $48''$!)

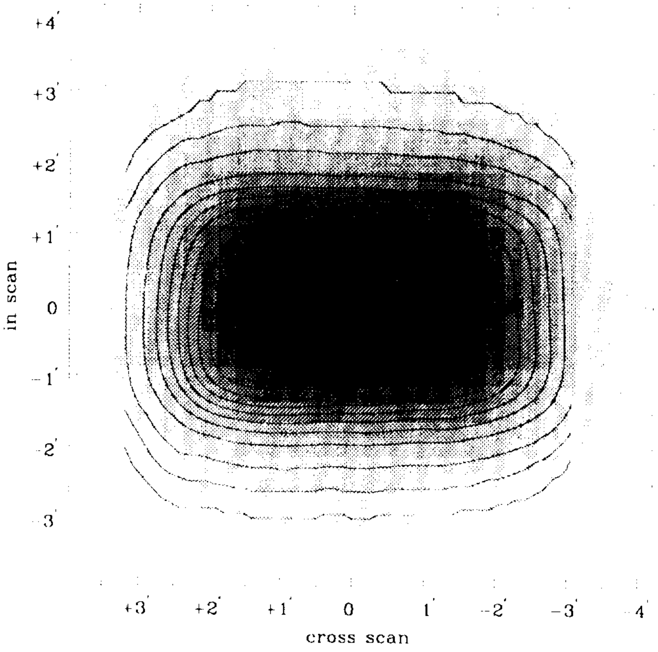

FIGURE 2 For detector 4 the new RF is displayed in graytones. It is overlaid with contours of Moshir's RF. Both contours and gray scales are at 2, 5, 10, 20, 30, 40, 50, 60, 70, 80, 90, 95, 98% of the maximum. It can be seen that in first order the new RF is a shifted version of Moshir's RF.

Figure 2 shows the old and new RF for detector 4.

DE-STRIPING WITHIN HIRAS

After a first convergence of HIRAS, mock data $\hat{d}$ are drawn from the image f, using the imaging equation. These data are compared with the real d, on detector scan basis. Whenever an offset or a drift could be determined with enough statistical significance, the real data d are corrected. HIRAS then continues with the improved data. This extra destriping operation gives a noticeable improvement in the results.

In addition, significant detector gain variations can be present, which are seldom seen in the data preprocessing using CoAdds. The reasons for this are twofold. First, the mock data from HIRAS, using the detector RFs, can follow the structure in the image better than when using rectangular apertures, as is done in CoAdds. Second, occasionally gain corrections arise from the steep flanks of the RFs. Some RFs rise 2% per arcsec in the cross scan direction. The data have a pointing accuracy of 10″ (*IRAS Explanatory Supplement* 1988), which combined with our standard pixel size of 15 ″, gives a worst case error of 50% in the mock data flux. This in turn would be translated into a large gain correction factor. This de-striping procedure is repeated until no significant deviations are present anymore.

CONCLUSION

Some results obtained with HIRAS can be seen in the contribution of Waters et al. at this workshop (pgs. 111-118).

We know that in some areas our knowledge is still incomplete, e.g. we would like to have a better model for the memory effects and new response functions for the other wavelength bands. In addition, a more fundamental solution to the digitization noise could improve things further.

IRAS performed much better than expected. We are still discovering new systematic and thus modelable effects. We are not yet down to the random noise of the instrument.

Currently we are planning to make the HIRAS program accessible via the mail server, which already is in place for coadded images and LRS spectra. More information can be obtained from irasman@sron.rug.nl.

ACKNOWLEDGMENTS

Many people have been involved in the development of the IRAS software. We would like to thank Timo Prusti, Pjotr Roelfsema, Albrecht de Jonge, Rens Waters, Rob Assendorp, Freddy Lahuis, Enrico Koper, Paul Wesselius.

REFERENCES

Bontekoe, Tj.R., Kester, D.J.M., Price, S.D., de Jonge, A.R.W., and Wesselius, P.R. 1991, *A&A*, **248**, 328

Bontekoe, Tj.R., Koper, E., and Kester, D.J.M. 1993, in preparation

van der Hulst, J.M., Terlouw, J.P., Begeman, K.G., Zwitser, W., Roelfsema, P.R. 1992, in *Astronomical Data Analysis and Software Systems I*, D.M. Worrall, Ch. Biemesderfer and J. Barnes (eds.), Astronomical Society of the Pacific Conference Series, **25**, 131

IRAS Catalogs and Atlases: Explanatory Supplement 1988, ed. C.A. Beichman, G. Neugebauer, H.J. Habing, P.E. Clegg, and T.J. Chester (Washington DC: GPO)

Millikan, A.G. 1974, *AJ*, **79**, 1279

Moseley, H. 1980, *ApJ*, **238**, 892

Moshir M., et. al. 1992, *Explanatory Supplement to the IRAS Faint Source Survey*, (Pasadena: JPL)

Pottasch, S.R. 1984, *Planetary Nebulae,* Reidel, Dordrecht

Roelfsema, P.R. and Kester, D.J.M. 1992, in *Astronomical Data Analysis and Software Systems I*, D.M. Worrall, Ch. Biemesderfer and J. Barnes (eds.), Astronomical Society of the Pacific Conference Series, **25**, 359

Wesselius, P.R., Beintema, D.A., de Jonge, A.R.W., Jurriens, T.A., Kester, D.J.M., van Weerden, J.E., de Vries, J. and Perault, M. 1985, *Chopped Photometric Channel Explanatory Supplement*, SRON-SRG, Groningen

Wesselius, P.R., de Jonge, A.R.W., Kester, D.J.M., and Roelfsema, P.R. 1992, in: *Infrared Astronomy with ISO.* Encrenaz T., Kessler M.F. (eds.) Nova Science Publishers, New York, p. 509

N95-21754

PUSHING THE LIMITS OF SPATIAL RESOLUTION WITH THE KUIPER AIRBORNE OBSERVATORY

D. LESTER
Department of Astronomy, University of Texas, Austin, TX 78712

THE PROBLEM OF HIGH SPATIAL RESOLUTION IN THE FAR-INFRARED

The study of astronomical objects at high spatial resolution in the far-IR is one of the most serious limitations to our work at these wavelengths, which carry information about the luminosity of dusty and obscured sources. At IR wavelengths shorter than 30 μm, ground based telescopes with large apertures at superb sites achieve diffraction-limited performance close to the seeing limit in the optical. At millimeter wavelengths, ground based interferometers achieve resolution that is close to this. The inaccessibility of the far-IR from the ground makes it difficult, however, to achieve complementary resolution in the far-IR.

The 1983 IRAS survey, while extraordinarily sensitive, provides us with a sky map at a spatial resolution that is limited by detector size on a spatial scale that is far larger than that available in other wavelengths on the ground. The survey resolution is of order 4′ in the 100 μm bandpass, and 2′ at 60 μm(*IRAS Explanatory Supplement*, 1988). Information on a scale of 1′ is available on some sources from the CPC. Deconvolution and image restoration using this database is one of the subjects of this workshop.

The highest spatial resolution in the far-IR has, however, for the last twenty years, been provided by the Kuiper Airborne Observatory (KAO). This telescope, in the fuselage of a C-141 transport plane based at NASA Ames Research Center, has been a mainstay for high resolution studies even preceding IRAS (Lester 1991). With optical components of quality high enough even for visible light studies, and commensurate tracking accuracy, diffraction-limited studies at far-IR wavelengths are possible ($\lambda/D=21''$ at 100 μm). From the time of its commissioning in 1974 through the publication of the IRAS survey, most of the far-IR studies with this telescope were done on spatial scales of an arcminute or so, not even approaching that ultimately achievable. Nevertheless, it is worth pointing out that all far-IR photometry ever done on the KAO has been done on scales considerably smaller than that of the IRAS survey. While the diffraction-limited resolution of the KAO is more than a factor of ten higher than that provided by the IRAS survey, the switched-beam background cancellation with that telescope puts an upper limit on the spatial scale that is transmitted. The secondary chopper on the KAO can exceed amplitudes of 10′, making for a spatial dynamic range of about 30 at 100 μm.

The accessibility of the KAO to instrument development teams has made it an observatory with a continually evolving instrument complement. Here new instruments can progress from the drawing board to the stratosphere in less than a year, and the design of these instruments and the modifications to them, can

S. Terebey and J. Mazzarella (eds.), *Science with High-Spatial Resolution Far Infrared Data*, 33–44, 1994, Jet Propulsion Laboratory, Pasadena, CA.

closely parallel, and directly address, timely astronomical questions. By virtue of its accessibility, the observatory promotes instrument development that is at the cutting edge of technology, where reliability and survivability is not a critical, expensive, and time-consuming proposition. High-risk, high payoff experiments are routinely accommodated. If an instrument doesn't work on one flight, it can more often than not be fixed before the next. It is reasonable to characterize the space IR astronomy that is done from the KAO in terms of the number of "launches" that it provides per year (about seventy).

CAPITALIZING ON THE SPATIAL RESOLUTION OF THE KAO IN THE FAR INFRARED

Starting in 1985, Paul Harvey and his team from the University of Texas made the first attempts to push the far-IR spatial resolution of the KAO to its ultimate limits. This required development of instrumentation with diffraction-limited detectors, and techniques for careful pointing. The first instrument to be used in this way was a three channel (0.8K bolometer) photometer, configured with diffraction-limited slits instead of large apertures. While the orientation of these slits on the sky was elevation and azimuth, careful flight planning allowed the slits to be scanned across astronomical sources at optimal angles.

It is important to understand that, while two dimensional spatial resolution is important, many of the most important questions in far-IR photometry hinge not so much on the detailed profile of an astronomical source, but simply on whether a large fraction of the luminosity of the source is from a component that is resolved at all. This question can easily be addressed with slit scans. For example, the optical depth (and hence dust column density) in a cloud, can be derived by comparison of its color temperature and brightness temperature. The latter requires an estimated size. The source of far-IR luminosity in galaxies with active nuclei remains a crucial problem and, for the more nearby galaxies, this problem can be reduced to whether the far-IR is point-like on the scale of the galaxy. This understanding provoked a lot of work with one dimensional slit scans by the Texas group over the next few years.

A novel guiding strategy was used to precisely scan the astronomical sources across the detector array. Motion of the photometer relative to the telescope is not permitted because of changing thermal offsets. The telescope itself had to be precisely moved across the sources. The low frequency end of the telescope stabilization loop is achieved, on the KAO, by video tracking on a star in the field. We move the telescope by precisely moving the camera, which is fiber coupled to the focal plane. As the camera feed moves across the focal plane in one direction, the tracking system moves the telescope in reflection. In this way, the telescope can be scanned precisely and reproducibly in a way that is independent of the (rather poor) isoplaneticity of the video tracker camera.

The success of high spatial resolution observations with diffraction- limited slits led to new generations of instruments with diffraction- limited detector arrays. The current Harvey et al. instrument employs a 2×10^3 He cooled bolometer array. Each detector in the array is sized $\lambda/D \times \lambda/2\mathrm{D}$, with the short axis of the detector aligned along the long axis of the array. Magnifying optics are used to make the array match the diffraction spot at either 50 or 100 μm.

The array can be scanned over bright sources, to give 2-D data (see below for Sgr A), or guided at a fixed location to give one dimensional profiles of faint sources (see below for NGC 4736).

A critical need for pushing the limits of spatial resolution on the KAO is the knowledge of, and stability of, the point source profile of the system. While at shorter wavelengths nature provides point sources in just about every field (background stars), and at longer wavelengths compact radio sources fit the bill, in the far-IR there are few reasonably bright objects that can be assumed, a priori, to be unresolved on a scale of a few arcseconds ($\sim \lambda/D$ in the 50, 100 μm bandpasses of the KAO photometer). As demonstrated much later by Hawkins (see below) using the KAO and IRAS, even red giants and supergiants can have far-IR structure on scales significantly larger than this. The sky is filled with sources that are intrinsically fuzzy in the far-IR, much more so than in the optical, for which point sources abound.

Solar system bodies are the only ones that are bright enough, and verifiably point like at our resolution. We have used the outer Galilean satellites (Ganymede and Callisto, sizes $\sim 1''$), Uranus ($\sim 4''$), and the brighter asteroids (Ceres and Vesta, sizes $<1''$) for this purpose. These objects are bright enough that, in most cases, the point source profile is not the limiting factor in the deconvolution. Other bona fide point-like sources are considerably fainter, and restricting ourselves to these five objects has sometimes resulted in serious constraints on the flight plans that can be carried out.

Fortunately, the stability of the point source profile is very good. This was verified early in our work, by looking at these sources several times in the course of a flight. In practice, the PSP stability is limited by the stability of the oscillating secondary mirror, which is moving the image by as much as $10'$ at more than 20 Hz. A new oscillating secondary mirror system, installed in 1989, was an important factor in our ability to do this work.

In the following, I present a retrospective covering some of the high points of high spatial resolution far-IR studies on the KAO. While this review concentrates on diffraction-limited studies by the Texas group, it should be clear to the reader that all of the work ever done on the KAO including, in particular, that done in beamsizes of order $1'$ by the Yerkes team is, by comparison to data from IRAS or balloon, very high spatial resolution also.

FAR INFRARED EMISSION FROM GALAXIES

Because of their relatively low flux levels, galaxies present a special challenge to high resolution studies in the far-IR. The easiest targets are those that are brightest, and that strongly selects nearby objects with high luminosity. Thus, with the modest aperture of the KAO, it is star forming regions and active galaxies that have received the most attention.

In addition to those individual objects that are discussed below, diffraction-limited scans of M82 (Joy, Lester, and Harvey 1987), the prototypical Seyfert 2 galaxy NGC 1068 (Lester et al. 1987), NGC 4945 (Brock et al. 1988), and Arp 299 (Joy et al. 1989) have been made.

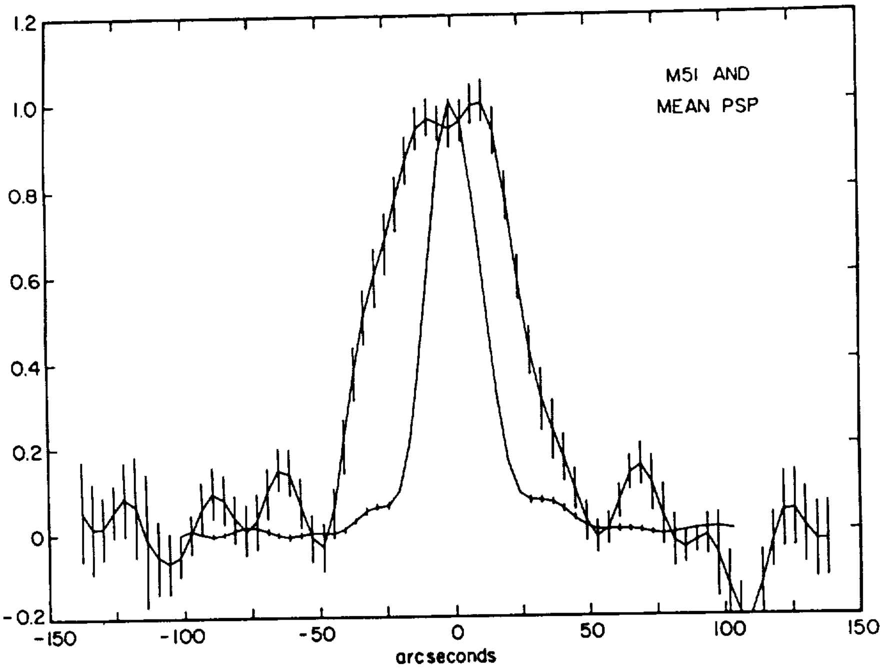

FIGURE 1 Co-added KAO slit scans at 100 μm across the nucleus of M51 are superimposed on a point source profile from observations of Vesta. The source is clearly resolved into two components.

M51

The limits of spatial resolution in the far-IR on the KAO were first probed, in galaxies, in M51. Scans across this nearby spiral galaxy constituted a first proof of the potential of our techniques on a relatively low surface brightness source. Figure 1 (Lester, Harvey and Joy 1986) shows co-added scans across the nucleus of M51 superimposed on a point source profile from identical scans across Vesta. The source is clearly resolved into double peaks, with separation 25″ (120 pc). In the context of a slit profile, this is most simply interpreted as ring of far-IR emission with that diameter. Two deconvolution algorithms (Richardson-Lucy, and MEM) were applied to the data, and these increased the contrast in the structure that was already evident in the raw data.

This structure corresponds well with that seen in CO interferometer studies, with spiral arms wrapping around the nucleus terminating in a nearly complete ring of this size (Rand and Kulkarni 1993). This structure also very nearly envelops the older nuclear bulge of the galaxy, as delineated well by near-IR continuum images (Thronson and Greenhouse 1988). The association of this far-IR structure with star formation around the nucleus is strongly supported by the optical images of Worden (1974).

It is worth noting at this point that, while M51 has been considered a test case for IRAS imaging and deconvolution techniques, that work pertains to a much larger scale. While the KAO observations do not have the S/N to easily detect the large scale emission (spiral arms, relationship to the companion) that is so accessible in the IRAS data, the structure that is seen in the KAO data is almost an order of magnitude smaller (25″ versus several arcminutes) than that available in the raw IRAS images, and a factor of several smaller than that seen in the best deconvolutions. This latter work is more comparable to the large beam KAO maps of Smith (1982).

ARP 220

Arp 220 (IC 4553) has been characterized as an "ultraluminous" galaxy that radiates almost all of its 10^{12} L$\odot$ in the far-IR. There is a rich literature on this galaxy, which shows evidence for a buried AGN. The optical extent of its disk, which is highly distorted, is more than 30″, corresponding to 10 kpc. KAO observations by Joy et al. (1986) showed conclusively, however, that the far-IR emitting region was a factor of four smaller than this, and most likely is produced in the nucleus. Using several deconvolution techniques, it was established that the 100 μm size of Arp 220 was less than 7.5″. Using this size to compare the color temperature to the brightness temperature, a far-IR optical depth in excess of 0.05 was derived. This in turn corresponds to a visual extinction of 25–50 magnitudes, which is consistent with the fact that the high nuclear velocity dispersion that is evident in the near IR is not seen in the visible (DePoy, Becklin, and Geballe 1987).

NGC 5128 (CEN A)

Ground based studies in the mid-IR have shown that the star formation in this galaxy is strongly concentrated in the dust lane that bisects it. Presumably this giant elliptical has swallowed whole a disk galaxy, and the gas attached to this disk galaxy is now involved in a strong starburst. High resolution scans of NGC 5128 in the far-IR were made from the KAO during its 1986 deployment to New Zealand. Scans at both 50 and 100 μm, perpendicular and parallel to the dust lane were obtained. The resulting profiles give a wealth of information (Joy et al. 1988). The 100 μm profiles are shown in Figure 2, where they are compared (with common scale and orientation) to an optical photograph.

The profile perpendicular to the disk (left side of figure) clearly shows that most of the far-IR emission is concentrated to the dark lane. ¿From the mid-IR work of Telesco (1978), this is not unexpected. The extent of the far-IR emission to high z, well away from the dust lane, was not expected, and suggests that

FIGURE 2 (*over*) Slit scans at 100 μm parallel and perpendicular to the dust lane in NGC 5128 are scaled and oriented for comparison with an optical photograph. Three separate emission components are clearly visible—extended emission from the starburst disk along the plane, extended emission at large z distances, and emission from an unresolved point source coincident with the nonthermal nucleus. The slit length is approximately 40″.

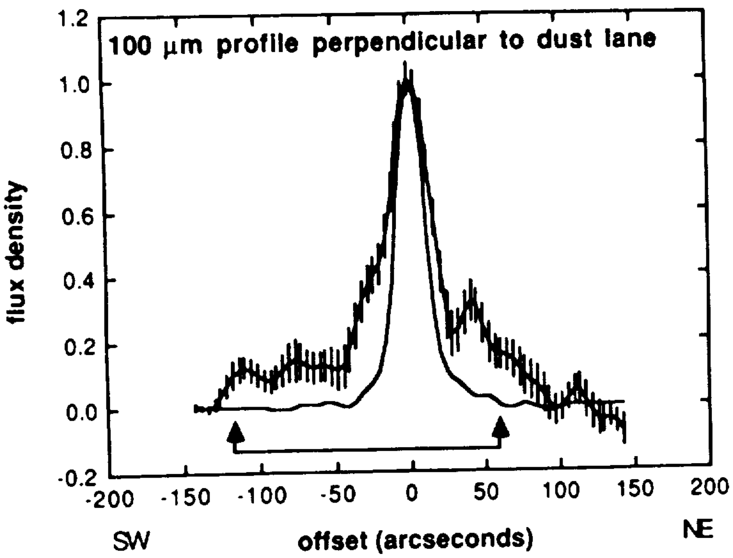
100 μm profile perpendicular to dust lane
flux density
1.2
1.0
0.8
0.6
0.4
0.2
0.0
-0.2
-200
-150
-100
-50
0
50
100
150
200
SW
offset (arcseconds)
NE

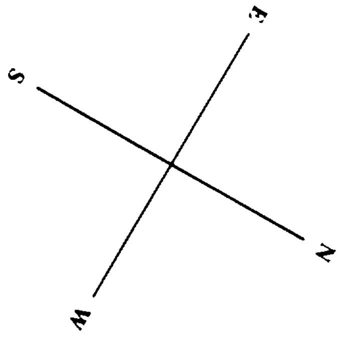
E
S
N
W

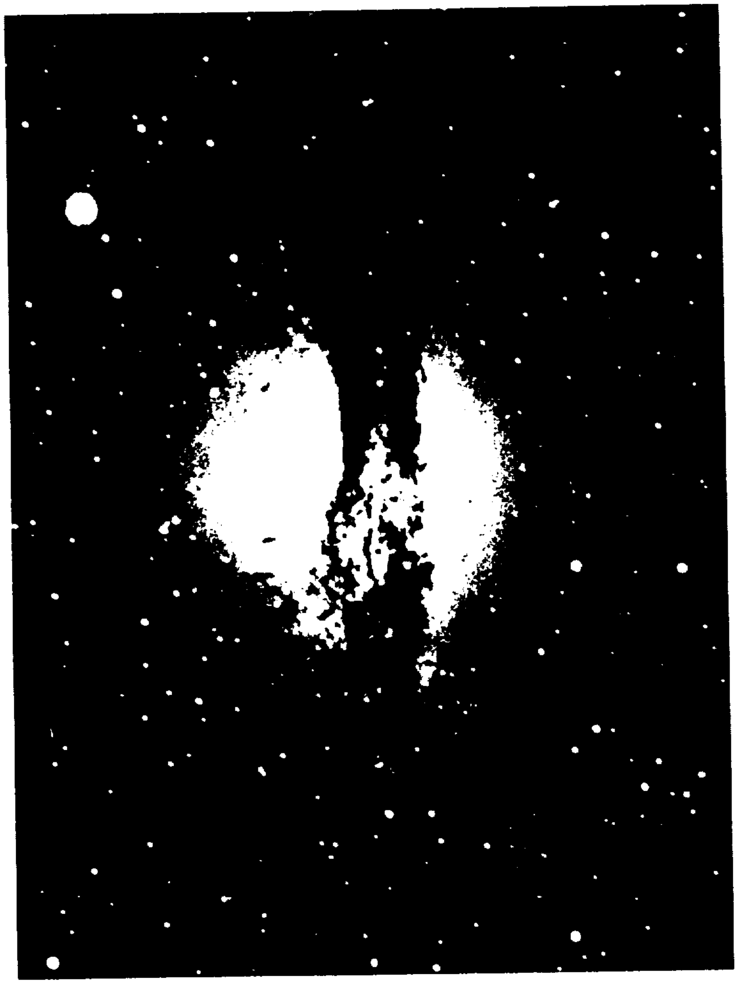

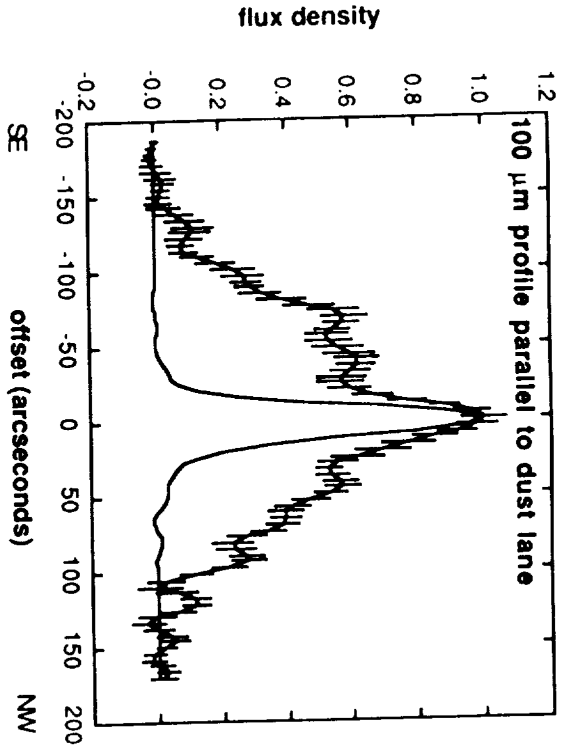
100 μm profile parallel to dust lane
flux density
1.2
1.0
0.8
0.6
0.4
0.2
-0.0
-0.2
-200
-150
-100
-50
0
50
100
150
200
SE
offset (arcseconds)
NW

dust at high latitudes contributes substantially to the luminosity of this galaxy. This dust is not heated by the central source, but by star formation in situ, or perhaps by the interstellar radiation field of a quiescent bulge population. The slit scan along the dust lane shows that the star formation is fairly uniform along the disk, to the outermost optical isophote of the bulge, but shows a marked unresolved peak that is coincident with the nuclear radio source. The extended equatorial emission has a profile that is well fit by a uniform disk model, and poorly fit by a thin ring. Thus the star formation in the disk of NGC 5128 is not restricted to those bits of peripheral pieces that we can see optically, but probably covers the disk.

NGC 4736

This galaxy shows a compact, high surface brightness bulge that, while relatively blue, shows no sign of ongoing star formation. The bulge is surrounded by a ring of ionized and molecular gas with a radius of about 50″ (1.6 kpc) that is clearly dominated by star formation. The far-IR profile across the galaxy shows striking differences compared with both the red starlight and the ionized gas. This comparison is shown in Figure 3 (Smith et al. 1991). In this face-on ringed galaxy, the morphological distinction between bulge stars (F-band profile) and star formation (H-alpha profile) is evident. Integrated-light studies of the far-IR emission from galaxies in the IRAS survey show that, while far-IR emission is dominated by star formation in many galaxies, in quiescent galaxies the far-IR emission comes from thermalization of diffuse starlight by interstellar grains. Our high resolution profiles of NGC 4736 show both mechanisms at work in different parts of the same galaxy. Note that the 100 μm profile in this galaxy resembles neither the quiescent bulge light or the star formation in the ring closely. Unlike the H-alpha profile, the 100 μm profile is peaked in the center. The far-IR emission from the inner parts of NGC 4736 is thus dominated by diffuse starlight. The elevation in the shoulders of the 100 μm profile at the H-alpha ring radius shows that this emission is from star formation.

FAR INFRARED EMISSION FROM STAR FORMATION REGIONS

Unlike for galaxies, star formation regions tend to be extraordinarily bright. With a surfeit of signal-to-noise, these objects are the ones that truly push the limits of image restoration in the far-IR. In fact, it is our conclusion that, for these objects, it is our poorer understanding of the point source response function that limits our work here (solar system "point" sources are considerably fainter).

In addition to those objects described in more detail below, diffraction-limited far-IR KAO data on W3OH (Campbell et al. 1989), Cep A (Ellis et al. 1990) and Sgr B2 (Goldsmith et al. 1992) have been obtained. For the prototypical disk source S106 (Harvey et al. 1987), the KAO data suggests far-IR elongation along the disk diameter, presumably reflecting the mass morphology. Recent work by DiFrancesco et al. (1993) on Herbig Ae/Be stars shows that a majority of these stars are resolved in the far-IR on scales very much larger than that of their predicted disks.

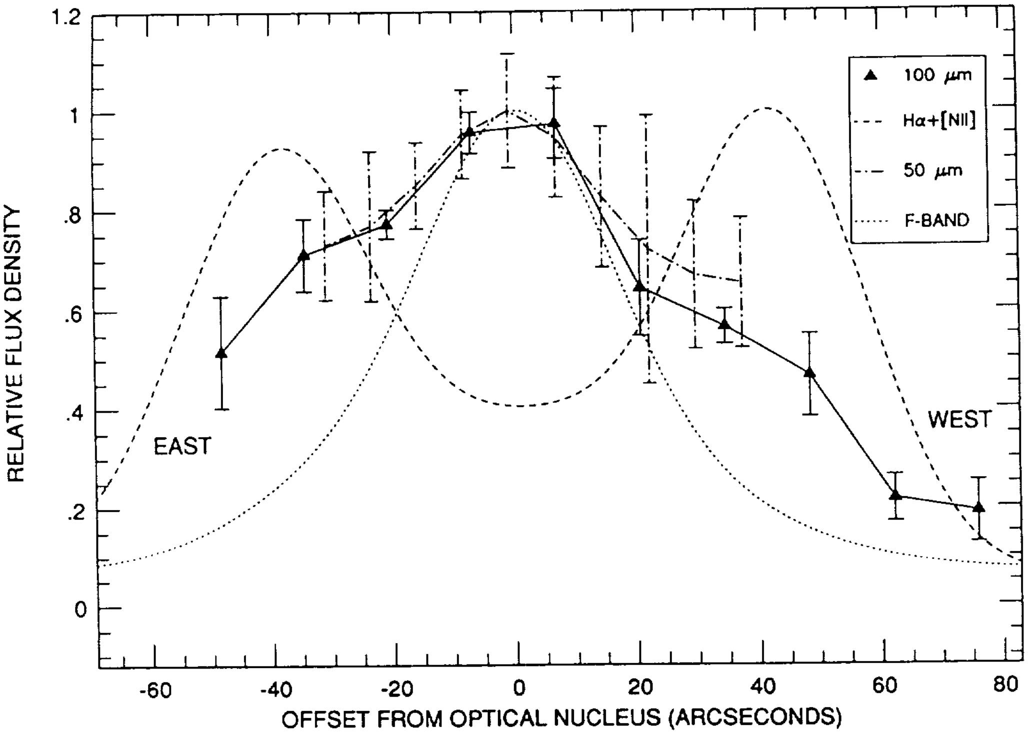

FIGURE 3 Profiles of the ringed galaxy NGC 4736. The far-IR emission follows the profile of diffuse starlight in the inner regions, yet shows enhancement at the radius of the starburst ring. Two dominant mechanisms for production of far-IR emission in galaxies are thus clearly spatially resolved for the first time in a single galaxy.

S140

Sharpless 140 was the first astronomical object studied with these techniques (Lester et al. 1986a). The temperature and density gradient across the S140 ionization front was clearly shown in these slit scans, which were oriented to sample the front with the highest resolution. In this object, the utility of Fourier "beam matching" was demonstrated, giving identically matched resolution at both 50 and 100 μm, and allowing direct ratioing of data at these two very different wavelengths.

L1551 IRS5

Slit scans along, and perpendicular to the outflow axis and putative disk in L1551 IRS5 were carried out by Butner et al. (1991). Simple deconvolution of these data show that the source is resolved on a 10″ scale at 100 μm, fully a factor of two smaller than the diffraction spot. There is some evidence that the far-IR source is slightly elongated with the flow. Comparison of these profiles to radiative transfer codes constrain the density profile through the source.

G05.89

This remarkable compact HII region and molecular outflow source is perhaps the ultimate test for spatial resolution in the far-IR, since it is extraordinarily bright (Harvey et al. 1993). The source was barely resolved by the KAO, on scales more than a factor of two below the diffraction limits ($6''$ at 50 μm, $9''$ at 100 μm). The high far-IR surface brightness corresponds to a brightness temperature that is actually fairly similar to the color temperature, and thus the source must be optically thick in the far-IR. Comparison with radiative transfer codes indicates a 100 μm optical depth of at least 2, and perhaps 5–10, as well as a steep density gradient. Using a canonical extinction law, visual extinctions of order several thousand are implied, making this the most optically thick source yet seen.

FAR INFRARED EMISSION FROM EVOLVED STARS

It is now well understood that many AGB stars are decidedly non-point like in the far-IR. While the work of Lester et al. (1986b) on IRC10216 indicated that much of the light from this source came from a compact region, it seems likely that a substantial fraction is emitted in this source, on a scale that is large compared to the KAO diffraction disk. The KAO work of Hawkins and Zuckerman (in preparation) shows, for example, that μ Cep is clearly resolved in the far-IR. Models of its small scale emission profile from the KAO, when compared with emission from its more extended envelope (from IRAS data) suggest large changes in the mass loss rate. It appears that the inner, more recent mass loss has been taking place at a rate about a factor of ten lower than that in the envelope.

FAR INFRARED EMISSION FROM THE GALACTIC CENTER

Recent work on Sgr A by Davidson et al. (1992) has been done from the KAO by scanning a linear array of bolometers, thus creating two-dimensional images. Application of a maximum entropy algorithm to this data produces a remarkable picture of the central few parsecs of our galaxy. The double-lobed emission there is clearly resolved, and it is centered on Sgr A*. Comparison of the KAO far-IR maps to molecular data is revealing (see Figure 4). While the molecular clouds in the vicinity of Sgr A are distributed in a ring-like structure, of diameter ~3pc, the far-IR emission is produced on the inside edge of this ring. Radiative transfer models show that the data is consistent with a flared-disk geometry inclined 60 degrees to our line of sight, with a 0.9 pc cavity at the center.

THE FUTURE OF HIGH SPATIAL RESOLUTION IN THE FAR INFRARED

Work in the last ten years has shown clearly that image restoration work from an airborne platform is highly profitable. Modest aperture diffraction limited space telescopes (ISO, SIRTF, Edison) of the future will provide enormous increases in sensitivity and, to some extent, these increases in sensitivity can be harnessed to

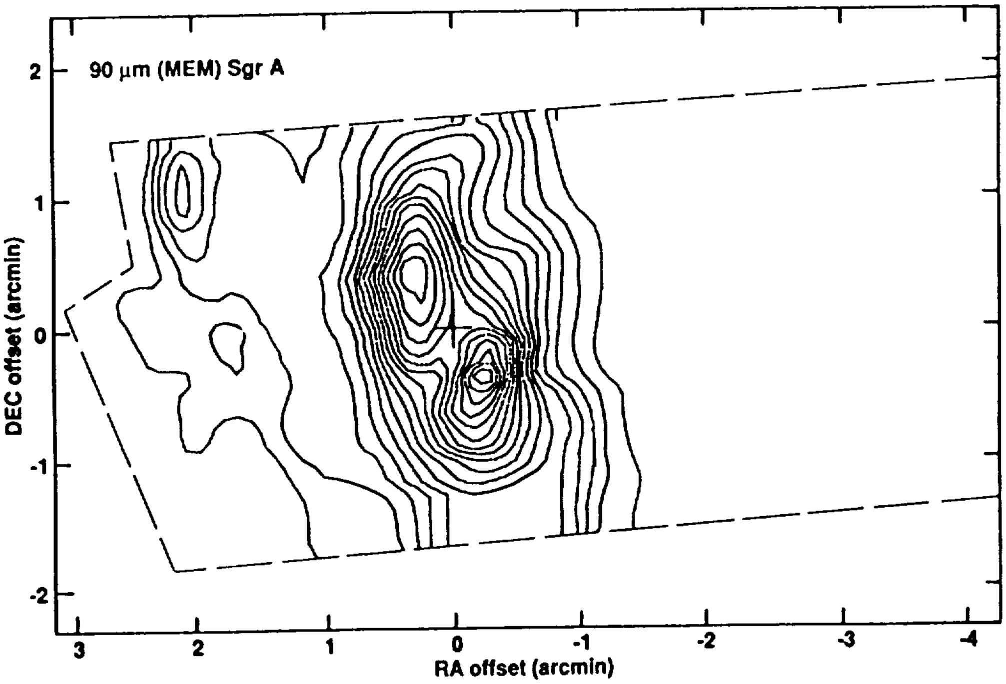

FIGURE 4 This far-IR continuum map of Sgr A was generated using a row-by-row maximum entropy image restoration routine on a map produced by scanning a linear array (1 × 8) of bolometers across the source. North is up and east is to the left. The beamshape in the reconstruction is roughly circular. The two far-infrared peaks in Sgr A are clearly distinguished, and are seen to have small scale elongations. This emission is nearly circumscribed by molecular gas seen in HCN and CO. The southern extension of the northern component of the pair is from a compact source, roughly coincident with IRS1, that dominates the map at shorter wavelengths.

provide, through image restoration, enhancements in spatial information. The fact remains, however, that for reasonably bright sources (and it should be noted that most of the sources that define infrared astronomy are, even in this post-IRAS era, bright sources), the biggest gain in spatial resolution comes with the largest aperture, however.

The Stratospheric Observatory for Infrared Astronomy (SOFIA) will answer this challenge. With an aperture of 2.5 m, SOFIA will provide a factor of three increase in spatial resolution over the KAO, as well as more than a factor of ten in sensitivity. For tens of thousands of the brightest far-IR sources, SOFIA will provide several times higher spatial resolution than any other space facility. Endorsed by the Bahcall panel as the highest priority new medium-price NASA mission, SOFIA is well studied, and ready to develop. With a twenty year operational lifetime, SOFIA will be used with a hundred different instruments in the course of its lifetime, each one optimized for a specific task. The accessibility of an airborne platform will, as it has for the KAO, encourage new technology that is not yet robust enough for space missions. Thus, SOFIA will always be equipped with leading-edge instrumentation. The hands-on instrumentation expertise that SOFIA will develop will be precisely that which, with a little foresight, we will need for the long-term future of high spatial resolution far-IR measurements, with large apertures in earth orbit or on the moon.

REFERENCES

Brock, D., Joy, M., Lester, D.F., Harvey, P.M., and Ellis, H.B. Jr. 1988, *ApJ*, **329**, 208

Butner, H.M., Evans, N.J. II, Lester, D.F., Levreault, R.M., and Strom, S.E. 1991, *ApJ*, **376**, 636

Campbell, M.F., Lester, D.F, Harvey, P.M., and Joy, M. 1989, *ApJ*, **345**, 298

Davidson, J.A., Werner, M.W., Wu, X., Lester, D.F., Harvey, P.M., Joy, M., Morris, M. 1992, *ApJ*, **387**, 189

DiFrancesco et. al. 1993, in preparation

DePoy, D., Becklin, E.E., and Geballe, T.G. 1987, *ApJ*, **316**, L63

Ellis, H.B. Jr., Lester, D.F., Harvey, P.M., Joy, M., Telesco, C.M., Decher, R., and Werner, M.W. 1990, *ApJ*, **365**, 287

Goldsmith, P.F., Lis, D.C., Lester, D.F., and Harvey, P.M. 1992, *ApJ*, **389**, 338

Harvey, P.M. et al. 1993, in preparation

Harvey, P.M., Lester, D.F., and Joy, M. 1987, *ApJ*,l, **316**, L75

Hawkins and Zuckerman. 1993, in preparation

IRAS Catalogs and Atlases: Explanatory Supplement 1988, ed. C.A. Beichman, G. Neugebauer, H.J. Habing, P.E. Clegg, and T.J. Chester (Washington, DC: GPO)

Joy, M., Lester, D.F., and Harvey, P.M. 1987, *ApJ*, **319**, 314

Joy, M., Lester, D.F., Harvey, P.M., and Ellis, H.B. Jr. 1988, *ApJ*, **326**, 662

Joy, M., Lester, D.F., Harvey, P.M., and Frueh, M. 1986, *ApJ*, **307**, 110

Joy, M., Lester, D.F., Harvey, P.M., Telesco, C.M., Decher, R Rickard, L., and Bushouse, H. 1989, *ApJ*, **339**, 100

Lester, D.F. July/August 1991, *Stardate Magazine*

Lester, D.F., Harvey, P.M., and Joy, M. 1986a, *ApJ*, **302**, 280

Lester, D.F., Harvey, P.M., and Joy, M. 1986b, *ApJ*, **304**, 623

Lester, D.F., Joy, M., Harvey, P.M., Ellis, H.B. Jr, and Parmar, P. 1987, *ApJ*, **321**, 755

Lester, D.F., Harvey, P.M., and Joy, M. 1986, *ApJ*, **302**, 280

Rand, R. and Kulkarni, S. 1993, preprint

Thronson, H., and Greenhouse, M. 1988, *ApJ*, **327**, 671

Smith, B.J., Harvey, P.M., Colome, C., Zhang, C.Y., DiFrancesco, J., and Pogge, R.W. 1991, *ApJ*, **373**, 66

Smith, J. 1982, *ApJ*, **261**, 463

Telesco, C.M. 1978, *ApJ*, **226**, L125

Worden, P. 1974, *Pub. A.S.P.*, **86**, 92

A HIGH RESOLUTION ATLAS OF THE GALACTIC PLANE AT 12 μm AND 25 μm

STEPHAN D. PRICE
Geophysics Directorate, Phillips Laboratory

ROSE M. KORTE, REBECCA S. SAMPLE, AND JOHN P. KENNEALY
Mission Research Corporation

ROBERT A. GONSALVES
Electro-Optics Center, Tufts University

ABSTRACT High resolution images of the 12 μm and 25 μm IRAS survey data from each HCON crossing the Galactic Plane are being created for those regions that the original IRAS processing labeled as confused. This encompasses the area within 100° longitude of the Galactic Center and within 3° to 10° of the Plane. The procedures used to create the images preserve the spatial resolution inherent in the IRAS instrument. The images are separated into diffuse and point source components and candidate sources are extracted from the point source image after non-linear spatial sharpening. Fluxes are estimated by convolving the candidate sources with the point response function and cross-correlating with the original point source image. A source is considered real if it is seen on at least two HCONs with a rather generous flux match but a stringent position criterion. A number of fields spanning a range of source densities from low to high have been examined. Initial analysis indicates that the imaging and extraction works quite well up to a source density of about 100 sources per square degree or down to roughly 0.8 Janskys.

INTRODUCTION

The present effort to improve the resolution of the IRAS data products arises from an interest in using such observations to study the structure of the Galaxy. Chester (1986) has shown that at a 12 μm limiting sensitivity of 0.4 Jy, IRAS could detect the moderately bright infrared beacons at least to the Galactic Center. However, previous studies of the properties of the inner Galaxy using the IRAS data (e.g., the shape of the bulge and distribution of AGB stars by Habing et al. (1985) and Habing (1986) and the warping of the Plane derived by Djorgovsky and Sosin (1989)) have discarded the IRAS Point Source Catalog (PSC) (Version 2 1988) data along the Galactic Plane as unreliable due to confusion, precisely in the region most sensitive to the distribution parameters sought. Weinberg (1992a, 1992b) argued that a color-selected sample of objects could be chosen from the PSC which were both bright enough that the PSC completely

S. Terebey and J. Mazzarella (eds.), *Science with High-Spatial Resolution Far Infrared Data*, 45–54, 1994, Jet Propulsion Laboratory, Pasadena, CA.

sampled them and of sufficiently uniform luminosity to trace the mass distribution. From this sample, Weinberg concluded that (1992a) the inner Galaxy was barred rather than having a 4 Kpc ring and (1992b) there was no evidence for a mid-infrared Galactic Bulge. Canterna et al. (private communication), on the other hand, found several different populations of objects in the direction of $l = 30°$ based upon color and apparent scale height and concluded that major constituents of the inner Galaxy were inadequately sampled due to confusion.

We have processed the IRAS survey data to obtain 12 μm and 25 μm images along the Galactic Plane which preserve the inherent spatial resolution of the IRAS instrument. Sources are extracted from each HCON image based on a signal-to-noise criterion. The source lists from the three HCONs are matched with a rather loose flux criterion and a more stringent position criterion. Based on the dLogN/dLog S vs Log S plots, the current processing seems to work well up to source densities of about 100 per square degree. This is some two to four times higher than the practical limit to the PSC. For two moderate density fields, one in the Plane at $l, b \sim (35°, -0.4°)$, the other at the edge of the Galactic Bulge ($l, b \sim 335.4°, 2.4°$) the "completeness" of the source counts were extended from 2.5 Jy in the PSC to 0.6-0.8 Jy. While the flux agreement between the PSC and the current processing is, in general, quite good, some notable exceptions exist where we have resolved sources that the PSC processing has combined into a single object.

PROCESSING

Initially, our intent was to super-resolve the IRAS survey data on the Galactic Plane with the Filtered Entropy Restoration described by Kennealy et al. (1987), Korte et al. (1989) and Gonsalves et al. (1990). Since this approach uses Fourier transform multiplications for the filtering required by the restoration, it is much faster than the equivalent matrix multiplications used by IPAC's YORIC or Gull and Skilling's MEMSYS. The Filtered Entropy Restoration produces comparable resolution and intensity distributions as the more complex algorithms and is computationally much faster, an important factor given the volume of data to be processed. However, in order for the Fourier Transform based procedure to work at best fidelity, the IRAS "footprint" data has to be projected onto a rectilinear grid with a routine that "whitens" the image resulting in an isoplanatic response function.

Since the primary objective of this effort is to enumerate and quantify the discrete sources down to relatively low signal-to-noise in the high density regions along the Galactic Plane, we subsequently decided it best to extract sources at the regridded stage and use the multiple images from the different HCONs to improve reliability of the flux estimates and confidence in the derived source lists. Sources are extracted from each of the three HCON grids and a two-out-of- three confirmation is used. In contrast, all the data have to be used together to fully realize the resolution enhancement of the maximum entropy procedure. Furthermore, the additional sources we expect to detect are at a signal-to-noise of five to 15 and the resolution of maximum entropy enhancement is known to vary as an inverse function of signal-to-noise (Narayan and Nityananda, 1986).

IMAGE GENERATION

IPAC has provided us with IRAS survey footprint data covering the Galactic Plane in roughly 6° × 6° fields. Each plate of these regions is divided into four overlapping quadrants covering 3.5° × 3.5°. Scan data in these fields are sorted by scan angle and SOP into three groups. Scans with nearly the same scan angle and SOPs closely spaced in time form a group which usually, but not always, corresponds to an HCON. Noise is estimated for each detector by high-pass filtering the data, then iteratively adjusting the rms value by rejecting deviations greater than 2.8σ. The high-pass filter is a Wiener filter which extracts the high-frequency noise component from the data stream of each detector scan. The resulting noise compares favorably with that determined with other methods such as the zero sum filter described in the *IRAS Explanatory Supplement* (1988).

The data from each detector scan are separated into a low frequency or background component and a point or small extended source component. The in-scan background is estimated by a lower bound numerical fitting procedure using a ten sample support. Thus, variations with coherency spanning a width of three detectors or greater than $2'$ are included in the background file; more rapid variations are put into a high frequency file. Residual striping is estimated by comparing the in-scan averages in the background file with the cross scan profiles. These baselines are removed. Since a lower bound is used (a few negative points are allowed) the result is biased for the noisy channels; the high frequency values are slightly too large and the background is somewhat too low. The bias adjustment in the background image compensates for the bias in this file.

A background and a source image is created for each quadrant by interpolating the data to an 876 × 876 point grid of 14.4 arc-second pixels. At each grid point, i_m, the brightness, f_g, is calculated by a minimum mean square error interpolation of the nearest twelve data values, d_k, from the irregularly spaced scans. The weights used in the interpolation are such that the resulting image is "whitened" to a uniform model isoplanatic response function, h_m . The model response is an average of the response functions of the largest detectors in the array, made even and symmetric by reflecting the leading response about the median peak to eliminate the tails, then averaging the result of folding the mean response function about the in-scan and cross-scan axes centered on the function. The end product is symmetric about any line drawn through the center of the function. The calculation of the interpolation weights requires the solution of a twelfth-order matrix equation involving the statistical averages of $d_k d_j$ and $d_k i_m$. In essence each scan is convolved with the transpose of the applicable point source response function centered on the cross-scan offset of the grid point in question. The detector response functions, h_d, are those of Moshir (private communication) which are described in the *Explanatory Supplement to the IRAS Faint Source Survey* (Moshir et al. 1992). Weights are assigned to the result proportional to the inverse of the noise of the detector that generated the data point. This 3 × 4 matrix is multiplied by the inverse matrix of the detector response centered on a data point and the transpose centered on the grid point (both suitably weighted by the noise) convolved with a model response.

Mathematically:

$$f_g = (h_d h_d^t + \mathrm{NSR})^{-1} h_m h_d^t F_d,$$

where NSR is a local noise-to-signal ratio and F_d is the vector of twelve data values. There is a slight amount of smoothing to the extent that h_m is slightly larger than h_d for some of the detectors.

The background and source images are added to produce the total image for the quadrant field. A noise grid is also generated based on the weighted averages of the noises multiplied by the whitening matrix.

SOURCE EXTRACTION

An iterative mean square error (mse) gradient image enhancement routine with a positivity constraint is used to sharpen or increase the resolution of the source image. If the stellar fluxes of amplitude a_i are distributed with a position variable x_i such that

$$s(x) = \sum a_i \delta(x - x_i)$$

which is related to the observed source map by

$$d(x) = s(x) * p(x) + n(x)$$

then the sharpening algorithm is

$$\begin{aligned}
s_n &= n^{th} \text{ estimate of } s(x) \\
&= s_{n-1} + \alpha g(x) > 0 \\
\alpha &= \text{step size } = \frac{\int v(x) e(x) dx}{\int v^2(x) dx} \\
v(x) &= g(x) * p(x) \\
g(x) &= \text{mse gradient } = -2\, \epsilon(x) * p(x) \\
\epsilon(x) &= \text{error} = d(x) - s_{n-1}(x) * p(x)
\end{aligned}$$

Potential sources are at the positions of the peaks of positive excursions from the local background in the sharpened source image. The source lists are subsequently thresholded to be greater than a local signal-to-noise ratio of 4.5. The SNR value was empirically chosen based on eliminating spurious sources in several fields of moderately high source density.

Fluxes are estimated by cross-correlating the positions of the extracted source convolved with the model response function and the match-filtered source image.

$$\begin{aligned}
z(x) &= \text{match-filtered source image } = d(x) * p(x) \\
d(x) &\approx s(x) * p(x) \quad \text{(plus noise)} \\
z(x) &\approx s(x) * p(x) * p(-x) = s(x) * r(x)
\end{aligned}$$

where $r(x)$ is the autocorrelation function of $p(x)$. Since

$$\begin{aligned} s(x) &= \sum a_i \delta(x - x_i), \\ z(x) &\approx \sum a_i r(x - x_i), \end{aligned}$$

which is the flux-weighted sum of the autocorrelation functions centered on the positions of the extracted sources. We evaluate $z(x)$ at the locations, x_k, and solve

$$z(x_k) = \sum a_i r(x_k - x_i) \text{ for the } a_i\text{'s.} \tag{1}$$

In crowded regions, the flux errors for overlapping sources couple with the position errors. We combine these errors by calculating a multiple-parameter Cramer-Rao bound using the Fisher information matrix. The errors are bounded in that they can be no smaller than the Cramer-Rao bound. The local signal-to-noise is increased by the ratio of the square root of the maximum in the autocorrelated response function to the peak input value. In the present case, the gain is about 6.7 for well-isolated sources. Part of this gain comes from smoothing the source image with a matched filter. The rest arises from the fact that the autocorrelation function used in the parameter estimation spans three to four samples of in-scan data from four to five detectors in an HCON. The autocorrelation is a weighted co-addition of these data points which, if the noise is uncorrelated, will improve the signal-to-noise. The "noise" due to confusion decreases this gain by an inverse function of the area common to overlapping sources.

A flux criterion and the distance between candidate sources were used in matching sources from different HCONs. The position uncertainties are well represented by Gaussian distributions; the procedures used to image sharpen the uncertainty distribution from the convolution of a Gaussian with a unit response (CGU) described in the *IRAS Explanatory Supplement* (1988) and by Fowler and Rolfe (1982). A source was included in the Galactic Plane catalog if a position match was found for at least two of the three HCONs and the flux measured on HCON1 was within a factor of two of that from HCON2; no flux criterion was used for matches with HCON3 sources. The output from the matches are positions, fluxes, the errors in these quantities, the SNR, and correlation coefficients derived from the match. The 12 μm and 25 μm lists are band-merged using a position criterion similar to that for the HCON matching. The individual HCON lists are examined for possible matches in the missing color if no band merge has occurred. If such a match is found, it is included in the final source list and appropriately annotated.

RELIABILITY AND COMPLETENESS

It is difficult to estimate the reliability and completeness of the sources detected by these procedures, as comparisons with internal and external source lists are limited. The source selection criteria on flux and number of times observed are certainly less restrictive than those used to create the PSC. On the other hand, the position matching is significantly tighter in the cross-scan direction. At the moment, our best estimates are inferential and qualitative. The reliability and completeness should be acceptably high because:

- for 24 3.5° × 3.5° fields we detect >95% of the PSC FQAL=3 sources, and more than half these fields have >98% association rate in the high density regions. There are no significant differences between our positions and those from the PSC. The linear regression between our fluxes and those from the PSC have a slope of 1 and an intercept of 0 within the respective errors. The standard deviation in the fit tends to be higher than the 5% calibration accuracy given in the Explanatory Supplement. This is traced to a broadening of the distribution at the fainter end of the regression and a few outliers where we resolve what the PSC classifies as a single source.
- the log N vs log S plots to fainter levels are consistent with the brighter counts from the PSC. The slopes of the log N vs log S plots are steeper, with physically more plausible values than that derived from the PSC alone. A typical set of flux vs density diagrams is shown in Figure 1. Figure 1a is the result derived from the PSC, while Figure 1b is that from the present study's Galactic Plane Catalog (GPC) for the same field.
- the differential flux vs density plots turn over sharply below the estimated completeness level, as seen below in Figure 2. A cursory examination of a few fields indicates that the source lists may be reliable and complete up to a source density of about 100 objects per square degree or down to a flux of about 0.8-1.0 Jy at 12 μm and 0.6-0.8 Jy at 25 μm. A noise-dominated distribution increases the slope as observed for the low density region shown in Figure 3. Scans from two of the HCONs for this field are, unfortunately, nearly parallel and phased such that the noisy detectors overlap, producing an overabundance of coincidences on noise peaks.

There are several analyses by which we hope to quantify reliability and completeness. The University of Wyoming is using MEMSYS-5 to super-resolve a number of IRAS AO's near the Galactic Plane. We will compare the survey results with this data set, which is independent both in acquisition and the method of restoration. We will use the mini-survey to compare the results of a two-out-of-three criterion with that derived from a larger number of images. We will randomize the positions of two of the HCONs for several fields to estimate the number of coincidental agreements.

RESULTS

For the 24 fields surveyed, the effort described in this paper produces from two to four times as many sources as in the PSC. If the qualitative arguments regarding completeness and reliability are valid, then we have indeed achieved our objective of improving the source counts along the Galactic Plane. Log_{10} (F_{12} / F_{25}) plots for an area in the Galactic Plane at $l \sim 35°$ and at the edge of the bulge ($l \sim -4.6°$, $l \sim 2.3°$) show a distribution sharply peaked near a value

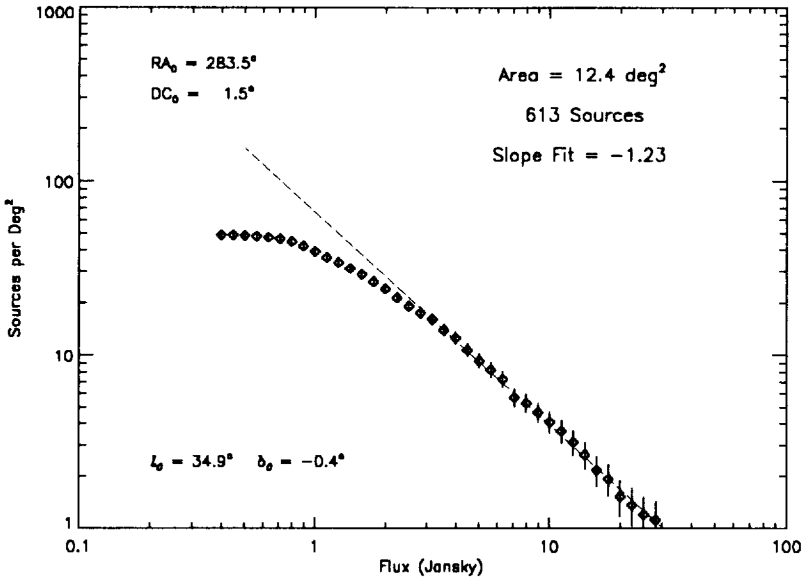

Figure 1a. Distribution of PSC Sources

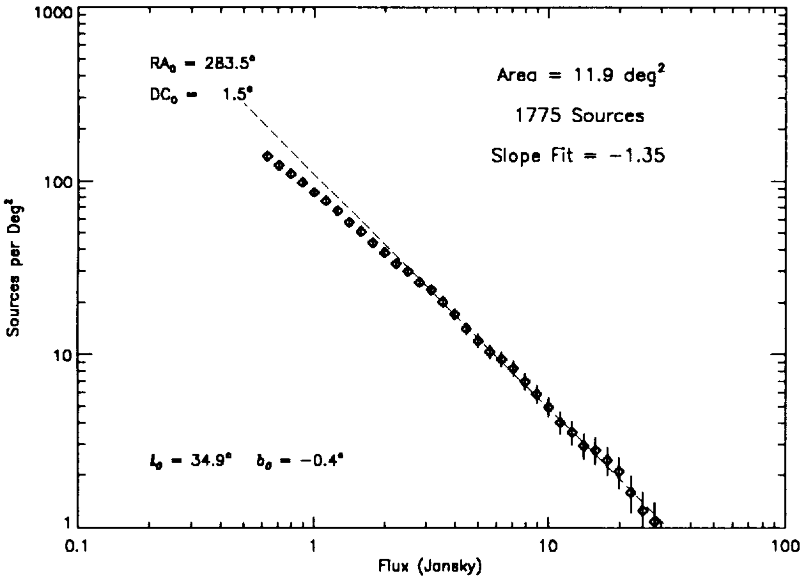

Figure 1b. Distribution of GPC Sources

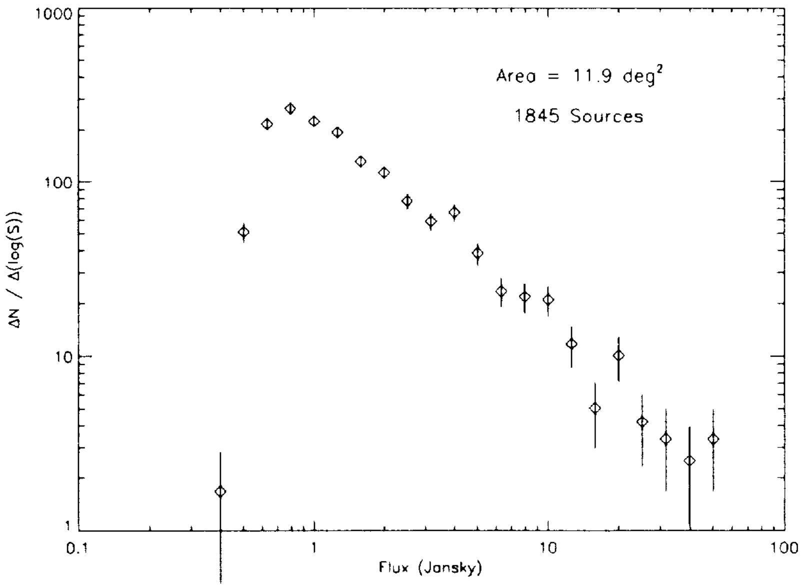

Figure 2a. Differential Band 1 (12μm) Distribution

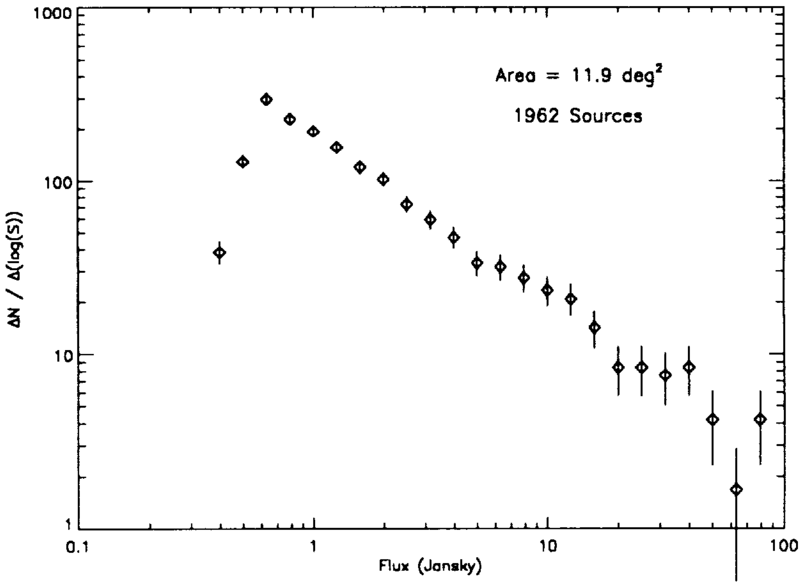

Figure 2b. Differential Band 2 (25μm) Distribution

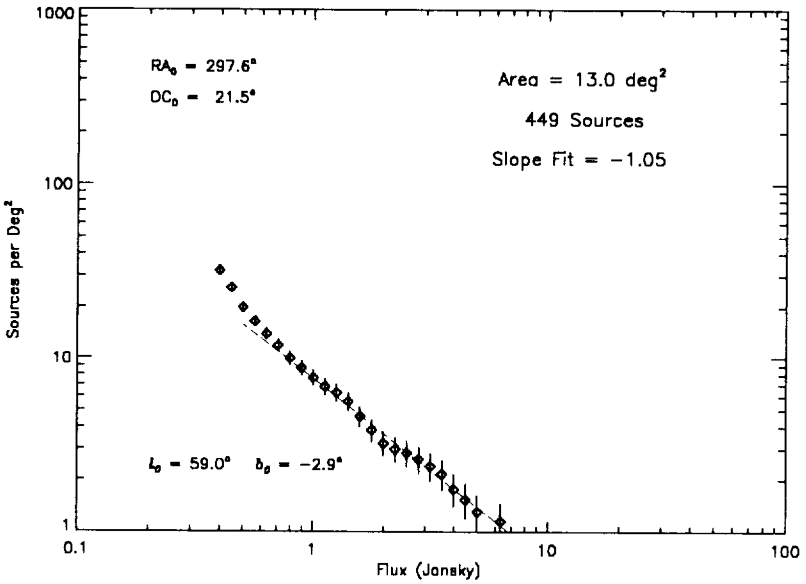

Figure 3. Low-density Band 1 data

of 0. This is similar to what Weinberg (1992b) found for the variable AGB stars he used as structure tracers. Unfortunately, this value for the peak is almost forced by the fact that most of the stars in a given field will have fluxes near the cutoff and the sensitivities at 12 μm and 25 μm are nearly the same.

REFERENCES

Chester, T.J. 1986, in *Light on Dark Matter*, ed. F.P. Israel, Dordrecht: Reidel, 3

Djorgovski, S., and Sosin, C. 1989, *ApJ*, **341**, L13

Fowler, J.W., and Rolfe, E.G. 1982, *Journal of Astronautical Sci.*, **Vol. XXX, No. 4**, pp. 385-402

Gonsalves, R.A., Kennealy, J.P., Korte, R.M., and Price, S.D. 1990, in *Maximum Entropy and Bayesian Methods*, ed. P.F Fougere, Kluweter Academic Press (Neth), 369

Habing, H.J. 1986, in *Light on Dark Matter*, ed. F.P. Israel, Dordrecht: Reidel, 329

Habing, H.J., Olnon, F.M., Chester, T. Gillett, F.C., Rowan-Robinson, M., and Neugebauer, G. 1985, *A&A*, **152**, L1

IRAS Catalogs and Atlases: Explanatory Supplement. 1988, ed. C.A. Beichman, G. Neugebauer, H.J. Habing, P.E. Clegg, and T.J. Chester (Washington, DC: GOP)

Kennealy, J.P., Korte, R.M., Gonsalves, R.M., Lyons, T.D., Price, S.D., LeVan, P.D., and Aumann, H.H. 1987, in it Advances in Image Processing, Proc. SPIE, **804**, 16

Korte, R.M., Kennealy, J.P., Gonsalves, R.A., and Wong, C. 1989, "Analysis of IR Celestial Survey Experiments, AF Geophysics Lab. Technical Report, *GL-TR-89-0265*

Moshir, M., et al. 1989, *Explanatory Supplement to the IRAS Faint Source Survey* (Pasadena: JPL)

Narayan, R., and Nityananda, R. 1986, *ARA&A*, **24** , 127

Weinberg, M. 1992a, *ApJ*, **384** , 81

Weinberg, M. 1992b, *ApJ*, **392**, L67

N95- 21756

7

6

CONSTRAINTS AS A DESTRIPING TOOL FOR HIRES IMAGES

YU CAO AND THOMAS A. PRINCE
Department of Physics, California Institute of Technology
Pasadena, CA 91125

ABSTRACT Images produced from the Maximum Correlation Method sometimes suffer from visible striping artifacts, especially for areas of extended sources. Possible causes are different baseline levels and calibration errors in the detectors. We incorporated these factors into the MCM algorithm, and tested the effects of different constraints on the output image. The result shows significant visual improvement over the standard MCM method. In some areas the new images show intelligible structures that are otherwise corrupted by striping artifacts, and the removal of these artifacts could enhance performance of object classification algorithms. The constraints were also tested on low surface brightness areas, and were found to be effective in reducing the noise level.

INTRODUCTION

The IPAC program LAUNDR invokes several one-dimensional flat fielding and deglitching techniques. For the purpose of destriping the one-dimensional algorithm works well for regions with a well-defined baseline, but the results are not satisfactory for regions where structure exists at all spatial frequencies (Fowler and Melnyk 1990).

Another IPAC utility KESTER, developed by Do Kester, is similar in principle to the approach we take. The idea is to process the data with YORIC to a certain iteration to obtain an image, which is then used to simulate a set of detector flux measurements. The original data are then calibrated against the simulated ones.

Our approach is to combine image construction and the destriping process. Since the striping gets amplified through the iterations, the idea of applying constraints to the correction factors is natural. We investigated the possibilities of both additive and multiplicative offsets, and from our preliminary analysis it seems the multiplicative treatment is superior.

ALGORITHM

The Maximum Correlation Method can be derived based on a Maximum Likelihood scheme. Assuming a Poisson process, the likelihood function for a set of

S. Terebey and J. Mazzarella (eds.), *Science with High-Spatial Resolution Far Infrared Data*, 55–60, 1994, Jet Propulsion Laboratory, Pasadena, CA.

measurements D_i is

$$P = \prod_i \frac{e^{-F_i} F_i^{D_i}}{D_i!}, \tag{1}$$

where F_i is the noiseless measurement value. If r_{ij} is the value of the ith footprint's response function at image pixel f_j, then

$$F_i = \sum_j r_{ij} f_j. \tag{2}$$

To maximize the likelihood estimate for f_j, we have

$$\frac{\partial \ln P}{\partial f_j} = \frac{\partial}{\partial f_j} \sum_i [-F_i + D_i \ln F_i - D_i \ln D_i + D_i] = \sum_i [-r_{ij} + r_{ij} D_i / F_i] = 0. \tag{3}$$

From this an iterative algorithm can be built (Aumann, Fowler and Melnyk 1990),

$$f_j^{(k)} = f_j^{(k-1)} C_j, \tag{4}$$

where

$$\begin{aligned} C_j &= \frac{\sum_i r_{ij} C_i}{\sum_i r_{ij}} \\ &= \frac{\sum_i r_{ij} D_i / F_i}{\sum_i r_{ij}}, \end{aligned} \tag{5}$$

starting from a uniform image $f_1^0 = f_2^0 = f_j^0$ for all j.

For *IRAS* data however, differing baselines and calibrations exist among the detectors, which results in striping artifacts in the HiRes images. Figure 1 (a) and (b) show the 1st and 20th iteration HiRes images for a field in the ρ Ophiuchus region at 100 μm. The input data were processed with the IPAC utility LAUNDR[1], which applied one dimensional flat fielding to the flux measurements (Fowler and Melnyk, 1990).

We now incorporate the estimation of leg offsets with image construction, i.e. we'll first try to maximize the likelihood function by choosing proper offsets for the legs, then proceed to compute the correction factors from the modified D_i's.

A. Assuming the offset is additive.

$D_i^* = D_i - O_L$ is the corrected measurement value. O_L is the offset, which is the same for all i's within the same scanline L.

$$P = \prod_i \frac{e^{-F_i} F_i^{D_i - O_L}}{(D_i - O_L)!}. \tag{6}$$

---

[1] The LAUNDR'ing was carried out for a 6.5° × 6.5° field, which was then clipped to obtain this 1° × 1° region.

Maximizing P with choice of O_L,

$$\begin{aligned}\frac{\partial \ln P}{\partial O_L} &= \frac{\partial}{\partial O_L} \sum_{i \text{ in leg } L} [-F_i + (D_i - O_L)\ln F_i \\ &- (D_i - O_L)\ln(D_i - O_L) + (D_i - O_L)] \\ &= \sum_{i \text{ in leg } L} [-\ln F_i + \ln(D_i - O_L)] \\ &= 0 \end{aligned} \tag{7}$$

So we have,

$$\prod_{i \text{ in leg } L} \frac{D_i - O_L}{F_i} = \prod_{i \text{ in leg } L} C_i = 1. \tag{8}$$

This polynomial equation in O_L can be solved with Newton's method. O_L's are computed starting from the second iteration, since in the first iteration $F_i^0 = \sum_j r_{ij} f_j^0 = \text{const.}$ and there is no reason to regard it as an approximation of the true F_i.

B. Assuming the offset is multiplicative.

Due to calibration error in the gains and the quasi-logarithmic digitization used in *IRAS*, the offset could be multiplicative in nature. In this case $D_i^* = m_L D_i$ and $\partial \ln P / \partial m_L = 0$ gives

$$\sum_{i \text{ in leg } L} D_i \ln \frac{F_i}{m_L D_i} = 0, \tag{9}$$

or

$$\prod_{i \text{ in leg } L} \left(\frac{m_L D_i}{F_i}\right)^{D_i} = \prod_{i \text{ in leg } L} C_i^{D_i} = 1. \tag{10}$$

RESULTS AND DISCUSSIONS

The test field we used is the 100 μm band of a region in ρ Ophiuchus (RA 16h23m, Dec −23°30′). It covers a 1.07° × 1.07° field (257 × 257 15 arcsec pixels), with a total of 12112 footprints in 227 scanlines.

The 20th iteration image produced from method A is shown in Figure 2(a). The calculated leg offsets are roughly Gaussian.

Corresponding image from method B is shown in Figure 2(b). The calculated leg offsets have a standard deviation of 0.12.

Both Figures 2(a) and 2(b) show significant improvement over Figure 1(b). Striping artifacts are greatly reduced, while believable high spatial freqeuncy features are retained. Figures 2(a) and 2(b) have much smoother contours than Figure 1(b).

We also notice that Figure 2(b) is smoother than Figure 2(a) in the high flux region. We assume the reason is that the additive offsets calculated were not able to compensate for the differences among nearby legs in the high flux region.

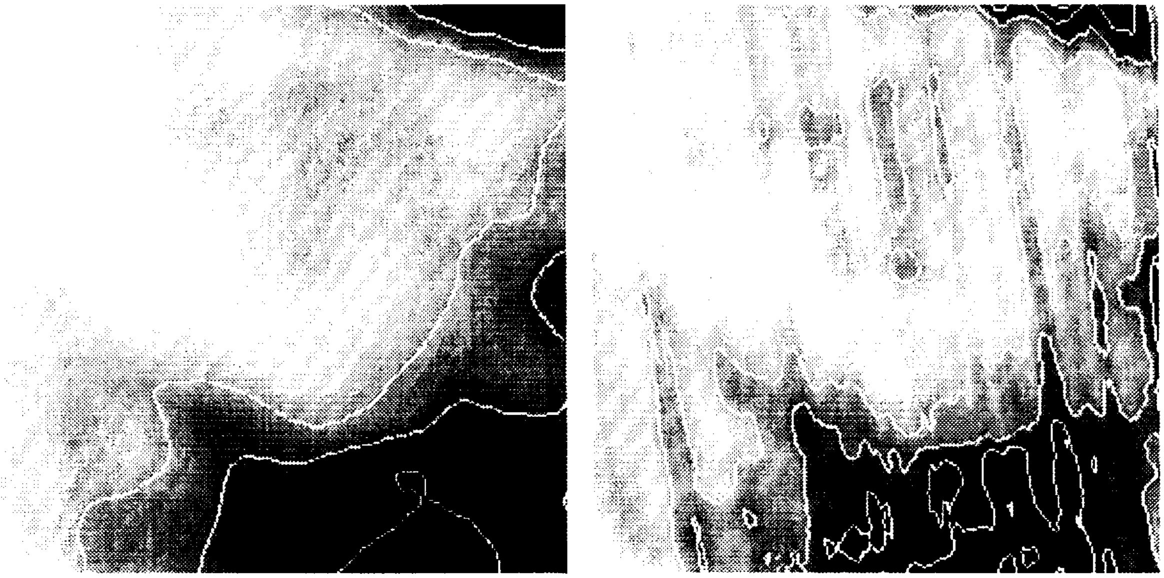

FIGURE 1 1st and 20th iteration, no offset. (Reverse video, contours start from 20th percentile, successive contours differ by factor 1.414.)

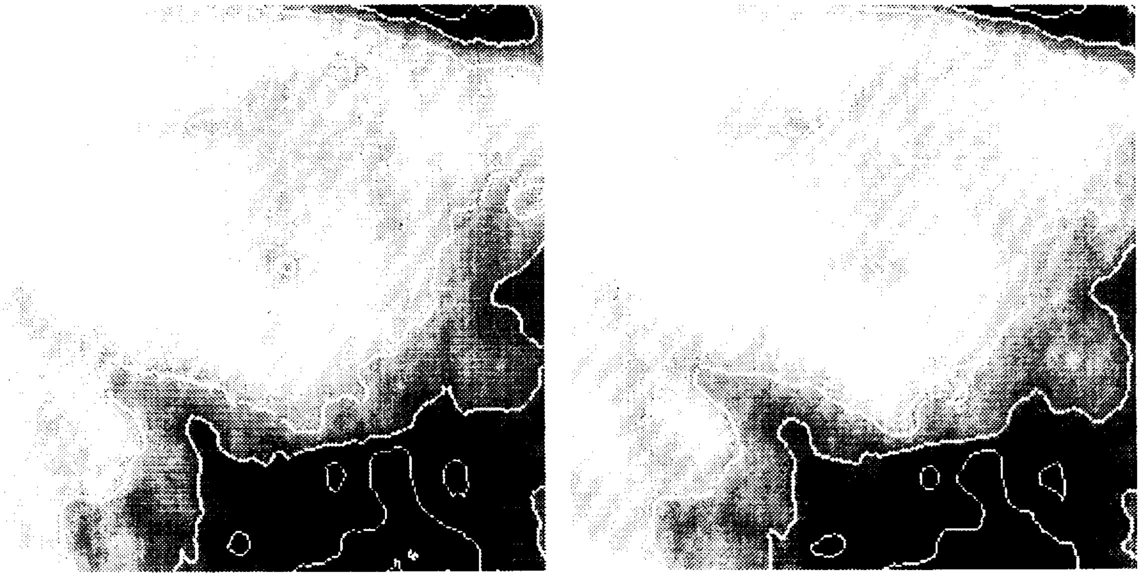

FIGURE 2 20th iteration, additive and multiplicative offsets

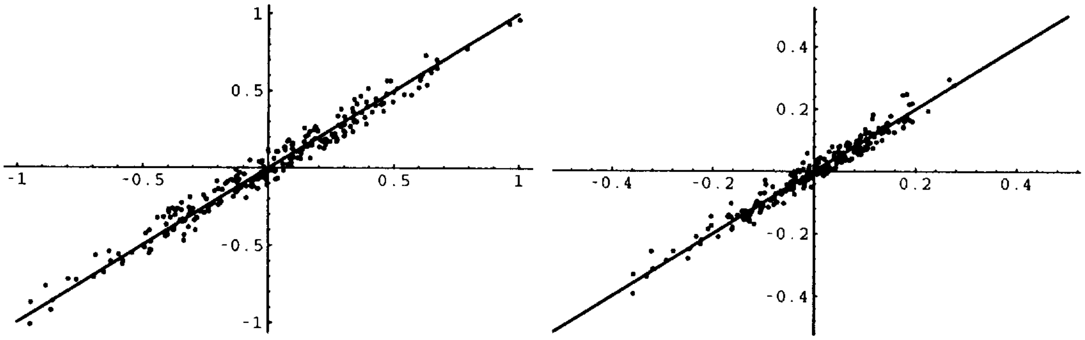

FIGURE 3 Recovery of Artificially Introduced Offsets

We carried out a simple statistical test on the nature of the leg offsets by comparing the likelihood function P obtained from the two assumptions for the first calibration. The multiplicative assumption results in a bigger likelihood for 145 legs out of a total of 227. This again seems to indicate the multiplicative assumption is closer to the truth.

In addition, we tried the constrained algorithms on the 100 μm band of M101. This field features intersecting scanlines, and because of the presence of a well-defined background, is calibrated quite well with the LAUNDR program. However the constrained image shows a reduction in noise. (Figure not shown. Calculated offsets have a standard deviation of 0.05).

VERIFICATION

We tested the algorithms' capability to recover offsets artificially introduced to a set of simulated detector fluxes. The detector fluxes were computed from a first iteration image of the same region, which is virtually stripe free. Gaussianly generated offsets (additive or multiplicative, magnitude being equal to that found for actual measurements) were then applied to the legs. This made-up set of detector fluxes was fed to our program, and scatter plots of the recovered vs. introduced offsets are shown in Figure 3. (left: Y-axis: recovered additive offset, X-axis: introduced additive offset; right: Y-axis: log of recovered multiplicative offset, X-axis: log of introduced multiplicative offset.)

In the additive case, we found the residual offsets after attempt of recovery have standard deviation roughly one-sixth of that for introduced offsets, meaning a 6 fold decrease in the striping amplitude (or 15 dB decrease in power). The performance is limited by the density of the scanlines.

In the multiplicative case, the introduced offsets were a Gaussian random variable with standard deviation 0.12. The standard deviation of residual offset is 0.024.

In these tests the recovered images are visually indistinguishable from the noiseless input image. This suggests that the algorithms are capable of doing what they are supposed to. So the residual striping seen in Figures 2(a) and (b) is due to inaccuracy of the underlying assumptions about the nature of the offsets. Test runs on neighboring fields showed indeed the offsets vary considerably within each leg over the spatial scale of 1°. One of the many possible causes is the change in responsivity of the detectors when they pass through a bright source. Our next step would be to try to understand this drifting behavior, and to incorporate it into our algorithm.

CONCLUSION

Our algorithm is just another way of trying to make use of the redundancy in the measurements. The standard HiRes processing uses it to pull out high spatial frequency information, while we take it a step further to let the scanlines calibrate each other. It resides in the same theoretical framework as the Maximum Correlation Method.

ACKNOWLEDGMENTS

We thank John Fowler and Susan Terebey for their suggestions and comments.

REFERENCES

Aumann, H. H., Fowler, J. W., and Melnyk, M. 1990, *AJ*, **99**, 1674

Fowler, J. W., and Melnyk, M. 1990, *LAUNDR Software Design Specification*, IPAC, Pasadena

BEYOND MAXIMUM ENTROPY: FRACTAL PIXON-BASED IMAGE RECONSTRUCTION

R. C. PUETTER AND R. K. PIÑA
Center for Astrophysics and Space Science,
University of California, San Diego
9500 Gilman Drive, La Jolla, CA 92093-0111

ABSTRACT We have developed a new Bayesian image reconstruction method that has been shown to be superior to the best implementations of other competing methods, including Goodness-of-Fit methods such as Least-Squares fitting and Lucy-Richardson reconstruction, as well as Maximum Entropy (ME) methods such as those embodied in the MEMSYS algorithms. Our new method is based on the concept of the pixon, the fundamental, indivisible unit of picture information. Use of the pixon concept provides an improved image model, resulting in an image prior which is superior to that of standard ME. Our past work has shown how uniform information content pixons can be used to develop a "Super-ME" method in which entropy is maximized exactly. Recently, however, we have developed a superior pixon basis for the image, the Fractal Pixon Basis (FPB). Unlike the Uniform Pixon Basis (UPB) of our "Super-ME" method, the FPB basis is selected by employing fractal dimensional concepts to assess the inherent structure in the image. The Fractal Pixon Basis results in the best image reconstructions to date, superior to both UPB and the best ME reconstructions. In this paper, we review the theory of the UPB and FPB pixon and apply our methodology to the reconstruction of far-infrared imaging of the galaxy M51. The results of our reconstruction are compared to published reconstructions of the same data using the Lucy-Richardson algorithm, the Maximum Correlation Method developed at IPAC, and the MEMSYS ME algorithms. The results show that our reconstructed image has a spatial resolution a factor of two better than best previous methods (and a factor of 20 finer than the width of the point response function), and detects sources two orders of magnitude fainter than other methods.

BAYESIAN IMAGE RECONSTRUCTION

Bayesian image reconstruction estimates the best image by statistically modeling the imaging process. To do this, one factors the joint probability distribution of the triplet, D, I, and M, i.e., $p(D, I, M)$, (where D, I, and M are the data, unblurred image, and model respectively) using Bayes' Theorem to derive an expression for the most probable or M.A.P. (Maximum A Posteriori) image. In deriving the expression for the M.A.P. image, most Bayesian methods assume that all aspects of the model, M, linking image and the data are to be held

S. Terebey and J. Mazzarella (eds.), *Science with High-Spatial Resolution Far Infrared Data*, 61–67, 1994, Jet Propulsion Laboratory, Pasadena, CA.

constant during the image reconstruction process. More advanced methods, such as Weir's multi-channel method (1991, 1993) and the method presented here (also see Piña and Puetter 1993 and Puetter and Piña 1993), systematically vary certain aspects of the model to improve the quality of the image reconstruction. Varying the image and the model simultaneously, places I and M on a more equal footing and begins to blur the distinction between image and model. Indeed, our Bayesian formulation of the image reconstruction problem treats them as full equals; see Piña and Puetter (1993) and Puetter and Piña (1993). With this in mind, a Bayesian formulation of the image reconstruction problem which is symmetric with respect to the image and model can be obtained by factoring $p(D, I, M)$ in the following manner:

$$p(D, I, M) = p(D|I, M)p(I, M) = p(I, M|D)p(D) \tag{1}$$

which implies

$$p(I, M|D) = \frac{p(D|I, M)p(I, M)}{p(D)} = \frac{p(D|I, M)p(I|M)p(M)}{p(D)} \propto p(D|I, M)p(I|M) \tag{2}$$

where in the standard notation $p(X|Y)$ is the probability of X given that Y is known, and the proportionality in equation (2) is obtained since D is constant (hence $p(D)$ is constant) and since we have no prior basis on which to discriminate between models (i.e., $p(M) = const$). Equation (2) is an expression for the M.A.P. image/model pair, i.e., the image/model pair which maximizes $p(I, M|D)$. Our method assumes that deriving the M.A.P. image/model pair represents the optimal reconstruction.

The significance of the two terms in the proportionality in equation (2) is readily understood. The first term, $p(D|I, M)$, is a goodness-of-fit (GOF) quantity, measuring the likelihood of the data given a particular image and model. The second term, $p(I|M)$, the "image prior", expresses the *a priori* probability of a particular realization of the image; note that equivalently we could use the image/model prior $p(I, M)$. In GOF image reconstruction, $p(I|M)$ is effectively set equal to unity, i.e., there is no prior bias concerning the image. A typical choice for $p(D|I, M)$ is to use $p(D|I, M) = \exp(-\chi^2/2)$, i.e., the standard chi-square distribution. This approach ensures a faithful rendition of the data, but typically results in images with spurious low signal-to-noise features. In Maximum Entropy (ME) image reconstruction, the image prior is based upon "phase space volume" or counting arguments and the prior is expressed as $p(I|M) = \exp(\alpha S)$, where S is the entropy of the image and α is a Lagrange multiplier that adjusts the relative importance of the GOF and image prior.

PIXONS AND A NEW IMAGE PRIOR

By varying the model simultaneously with the image during the reconstruction process, the solution to the reconstruction process is optimized over a significantly larger solution space. This solution space contains, for example, the solutions spaces of the standard GOF and ME methods. Consequently, the results of our methods theoretically should be no worse than those of competing methods. While the advantage of varying the model seem clear, it is less obvious how to do this in a productive manner. Certain aspects of the model, for example, should not be varied. The model includes, for instance, a description of the physics of the imaging process, e.g., that the data is the convolution of the point-spread-function (PSF) and the blur-free underlying image. The model also includes the description of the noise processes, e.g., the noise might have a Gaussian or Poisson distribution. These aspects of the model should not be varied if ones wishes to remain faithful to the truth. However, the mathematical model or representation of the image can be varied. Furthermore, varying the mathematical model of the image can substantially improve the quality of the image reconstruction. One relatively successful approach to image modeling was suggested by Piña and Puetter 1993 and Puetter and Piña 1993. They pointed out that in the most general of terms, an image is a collection of distinguishable events which occur in distinct cells. Hence the value for the image prior can be determined from simple counting arguments. If there are N_i events in cell i, and a total of n cells, then the prior probability of that particular image is:

$$p(\{N_i\}, n, N) = \frac{N!}{n^N \prod_i N_i!} = p(I|M) \quad , \tag{3}$$

where $\{N_i\}$ is the set of all numbers of events in cells i, and N is the total number of events, i.e., $N = \sum_i N_i$. The cells used in equation (3) are quite general. In fact, we have not specified a size, shape, or position for the cells. The goal of selecting cells for a specific image is to maximize $p(I|M)$ subject to the constraint that an adequate GOF is maintained. Equation (3) clearly indicates the desirable properties of the model, i.e., the model should contain the fewest number of cells with each containing the largest number of events. We have termed these generalized cells *pixons*. This terminology is not simply whimsical. An image's pixons represent the smallest number of cells (of arbitrary shape, position, etc.) required to fit the data and represent the minimum degrees of freedom necessary to specify the image within the accuracy of the noise. If properly selected, this set is not reducible to a smaller set. In this sense, the pixons are the fundamental particles of information in the image. In fact, using a pixon basis is the fulfillment of *Occam's Razor* formalized in Bayesian terms. Intuitively, this is the goal of every modeling effort, i.e., to fit the data with the simplest model. Equation (2) is the embodiment of that goal with the $p(D|I, M)$ term insisting on a good fit and $p(I|M)$ acting for the cause of simple models, i.e., acting as an *Occam's Razor* term.

While the goal of pixon-based image reconstruction is now clear, there is still considerable uncertainty associated with how to actually select the pixon basis. Piña and Puetter (1993) suggested a particular formulation: The Uniform Pixon Basis (UPB). In the UPB, each of the pixons contain the same amount of information, i.e., N_i is identical for each pixon. Because of this, the UPB image representation provides a sort of "Super-ME" reconstruction. This is because in the UPB representation each pixon is identical, i.e., in this basis the image is exactly flat. Hence entropy is maximized exactly. All of the image's structural information is inherent in the pixon basis. Because entropy is maximized exactly, and because the number of cells in the UPB representation is typically much smaller that the number of data pixels used in standard ME reconstructions, the formal value of the image prior and hence the value of $p(I, M|D)$ is vastly improved. Crudely speaking, using the UPB representation is the mathematical equivalent of imaging the sky with a magical CCD which can interactively change its number of pixels, their positions, sizes, and shapes in a manner in which each pixel collects the same number of photons.

A FRACTAL PIXON BASIS

While the UPB image representation is a major advance, the UPB basis is rather *ad hoc*. It can not be justified as an optimal pixon basis. A more satisfying pixon basis can be chosen using fractal concepts as we shall now describe–also see Puetter and Piña 1993.

There are numerous definitions for the fractal dimension of a geometric object. However all definitions have one thing in common. Each calculates a quantity that changes as a scale (or measurement precision) changes. For example, the compass dimension (also referred to as the divider or ruler dimension) of a line in a plane surface is defined in terms of how the measured length of the line varies as the length of the ruler used to measure the length varies. These ideas are closely related to pixons and the image reconstruction problem since choice of a pixon basis is essentially asking the question: "How does the GOF change as the size of the pixons are varied?"

In forming their UPB image model, Piña and Puetter (1993) use a pseudo-image calculated on a pseudo-grid (usually equal to or finer than the data pixel grid). At each point of the pseudo-grid a local scale is determined. This is the local pixon size. The image is then set equal to the pseudo-image convolved with the pixon kernel (or shape) function of the local width. This image is then convolved with the PSF and compared to the data to determine the GOF. Using the above prescription, the pixons are not cells with sharp boundaries, but are "fuzzy". However, since the image values on the pseudo-grid are correlated, the number of degrees of freedom in the image are significantly less than the number of pseudo-pixels.

We are now ready to consider how to improve the UPB representation using fractal concepts. *Occam's Razor* tells us that we must use the fewest number of pixons each containing the largest information content. The GOF term tells us we must fit the data as well as possible. Using fuzzy pixons, we know that at each point in the image we are going to smooth a pseudo-image over a local scale. What aspect of the smoothing process will prevent an adequate GOF value? Clearly, if the underlying image is locally smooth on a given scale, smoothing the pseudo-image on scales less than or equal to this scale loses nothing. The GOF term is unaffected and the image prior improves. On the other hand, smoothing on scales larger than the local scale is detrimental. So how does one tell if the pseudo-image is being smoothed too much? If the true image is smoothed with pixons of very small width, the value of the smoothed image changes inappreciably. As the widths of the pixons are increased, deviations of the smoothed value from the unsmoothed value become appreciable when the pixon size exceeds the local smoothness scale of the image. This provides an over-smoothing signal. The only remaining issue is determining what size signal is significant. We know, however, by what tolerance we can allow the smoothed image to depart from the unsmoothed image. The departure must not exceed the local noise. Hence the determination of the local pixon size is an inverse fractal dimension problem. What we are seeking is the largest local smoothing scale consistent with the tolerance set by the noise.

RESULTS: 60 MICRON IRAS IMAGING OF M51

As a test of the ability of FPB-based image reconstruction we have reconstructed an image from $60\mu m$ IRAS survey scans of the interacting galaxy pair M51. This data was selected for several reasons. First, M51 is a well studied object at optical, IR, and radio wavelengths. Hence "reality" for this galaxy is well known. Second, this particular data set was chosen as the basis of an image reconstruction contest at the 1990 MaxEnt Workshop in Laramie, Wyoming (see Bontekoe 1991). Consequently, there have been a number of serious attempts at performing image reconstruction on this data set by specialists in the field. Finally, the IRAS data for this object is particularly strenuous for image reconstruction methods. This is because first, all the interesting structure is on sub-pixel scales (IRAS employed relatively large, discrete detectors ($1.5\,'$ by $4.75'$ at $60\mu m$) and the position of M51 in the sky caused all scan directions to be nearly parallel. This means that reconstructions in the cross-scan direction (i.e., the $4.75'$ direction along the detector length) should be significantly more difficult than in the scan direction. In addition, the point source response of the 15 IRAS 60 μm detectors (pixel angular response) is known only to roughly 10% accuracy, and finally, the data are not an image, but incompletely and irregularly sampled scans of individual detectors across the galaxy.

Our FPB reconstruction appears in Figure 1 along with Lucy-Richardson and Maximum Correlation Method (MCM) reconstructions (Rice 1993) and a MEMSYS 3 reconstruction (Bontekoe *et al.* 1991)–see Gull (1991) for a description of the MEMSYS algorithms. The winning entry to the MaxEnt 90 image reconstruction contest was produced by Nick Weir of Caltech and is not presented here since quantitative information concerning this solution has not been published–see Bontekoe (1991) for a gray-scale picture of this reconstruction. However, Weir's solution is qualitatively similar to Bontekoe's solution (Weir 1993). Both were made with MEMSYS 3. Weir's solution, however, used a single correlation length channel in the reconstruction. This constrained the minimum correlation length of features in the reconstruction, preventing break-up of the image on smaller size scales. This is probably what resulted in the winning edge for Weir's reconstruction in the MaxEnt 90 contest (Weir 1993).

As can be seen from Figure 1, our FPB-based reconstruction is clearly superior to those produced by other methods. The Lucy-Richardson and MCM reconstructions fail to significantly reduce image spread in the cross-scan direction, i.e., the rectangular signature of the 1.5 by 4.75 *arcmin* detectors is still clearly evident, and fail to reconstruct even gross features such as the "hole" (black region) in the emission north of the nucleus–this hole is clearly evident in optical images of M51. The MEMSYS 3 reconstruction by Bontekoe is significantly better. This image clearly recovers the emission "hole" and resolves the NE and SW arms into discrete sources. Nonetheless, the level of detail present in the FBP reconstruction is clearly absent, e.g., the weak source centered in

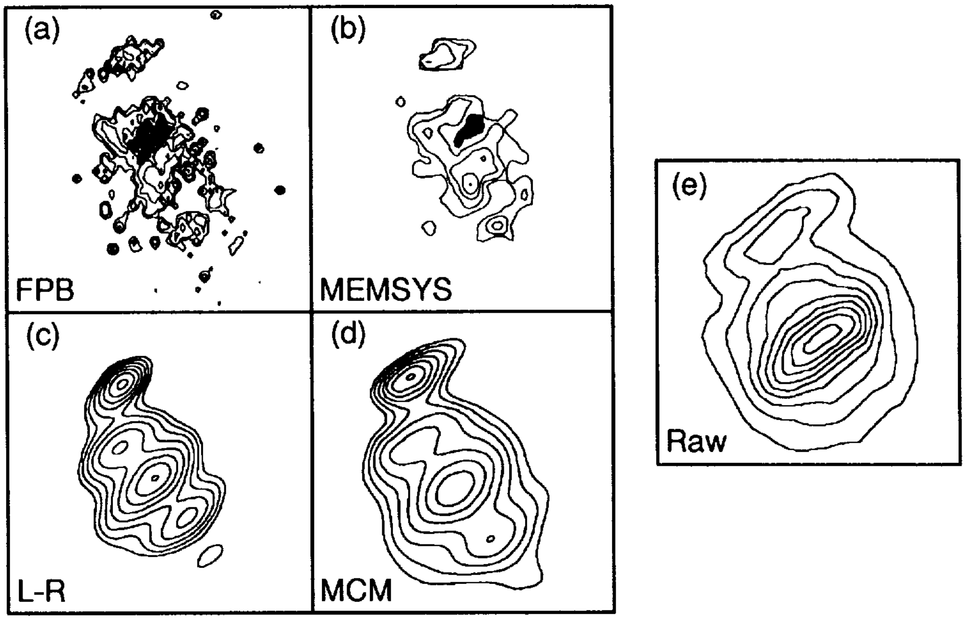

FIGURE 1 Image reconstructions of the Interacting galaxy M51. (a) FPB-based reconstruction; (b) MEMSYS 3 Reconstruction; (c) Lucy-Richardson Figure of panel (b) reproduced from Bontekoe (1991), by permission of the authors. Figures of panels (c) and (d) reproduced from Rice 1993 by permission of the author.

the emission hole (again, this feature corresponds to a known optical source), and the fainter sources around the periphery of the image (most of which are known radio or optical sources). One also notes that the resolution of the FPB reconstruction is roughly a factor of two greater than the MEMSYS 3 reconstruction. However, to be fair to the MEMSYS 3 reconstruction, the authors rebinned their reconstruction by a factor of two to eliminate any possible spurious features. However, we are quite confident that all of the features present in our reconstruction are real.

Aside from the fact that most of the sources can be identified with emission at other wavelengths, the residual errors in our reconstruction are much smaller than in the MEMSYS 3 reconstruction. As pointed out by Bontekoe *et al.* (1991) the peak flux in the MEMSYS 3 reconstruction is 2650 units. The residual errors are correlated with the signal and lie between 0 and 430 units. By contrast, the peak value in the FPB reconstruction is 3290 units, the residuals are uncorrelated with the signal, and the residuals lie between -9 and 17 units. (The contour levels for the MEMSYS 3 and FPB reconstructions are identical and are 150, 300, 600, 1200, and 2400 units.) Furthermore, the large deviation residuals in the FPB reconstruction are due to systematic errors involving incomplete scan coverage of M51. As mentioned above, these errors do not lie under the significant flux emitting portions of the M51 image. The residual errors associated with emitting regions in M51 are significantly smaller and show a roughly Gaussian distribution. Consequently, the residuals in the FPB reconstruction represent a two order-of-magnitude improvement over the MEMSYS 3 residuals. This, of course, immediately explains the absence of the fine features in the MEMSYS 3 reconstruction. The weak sources present in the FPB reconstruction all lie in the 150 to 300 unit range, and hence are 30 or greater detections in the FPB reconstruction. By contrast, these same features would be less than one detection in the MEMSYS 3 reconstruction.

ACKNOWLEDGMENTS

The authors would like to thank Romke Bontekoe and Do Kester for useful conversations on image reconstruction, IRAS data in general, and the 60 μm IRAS data for M51 in particular. The authors would also like to thank Nick Weir for numerous fruitful conversations both past and present. A patent application on the pixon is currently pending by the authors and The Regents of the University of California. This work was supported by NASA and the NSF.

REFERENCES

Bontekoe, Tj., R. 1991, in *Maximum Entropy and Bayesian Methods*, eds. W. T. Grady, Jr. and L. H. Schick, (Dordrecht: Kluwer Academic Publishers), 319

Bontekoe, Tj., R., Kester, D. J. M., Price, S. D., de Jonge, A. R. W., and Wesselieus, P. R. 1991, *A&A*, **248**, 328

Gull, S. F., and Skilling, J. 1991, *MemSys5 Quantified Maximum Entropy Users Manual*

Piña, R. K., and Puetter, R. C. 1993, *PASP*, **105**, 630

Puetter, R. C., and Piña, R. K. 1993, *Proc. SPIE*, in press

Rice, W. 1993, *AJ*, **105**, 67

Weir, N. 1991, in *Proceedings of the ESO/ST-ECF Data Analysis Workshop, April 1991*, P. Grosbo and R. H. Warmels, Eds. (Garching: ESO), 115

Weir, N. 1993, *J. Opt. Soc. Am.*, in press

Weir, N. 1993, private communication

9

HIRAS: HIGH-RESOLUTION IRAS IMAGES [1]

TJ. ROMKE BONTEKOE
European Space Agency - ESTEC
Astrophysics Division
Postbus 299, 2200 AG Noordwijk, The Netherlands

DO KESTER
Laboratory for Space Research
Postbus 800, 9700 AV Groningen, The Netherlands

ABSTRACT We describe a process of pyramid maximum entropy reconstruction of images from the IRAS survey data.

The Infrared Astronomical Satellite (IRAS) all-sky survey was designed and optimized for the detection of point sources. This allowed the survey to be conducted in the form of narrow strip scans with redundant coverage of the sky, but with non-uniform covering densities. The data show in addition to point sources many sources of extended emission, which are best analyzed from images. However, the non-uniform coverage now forms a significant obstacle in the image (re-)construction. Low resolution images, such as in the Infrared Sky Survey Atlas, yield spatial resolutions of 5–10 times the IRAS telescope diffraction limit; HIRAS improves this to 1–2 times!

HIRAS is a Groningen Image Processing SYstem (GIPSY) task which drives the MEMSYS5 algorithm and is specifically designed for IRAS image construction (MEMSYS is a trademark of Maximum Entropy Data Consultants Ltd. Cambridge, UK). In HIRAS the imaging equation

$$D = R * f \pm \sigma,$$

is solved. Here D is the data, f is the image, the matrix R describes the instrumental response, and σ is the estimated noise in the data. High demands are places on the quality of the data and the response matrix R. Therefore, HIRAS utilizes the individual response functions of the focal plane detectors and rotates them according to the scan angle over the requested map.

The data D, still in the form of scans, are first calibrated against a low-resolution map by the IMAGE task in GIPSY. After a first convergence of HIRAS, subsequent refinements in the calibration can be performed, now against the new high-resolution map. Corrections in the baseline, drift, and detector gain are applied and continuation of the HIRAS run shows a significant improvement in the result.

---

[1] THIS IS AN ABSTRACT OF THE PAPER "PYRAMID MAXIMUM ENTROPY IMAGES OF THE IRAS SURVEY DATA," BONTEKOE ET AL., TO APPEAR IN THE APRIL 1994 ISSUE OF *ASTRONOMY & ASTROPHYSICS.*

S. Terebey and J. Mazzarella (eds.), *Science with High-Spatial Resolution Far Infrared Data*, 69–70, 1994, Jet Propulsion Laboratory, Pasadena, CA.

In HIRAS the spatial correlations in an image can be controlled interactively. This is done via a new multi-channel method, pyramid images, in which virtually all spatial frequencies are represented. In a pyramid image a 64×64 pixel image is the sum of a 64×64, a 32×32, ..., a 2×2, and a 1×1 pixel channel, all covering the same map area.

In image reconstruction there is an inevitable amplification of the noise in the data, due to the ill-conditioned nature of the inversion of the imaging equation. In HIRAS this amplification of the noise can be visualized by the computation of an error map, having identical dimensions to the requested map. The error map represents a full propagation of σ through the inversion of the imaging equation. Comparing the image with the error map gives indispensable information about the authenticity of detailed features. For example, the flux of point sources in the IRAS Point Source Catalog is usually within the error as determined by HIRAS.

REFERENCES

Bontekoe, Tj.R., Koper, E., and Kester, D.J.M. 1994, A&A, in press.

N95- 21759

INTERACTING GALAXIES RESOLVED BY IRAS

J. M. MAZZARELLA AND J. A. SURACE
Infrared Processing and Analysis Center, MS 100-22
California Institute of Technology, Jet Propulsion Laboratory
Pasadena, CA 91125

ABSTRACT We discuss procedures, limitations and results of high resolution processing of interacting galaxies observed by the Infrared Astronomical Satellite (IRAS). Among 56 potentially resolvable interacting groups selected from the IRAS Bright Galaxy Sample, 22 systems have been resolved yielding fluxes for a total of 51 galaxies. In about 2/3 of the resolved pairs, both galaxies were detected in the far-infrared. A set of isolated non-interacting galaxies was chosen from the Bright Galaxy Sample for comparison with the interacting galaxies. For the current sample, which naturally excludes close pairs and ultraluminous merging systems, the primary conclusions are: (a) It is not possible to distinguish *individual* interacting galaxies from isolated galaxies of similar luminosity on the basis of infrared properties alone. (b) No direct correlation was found between measures of interaction strength and indicators of enhanced star formation within the resolved systems. (c) Comparison of the interacting and isolated samples indicates *statistically significant differences between their distributions of far-infrared color ratios, luminosities, and surface brightnesses.* Even during the early stages of interaction spanned by these systems, in a statistical sense, tidal perturbations substantially boost far-infrared indicators of star formation compared to non-interacting systems. We also briefly discuss future prospects for pushing the IRAS data to its limits for additional interacting systems.

INTRODUCTION

Results derived from IRAS observations have been largely responsible for the current surge of interest in interacting galaxies (IGs). The empirical and theoretical stage was set in the pre-IRAS era in the seminal studies of Larson & Tinsley (1978), who explained the large dispersion in the UBV colors of IGs compared to non-IGs using global starburst models, and Toomre & Toomre (1972), who used restricted 3-body simulations to demonstrate the gravitational tidal origin of the tails and bridges often observed in peculiar galaxies. Results from studies of IRAS-selected samples showed very early a predominance of IGs; for example, ≈ 30% of IRAS MiniSurvey galaxies were noted to be IGs (Lonsdale et al. 1984). As a baseline, it is useful to note that ≈ 8% (6440/77838) of field galaxies are *optically* "peculiar" (e.g., Arp & Madore 1987), which usually means gravitationally perturbed. The frequency of IGs in the IRAS Bright Galaxy Sample, a flux-limited sample complete to 5 Jy at 60 μm (Soifer et al. 1989),

S. Terebey and J. Mazzarella (eds.), *Science with High-Spatial Resolution Far Infrared Data*, 71–79, 1994, Jet Propulsion Laboratory, Pasadena, CA.

increases steadily with infrared luminosity, from ≈ 10% at $L_{ir}= 10^{10} - 10^{11} L_{\odot}$, to ≈ 40% at $L_{ir}= 10^{11} - 10^{12} L_{\odot}$, and ≈ 100% at $L_{ir} > 10^{12} L_{\odot}$(Sanders et al. 1988). Likewise, the warmest global dust temperatures ($f_{60\mu m}/f_{100\mu m} \gtrsim 0.6$) are found primarily in the closest, overlapping IGs and mergers (Telesco et al. 1988; Mazzarella et al. 1991). The most luminous galaxies discovered in the IRAS database have bolometric luminosities comparable to QSOs ($L_{ir} > 10^{12} L_{\odot}$) and emit the bulk of their radiation (> 50%) in the far-infrared part of the spectrum. These "ultraluminous" far-infrared galaxies are the dominant population in the local universe at such high bolometric luminosities, and they have been proposed to be the dusty precursors of classical UV-excess QSOs (Sanders et al. 1988) and some powerful radio galaxies (Mazzarella et al. 1993). Numerical simulations of the dynamics of IGs have shown that dissipative mergers can be very effective in driving material from a gas-rich galaxy disk inward to fuel a nuclear starburst and in some cases an active nucleus (e.g., Barnes & Hernquist 1992).

Despite the observational and theoretical progress which has been made in studies of IGs (see, for example, recent reviews by Shlosman 1990 and Barnes & Hernquist 1992), numerous outstanding questions remain concerning proposed evolutionary connections between IGs, starbursts, and active galactic nuclei. For example, in a study of optically selected IGs with a median separation of about 20 kpc, Bushouse et al. (1988) found a wide dispersion in far-infrared properties compared to non-IGs, with some IGs in their sample showing no emission-line spectra indicative of currently active star formation. What parameters of the interaction and of the participating galaxies determine the strength of the induced star formation? Since the most excessive far-infrared enhancements are observed only in the most advanced mergers, how does starburst activity evolve during earlier stages of galaxy collisions? Can we track episodic/repetitive starbursts suggested from the simulations of Noguchi (1991)? Answers to these and related questions require far-infrared data for the *individual components* of IGs to match available data at other wavelengths, such as near-infrared and optical array images, spectra, molecular and atomic gas (CO, H_2, H I) measurements, and radio continuum synthesis images.

The nominal IRAS resolution is $2' \times 5'$ at 60 μm; this corresponds to a large galaxy separation of ~85 kpc at a distance of 75 Mpc (cz = 5500 km s^{-1}, assuming H_o = 75 km s^{-1} Mpc^{-1}), and fails to resolve galaxies at $R \lesssim 1$-2 diameters, where starburst galaxies begin to "light up" substantially. However, HiRes processing of the IRAS data has the potential to improve resolution by a factor of four or five, to $1'$at 60 μm, or ~20 kpc at cz = 5500 km s^{-1}. HiRes processing thus presents an opportunity to push the IRAS data to its limits, and begin to investigate questions that will otherwise be untouchable until the next generation of far-infrared satellite observatories become available (ISO and SIRTF). Below we summarize procedures, limitations and results of high resolution processing of some interacting galaxies observed by IRAS.

GROUPS IN THE IRAS BRIGHT GALAXY SAMPLE

Sample Selection

The IRAS Bright Galaxy Sample (Soifer et al. 1989, hereafter referred to as the BGS) is a complete flux-limited sample of galaxies with an integrated $60\mu m$ flux density greater than 5.24 Jy. Due to the low resolving power of the IRAS survey at 60 μm ($\approx 4'$), many of the BGS objects are actually systems of two or more galaxies. In some cases these galaxies are undergoing significant apparent interaction, as indicated by optical tidal features. For purposes of constructing a sample of interacting galaxies which could potentially be resolved by IRAS, an interacting pair was defined as one for which $2S/(D_1 + D_2) < 3$, where D_1 and D_2 are the major diameters of the two galaxies and S is the separation between their centers. Thus, an interacting galaxy is one for which there is a clearly identifiable companion at a distance which is less than three times their average diameter away (c.f., Byrd et al. 1987; Dahari 1984). Candidates were identified by examining 3× enlarged prints taken from the Palomar Observatory Sky Survey (POSS) plates. Any BGS source that could be identified as consisting of two or more galaxies meeting the above distance–diameter criteria, and which furthermore had a difference in redshift between galactic components of not more than 1000 km s^{-1}, was placed in the interacting sample. This selection criterion naturally excludes sources whose extreme distance makes it impossible to distinguish whether they are interacting groups or single galaxies. This also excludes those strongly interacting systems with merging or unrecognizable disks, such as the ultraluminous mergers studied by Sanders et al. (1988). A complete listing of the 56 objects meeting the selection criteria for this interacting sample appears in Surace et al. (1993).

IRAS Data Processing and Limitations of HiRes

Due to the highly non-circular nature of the IRAS beam, IRAS observations provide greater resolution of targets aligned in the in-scan direction, as opposed to being aligned normal to the in-scan direction (cross-scan). Therefore, the position angle of the galaxies relative to the IRAS scan tracks was examined to determine if additional processing would likely resolve them. Those which showed a sufficiently favorable alignment and separation were reprocessed with the 2-dimensional spatial deconvolution processing of IRAS data known as HiRes (Aumann et al. 1990). For those interacting systems with very large separations ($S \gtrsim 3'$) and with favorable scan coverage, an attempt was made to resolve the target using the ADDSCAN/SCANPI one-dimensional scan coadder instead of HiRes. Because HiRes processing is highly computer intensive, it was not possible to apply this analysis tool to all the interacting systems chosen from the BGS. To reduce the number of sources where HiRes was applied, the following criteria were applied. First, HiRes is only effective for sources brighter than about 1 Jy. If there is considerable background noise, the local signal-to-noise should be at least 10. All the interacting sources met the brightness criteria at 60 μm by virtue of being in the BGS. Also, sources must be adequately sampled by the IRAS detectors; they should be covered by at least two survey Hours-Confirmation scans. Again, all the BGS sources met this criteria. Finally, candidate sources must be sufficiently separated; this was determined by examining the galaxy separations on the POSS prints.

For the selected galaxies, all four IRAS bands were processed with twenty iterations of HiRes. The pixel size was set to 15″ with a 1° field centered on the target, and all fields received iterative baseline removal. A source was considered detected if a signal was found within 30″ of the known optical position and had a flux density at least three times that of nearby processing artifacts. If the source was not seen, the flux at its presumed position was measured and reported as a 3σ upper limit.

Examination of the processed IRAS data was complimented by studies of simulated galaxy pairs which were processed through the same IRAS observation simulator as the real data. Simulations in which the position angle of the vector separating the galaxies was in the cross-scan direction indicated that the resolving power dropped by roughly a factor of three compared to that achieved for galaxies aligned along the in-scan direction. The IRAS detector coverage of the field, both the scan density and the position angles of the scans with respect to the vector separating the galaxies, greatly influences whether or not a source will be resolved by HiRes. The variation of HiRes resolving power with galaxy separation is reported in Table 1.

TABLE 1 HiRes Resolving Power for Galaxy Pairs[a]

Band (μm)	Unresolved (arcsec)	Resolved (arcsec)	Separated (arcsec)
12	< (33) × (99)	(33 – 99) × (45 – 130)	> (99) × (130)
25	< (33) × (99)	(33 – 99) × (48 – 150)	> (99) × (150)
60	< (36) × (90)	(36 – 108) × (90 – 280)	> (108) × (280)
100	< (72) × (132)	(72 – 216) × (132 – 390)	> (216) × (390)

---

[a] Values reported are (in-scan)×(cross-scan) separations in arcseconds.

Several stages of resolution were achieved. In cases where the model sources were completely separated, component fluxes were measured simply using aperture photometry. From the simulations, it was found that HiRes was able to reconstruct the flux ratio between two well separated components with a typical uncertainty of 5–8%. In cases of partial resolution, since the typical HiRes footprint for a single point source has the shape of an elliptical Gaussian, the AIPS routines IMFIT and JMFIT were used to fit 2-d elliptical Gaussian components to the HiRes images. The number of Gaussians fitted was determined by the number of galaxies present. Differences in detector coverage led to appreciable differences in resolution, and the estimated uncertainty was greatly affected by the degree of resolution, particularly in the case where the galaxy separation required Gaussian fitting.

Results

Figure 1 shows the result of HiRes processing of the IRAS data on the galaxy pair Arp 271. For comparison, contour plots of normal IRAS coadded images and HiRes images are shown overlaid on visible pictures of the galaxies. Although

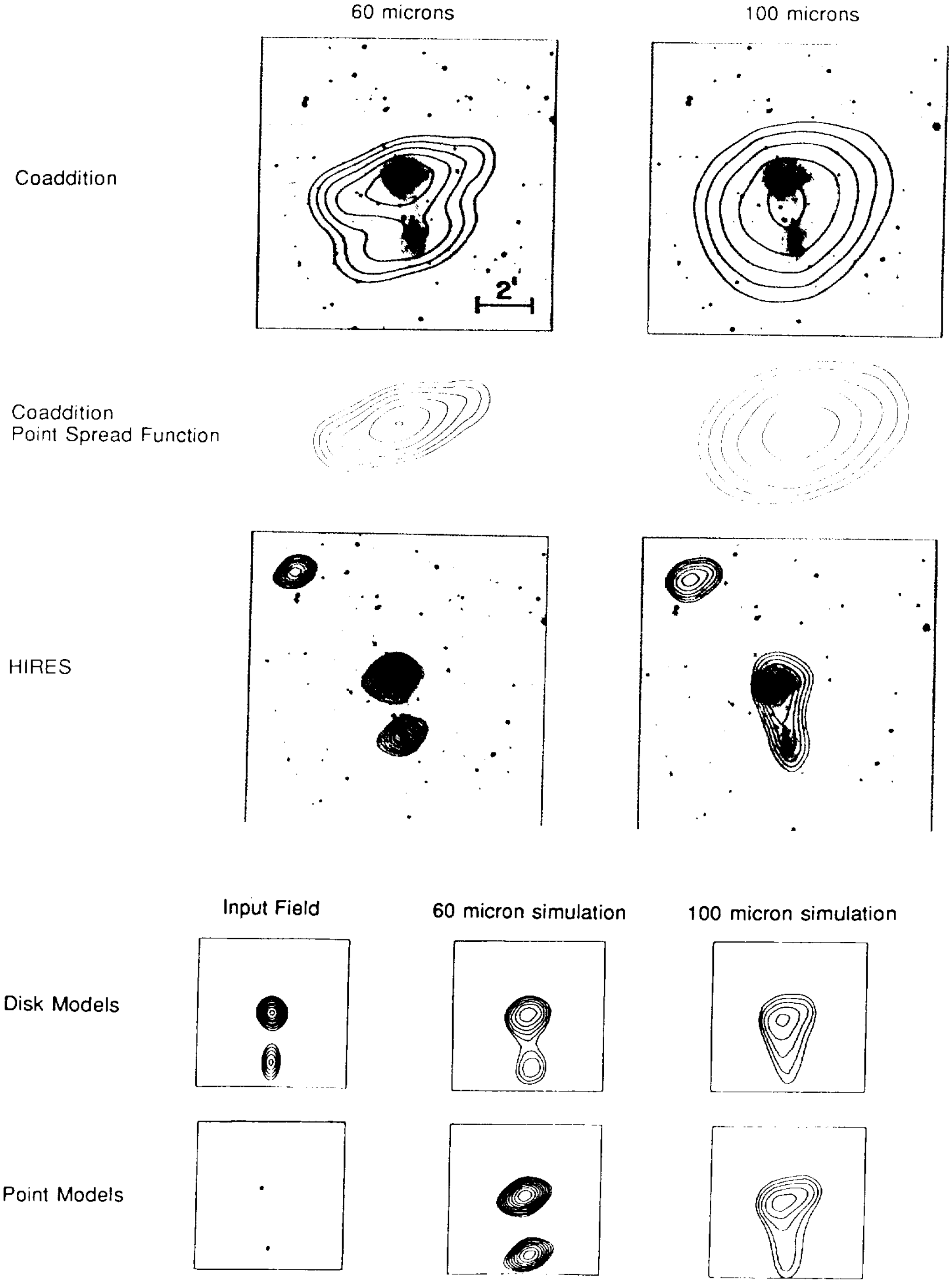

FIGURE 1 HiRes processing of Arp 271. The top two panels show the coadded 60 and 100 μm IRAS images at the nominal resolution, with contours of the corresponding point-spread functions plotted below each image. The bottom two panels show the result of HiRes processing at 60 and 100 μm; the HiRes point-spread functions are shown in the upper left corner.

normal coaddition is barely able to resolve the galaxies at 60 μm, and achieves no resolution at 100 μm, HiRes is able to resolve two distinct point sources at 60 μm and is able to significantly resolve the pair at 100 μm. Of the 56 interacting systems processed with HiRes, 22 were resolved, yielding fluxes for a total of 51 individual galaxies; 24 galaxies have only upper limits for their fluxes at one or more wavelengths. The complete table of data is reported in Surace et al. (1993).

We attempted to quantify whether the infrared properties of the systems correlate with the degree of interaction. The simplest measure is the projected physical separation. For the resolved systems, the mean projected separation is 34 ±18 kpc, and for the unresolved systems 19±13 kpc. We also utilized the Q parameter of Dahari (1984), $Q = (D_1 D_2)^{3/2}/S^3$, where D_1 and D_2 are the diameters of the galaxies, and S is the separation between their centers. This quantity is proportional to the degree of tidal perturbation between the galaxies; increasing size (and presumably mass) and decreasing separation increases the parameter, and thus more perturbed galaxies have higher Q parameters. The physical projected separations and Q values were treated as independent variables, and L_{ir}, SB_{fir}, $f_{60\mu m}/f_{100\mu m}$, and $f_{12\mu m}/f_{25\mu m}$ were treated as dependent variables to see if the measures of interaction strength manifested themselves in a significant change in infrared properties of the individual galaxies. No correlations were found. Similarly, the tests were performed by examining the *system* parameters; that is, for each interacting system, the average of the component Q values and FIR measurements was used in the statistical tests. No correlations were found. We might also expect the degree of perturbation to be a function of the relative velocities of the galaxies; small velocities make for longer encounters and hence a greater degree of perturbation. However, again, no correlation was found. These null results indicate that either these simplistic measurements of interaction strength are inadequate, or there are numerous complicating factors which must be considered in order to isolate various sources of scatter which may wash out possible correlations between intrinsic, physical processes which are only weakly sampled by the variables used here.

More encouraging results were obtained in statistical comparisons between the properties of the IGs and non-IGs. To minimize selection biases incurred by using optically-selected galaxies, the non-IGs were chosen from the BGS on the basis of optical morphology. The non-IG set was selected by comparing the distributions of the blue luminosities of the IGs and non-IGs, and then randomly deleting galaxies from the non-IGs until both samples had the same normalized frequency distribution of blue luminosity. Figure 2a shows that the IGs and non-IGs span the same range of far-infrared color ratios, and thus *individual* IGs are not distinguishable from non-IGs in these properties. However, it is clear that over all the IGs are distributed more toward lower values of the f_{12}/f_{25} flux ratio and larger values of the f_{60}/f_{100} flux ratio than the non-IGs. A similar effect was seen by Bushouse et al. (1988) in an optically selected sample. The cumulative distribution functions of these color ratios (Figs. 2b and 2c) indeed show statistically significant differences in the distributions; the two-sample Kolomogorov-Smirnov statistic indicates that the probability that the distributions for the two samples are drawn from the same underlying population is less than 1%. A similar effect is seen in the distributions of the infrared surface brightness, SB_{fir} (which correlates strongly with the color ratios); the infrared surface brightness

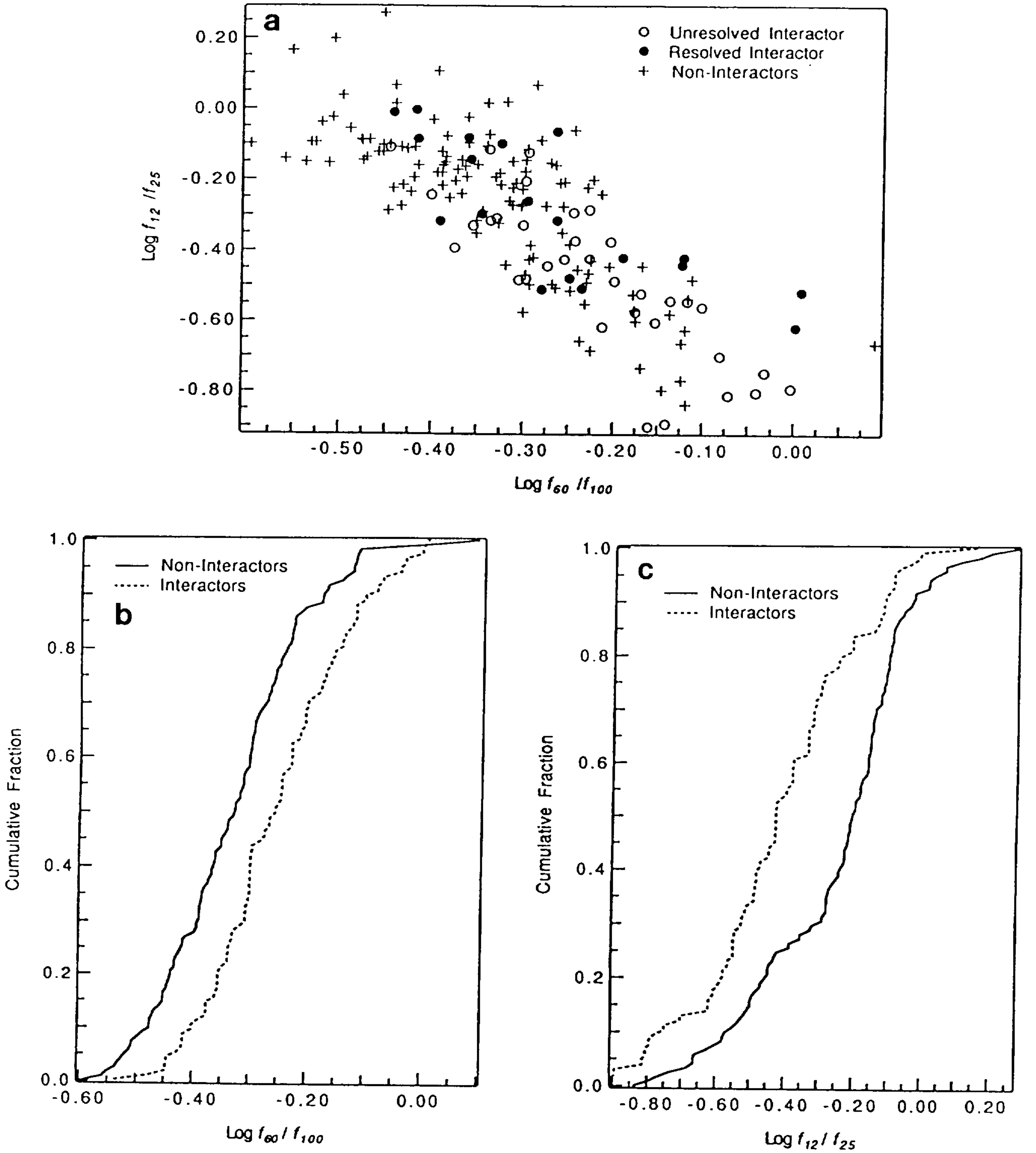

FIGURE 2 (a) Far-infrared color-color diagram for interacting and non-interacting galaxies in the IRAS Bright Galaxy Sample, and cumulative frequency distributions for (b) $f_{60\mu m}/f_{100\mu m}$ and (c) $f_{12\mu m}/f_{25\mu m}$.

distribution of the interacting systems rapidly reaches higher values than those of the non-interactors. The IGs have a median SB_{fir} which is a factor of ≈ 10 greater than the median SB_{fir} for the non-IGs; likewise, the median L_{fir} is a factor of ≈ 2.5 higher than the median L_{fir} for the non-IGs. The probability of the samples being drawn from the same underlying population is less than 1%. Additional details of the HiRes processing, simulations and results are presented by Surace et al. (1993).

FUTURE PROSPECTS

There is, of course, a limit to how far the IRAS data can be pushed for studies of IGs: for example, ultraluminous far-infrared galaxies are much too close together to resolve with IRAS, and it is not possible to separate nuclear and disk components or to study the detailed spatial distribution of the far-infrared emission in even the closest IGs. The high resolution and sensitivity provided by future far-infrared satellites (ISO & SIRTF) will allow us to track the full range of galaxy interaction stages, push to higher redshifts and L_{ir}, produce far-infrared color maps to study dust temperature distributions, and investigate nuclear versus disk far-infrared emission components. In the mean time, what can HiRes processing of IRAS data for additional IGs do for us? Studies of far-infrared selected IGs such as those in the Extended IRAS Bright Galaxy Sample (Sanders et al. 1994, in preparation), as well as optically selected binary galaxies, can improve upon the current low-number statistics and selection biases. The IRAS data for additional IGs could also be combined with existing observations at other wavelengths to begin disentangling the numerous factors that are likely responsible for the large scatter in the far-infrared properties of IGs, such as their molecular and atomic gas properties, Hubble types, and interaction dynamics (prograde versus retrograde encounters, etc.).

SUMMARY

We have reviewed procedures, limitations and results of high resolution processing of interacting galaxies potentially resolvable by IRAS. Simulations and processing of real sources show that the IRAS detector coverage, both the scan density and the position angles of the IRAS scans with respect to the vector separating the galaxies, greatly influences whether or not any particular galaxy pair will be resolved by HiRes. Among 56 groups chosen from the IRAS Bright Galaxy Sample for HiRes processing, 22 systems have been resolved yielding fluxes for a total of 51 galaxies. In about 2/3 of the resolved pairs, both galaxies were detected in the far-infrared. A set of isolated non-interacting galaxies was chosen from the Bright Galaxy Sample for comparison with the interacting galaxies. For the current sample of interacting systems resolved by IRAS, which naturally excludes close pairs and ultraluminous merging systems, the primary conclusions are: (a) It is not possible to distinguish individual interacting galaxies from isolated galaxies of similar luminosity on the basis of infrared properties alone. (b) No direct correlation was found between measures of interaction strength and indicators of enhanced star formation within the resolved systems. (c) Comparison of the interacting and isolated samples indicates statistically significant differences between their distributions of far-infrared color ratios, luminosities, and surface brightnesses. These differences can be attributed to heating of the dusty, gas-rich interstellar medium due to the triggering of starbursts in the interacting galaxies. Even during the early stages of interaction spanned by these systems, in a statistical sense, tidal perturbations substantially boost far-infrared indicators of star formation compared to non-interacting systems. HiRes processing of additional interacting galaxies observed by IRAS can provide us with a head start in identifying the best candidates for more sensitive, high-resolution studies with ISO and SIRTF.

ACKNOWLEDGMENTS

This work was supported by the Jet Propulsion Laboratory, California Institute of Technology, under a contract with the National Aeronautics and Space Administration (NASA). This research was done in collaboration with B. T. Soifer and A. E. Wehrle. We thank J. Fowler for useful discussions concerning HiRes processing.

REFERENCES

Arp, H. C., & Madore, B. F. 1987, *A Catalogue of Southern Peculiar Galaxies and Associations* (Cambridge: Cambridge University Press)

Aumann, H. H., Fowler, J. W., & Melnyk, M. 1990, AJ, 99, 1674

Barnes, J. E., & Hernquist, L. 1992, ARA&A, 30, 705

Byrd, G. G., Sundelius, B., & Valtonen, M. 1987, A&A, 171, 16

Bushouse, H. A., Lamb, S. A., & Werner, M. W. 1988, ApJ, 335, 74

Dahari, O. 1984, AJ, 89, 966

Larson, R. B., & Tinsley, B. M. 1978, ApJ, 219, 46

Lonsdale, C. J., Persson, S. E., & Matthews, K. 1984, ApJ, 287, 95

Mazzarella, J. M., Bothun, G. D., & Boroson, T. A. 1991, AJ, 101, 2034

Mazzarella, J. M., Graham, J. R., Sanders, D. B., & Djorgovski, S. 1993, ApJ, 409, 170

Noguchi, M. 1991, MNRAS, 251, 360

Sanders, D. B, Soifer, B. T., Elias, J. H., Madore, B. F., Matthews, K. Neugebauer, G., & Scoville, N. Z. 1988, ApJ, 325, 74

Shlosman, I. 1990, in Paired and Interacting Galaxies, I.A.U. Colloquium No. 124, eds. J. W. Sulentic, W. C. Keel, & C. M. Telesco (NASA CP-3098), p. 689

Soifer, B. T., Boehmer, G., Neugebauer, G., & Sanders, D. B. 1989, AJ, 98, 766

Surace, J. A., Mazzarella, J. M., Soifer, B. T., & Wehrle, A. E. 1993, AJ, 105, 864

Telesco, C.M., Wolstencroft, R.D., & Done, C. 1988, ApJ, 329, 174

Toomre, A., & Toomre, J. 1972, ApJ, 178, 623

N95-21760

AZIMUTHALLY AVERAGED RADIAL $S_{100\mu M}/S_{60\mu M}$ DUST COLOR TEMPERATURES IN SPIRAL GALAXIES

NICK DEVEREUX
New Mexico State University, Astronomy Department, Box 30001/Dept. 4500, Las Cruces, NM 88003

ABSTRACT The IRAS $S_{100\mu m}/S_{60\mu m}$ dust color temperature profiles are presented for two nearby spiral galaxies M 101 and M 81. The radial dust temperature profiles provide an important constraint on the origin of the far-infrared luminosity. The observed dust temperature is compared with that expected for diffuse interstellar dust heated by the general interstellar radiation field within each galaxy. The implications for the contribution of cirrus to the far-infrared luminosity of M 101 and M 81 are discussed.

INTRODUCTION

The IRAS HiRes images provide the unique opportunity to quantify the radial dependence of the dust color temperature in several nearby spiral galaxies of large angular size. The radial dependence of the $S_{100\mu m}/S_{60\mu m}$ dust color temperature, in particular, is important for constraining the origin of the far-infrared luminosity in spiral galaxies for two reasons. First, the bulk, ~ 80 %, of the far-infrared luminosity is radiated between 60 and 100 μm due to the fact that the far-infrared spectral energy distribution of spiral galaxies typically peaks at a wavelength of about 100μm. Second, the radial dependence of the $S_{100\mu m}/S_{60\mu m}$ dust color temperature profile can, in some cases, distinguish between the two primary contending models for the origin of the far-infrared luminosity in spiral galaxies; the star formation model in which the far-infrared luminosity is dominated by the radiation from dust heated by O and B stars, and the cirrus model, in which the far-infrared luminosity is produced by diffuse dust heated by the general interstellar radiation field of non-ionizing stars.

At issue in the controversy surrounding the origin of the far-infrared luminosity is whether or not the far-infrared fluxes that were measured for literally thousands of galaxies by the Infrared Astronomical Satellite (IRAS) can be utilized to measure high mass star formation rates. Although use of the Hα emission line luminosity is a less controversial way to measure high mass star formation rates, the number of galaxies for which the Hα emission line luminosity has been measured is limited to about 200 galaxies at present (Kennicutt and Kent 1983; Bushouse 1987; Romanishin 1990). In contrast, IRAS measured far-infrared fluxes for literally thousands of galaxies. Consequently, the IRAS database is regarded as a potentially valuable resource for quantifying high mass star formation rates (Young et al. 1986; Helou et al. 1985; Gavazzi et al. 1986; Leech et al. 1988; Devereux and Young 1990; 1991, 1992).

S. Terebey and J. Mazzarella (eds.), *Science with High-Spatial Resolution Far Infrared Data*, 81–85, 1994, Jet Propulsion Laboratory, Pasadena, CA.

Evidence supporting high mass stars as the origin of the far-infrared luminosity includes the fact that the O and B stars, which are required to generate the Hα emission line radiation in galaxies, can also supply the luminosities measured in the far-infrared, independent of the $S_{100\mu m}/S_{60\mu m}$ dust color temperature (Devereux and Young 1990) and spiral type (Devereux and Young 1991). Nevertheless, the ambiguity surrounding the origin of the far-infrared luminosity in spiral galaxies remains due to the perception that 70 - 90 % of the far-infrared luminosity may be produced by cirrus, or more specifically, diffuse interstellar dust heated by the radiation field of non-ionizing stars (Walterbos and Schwering 1987; Lonsdale-Persson and Helou 1987; Bothun, Lonsdale and Rice 1989).

We know that the general interstellar radiation field can, in principle, supply the luminosities measured in the far-infrared because it requires only a moderate amount of extinction of the optical light, corresponding to A_v = 0.5 - 1.0 magnitudes, to account for the L_{fir}/L_{blue} luminosity ratios observed for spiral galaxies. What may be more difficult to explain are the warm dust temperatures indicated by the $S_{100\mu m}/S_{60\mu m}$ ratio. The purpose of this contribution is to show how the radial dependence of the $S_{100\mu m}/S_{60\mu m}$ dust color temperature can provide an important constraint on the origin of the far-infrared luminosity within spiral galaxies.

Since the angular resolution of the HiRes 100 μm images is about 100″ and lower than the ~ 60″ resolution of the HiRes 60 μm images, it is necessary, for the purposes of calculating dust color temperatures, to convolve the 60 and 100 μm HiRes images to the same resolution. The following procedure was adopted:

1. Display the beam resolution maps in order to determine the half power beam size and shape at 60 and 100 μm.
2. By trial and error, determine the kernels necessary to convolve the 60 and 100 μm beam profiles to the same resolution. With a little practice it is usually possible to achieve circular beams with a full width half maximum size of 105″ at both 60 and 100 μm.
3. Perform the same convolutions on the HiRes 60 and 100 μm galaxy images.
4. Measure the 60 and 100 μm galaxy fluxes at a resolution that is no higher than the resolution of the convolved beams. Generate azimuthally averaged radial dust temperature profiles by taking the ratio of the 60 and 100 μm fluxes measured within elliptical annulae. The major axis of the ellipse, r, is aligned with the major axis of the galaxy and the minor axis width of the ellipse is r cos (i), where i is the galaxy inclination.
5. Quantify the uncertainty in each of the annular fluxes by measuring the noise (Jy/sr) at several background locations well away from the galaxy. This is possible using only HiRes images that have been processed with the *fbias* option which preserves the noise inherent in the original data. Determine the average noise (Jy/sr) and multiply the noise by the solid angle of each annulus within which the fluxes were measured. Propagate the uncertainties to determine the error in the $S_{100\mu m}/S_{60\mu m}$ flux ratio at each radius.
6. Convert the $S_{100\mu m}/S_{60\mu m}$ flux ratios into dust color temperatures in order to facilitate comparison with models.

RESULTS

The azimuthally averaged $S_{100\mu m}/S_{60\mu m}$ radial dust color temperature profiles are illustrated in Figure 1 for the nearby spiral galaxies M 101 and M 81. The dashed lines in Figure 1 represent the temperatures expected for dust grains of a variety of sizes and compositions when heated by the general interstellar radiation field. The intensity of the general interstellar radiation field was determined from the extinction corrected visual surface brightness profile for each galaxy. The dashed line labelled cirrus indicates the temperature expected for a dust grain size distribution that is required to explain IRAS measurements of Galactic cirrus (Low et al. 1984). The temperatures are based on the models of Desert, Boulanger and Puget (1990) who calculated the $S_{100\mu m}/S_{60\mu m}$ flux ratios expected for a cirrus grain size distribution that is irradiated by stellar radiation fields ranging in intensity from 0.3 to 1000 times that in the solar neighborhood. A visual surface brightness of 23.2 mag/(arc sec)^2 was adopted for the solar neighborhood. The $S_{100\mu m}/S_{60\mu m}$ flux ratios are converted into dust temperatures assuming a λ^{-1} emissivity law, although qualitatively, the results described below remain unchanged if a λ^{-2} emissivity law were used instead. The dust temperatures expected for large, $\geq 0.1\mu m$, Si and C grains are based on the models of Jura (1982).

M 101

M 101 is a late type (SABcd) spiral galaxy. The radial $S_{100\mu m}/S_{60\mu m}$ dust color temperature profile is remarkably uniform. The mean dust temperature is 31 ± 2 K for a λ^{-1} emissivity law (see Figure 1a). The observed dust temperature is well in excess of the temperature expected for large, $\geq 0.1\mu m$, dust grains heated by the general interstellar radiation field. The observed dust temperature is also higher than expected for cirrus. Evidently the general interstellar radiation field is unable to heat cirrus up to the high temperature that is observed for the dust in M 101. The surface brightness of M 101 would, in fact, have to be at least 1.5 magnitudes brighter in the V band in order for the general interstellar radiation field to be able to heat the cirrus up to the observed temperature.

M 81

M 81 is an early type (SAab) spiral galaxy. The radial $S_{100\mu m}/S_{60\mu m}$ dust color temperature profile varies with radius from a peak value of about 35 K (λ^{-1}) in the nucleus to about 28 K (λ^{-1}) in the disk (see Figure 1b). The observed dust temperature is well in excess of the temperature expected for large, $\geq 0.1\mu m$, dust grains heated by the general interstellar radiation field. On the other hand, the observed dust temperature appears to be consistent with that expected for diffuse interstellar dust, or equivalently cirrus, that is heated by the general interstellar radiation field within M 81.

DISCUSSION

The results presented for M 101 and M 81 highlight the importance of the radial dust temperature profiles in constraining the origin of the far-infrared luminosity within spiral galaxies. In the case of the late type spiral galaxy

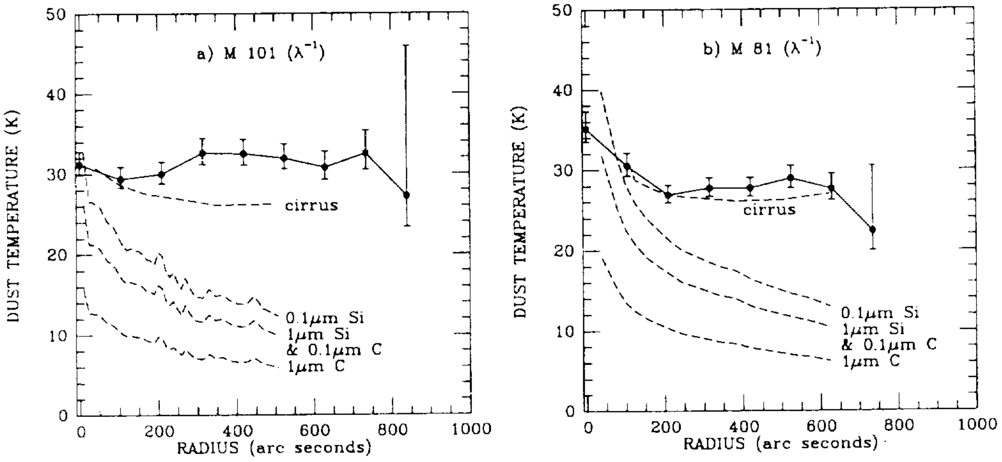

FIGURE 1 The solid lines indicate the azimuthally averaged $S_{100\mu m}/S_{60\mu m}$ dust color temperature profiles observed for the nearby spiral galaxies M 101 (left panel) and M 81 (right panel). The dashed lines indicate the temperatures expected for dust grains of a variety of sizes and compositions when heated by the general interstellar radiation field within each galaxy.

M 101, an explanation of the origin of the far-infrared luminosity in terms of cirrus, or more specifically, diffuse interstellar dust heated by the radiation field of non-ionizing stars, is untenable because the intensity of the general interstellar radiation field is too low, by at least 1.5 magnitudes, to heat the dust up to the observed temperatures. The limit is necessarily a lower limit because of the inevitable contribution of ionizing stars to the V band surface brightness profile that was used to estimate the intensity of the non-ionizing interstellar radiation field within M 101. On the other hand, O and B stars do provide a viable alternative explanation for the origin of the far-infrared luminosity because the dust temperature is comparable to that observed for Galactic and extragalactic HII regions (Scoville and Good 1989; Sodroski et al. 1989; Rice et al. 1990) at all locations within M 101.

In the case of the early-type spiral galaxy M 81, the far-infrared luminosity may be attributed to diffuse dust heated by the general interstellar radiation field, because the expected temperature is very similar to the temperature that is actually observed. The distinction between ionizing and non-ionizing stars as the origin of the far-infrared luminosity would, however, require a further determination of the relative contribution of ionizing and non-ionizing stars to the general interstellar radiation field within M 81.

REFERENCES

Bothun, G.D., Lonsdale, C.J., and Rice, W. 1989, *ApJ*, **341**, 129

Bushouse, H. 1987, *ApJ*, **320**, 49

C-2.

Desert, F.X, Boulanger, F., and Puget, J.L. 1990, *A&A*, **237**, 215

Devereux, N.A., and Young, J.S. 1990, *ApJ*, **350**, L25.

Devereux, N.A., and Young, J.S. 1991, *ApJ*, **371**, 515

Devereux, N.A., and Young, J.S. 1992, *AJ*, **103**, 1536

Gavazzi, G., Cocito, A., and Vettolani, G. 1986, *ApJ*, **305**, L15

Helou, G., Soifer, B.T., and Rowan-Robinson, M. 1985, *ApJ*, **298** L7.

Jura, M. 1982, *ApJ*, **254**, 70

Kennicutt, R.C., and Kent, S.M. 1983, *AJ*, **88**, 1094

Leech, K.J., Lawrence, A., Rowan-Robinson, M., Walker, D., and Penston, M.V. 1988, *MNRAS*, **231**, 977

Lonsdale-Persson, C.J., and Helou, G. 1987, *ApJ*, **314**, 513

Low, F.J., et al. 1984, *ApJ*, **278**, L19

Rice, W., Boulanger, F., Viallefond, F., Soifer, B.T., and Freedman, W.L. 1990, *ApJ*, **358**, 418

Romanishin, W. 1990, *AJ*, **100**, 373

Scoville, N.Z., and Good, J.S. 1989, *ApJ*, **339**, 149

Sodroski, T.J., Dwek, E., Hauser, M.G., and Kerr, F.J. 1989, *ApJ*, **336**, 762

Walterbos, R.A.M., and Schwering, P.B.W. 1987, *A&A*, **180**, 27

Young, J.S., Schloerb, F.P., Kenney, J.D., and Lord, S.D. 1986, *ApJ*, **304**, 443

32

FAR-INFRARED SOURCES AND DIFFUSE EMISSION IN M31

CONG XU
Max-Planck-Institut für Kernphysik, W6900 Heidelberg, Germany

GEORGE HELOU
IPAC 100-22, California Institute of Technology, Pasadena, CA 91125

ABSTRACT A study on the far-infrared (FIR) emission of M31 has been carried out with the HiRes maps ($\sim 1'$) derived from IRAS data. Sixty-eight FIR sources are detected in M31, which in general coincide with optical HII regions, and contribute 15%, 23%, 29%, and 23% to the fluxes in 12 μm, 25 μm, 60 μm, and 100 μm bands, respectively. The remaining diffuse emission, which dominates the FIR emission of M31, is studied using a dust heating model which utilizes the UV and optical photometry maps and the HI maps available in the literature. It is found that the global dust-to-gas ratio in M31 disk is 6.5 10^{-3}, very close to the dust-to-gas ratio in the solar neighborhood. There is a significant galactocentric gradient of the dust-to-HI-gas ratio, with an e-folding scale length of 9 kpc. The diffuse dust correlates tightly with the HI gas. The model indicates that the non-ionizing UV (913—4000Å) radiation from massive and intermediate massive stars contributes only about 30% of the heating of the diffuse dust, while the optical-NIR (4000—9000Å) radiation from the old stellar population is responsible for the most of the heating.

INTRODUCTION

Two characteristics make M31 unique for a far-infrared (FIR) study. The first is its proximity: Being the nearest spiral galaxy outside the Milky Way, it offers the best linear resolution for observations of spirals with a given angular resolution. This is a significant advantage given the relatively poor angular resolutions of the current generation of FIR instruments. Second, it is known to have very low current star-formation rate, perhaps an order of magnitude lower than that of the Milky Way (Walterbos 1988). Not many such quiescent spirals can be studied in the FIR, and none beside M31 with such high spatial resolution.

The FIR emission of M31 has been studied by Habing et al. (1984), Soifer et al. (1985), and very extensively by Walterbos and Schwering (1987) using IRAS maps. We report preliminary results from a new study using the HiRes maps. Our emphasis is to study the properties of FIR sources and the diffuse emission separately. This was not possible in the previous studies because of the relatively coarse resolution of earlier maps based on IRAS observations.

S. Terebey and J. Mazzarella (eds.), *Science with High-Spatial Resolution Far Infrared Data*, 87–93, 1994, Jet Propulsion Laboratory, Pasadena, CA.

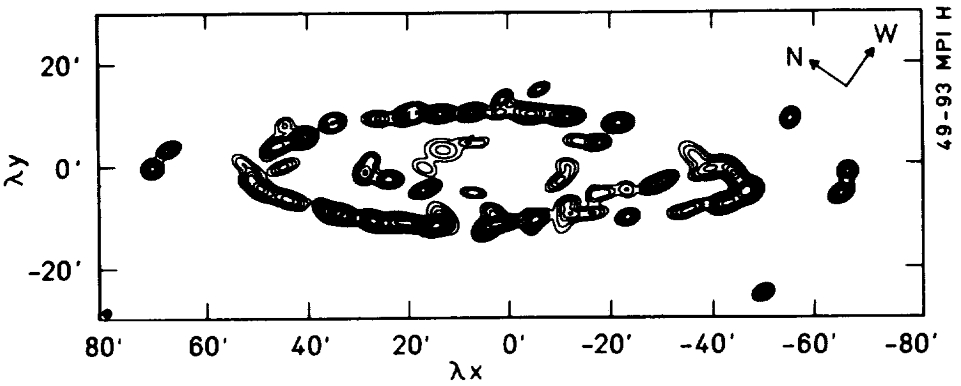

FIGURE 1 Contour map of M31 showing unresolved 60 μm sources only. The resolution has been degraded to 1.7′, indicated by the hatched circle in the lower left corner.

FIR MORPHOLOGY

The FIR morphology revealed by the HiRes maps (see Fowler and Aumann, this volume) is obviously very different from the optical morphology of M31 (Walterbos and Kennicutt 1987). Most of the FIR emission is confined in surprisingly thin arms which are hardly resolved by the HiRes beam, and in a nucleus much smaller than the optical bulge. The contrast between the arms and interarm regions is more than an order of magnitude. At similar spatial resolution, the optical emission is much smoother than the FIR emission. There is a kind of anti-correlation between the optical and FIR emission: many thin dark lanes in the optical map appear as thin bright arms in the 60 μm HiRes map.

FIR SOURCES

There are many bright sources on the 60 μm HiRes map. The brightest ones are concentrated on the famous ring at about 10 kpc (50′) galactocentric radius. Thanks to the high resolution (∼ 1′), most of them are well separated from each other, so we can do a relatively clean and complete source extraction using Gaussian fitting. We found 68 60 μm sources (Figure 1), all coincident with known giant HII regions or HII region complexes (Pellet et al. 1978).

Unresolved sources account for a small fraction of the emission. They contribute 15%, 23%, 29%, and 23% to the total fluxes of M31 at 12 μm, 25 μm, 60 μm, and 100 μm, respectively. By comparison, unresolved sources in M33 contribute 50%, 92%, 68% and 56% of the total fluxes of that galaxy in the four corresponding bands (Rice et al. 1990).

In addition, the sources in M31 are not as warm as the M33 sources. Figure 2 compares the average FIR spectrum of the M31 sources to that of the M33 sources, and to the spectrum of the integrated emission of M31.

The 60 μm-to-100 μm color ratio of the M31 sources is warmer than that of the integrated emission, but significantly cooler than that of the M33 sources.

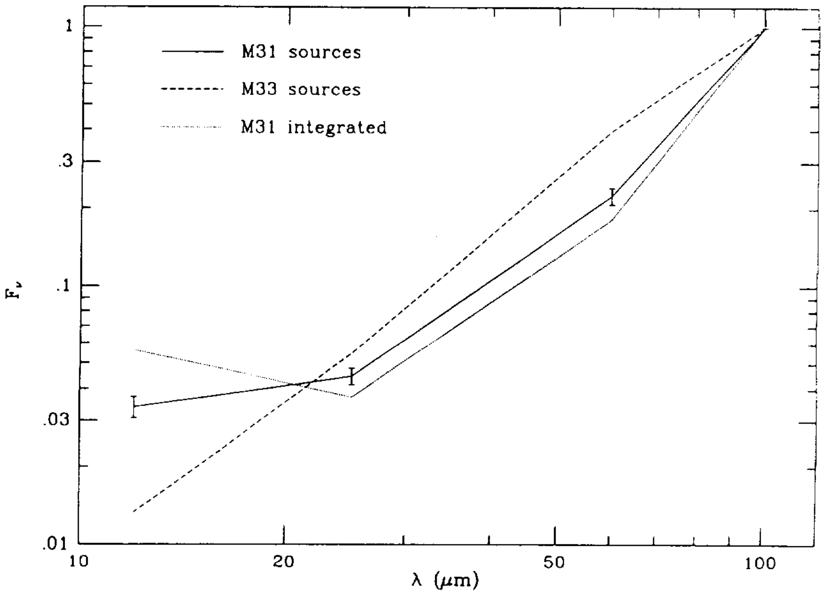

FIGURE 2 Average FIR spectrum (normalized by $F_{100\,\mu m}$) of the M31 sources (solid line) compared to that of the M33 sources (dashed line), and that of the integrated emission of M31 (dotted line).

DIFFUSE DUST

We define the diffuse component as the emission from areas in M31 where unresolved sources contribute less than 20% of the emission; the bulge area is also excluded from the following discussion. By studying this dominant component, we attempt to answer the following questions:

1. How is the interstellar dust distributed in M31? How does it correlate with HI gas?
2. How much interstellar dust does M31 have? What is the dust-to-gas ratio?
3. What is the energy budget of the diffuse interstellar dust?

We developed a dust-heating model, in which we assume that the heating of the diffuse dust is provided by the non-ionizing UV and optical interstellar radiation. We adopt an infinite-plane-parallel-slab geometry for the radiation transfer problem (van de Hulst and De Jong 1969), and assume that the dust and the UV light have the same scale height, while the scale height of the optical radiation is a factor of 2 larger. The model is applied to a complete sample of small areas (cells), each of size $2' \times 2'$, within the M31 disk. The sample selection is described in Xu and Helou (1993a). With the adopted distance (690 kpc) and inclination (13°, 90° for seen face-on), the linear size of the cells is 0.4×1.8 kpc in the plane of M31. Cells are included only if their FIR (40–120 μm) surface brightness $B_{\rm fir}$, calculated from the 60 μm and 100 μm surface brightness (Helou et al. 1988), exceeds a signal-to-noise ratio of five.

The radiation transfer model predicts for each cell the ratio between the FIR surface brightness due to heating of dust by the radiation in a given band,

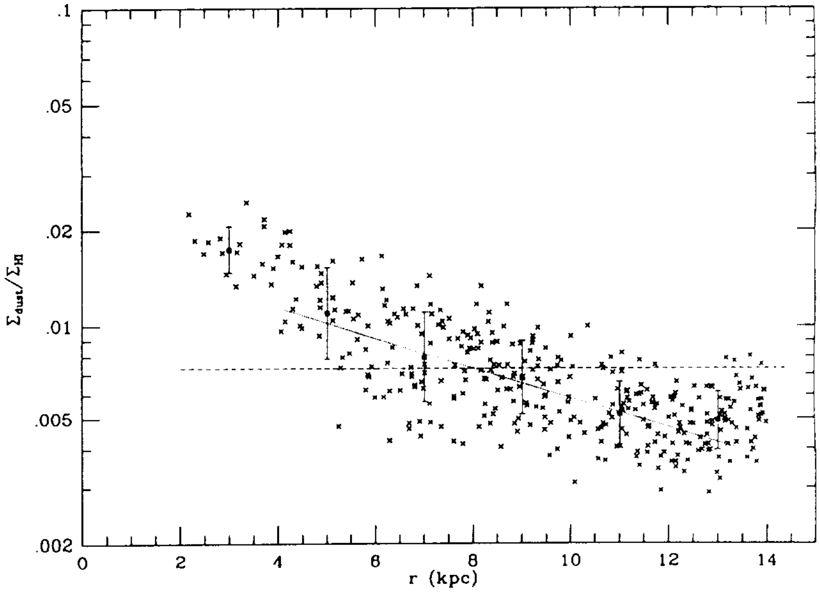

FIGURE 3 Plot of the dust-to-HI-gas ratio versus the galactocentric radius of the diffuse FIR emission in M31.

and the observed radiation surface brightness of the same band, as a function of the optical depth:

$$Q_i(\tau_{\lambda,i}) = \frac{\Delta_i B_{fir}}{B_{\lambda,i}}. \tag{1}$$

Surface brightness maps of the non-ionizing UV and the optical (UBVR) radiation have been taken from corresponding maps (Milliar 1984; Walterbos and Kennicutt 1987), and the FIR emission is assumed to be due to dust heated by the radiation in these bands:

$$B_{fir} = \sum_{i}^{5} B_i \times Q_i. \tag{2}$$

The summation of the right side of Eq.(2) is over five radiation bands: UV (912 — 3000Å, U (3000 — 4000Å), B (4000 — 5000Å), V (5000 — 6000Å), and R/NIR (6000 — 9000Å). Assuming an extinction law which is the same as the local one (Savage and Mathis 1979), the extinction at different wavelength bands depends on a single parameter, i.e., the dust column density which, consequently, can be determined using Eq.(2) (see Xu and Helou 1993b for more details).

The results of our model are shown in the following three figures. Figure 3 is the plot of the dust-to-HI-gas ratio versus the galactocentric radius.

The HI column density is taken from the HI map of Brinks (1984). The dashed line shows the dust-to-gas ratio in the solar neighborhood. It can be seen that the dust-to-HI-gas ratios of the M31 cells is not very different from the local value. The solid squares show the average value for the cells in each 2 kpc bin of galactocentric radius. The error bars represent one-σ dispersions, and amount only to about 30%. There is a clear trend that the dust-to-HI-gas

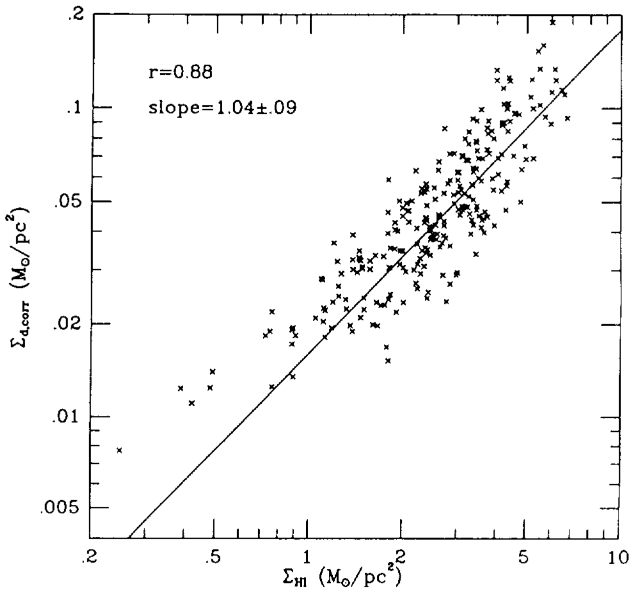

FIGURE 4 Diagram of the 'gradient-corrected' dust column density versus HI column density in the M31 disk.

ratio decreases with increasing radius, suggesting a galactocentric gradient in the dust-to-gas ratio. The set of average values can be fitted reasonably well by the dotted line, corresponding to an e-fold scale length of the gradient of 9 kpc.

Figure 4 is the diagram of the 'gradient-corrected' dust column density versus HI column density.

By 'gradient-corrected' we mean the dust column density multiplied by exp (r/9 kpc), to balance the gradient of the dust-to-gas ratio. A strong and linear correlation is found in this diagram: the correlation coefficient is 0.88 and the slope of the log-log plot is 1.04±0.09, which is shown by the solid line. Thus in M31, dust correlates tightly with the HI gas, and the local dust column density scales linearly with the column density of HI gas, while the scaling factor decreases with increasing galactocentric radius. Integrating the dust in the entire disk of M31, we find that there is $2.0\ 10^7$ M dust within a 16 kpc radius in the M31 disk. The global dust-to-HI gas ratio is $6.6\ 10^{-3}$, quite close to the local value of $7.3\ 10^{-3}$ (Désert et al. 1990).

In Figure 5, we compare the radial distributions of the FIR emission and of dust heating predicted by the model. The solid curve is the FIR distribution. The dashed curve is the total heating which accounts for about 80% of the FIR. The difference between the FIR emission and the heating is likely to be due to the sources. For example, the difference is most significant around the ring and in the outer region of the disk, where most of the bright sources are (Figure 1). The non-ionizing UV radiation contributes only 26% of the total heating, which is represented by the dotted-dashed curve. It is most prominent at the ring, but never dominant. Throughout the M31 disk, the optical radiation, shown as the dotted curve, dominates the heating of the diffuse dust. This indicates that the FIR emission of M31 is mainly due to heating by the optical radiation from relatively old stars, i.e., stars older than a few 10^9 years.

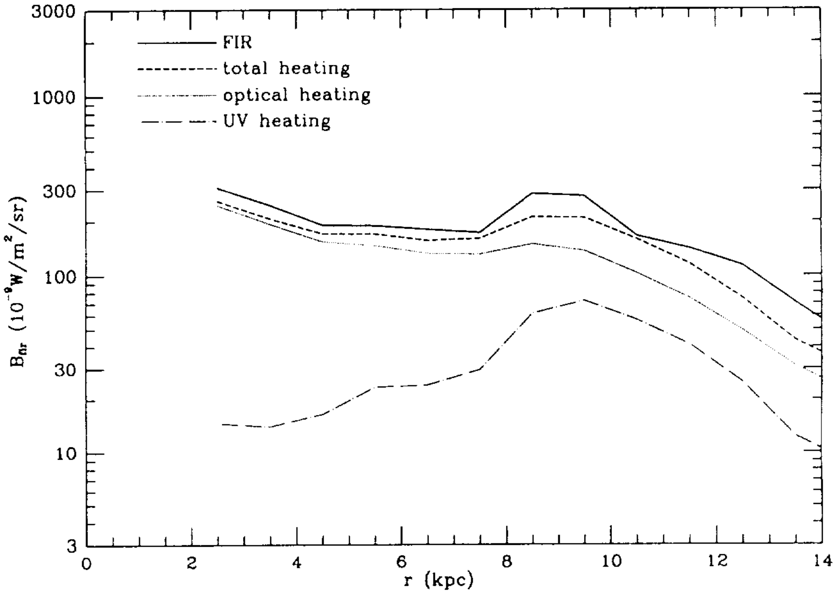

FIGURE 5 Plot of the radial distributions of the FIR emission and of dust heating predicted by the model.

ACKNOWLEDGMENTS

This work was carried out in part at the Jet Propulsion Laboratory, California Institute of Technology, under a contract with the National Aeronautics and Space Administration.

REFERENCES

Brinks, E. 1984, Ph.D. thesis, University of Leiden

Désert, F.A., Boulanger, F., and Puget, J.L. 1990, *A&A*, **273**, 215

Habing, H.J., *et al.* 1984, *ApJ*, **278**, L59

Milliard, B. 1984, These, d'Etat, University de Marseille

Pellet, *et al.* 1978, *A&AS*, **31**, 439

Rice, W., *et al.* 1990, *ApJ*, **358**, 418

Savage, B.D. and Mathis, J.S. 1979, *ARA&A*, **17**, 73

Soifer, B.T., *et al.* 1986, *ApJ*, **304**, 651

van de Hulst, H.C. and De Jong, T. 1969, *Physica* **41**, 151

Walterbos, R.A.M. 1988, in *Galactic and Extragalactic Star Formation*, eds. R.E. Pudritz and M. Fich, Kluwer, Dordrecht, p361

Walterbos, R.A.M. and Kennicutt, R.C. 1987, *A&AS*, **69**, 311

Walterbos, R.A.M. and Schwering, P.B.W. 1987, *A&A*, **180**, 27

Xu, C. and Helou, H. 1993a, to appear in *Infrared Cirrus and Diffuse Interstellar Clouds*, eds. R. Cutri and W. Latter

Xu, C. and Helou, H. 1993b, in preparation

3
6

CORRELATION OF FAR-INFRARED EMISSION AND RADIO CONTINUUM EMISSION ALONG THE MAJOR AXIS OF EDGE-ON SPIRAL GALAXIES

B. HEIKKILA AND W.R. WEBBER
Astronomy Department, New Mexico State University, Las Cruces, NM 88003

ABSTRACT Using new High Resolution far-infrared (FIR) images we have determined FIR flux densities, the FIR luminosity, and intensity profiles along the major axis for eight nearby edge-on spiral galaxies. We present spatial comparisons between the FIR profiles in three of the four IRAS Bands (25, 60, 100 μm). We also present direct spatial comparisons between the 60 μm intensity profiles and intensity profiles from 20 cm radio continuum maps with identical resolution ($\sim 60''$) obtained from J.J. Condon. Using these profiles we have evaluated the 60 μm-to-20 cm ratio Q_{60} along the major axis for each galaxy and have compared the results to global Q_{60} values. This analysis reveals that a considerable amount of complicated structure exists within the disks of spiral galaxies. Closer examination of this disk structure will make it possible to place further constraints on the well known global far-infrared and radio continuum emission correlation.

INTRODUCTION

The discovery, in the early eighties, of the tight correlation between integrated thermal far-infrared emission and non-thermal radio continuum emission from spiral galaxies (Dickey and Salpeter 1984) has prompted numerous studies to see if the correlation holds spatially within the disks of individual spiral galaxies (e.g. Beck and Golla 1988; Bicay and Helou 1990). These studies, however, have been hampered by the lack of resolution in the far-infrared images. The development of the new High Resolution (HiRes) processing capabilities of the Infrared Processing and Analysis Center (IPAC) has resulted in far-infrared images with a five-fold increase in resolution compared with previous maps produced by the Full Resolution Survey Coadder (FRESCO). This increased resolution allows the infrared detections made by IRAS to be analyzed in greater detail than previously possible. In addition, the resolution of the 60 μm maps ($\sim 60''$ at 20 iterations) is almost exactly the same as the resolution of the National Radio Astronomy Observatory Very Large Array (VLA) in D-array at 20 cm. We have used this unique resolution relationship to directly compare the 60 μm far-infrared distribution and the 20 cm (predominantly non-thermal) radio continuum emission in a sample of spiral galaxies. Studies concerning the global far-infrared radio correlation (e.g. Devereux and Eales 1989; Chi and Wolfendale

S. Terebey and J. Mazzarella (eds.), *Science with High-Spatial Resolution Far Infrared Data*, 95–100, 1994, Jet Propulsion Laboratory, Pasadena, CA.

94

1990) have shown that the emission mechanisms for the far-infrared and radio continuum are most probably linked through massive star formation. It is the goal of this present study to try to understand this relationship better.

GALAXY SAMPLE

For this initial part of our analysis we have selected eight nearby (D< 20 Mpc) edge-on ($i > 75°$) spiral galaxies of morphological type Sb or later. The HiRes processing also required that the sources be sufficiently bright with flux densities greater than ~ 2 MJy/Sr and sufficiently sampled by IRAS with at least 2 all-sky Hours-Confirmation scans. The list of selected galaxies, inclination, far-infrared luminosity, L_{fir}, evaluated using

$$L_{fir} = 3.94 \times 10^5[2.58 S_{60\mu m}(Jy) + S_{100\mu m}(Jy)]D^2(Mpc)L_\odot \qquad (1)$$

(*Cataloged Galaxies and Quasars Observed in the IRAS Survey* 1985) and the integrated flux densities from the 25, 60 and 100 μm HiRes images are shown in Table 1. Also shown are published 20 cm flux densities (Condon 1987) and the global 60 μm-to-20 cm ratio Q_{60} for each galaxy.

TABLE 1 Luminosity and Integrated Fluxes

Galaxy	i [a]	L_{FIR}		Flux	Density (Jy)		Global
		($1 X 10^9$)	25 μm	60 μm	100 μm	20 cm	Q_{60}
NGC 4565	90°	2.42	0.94	9.62	40.42	0.131	73.44
NGC 5907	90°	7.78	1.15	13.79	53.42	0.089	154.94
NGC 4157	90°	10.15	1.31	15.56	49.02	0.242	64.22
NGC 4517	90°	1.42	0.60	6.71	20.25	0.036	186.39
NGC 4631	85°	7.06	7.33	79.50	171.17	1.200	66.25
NGC 0891	84°	12.27	5.75	63.57	173.80	0.701	90.68
NGC 3556	81°	10.14	3.27	30.07	51.93	0.306	98.27
NGC 2683	79°	0.60	0.54	7.22	28.25	0.066	109.39

---

[a] Inclination (Tully 1988)

DATA ANALYSIS

For each galaxy in our sample, a cut, averaged over 3 pixels (~45″), was made along the major axis defined by the optical position angle. The same cuts were made on the 25, 60, and 100 μm maps as well as the 20 cm radio continuum images (Condon 1992).

The 25 μm and 100 μm major axis intensity profiles were numerically scaled to the 60 μm profile to try to identify structure such as peaks or "hot spots" within the dust distribution in the disk of each spiral galaxy. The peaks show up predominantly in the 25 μm profile due to the increased resolution and higher dust temperatures associated with this band. These peaks may be tracers of

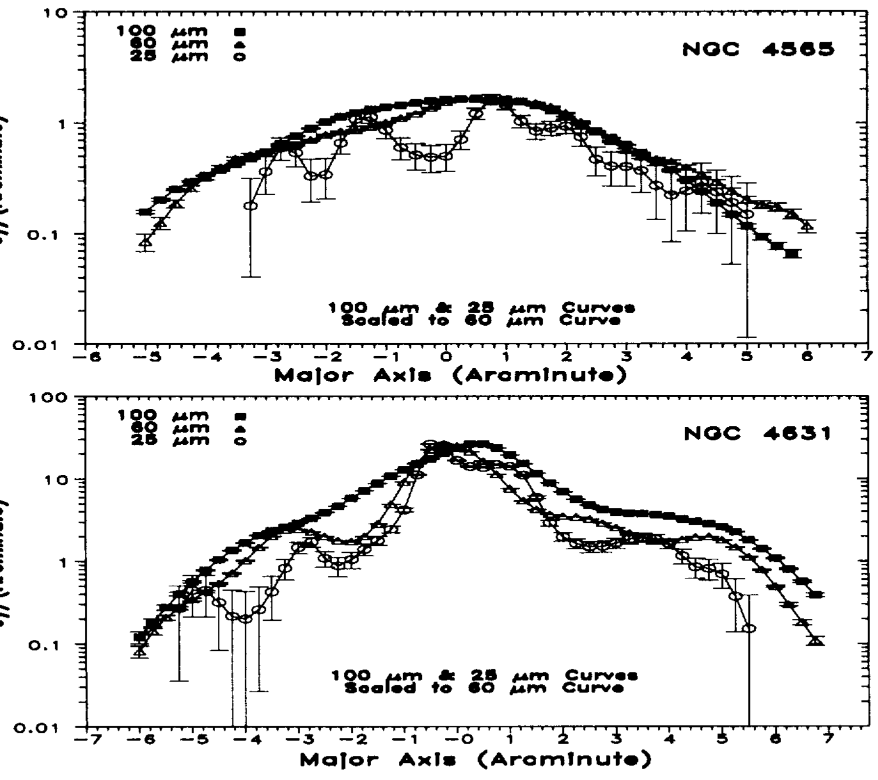

FIGURE 1 Example 25, 60, and 100 μm Major Axis Profiles

giant HII regions within spiral arms. The major axis profiles extend out to the 5σ noise level determined from the maps, and the error bars represent the 1σ noise in the individual data points. Profiles for two galaxies are shown in Figure 1. In this figure the resolution along the major axis is $\sim 45''$ for the 25 μm profile, $\sim 60''$ for the 60 μm profile, and $\sim 75''$ for the 100 μm profile.

For each galaxy the 60 μm cuts are then compared to the 20 cm major axis profiles determined in exactly the same way. These comparisons are shown in Figure 2 and Figure 3 for all eight galaxies. We then calculated Q_{60} $(S_{60\mu m}/S_{20cm})$ values along the major axis. These profiles are also shown in Figure 2 and Figure 3 along with the global Q_{60} values represented by a dashed line. The 1σ errors in these figures are approximately the size of the data points. These Q_{60} profiles show considerable structure. At this early stage of data analysis using both the Q_{60} profiles and the individual 60 μm and 20 cm profiles (and before a similar study of face-on galaxies) we believe there is evidence for two classes of galaxies. NGC 2683 and NGC 4157 show a strongly decreasing Q_{60} profile as well as decreasing 60 μm and 20 cm profiles along the major axis. For these galaxies it appears that the IR and radio emission are both concentrated in the center. If the sources of electrons that are producing the radio emission are concentrated in the center then the decreasing Q_{60} profile may be explained by the outward diffusion of these electrons.

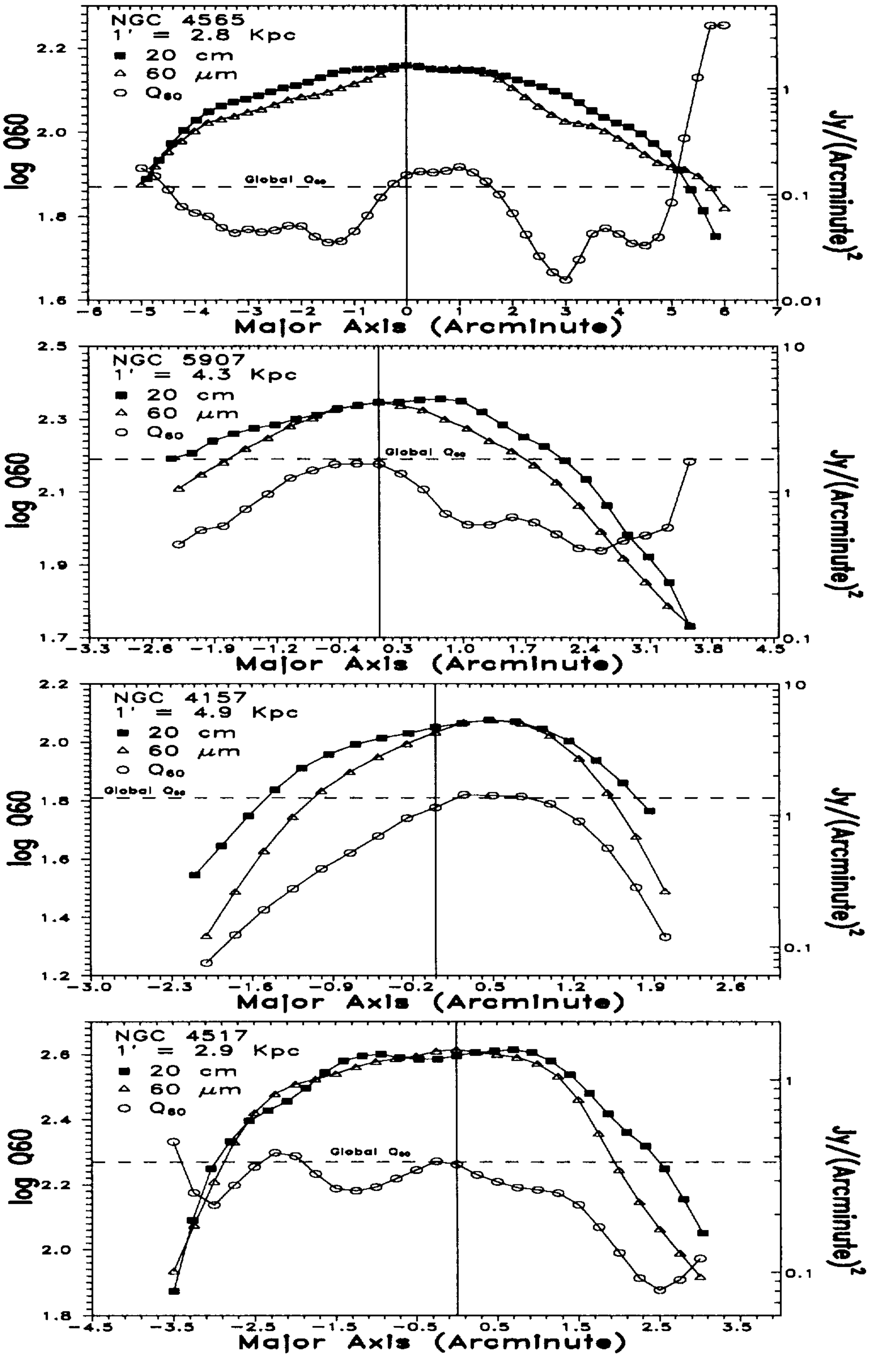

FIGURE 2 60 μm 20 cm Comparison Profiles and Q_{60} Values

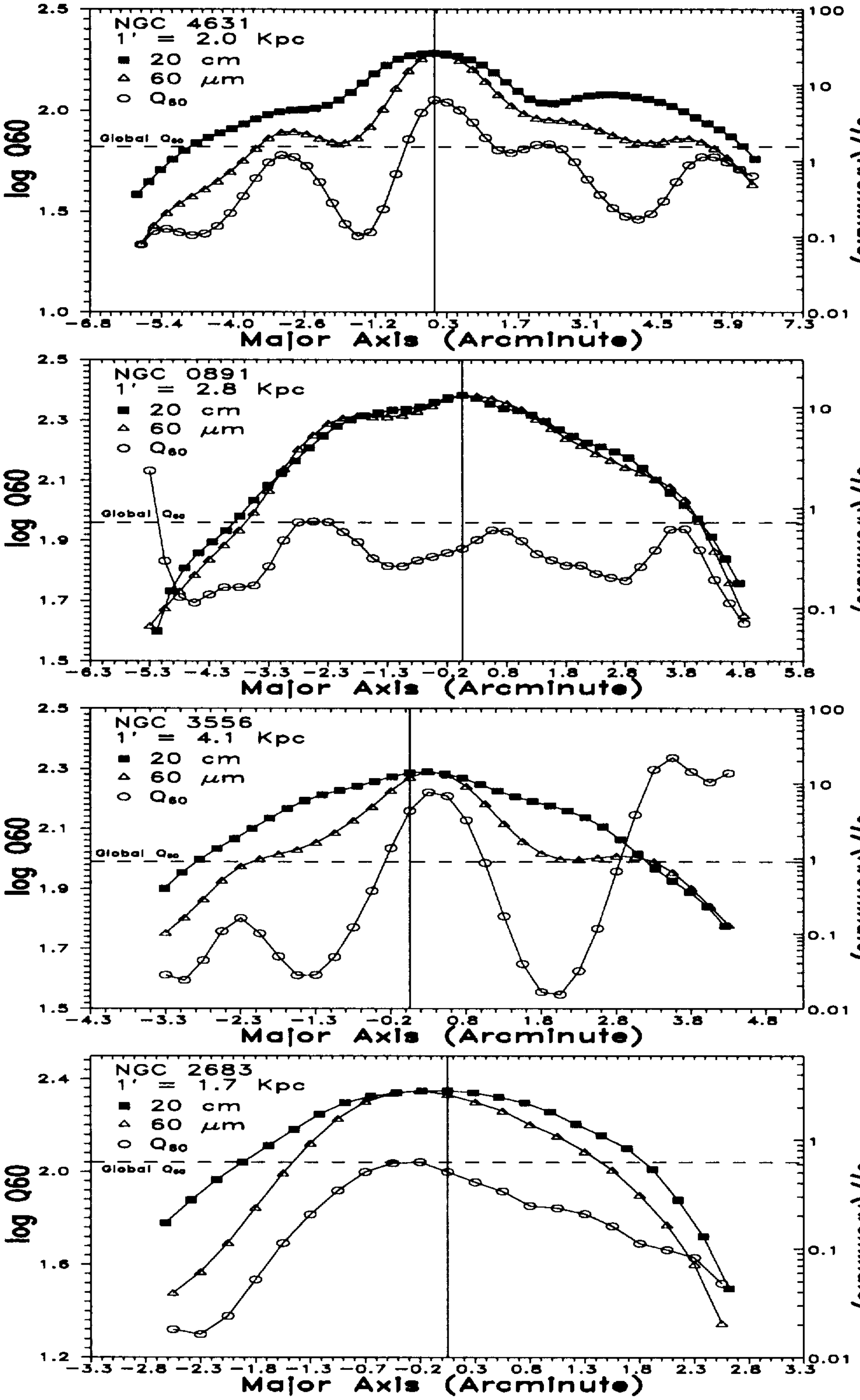

FIGURE 3 60 μm 20 cm Comparison Profiles and Q_{60} Values

The other six galaxies show more complicated Q_{60} profiles but basically they can be interpreted in terms of an almost constant Q_{60} ratio out to the distance at which both the 60 μm and 20 cm profiles decrease rapidly - e.g., the edge. Some galaxies have more structure on top of this constant profile than others and some such as NGC 3556 and NGC 4631 appear to have a central 60 μm peak as well which gives the appearance of a central bulge in the Q_{60} profile. All of these galaxies may be interpreted in terms of the sources of the electrons that are producing the radio emission being more uniformly distributed in radius out to the edge, beyond which both the 60 μm and 20 cm radiation decrease rapidly.

CONCLUSIONS

The global FIR Radio correlation for an individual galaxy will be affected by the relative contributions from the the disk and central bulge components to the total FIR and Radio emission. Our analysis shows a more complicated structure within these components than previously indicated. In particular, the 25 μm major axis profiles show numerous peaks within both the central bulge and disks of spiral galaxies. These "hot spots" are probably associated with recent star formation.

The Q_{60} profiles show considerable structure. A preliminary analysis of these profiles suggests two classes of galaxies — one in which the radio and IR emission is concentrated in the center and the outward diffusion of electrons is responsible for the decreasing Q_{60} profile — the other in which most of the radio and IR emission is distributed more uniformly out to the edge. The Q_{60} ratio in these galaxies can be thought of as roughly constant upon which considerable structure exists including a separate central IR bulge in some cases.

ACKNOWLEDGMENTS

We are grateful to J.J. Condon for providing us with 20 cm VLA maps.

REFERENCES

Beck, R., and Golla, G. 1988, *ApJ*, **191**, L9

Bicay, M. D., and Helou, G. 1990, *ApJ*, **362**, 59

Cataloged Galaxies and Quasars Observed in the IRAS Survey, 1985, prepared by C. J. Lonsdale, G. Helou, J. C. Good, and W. Rice

Chi, X., and Wolfendale, A. W. 1990, *MNRAS*, **245**, 101

Condon, J. J. 1987, *ApJS*, **65**, 485

Condon, J. J. 1992, *Private Communication*

Devereux, N. A., and Eales, S. A. 1989, *ApJ*, **340**, 708

Dickey, J. M., and Salpeter, E. E. 1984, *ApJ*, **284**, 461

Tully, R. B. 1988, *The Nearby Galaxies Catalog*, (Cambridge University Press)

514-90

N95- 21763

4

P 6

FAR-INFRARED MAPPING OF DUSTY ELLIPTICAL GALAXIES

JOANNA F. LEES AND D. A. HARPER
Dept. of Astron. and Astroph., the University of Chicago, 5640 S. Ellis Ave., Chicago, IL 60637

M. P. RUPEN
National Radio Astron. Obs., P.O. Box O, Socorro, NM 87801

G. R. KNAPP
Dept. of Astroph. Sci., Princeton University, Princeton, NJ 08544

ABSTRACT Preliminary results from a program to map the thermal far-infrared emission from cool dust in elliptical galaxies using the Yerkes 60-Channel Camera on the Kuiper Airborne Observatory (KAO) are presented. The 160 μm emission from the elliptical NGC 6524 is apparently extended over the optical galaxy whereas the 100 μm emission is unresolved. This implies a dust temperature gradient consistent with that expected for dust with Galactic properties exposed to the general interstellar radiation field of the elliptical galaxy. Observations of the elliptical NGC 5666 and the NGC 7463/4/5 compact group (consisting of the elliptical NGC 7464, the S0 NGC 7465, and the spiral NGC 7463) are also discussed.

INTRODUCTION

Early-type galaxies generally are dominated by an old stellar population and contain little gas and dust compared to the typical late-type spiral. However, since the launch of the IRAS satellite in the mid-1980's, it has been known that many of these systems contain small quantities of cold interstellar matter: 45% of all elliptical galaxies show thermal dust emission at $60 - 100\mu$m (Knapp *et al.* 1989) with temperatures apparently similar to dust in spiral galaxies. Ratios of global gas quantities (such as CO and HI 21 cm emission) to the far-infrared emission are also indistinguishable from those for spirals (Lees *et al.* 1991).

However, before last year, only one dusty elliptical galaxy (NGC 5128; Cen A) was close enough to be fully mapped by IRAS (Eckart *et al.* 1990) and at higher resolution with the KAO (Joy *et al.* 1988; see also Lester 1993, these proceedings). Only two dusty ellipticals, both strong radio sources (Cen A and Per A), had been observed at all at wavelengths between 100 μm and 2 mm.

S. Terebey and J. Mazzarella (eds.), *Science with High-Spatial Resolution Far Infrared Data*, 101–106, 1994, Jet Propulsion Laboratory, Pasadena, CA.

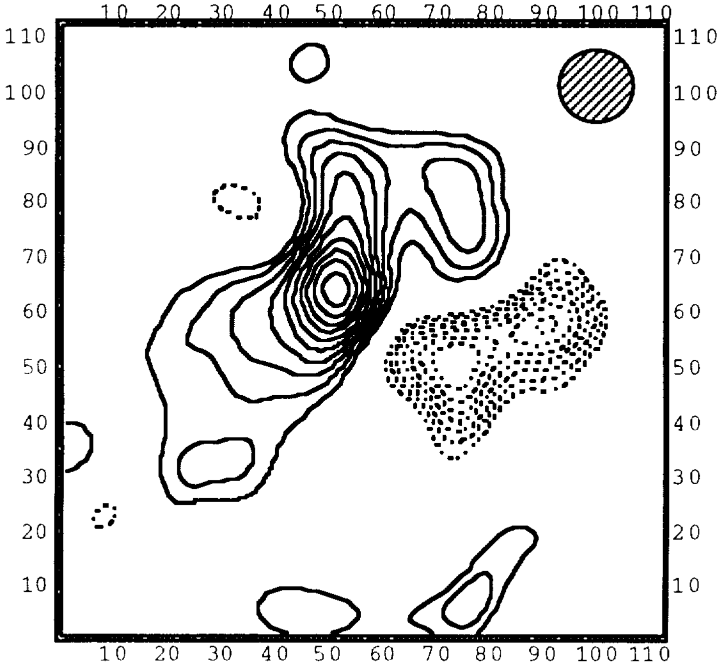

FIGURE 1 The 160 μm KAO map of NGC 6524. The positive contours show the ON beam (see text) at 1.5σ, 2.1σ, 2.7σ, 3.3σ, etc. The negative (dashed) contours show the OFF beams. Each pixel in the image is $3''.5$ and the resolution, shown in the upper right, is $44''$.

OBSERVATIONS

In 1992 we began a program to study the infrared properties of IRAS-bright elliptical galaxies. In April and July 1992 we mapped three ellipticals in the far-infrared using the Yerkes 60-channel camera on the Kuiper Airborne Observatory. The camera is an 8×8 bolometer array (without the corner pixels) operating at the diffraction limit of the KAO telescope with pixel sizes of $16''$, $25''$, $44''$, and $44''$ at wavelengths of 60, 100, 160, and 200 μm respectively (results from an earlier version of the camera with 32 pixels are presented in Engargiola 1991).

We are also involved in projects to obtain JHK images of dusty ellipticals using the GRIM near-infrared camera on the ARC telescope at Apache Point, New Mexico and to define the 350-1100 μm submillimeter spectra of these galaxies using the James Clark Maxwell Telescope in Hawaii. Our ultimate goal is to use the stellar radiation field derived from the near-infrared images and the far-infrared and submillimeter photometry of the thermal dust emission to accurately model the equilibrium dust emission from elliptical galaxies.

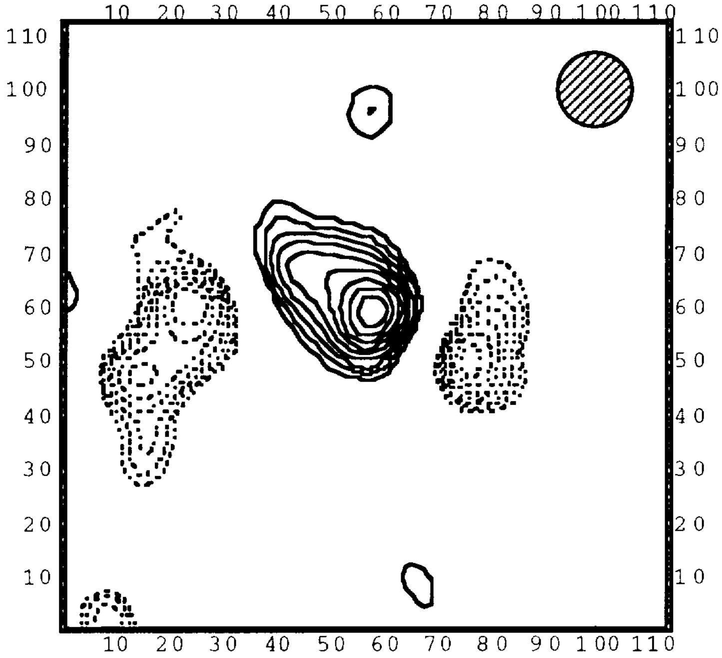

FIGURE 2 The 100 μm KAO map of NGC 6524. The positive contours show the ON beam (see text) at 2σ, 2.5σ, 3.1σ, 3.6σ, etc. The negative (dashed) contours show the OFF beams. Each pixel in the image is 2″ and the resolution, shown in the upper right, is 25″.

RESULTS

In Figures 1–3 we show the far-infrared maps of NGC 6524 (at 160 and 100 μm) and of NGC 5666 (at 160 μm) obtained from the KAO. At 160 μm our resolution is 44″ and the area plotted in Figures 1 and 3 is about 6′.4 on a side. At 100 μm the resolution is 25″ and the field of Figure 2 is about 3′.7 × 3′.7.

In order to maximize the integration time on these relatively faint objects we used a small chop throw of about 2′which meant the source was on the array on both ON and OFF beams. The result of doing the background subtraction (ON−OFF) produces two negative half-intensity images of the source on either side of the positive image. This can be seen clearly in Figures 1–3.

NGC 6524 is classified as E/S0 in the UGC catalog. It is quite isolated, with the nearest neighbor being almost a degree away, and has a weak active nucleus with broad emission lines (Merighi *et al.* 1991). It has the distinction of being the second-brightest elliptical at far-infrared wavelengths (after Cen A) with flux densities measured by IRAS of 7.9 Jy at 100 μm and 3.9 Jy at 60 μm (Knapp *et al.* 1989).

The most striking result from our KAO observations of NGC 6524 shown in Figures 1 and 2 is that the galaxy appears to be clearly resolved perpendicular

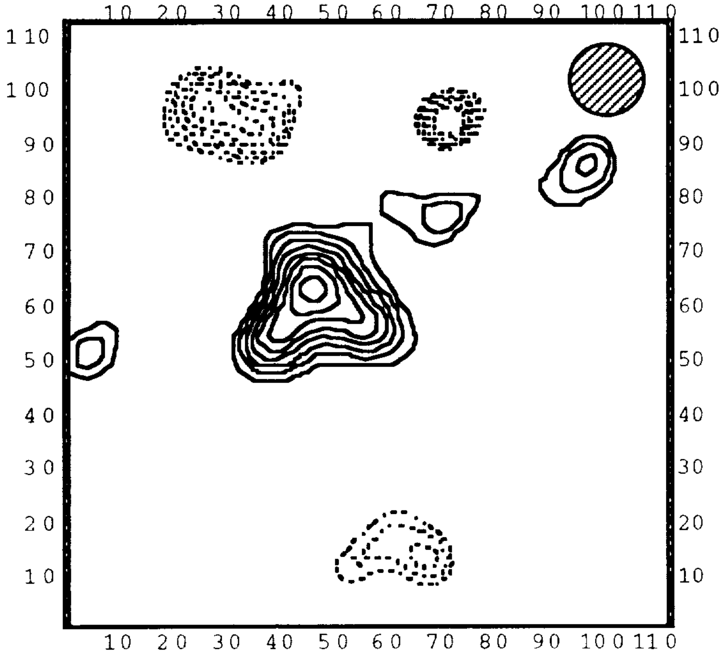

FIGURE 3 The 160 μm KAO map of NGC 5666. The positive contours show the ON beam (see text) at 2σ, 2.4σ, 2.8σ, 3.2σ, etc. The negative (dashed) contours show the OFF beams. Each pixel in the image is 3″.5 and the resolution, shown in the upper right, is 44″.

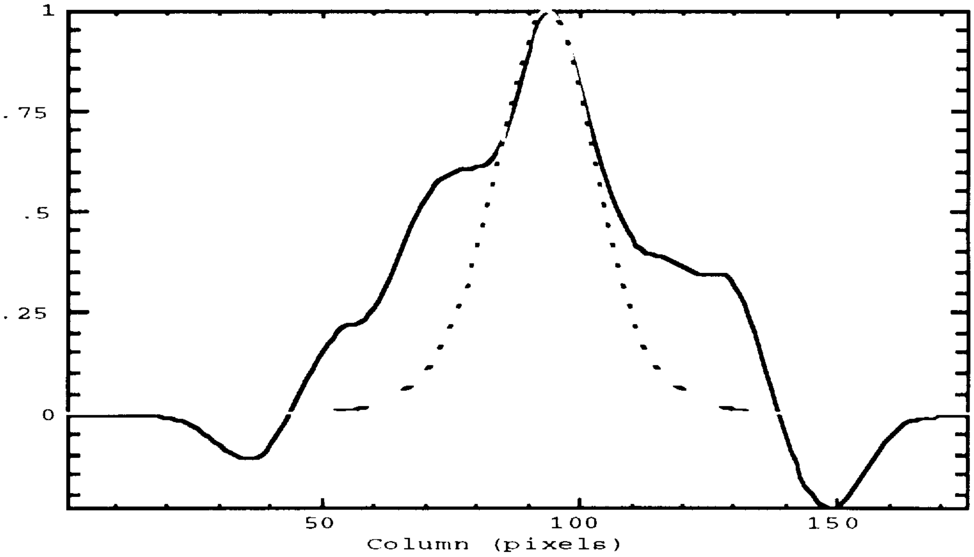

FIGURE 4 Cut through the NGC 6524 160 μm peak, perpendicular to the chop direction (solid line), and through a point source observed on the same night (dashed line). The abscissa is column number in pixels (each pixel is 3″.5 and the ordinate is far-infrared flux density relative to the peak. The resolution is 44″ or about 13 pixels.

to the chop direction at 160 μm (Fig. 1). A one-dimensional cut through the KAO 160 μm map is compared to that for a point source observed on the same night in Figure 4. The NGC 6524 profile resembles a point source superposed on lower-level extended emission. This extended emission is at about the 4σ level in our data, and we intend to reobserve this galaxy in 1993 to confirm this result. The 100 μm map in Figure 2, in contrast, shows no such extent, even though the resolution and map scale are almost twice as high. The FWHM of the 160 μm emission is about $2'$ (the optical size is $1'.7$), but at 100 μm the FWHM is less than $25''$.

The 160 and 100 μm KAO data imply a radial dust temperature gradient in NGC 6524. For a dust emissivity ($n = 2$) and grain parameters like those in our Galaxy, the central dust temperature is 29°K, in agreement with the observed IRAS 60 and 100 μm flux densities (Knapp *et al.* 1989) and our recent submillimeter photometry at the JCMT (Knapp, Lees & Rupen, in preparation). In the outer parts of the galaxy ($r \approx 1'$) the dust temperature must be less than 22°K. A simple model for optically thin dust in equilibrium in the old stellar radiation field defined by recent H and K band photometry by us at Apache Point predicts a dust temperature gradient of 29°K in the inner KAO beam to 20°K in the outer parts, in excellent agreement with our data. We hope to acquire additional observations of NGC 6524 this year on the KAO to actually measure the dust temperature in the outer parts of the galaxy.

Figure 3 shows our 160 μm KAO map of the isolated, gas-rich compact elliptical NGC 5666. NGC 5666 appears to be unresolved at this wavelength, which is not surprising considering the fact that its optical size is less than an arcminute. Its CO emission is also probably very compact (Lees *et al.* 1991) as is the central Hα and thermal radio emission (Wrobel & Heeschen 1988), but it has an extended, rotating HI disk over $3'$ (Lake, Schommer & van Gorkom 1987) which apparently does not emit strongly at 160 μm. Like NGC 6524, the IRAS 60-100 μm measurements, our 160 μm data point, and our recent JCMT submillimeter photometry indicate a central dust temperature of about 27°K.

The compact interacting system NGC 7463/4/5 was also mapped at 160 μm, but unfortunately the data were of poor quality due to telescope stability problems on the KAO last July. The S0 NGC 7465 and the spiral NGC 7463 were both apparently detected, with NGC 7463 having significantly cooler dust emission. This is also evident in the IRAS CPC images of this group (van Driel *et al.* 1993).

ACKNOWLEDGMENTS

This research was supported by NASA grant NGR 14-001-227.

REFERENCES

Eckart, A., *et al.* 1990, *ApJ*, **363**, 451

Engargiola, G. 1991, *ApJS*, **76**, 875

Joy, M., Lester, D. F., Harvey, P. M., & Ellis, H. B. 1988, *ApJ*, **326**, 662

Knapp, G. R., Guhathakurta, P., Kim, D.-W., & Jura, M. 1989, *ApJS*, **70**, 329

Lake, G., Schommer, R.A., & van Gorkom, J.H. 1987, *ApJ*, **314**, 57

Lees, J.F., Knapp, G.R., Rupen, M.P., & Phillips, T.G. 1991, *ApJ*, **379**, 177

Merighi, R., Basso, L., Vigotti, M., Lahulla, J.F., & Lopez-Arroyo, M. 1991, *A&AS*, **89**, 225

Wrobel, J.M., & Heeschen, D.S. 1988, *ApJ*, **335**, 677

Van Driel, W., de Graauw, Th., de Jong, T., & Wesselius, P.R. 1993, *A&AS*, in press

N95- 21764

EXTENDED FAR-INFRARED EMISSION AND STAR FORMATION IN SEYFERT GALAXIES

A. P. MARSTON
Dept. of Physics & Astronomy, Drake University, Des Moines, IA 50311

ABSTRACT An investigation into the extended distribution of far-infrared (FIR) emission associated with nearby Seyfert galaxies is made using a set of MEM reconstructions of IRAS Chopped Photometric Channel (CPC) data (Marston 1993). The data is compared to a set of H II/starburst galaxy images similarly processed in order to compare distributions and FIR color properties. It is shown that the central 1 kpc or so of Seyfert galaxies show extended FIR emission. FIR colors suggest that the bulk of this emission is not directly associated with an active nucleus. They further suggest that the origins of the majority of the emission is from heated dust associated with star formation surrounding the nucleus rather than dust heated by the active nucleus. Nearby Seyfert galaxies are shown to have a higher concentration of far-infrared emission from their centers than the H II/starburst galaxies and a number appear to reside in disk galaxies with relatively low ongoing star formation in their disks. An example of this is NGC 7582 which has a smooth disk but an active nucleus/starburst center.

INTRODUCTION

IRAS point source results showed Seyfert galaxies to be strong FIR emitters. There are three main candidates for this emission:

i) direct association with an active nucleus
ii) circumnuclear dust heated by the active nucleus
iii) circumnuclear dust heated by hot stars.

Although direct emission from a central nucleus is unlikely in all but the brightest of blazers, there is some debate as to the which of the other two possibilities are the main cause for the FIR emission (see, e.g., Miley et al. 1985; Rodriguez Espinosa et al. 1986). There is also the possibility that unresolved disk emission from the Seyfert galaxies may contribute to the IRAS point source fluxes used in these studies.

A link between star formation and the presence of an active nucleus has been presented by Rodriguez Espinosa et al. 1987 and Edelson et al. 1987. They suggest that Seyfert host galaxies are substantially more luminous than galaxies in the field which might be explained by a link between global star formation and the activity observed in the nuclei.

S. Terebey and J. Mazzarella (eds.), *Science with High-Spatial Resolution Far Infrared Data*, 107–113, 1994, Jet Propulsion Laboratory, Pasadena, CA.

PROGRAM OF INVESTIGATION

In order to investigate the distribution of FIR emission in Seyfert galaxies and its possible connection to the active nucleus and star formation, a study of MEM processed IRAS CPC images of 13 nearby Seyferts, 4 LINERs and 12 H II/SB galaxies has been made. The procedure for this is detailed in Marston (1992) and Marston (1993). Basically, several raster scans of a given object, made at 50 and 100 μm by the IRAS CPC, were background subtracted and then coadded. This image was then reconstructed using MEM, with a noise estimate based on the image repeatability being used to constrain the MEM image reconstructions.

The specific intent of this investigation was to:

i) to search for extended FIR emission in Seyfert galaxies

ii) to compare their FIR properties with those of H II/SB galaxies

iii) To consider their star formation properties based on their FIR emission, in particular their disk emission properties compared to that of more normal galaxies.

EXTENDED FAR-INFRARED EMISSION IN SEYFERT GALAXIES

In 11 out of 13 Seyfert galaxies investigated, extended FIR emission was observed. Extended emission included elongated contours up to a full, distinct disk component in the images. Some examples of images obtained are shown in Figure 1. Extended emission was noted in 9 out of the 12 H II galaxies and all 4 LINERs (examples shown in Figure 2). Taking the full width at half maximum of the processed image of a point source to be 24″, estimates of the size of the FIR emitting regions were made. Estimates for emitting region sizes ranged from unresolved to 8 kpc (NGC 1566, a Seyfert 1). A synopsis of these results are given in Table 1.

The extended x-ray emission in NGC 2992 and NGC 1566 have the same positional angle along the extension as compared to the extended FIR emission (Elvis et al. 1990).

The existence of significant extended emission rules out direct FIR emission from the nucleus as a possible source in Seyfert galaxies.

COLORS IN RESOLVED GALAXIES

Estimates of the optical depth for the nuclear regions of these galaxies did not exceed 0.1 at 100 μm. So FIR colors should be relatively unaffected by optical depth effects.

It is worth noting that of the 6 Seyfert 1 galaxies observed, those with the smallest optical depth were NGC 1566 and NGC 2992, both of which were shown to have extended x-ray emission in the study of Elvis et al. (1990).

For Seyfert and H II region galaxies where the disk and nuclear emission regions were resolved, their FIR colors were obtained and compared. In the case where an active nucleus is heating dust we might expect a significant portion of the FIR emission to be from higher temperature dust at the center. This would show as a high 50/100 μm FIR ratio. Comparison of nuclear to disk

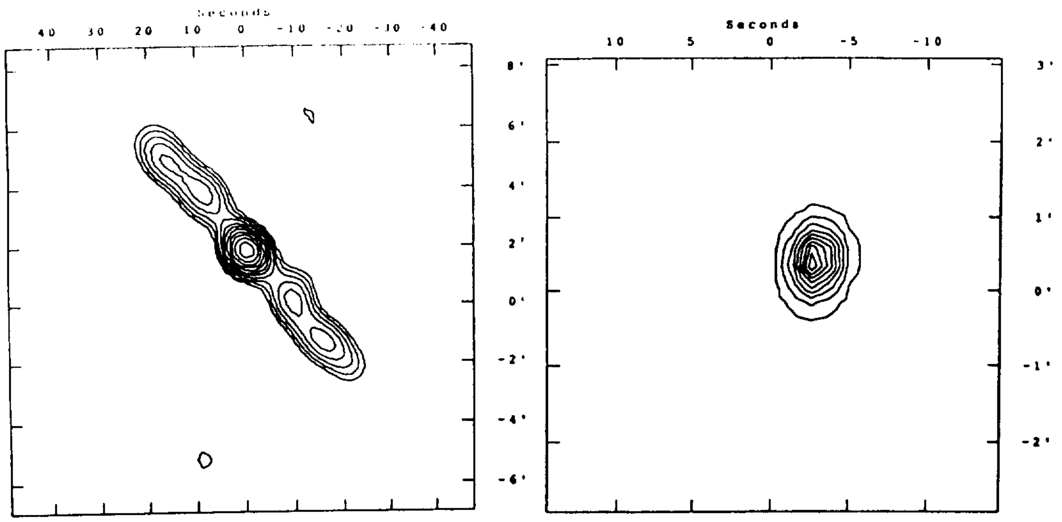

FIGURE 1 MEM reconstructions of the galaxy NGC 4945 (a Seyfert 1 galaxy) at 50 μm (left) showing a FIR disk, and NGC 3281 (a Seyfert 2 galaxy) at 100 μm (right) showing extended FIR emission but no obvious disk.

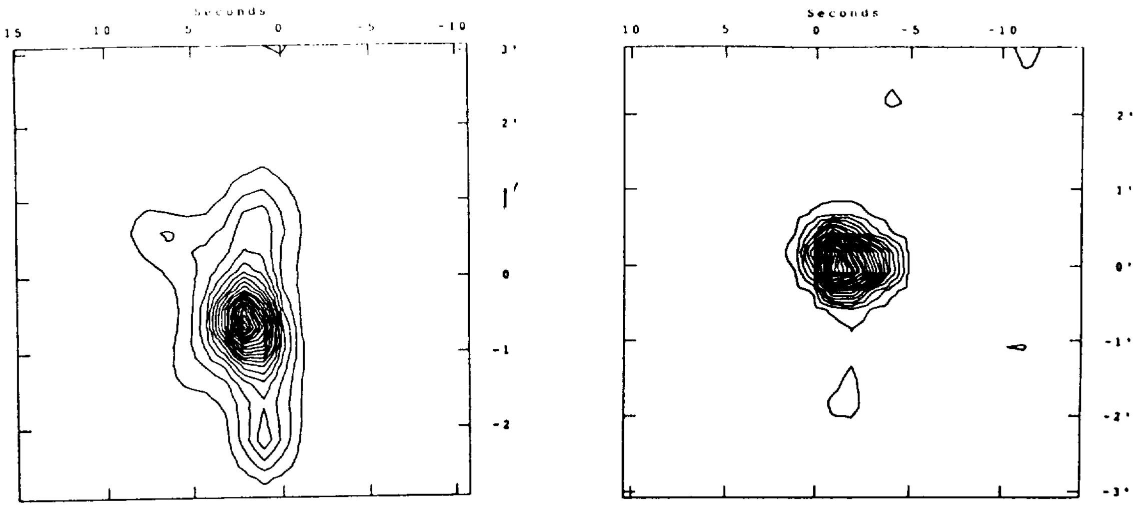

FIGURE 2 MEM reconstructions of the H II galaxies NGC 2903 at 50 μm (left) and NGC 660 at 50 μm (right) showing disk and extension.

Table 1 – Sample Listing and Far-Infrared Source Sizes.

Name (NGC)	Type	Disk	Nuclear size (kpc)	Name (NGC)	Type	Disk	Nuclear size (kpc)
660	H II	No	2.1	1275	Sy1	No	-
1365	Sy1	Yes	4.0	1566	Sy1	No	7.8
1569	H II	Yes	0.5	1808	H II	Yes	1.9
2377	H II	No	-	2903	H II	Yes	1.2
2992	Sy1	No	2.9	2993	H II	No	2.9
3079	LINER	Yes	3.8	3281	Sy2	No	2.6
3310	H II	No	-	4438	LINER	No	1.9
4631	H II	Yes	3.0	4945	Sy1	Yes	1.2
5033	Sy1	Yes	1.0	5055	LINER	Yes	1.0
5194	Sy2	Yes	2.2	5195	H II	No	-
5236	SB	Yes	0.9	5866	H II	No	0.8
6221	Sy2	Yes	2.6	6300	Sy2	Yes	-
7331	LINER	Yes	1.9	7469	Sy1	No	-
7552	H II	No	4.5	7582	Sy2	Yes	1.2
7590	Sy2	No	2.5				

Sy1 = Seyfert 1, Sy2 = Seyfert 2, SB = Starburst, H II = H II region galaxy, LINER = Low Ionization Narrow Emission-line Region (from Marston 1992).

colors shows no significant difference between Seyfert and non-Seyfert nuclear and disk color ratios (see Figure 3, taken from Marston 1992). Further, if the nuclear emission dominated the rest of the emission in the Seyfert galaxies we might expect the nuclear FIR ratio be particularly high for these galaxies. In Figure 4 (from Marston 1992) this is again shown not to be the case. However, the Seyferts observed do have a greater tendency for nuclear rather than disk FIR emission.

STAR FORMATION IN THE DISKS OF SEYFERT GALAXIES

In order to investigate whether the active nucleus has any effect on star formation in the disk of the host galaxies we can compare the FIR disk luminosity of the Seyfert galaxies with that of the non-Seyfert galaxies. The FIR luminosity was calculated from the FIR flux obtained from the following equation

$$F(FIR) = 1.26[3.1S(50) + S(100)] \times 10^{-14} W\ m^{-2} \qquad (1)$$

where $F(FIR)$ is the FIR flux, $S(50)$ is the flux at 50 μm in Janskys and $S(100)$ is the flux at 100 μm measured in Janskys (from Marston 1991). For resolved galaxies, non-Seyferts have an average disk luminosity of $1.7 \pm 0.7 \times 10^{10} L_{\odot}$, while the Seyferts have an average disk luminosity of $1.4 \pm 0.6 \times 10^{10} L_{\odot}$. But 3 out of 6 disk resolved Seyferts have $< 5 \times 10^{9} L_{\odot}$ in their disks.

These findings are consistent with the longslit findings of Carone (1992), where no differences could be discerned between the properties of H II emission line complexes in RnormalS and Seyfert galaxies.

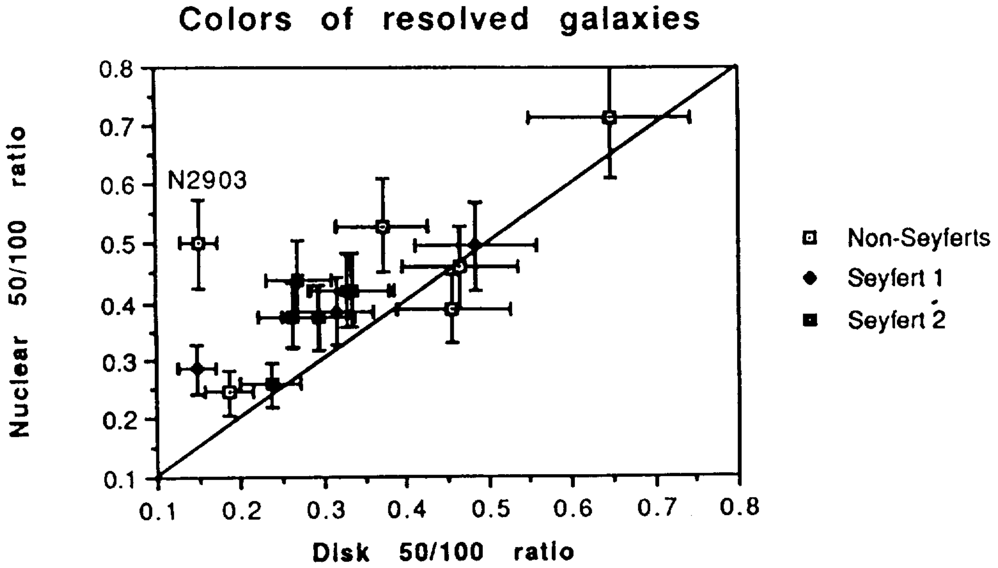

FIGURE 3 FIR disk and nuclear colors compared for the Seyfert and H II region galaxy samples. The distribution suggests no extra heating components are obvious from the emission of the central regions of Seyfert galaxies (from Marston 1992).

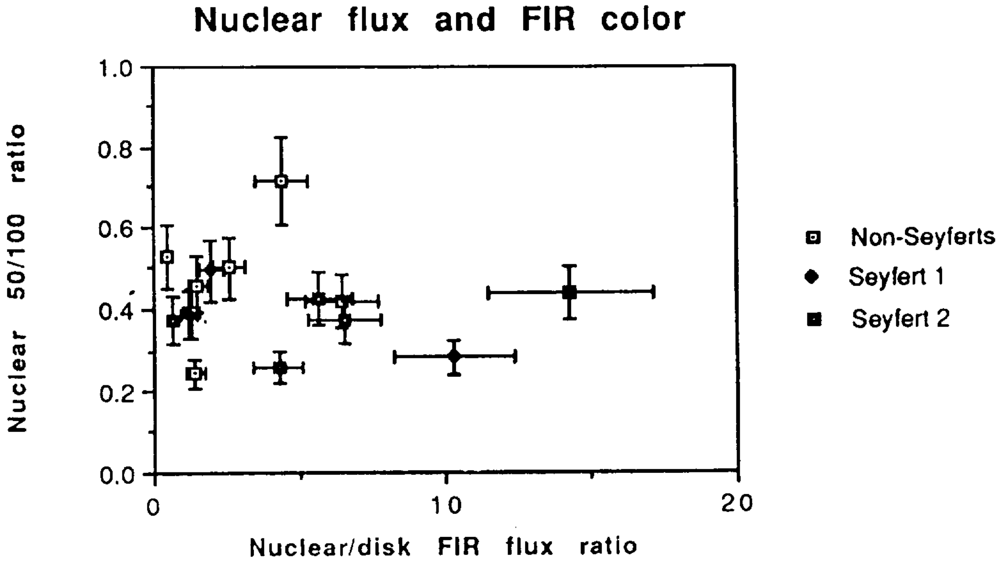

FIGURE 4 Nuclear color compared to the nuclear/disk FIR luminosity ratio. The presence of a dominant nuclear region in the FIR does not affect the nuclear colors (from Marston 1992).

CONCLUSIONS

The extended nature of the FIR emission in nearby Seyfert galaxies indicates that little if any FIR emission comes directly from their nuclei.

Few observable differences exist between the FIR properties of the disks and nuclei of the Seyfert and H II galaxies investigated. Their disk and nuclear colors suggest similar heating mechanisms, which would indicate that the FIR emission associated with the heating of dust by an active nucleus is minimal. A more likely source of dust heating is hot, new stars in both the disks and nuclei of Seyfert galaxies.

The FIR colors seen in the disks of Seyfert galaxies and the FIR luminosity from these disks suggest that the host galaxies of Seyferts have similar star formation properties to more "normal" galaxies. Typically, Seyfert galaxies have higher FIR luminosity nuclei compared to their disks than the other galaxies investigated, which suggests that star formation is often proceeding at an enhanced rate in the central few kiloparsecs of Seyferts.

The low FIR emission observed in the disks of Seyfert galaxies suggests that there is a lack of star formation in these regions, and suggest that the active nucleus has little or no effect on star formation this far out. However, the excess FIR emission seen in the central regions suggests there may be a causal link here, the star formation possibly being induced by the output from an active nucleus and its interaction with the interstellar medium in the central few kiloparsecs of Seyfert galaxies. A good example of this combination is NGC 7582 which has an H II region surrounding the active nucleus but also has a smooth, quiescent disk (Morris et al. 1985). This agrees with the suggestions of Rodriguez Espinosa et al. (1987) and Edelson et al. (1987) of a connection between the active nucleus and star formation in Seyfert galaxies.

REFERENCES

Carone, T. E. 1992, In *Relationships Between Active Galactic Nuclei and Starburst Galaxies*, ed. A. V. Filippenko, ASP Conference Series, Vol. 31, p.375

Edelson, R. A., Malkan, M. A., and Rieke G. H. 1987, *ApJ*, **321**, 233

Elvis, M., Fassnacht, C., Wilson, A. S., and Briel, U. 1990, *ApJ*, **361**, 459

Marston, A. P. 1991, *ApJ*, **366**, 181

Marston, A. P. 1992, In *Relationships Between Active Galactic Nuclei and Starburst Galaxies*, ed. A. V. Filippenko, ASP Conference Series, Vol. 31, p. 117

Marston, A. P. 1993, in *Proceedings of the Workshop on Science with High Spatial Resolution Far-Infrared Data*, JPL, pp. 11-16

Miley, G. K., Neugebauer, G., and Soifer, B. T. 1985, *ApJ*, **293**, L11

Morris, S. M., Ward, M., Whittle, M., Wilson, A. S., and Taylor, K. 1985, *MNRAS*, **216**, 193

Rodriguez Espinosa, J. M., Rudy, R. J., and Jones, B. 1986, *ApJ*, **309**, 76

Rodriguez Espinosa, J. M., Rudy, R. J., and Jones, B. 1987, *ApJ*, **312**, 555

36

p 6

TWO-DIMENSIONAL MAPS OF THE INFRARED-TO-RADIO RATIO IN SPIRAL GALAXIES

KENNETH A. MARSH[1] AND GEORGE HELOU
Infrared Processing and Analysis Center, MS 100-22
California Institute of Technology, Jet Propulsion Laboratory
Pasadena, CA 91125

ABSTRACT We have produced two-dimensional maps of the intensity ratio Q_{60} of 60 μm infrared to 20 cm radio continuum emission, for a set of 25 nearby galaxies, mostly spirals. The ratio maps were obtained from infrared images made using Infrared Astronomical Satellite (IRAS) data with the Maximum Correlation Method, and radio images made using VLA data. Before taking the ratio, the radio images were processed so as to have the same resolution properties as the infrared images; the final spatial resolution in all cases is approximately 1′, corresponding to 1–2 kpc for most galaxies. These images allow us to study the variations of the Q_{60} ratio with unprecedented spatial resolution, and thus represent a major improvement over earlier work.

Our new high-resolution maps confirm the slow decrease of Q_{60} with increasing radial distance from the nucleus, but show additional structure which is probably associated with separate sites of active star formation in the spiral arms. The maps show Q_{60} to be more closely related to infrared surface brightness than to the radial distance in the galaxy disk. We expect that the results will provide improved constraints on the evolution (diffusion, decay and escape) of cosmic-ray electrons in the magnetic field of the disks.

INTRODUCTION

The strong correlation, observed in spiral galaxies, between flux densities at far-infrared and centimeter wavelengths (Helou, Soifer, and Rowan-Robinson 1985) has prompted comparisons between the spatial structure in these two wavelength regimes. In a recent study, Bicay and Helou (1990) compared the spatial distributions, at 60 μm and 20 cm wavelength, for 25 galaxies (24 late-type spirals and one irregular). They found that the radio images had the appearance of smeared versions of the infrared images, and that the smearing could be understood in terms of the diffusion of cosmic ray electrons. In their model, discussed in more detail by Helou and Bicay (1993), the correlation between infrared and radio emission is driven by massive stars heating up the dust, and causing cosmic-ray electrons to be accelerated during the supernova phase; the cosmic rays then give

---

[1] Jet Propulsion Laboratory 306-451, 4800 Oak Grove Drive, Pasadena, CA 91109

S. Terebey and J. Mazzarella (eds.), *Science with High-Spatial Resolution Far Infrared Data*, 115–120, 1994, Jet Propulsion Laboratory, Pasadena, CA.

114

rise to synchrotron radio emission which dominates at 20 cm. The difference in spatial distribution between infrared and radio arises because cosmic rays diffuse up to a few kpc before being lost to radiative decay or escape.

Bicay and Helou (1990) used the raw detector data from the Infrared Astronomy Satellite (IRAS), which are of rather coarse spatial resolution ($1.5' \times 4.7'$). Since the latter dimension was comparable to the sizes of the galaxies themselves, the study was basically one-dimensional in terms of spatial structure. In this paper we describe an improved approach to the same question using infrared data of higher spatial resolution ($\sim 1'$ in both coordinates).

DATA

The galaxy sample used in the current investigation consisted of the same 25 galaxies studied by Bicay and Helou (1990). Our input data for each galaxy consisted of:

(1) Radio continuum image at 20 cm wavelength (frequency 1.49 GHz) made using the VLA, and described by Condon (1987). The CLEAN algorithm was used for deconvolution, with circular Gaussian restoring beams of FWHM $0.8'$, $0.9'$, or $1.0'$.

(2) Infrared continuum image at 60 μm wavelength, made using data from the Infrared Astronomy Satellite (IRAS), and the imaging technique known as the Maximum Correlation Method (MCM), described by Aumann, Fowler, and Melnyk (1990). The number of iterations used was 20.

Although the infrared and radio images had comparable spatial resolution ($\sim 1'$), the infrared images were nonisoplanatic. The behavior of their resulting point spread functions (PSF) was determined by the IRAS scanning geometry, the spatial responses of the set of IRAS detectors, and the inherent properties of the MCM. Since the goal of the study was to compare radio and infrared images at the same spatial resolution, further processing was necessary.

ANALYSIS PROCEDURE

In order to produce pairs of images (radio and infrared) with the same spatial resolution, we re-CLEANed the radio images and restored them using an effective PSF corresponding to the infrared images. The procedure involved the following steps:

(1) Deconvolve the radio PSF. This step was necessary since the original sets of CLEAN components involved in Condon's (1987) maps were not available. The deconvolution was performed by a reapplication of the CLEAN algorithm, based on the same circular Gaussian beam which Condon had used to restore each map. The image was CLEANed down to the residual noise level (0.1 mJy/beam), yielding a source model in the form of a set of delta-function components.

(2) Generate synthetic "raw detector data" as would be observed if this source model were scanned using detectors whose spatial responses were the same as for IRAS, and using the same scanning geometry as for the original IRAS observations.

(3) Run these data through the same MCM imaging algorithm as was used to generate the infrared images. The pixel size (15″), field of view, and position of the center pixel, were the same as for the corresponding infrared image.

The result in each case was a radio image with spatial resolution properties similar to that of the infrared image.

Because of uncertainties in the absolute positioning of the IRAS data (resulting in errors comparable to a pixel width in the infrared images), it was necessary to perform a final registration step. The required position offset of the infrared image, $(\Delta\alpha,\Delta\delta)$, was estimated by minimizing the sum of squares of residuals, $\phi(\Delta\alpha, \Delta\delta, q)$, defined by:

$$\phi(\Delta\alpha, \Delta\delta, q) = \sum_{\alpha,\delta}[I_{20\text{cm}}(\alpha, \delta) - q^{-1}I_{60}(\alpha - \Delta\alpha,\ \delta - \Delta\delta)]^2 \qquad (1)$$

where $I_{20\text{cm}}(\alpha, \delta)$ and $I_{60}(\alpha, \delta)$ represent the intensity distributions at wavelengths 20 cm and 60 μm, respectively, as a function of right ascension, α, and declination, δ, and q is a scaling factor representing the weighted-mean ratio of infrared to radio intensity. The summation was performed over all positions which fell within a rectangular box, constructed so as to include the galaxy but exclude background sources.

The final numerical step was to calculate the infrared-to-radio intensity ratio, $Q_{60} = I_{60}/I_{20\text{cm}}$, as a function of position. This quantity was then plotted, in the form of a greyscale image, for all positions for which $Q_{60} \geq 3\sigma_Q$, where σ_Q is the standard deviation in Q. The quantity σ_Q was determined by the noise levels in the infrared and radio images, which were dominated by the dynamic ranges of the processed radio maps, typically 70:1.

RESULTS

Figure 1 shows the results for three sample cases, namely NGC 5194, NGC 5236, and NGC 6946.

We have compared all 25 ratio maps with the corresponding infrared intensity maps, and find that in nearly all cases, there is a local maximum in Q_{60} coincident with the galactic nucleus, and that the average Q_{60} in an annulus centered on the nucleus decreases monotonically with radial distance, r, from the nucleus, in a manner which is in qualitative agreement with the Bicay and Helou (1990) model. The principal exceptions to this behavior were IC 10 (an irregular galaxy) and NGC 3031 (a disk galaxy with a strong Seyfert nucleus), neither of which were expected to fit the model.

In addition to the general radial behavior of Q_{60} described above, the improved spatial resolution reveals in some galaxies off-nucleus local maxima in Q_{60}, which coincide with local maxima in I_{60}. These new details are seen in the well-resolved face-on spirals, and are particularly prominent in NGC 5194, NGC 5236, and NGC 6946. They also appear in the edge-on spiral, NGC 4631. These local maxima correspond to locally prominent star formation regions in the spiral arms. The new features cannot be accounted for in the simple model by Helou and Bicay (1993), which describes the I_{60} distribution as an exponential disk. They therefore partially destroy the predicted gradient of Q_{60} as a

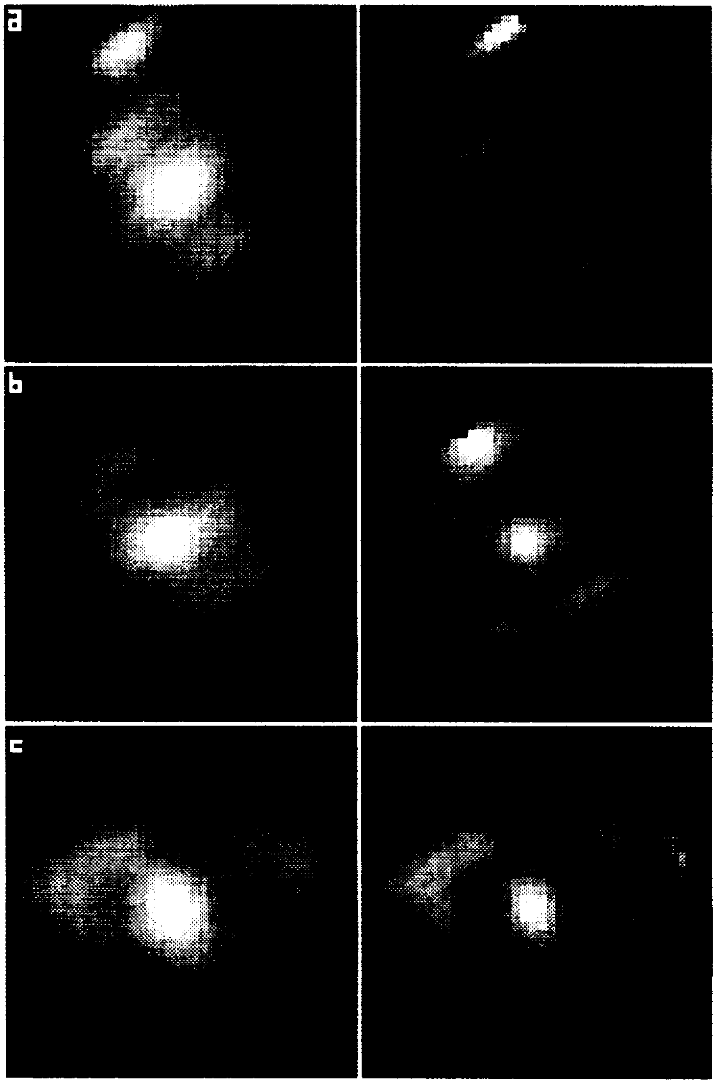

FIGURE 1 Maps of 60 μm infrared surface brightness, presented on a logarithmic scale of 2.5 decades (left hand plots) and the intensity ratio of 60 μm infrared to 20 cm radio emission, presented on a linear scale (right hand plots). The field of view in all cases is 16′ × 16′. (a) NGC 5194 (Peak value of ratio map = 284); (b) NGC 5236 (Peak value of ratio map = 266); (c) NGC 6946 (Peak value of ratio map = 220).

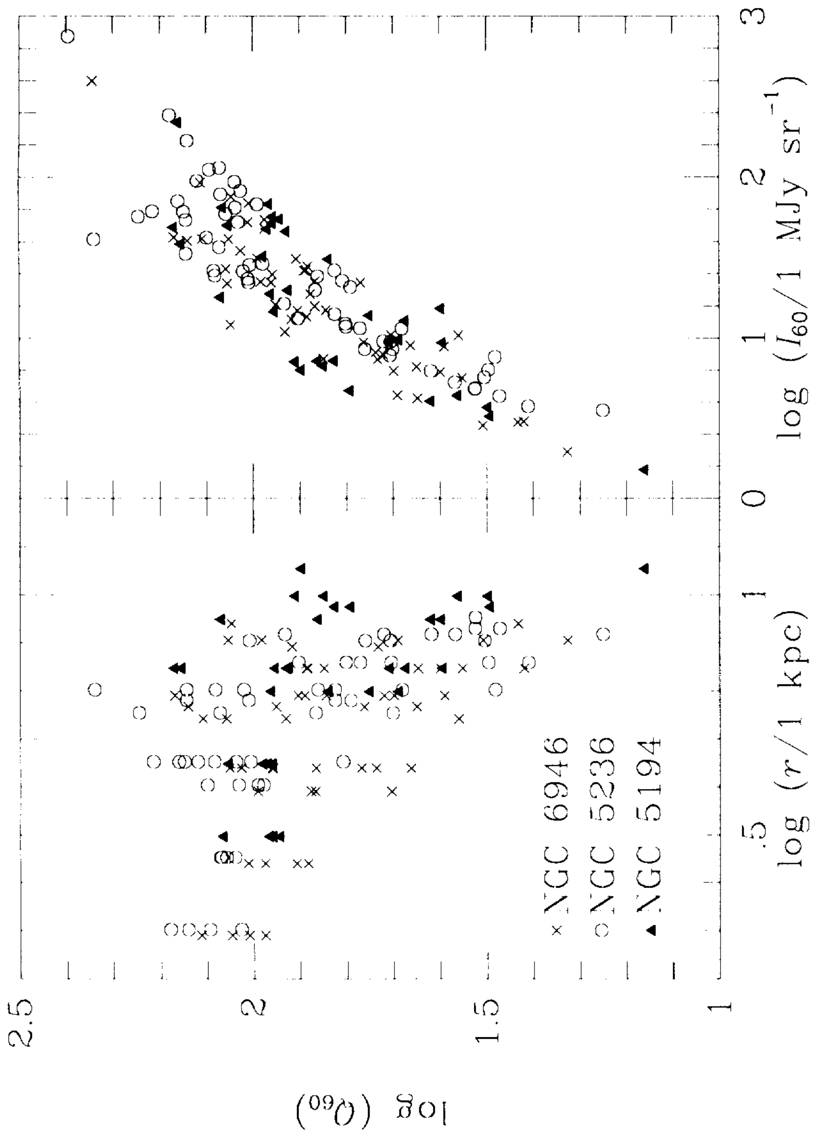

FIGURE 2 Scatter plots of Q_{60} as a function of radial distance from nucleus, r, and infrared surface brightness, I_{60}, for NGC 5194, NGC 5236, and NGC 6946.

function of r. This is clearly visible in Figure 2, which shows scatter plots of Q_{60} *vs.* r for NGC 5194, 5236 and 6946.

The essential content, however, of the Bicay and Helou model is not in the geometry, but in the physics of diffusion, escape and decay of cosmic-ray electrons, and the effects on the appearance of the radio map. These effects should apply locally to each center of star formation activity, and cause the ratio Q_{60} to fall with increasing distance from each center. Since I_{60} also falls with increasing distance from a center of activity, one would expect Q_{60} and I_{60} to be positively correlated. We test this hypothesis using scatter plots of Q_{60} v. r and Q_{60} v. I_{60}. The results for NGC 5194, NGC 5236, and NGC 6946 are shown in Figure 2. The three plots are clearly consistent with our expectations, i.e., Q_{60} is more closely related to infrared surface brightness than to the radial distance in the galaxy disk.

In a forthcoming paper we will present the complete results for all 25 galaxies in the sample, and discuss the physical constraints that these results impose on the evolution of cosmic rays in the magnetic field of the disks.

ACKNOWLEDGMENTS

We acknowledge stimulating discussions with M. D. Bicay and Zhong Wang. We thank Diane Engler for running the MCM software. This research has been supported through the IRAS Extended Mission Program by the Jet Propulsion Laboratory, California Institute of Technology, under contract with the National Aeronautics and Space Administration.

REFERENCES

Aumann, H. H., Fowler, J. W. and Melnyk, M. 1990, *AJ* **99**, 1674

Bicay, M. D. and Helou, G. 1990, *Ap. J.* **362**, 59

Condon, J. J. 1987, *Ap. J. (Suppl.)* **65**, 485

Helou, G. and Bicay, M. D. B. 1993, *Ap. J.* (in press)

Helou, G., Soifer, B. T. and Rowan-Robinson, M. 1985, *Ap. J.* **298**, L7

[illegible]-32

N95-21766

7

1 - 6

THE VARIATION OF THE DUST TEMPERATURE WITHIN LATE–TYPE SPIRAL GALAXIES

RH. EVANS
Dept. of Physics and Astronomy, University of Toledo, Toledo, OH 43606

ABSTRACT We use HiRes 60 and 100 μm data to investigate the variation of the dust temperature in a sample of 4 late–type spiral galaxies. We have investigated the radial variation of the azimuthally averaged 60 and 100 μm surface brightness profiles to see how the dust temperature (or, more correctly, the relative strength of the two components) varies as a function of radius within the galaxies. We find strong evidence for a decrease in the dust temperature (or an increase in the relative contribution of the 100 μm flux compared to the 60 μm flux) as a function of radius. We discuss these results in the light of the continuing debate as to whether massive star formation or the general interstellar radiation field is the major heating source of the dust.

DISCUSSION

The profiles (Figs. 1 – 4) in general show a decrease in the relative contribution of the 60 to 100 μm flux, as one would expect from a cirrus component heated by a weakening general interstellar radiation field. However, there is also clear evidence for warmer regions, which can be tied in with spiral arm features seen in the HiRes images. Because we have azimuthally smoothed the images we are not able from these data to determine the relative temperatures of the "warm" and "cool" dust components. However, by doing aperture photometry on individual giant H II complexes, where we would expect the warm component to nearly totally dominate the cool component, we hope to be able to better tie down the warm dust component. The cooler component can then also be determined, as it will be just the excess required to fit the observed 60 to 100 μm flux ratios in other regions. HiRes and KAO data thus provide a unique opportunity to better determine the relative contributions of each of these components in both individual galaxies and individual regions of galaxies.

Elsewhere in this workshop Devereux has shown 60 to 100 μm ratio profiles for the galaxies M101 and M81 which show a constancy of dust temperature with increasing radius. In fact, Devereux (1993) has also found a constancy for the same galaxies as in this study, a discrepancy which is disconcerting, but could be due to the different default values used in the HiRes images used in this studies and those in Devereux's. Clearly this vital question needs further study.

S. Terebey and J. Mazzarella (eds.), *Science with High-Spatial Resolution Far Infrared Data*, 121–126, 1994, Jet Propulsion Laboratory, Pasadena, CA.

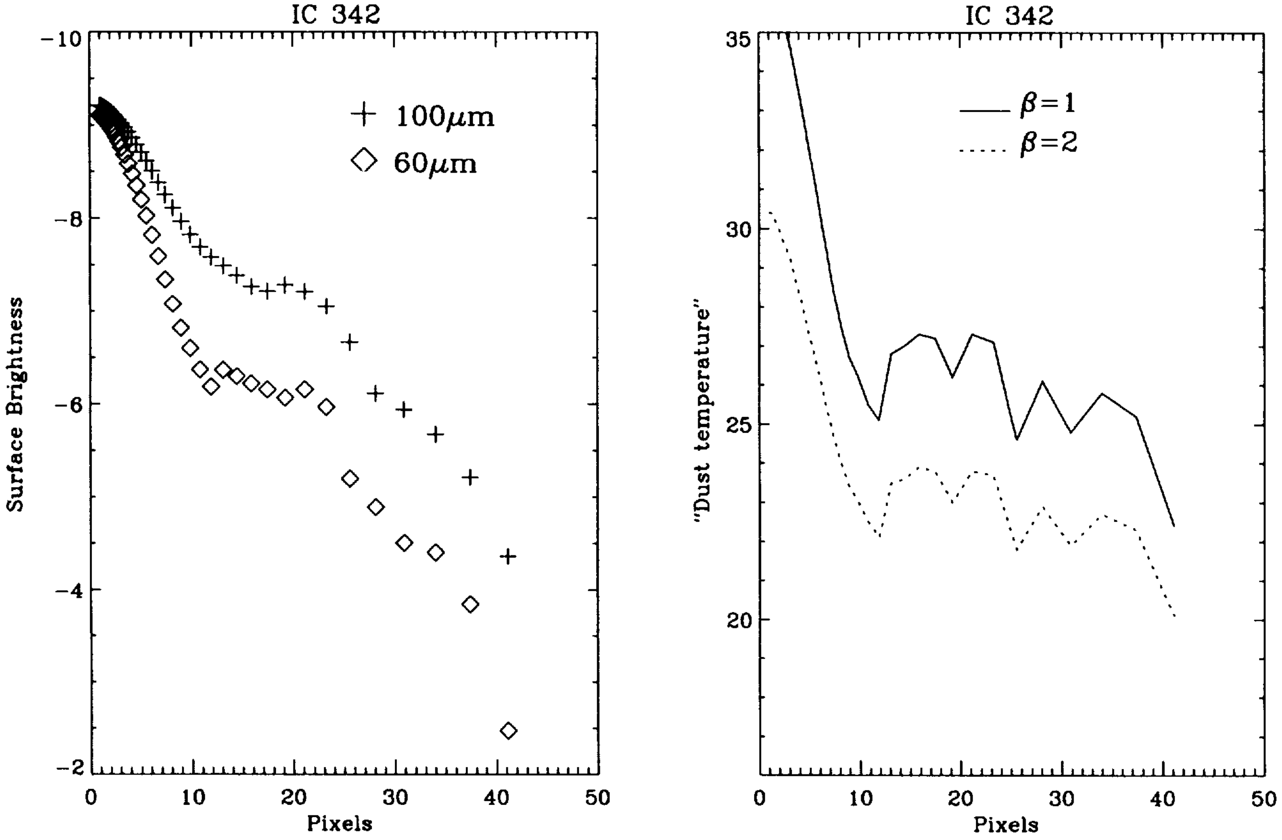

FIGURE 1 The 100 and 60 μm surface brightness profiles of IC 342, and the "dust temperature" derived from the 60 to 100 μm flux ratios, for the two emissivity indices $\beta = 1$ and 2. In addition to the increase in 60/100 ratio due to the spiral arms, which can still be seen in the convolved 60 μm image of IC 342, the underlying disk shows a decrease in temperature with radius. The global "dust temperatures" (i.e., those found by measuring the total 60 and 100 μm fluxes from the whole galaxy) are 32.2 K and 27.4 K in the $\beta = 1$ and 2 cases, respectively.

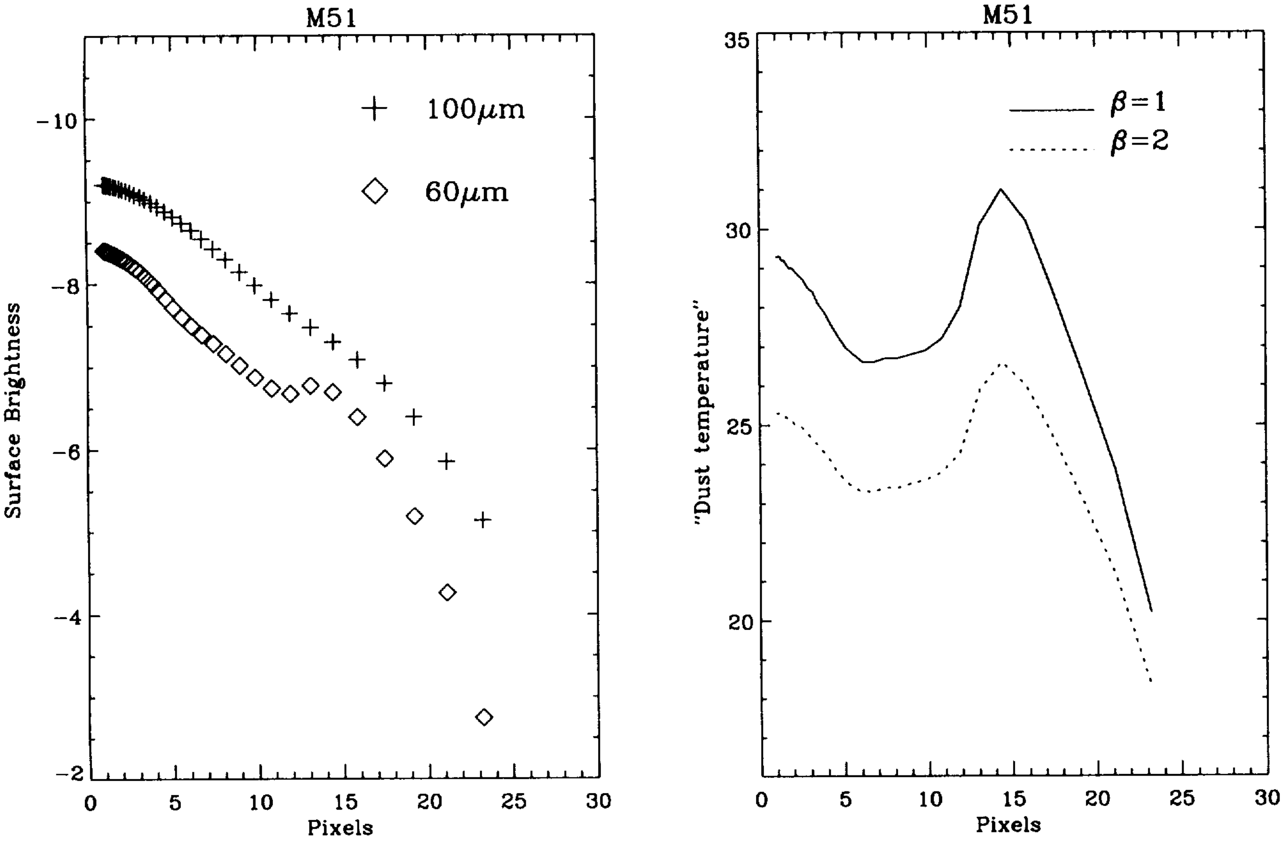

FIGURE 2 The 100 and 60 μm surface brightness profiles of NGC 5194, and the "dust temperature" derived from the 60 to 100 μm flux ratios, for the two emissivity indices $\beta = 1$ and 2. NGC 5195 was removed from the image (using the IRAF badpixel routine) before profiling the image. Apart from a prominent spiral arm feature, which can be seen in the 60 μm profile and is shown by the two maxima in the full resolution 60 μm image of M51, the underlying disk shows a decrease in temperature with radius. The global "dust temperatures" are 33.7 K and 28.5 K in the $\beta = 1$ and 2 cases, respectively.

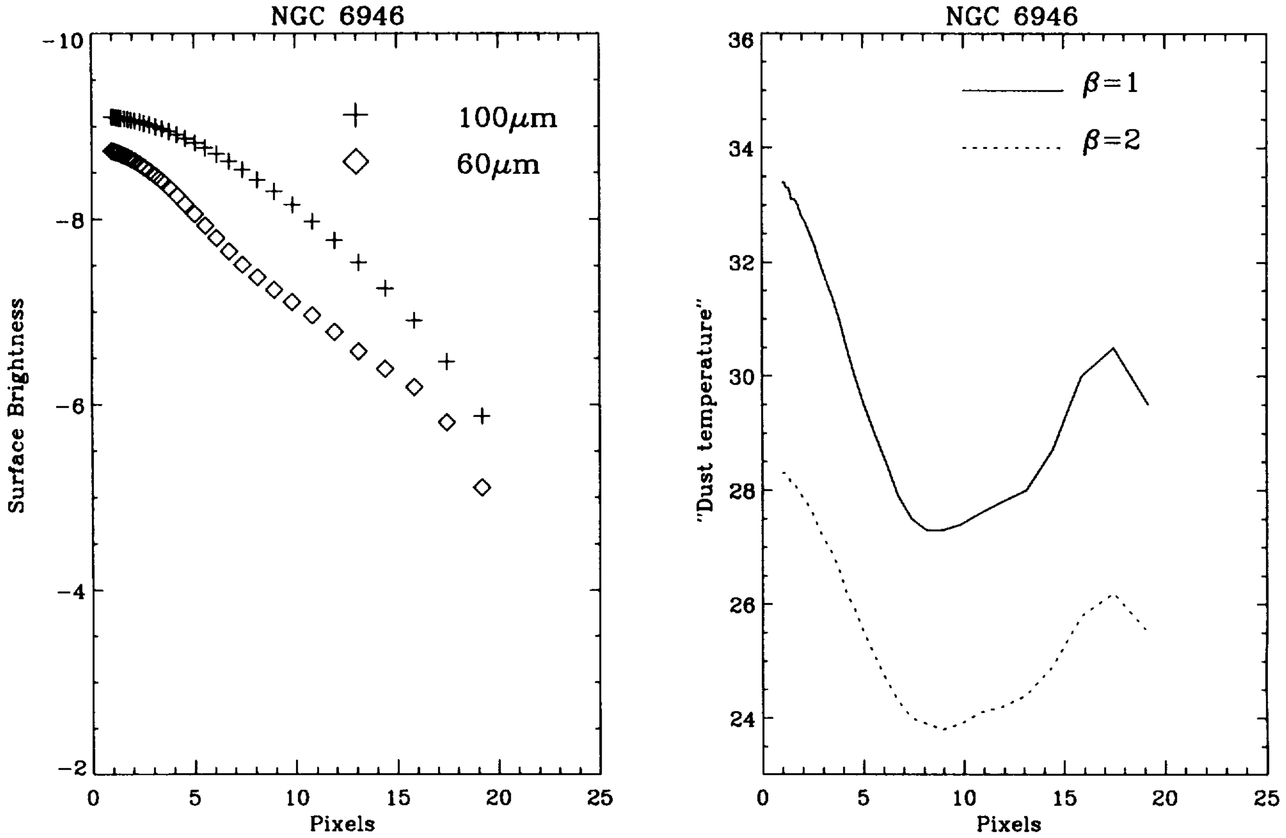

FIGURE 3 The 100 and 60 μm surface brightness profiles of NGC 6946, and the "dust temperature" derived from the 60 to 100 μm flux ratios, for the two emissivity indices $\beta = 1$ and 2. The sharp rise in the 60/100 ratio at the outer radii is probably due to the two features which cause extensions either side of the nucleus in the HiRes image of NGC 6946. The global "dust temperatures" are 32.9 K and 28.0 K in the $\beta = 1$ and 2 cases, respectively.

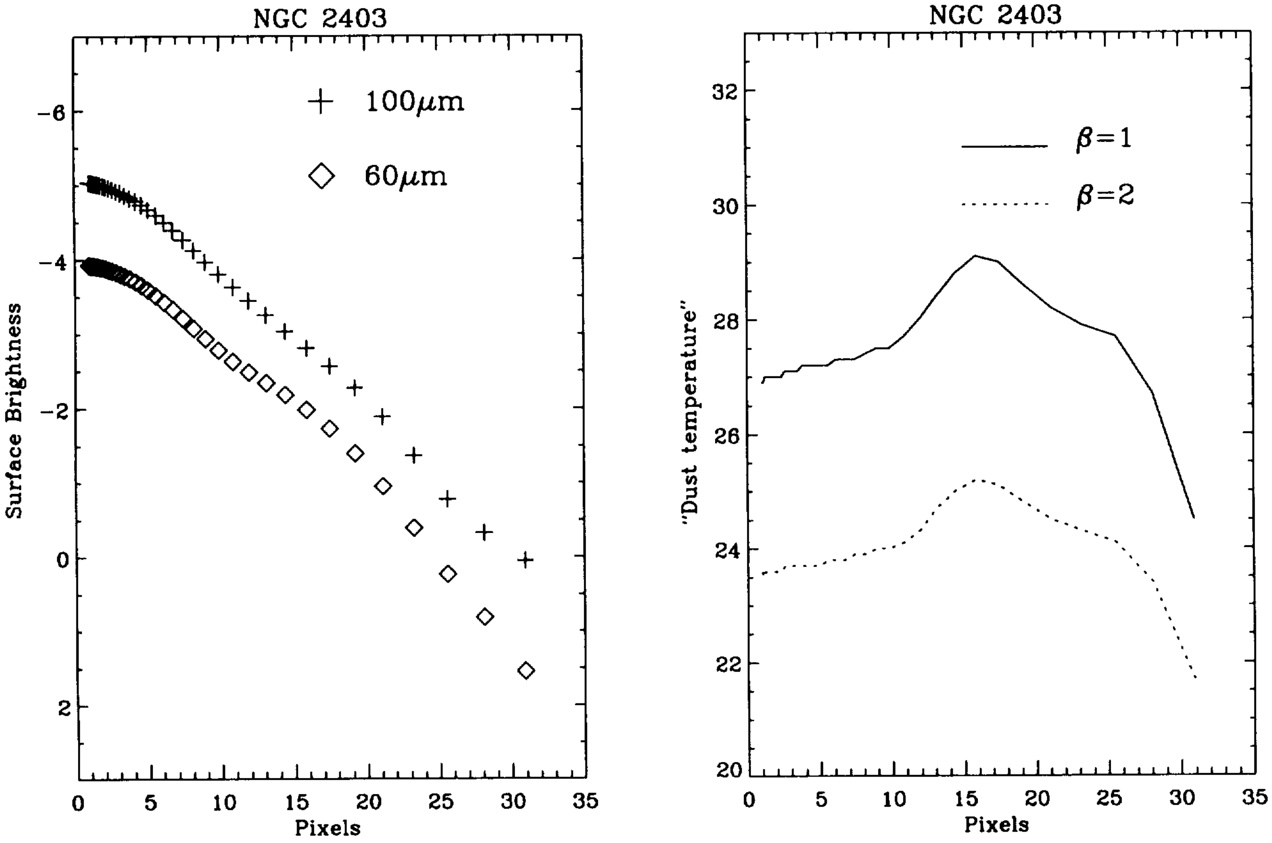

FIGURE 4 The 100 and 60 μm surface brightness profiles of NGC 2403, and the "dust temperature" derived from the 60 to 100 μm flux ratios, for the two emissivity indices $\beta = 1$ and 2. The 60/100 flux ratio shows a near constant behavior for the inner parts, after which it falls. The rise in 60/100 is due to the feature picked up in the 60 μm profile at ~ 15–20 pixels, but not in the 100 μm profile. The global "dust temperatures" are 31.1 K and 26.6 K in the $\beta = 1$ and 2 cases, respectively.

REFERENCES

Devereux, N.A., 1993, Private communication

AN IRAS HIRES STUDY OF LOW MASS STAR FORMATION IN THE TAURUS MOLECULAR RING

S. TEREBEY
Infrared Processing and Analysis Center, MS 100-22
California Institute of Technology, Jet Propulsion Laboratory,
Pasadena, CA 91125

J. SURACE
Institute for Astronomy, University of Hawaii, Honolulu HI 96822

ABSTRACT The Taurus molecular cloud supposedly has no star clusters but only isolated star formation. However, the Infrared Astronomical Satellite (IRAS) shows us that a small star cluster is currently forming in Taurus. Most of the sources are deeply embedded and are probably low-mass protostars.

We use High Resolution (HiRes) images of the IRAS data from the Infrared Processing and Analysis Center (IPAC) to look for additional infrared members of the cluster. We also investigate the question of whether the infrared emission matches predictions for protostellar sources by examining whether the dust emission is resolved on scales of one arcminute ($\sim 10^{17}$ cm). With the exception of a luminous visible star, HD 29647, we find that the sources L1527, TMC1A, TMC1, TMC1C, TMR1, and IC2087 are unresolved in the HiRes images at 60 μm. Further analysis of IC2087 shows that it is unresolved at all four IRAS wavelengths.

INTRODUCTION

The nearest star forming regions are the Taurus and ρ Ophiuchus molecular clouds, both of which are located at a distance of approximately 160 pc. Both regions are currently forming low-mass stars, but otherwise have very different morphologies. The embedded star cluster in the ρ Oph cloud core has been viewed as an example of cluster formation while the Taurus cloud is often cited to contain only isolated star formation. Some authors have tried to explain the apparent difference in star formation content and cloud structure as due to differences in physical conditions in the clouds, such as magnetic field strength.

However the distinction between cluster or isolated star formation may be too simplistic. Recent near-infrared mapping of the Orion cloud has shown (Strom & Strom 1993) that star formation seems to be quite common in aggregates of 10 – 50 stars. It is important to understand the physical conditions in these regions, and relate them to current theories of isolated star formation. We undertake a study in nearby Taurus, where we identify a currently forming star cluster using the IRAS data.

S. Terebey and J. Mazzarella (eds.), *Science with High-Spatial Resolution Far Infrared Data*, 127–136, 1994, Jet Propulsion Laboratory, Pasadena, CA.

The IRAS data covering the densest part of the Taurus molecular cloud (sometimes called Heiles Cloud 2 or the Taurus Molecular Ring, hereafter TMR) reveals a 'ring' of embedded stars about 1 pc in radius. The projected stellar density corresponds to 4 – 8 stars pc^{-2}, which falls below the typical range considered to constitute a stellar cluster. However this is only a lower limit to the stellar density since there are likely to be other (visible) members than the seven far-infrared sources detected by IRAS.

To further investigate the infrared properties of the cluster we use High Resolution (HiRes) images of the IRAS data obtained from IPAC made using the Maximum Correlation Method (MCM) (Aumann, Fowler, & Melnyk 1990) as implemented by YORIC, the IPAC MCM processor. We use the improved resolution of roughly one arcminute in the HiRes images to search for additional infrared cluster members.

We also measure the sizes of the cluster sources. Models of the infrared emission from young embedded stars suggest that the mid-infrared (12 and 25 μm) comes primarily from a circumstellar disk, while the far-infrared (60 and 100 μm) comes from a circumstellar envelope. The circumstellar envelope is larger than the disk, and at 100 μm is expected to be roughly 10″ (Butner et al. 1991) for low-luminosity ($\leq 50\ L_\odot$) sources. Therefore only high luminosity protostellar sources are likely to be resolved by IRAS, even in the HiRes images. However sizes determined from HiRes images do provide an important check on the protostar models. In addition, most protostar models ignore the extended infrared component associated with outflows, such as has been observed around L1551 by IRAS at 60 μm (Edwards et al. 1986). Therefore it is interesting to use HiRes to measure whether protostellar sources are resolved.

GENERATION OF THE HIRES IMAGES

The HiRes images were generated at IPAC for a 2 degree field using the MCM algorithm with default parameters, including the now standard FBIAS processing. FBIAS processing provides for the addition of a small bias level to ensure the data are positive during the image reconstruction, and is particularly important for fields containing extended emission, such as star forming regions (*IPAC Users Guide 1993*).

AO Data

In addition to using standard survey data, HiRes images were generated using IRAS AO data (Additional Observations, also known as pointed observations). Each AO covers a skinny rectangular region running roughly north-south, but when mosaiced together they subtend the entire region of interest.

Spatial Resolution Studies Using the IRAS Simulator

To study the effective resolution of the HiRes images, extensive use was made of the HiRes IRAS Simulator. The simulation mode takes a model image and generates synthetic IRAS data that mimic what IRAS would have detected. The synthetic IRAS data is then processed as usual with the MCM algorithm (Surace et al. 1993).

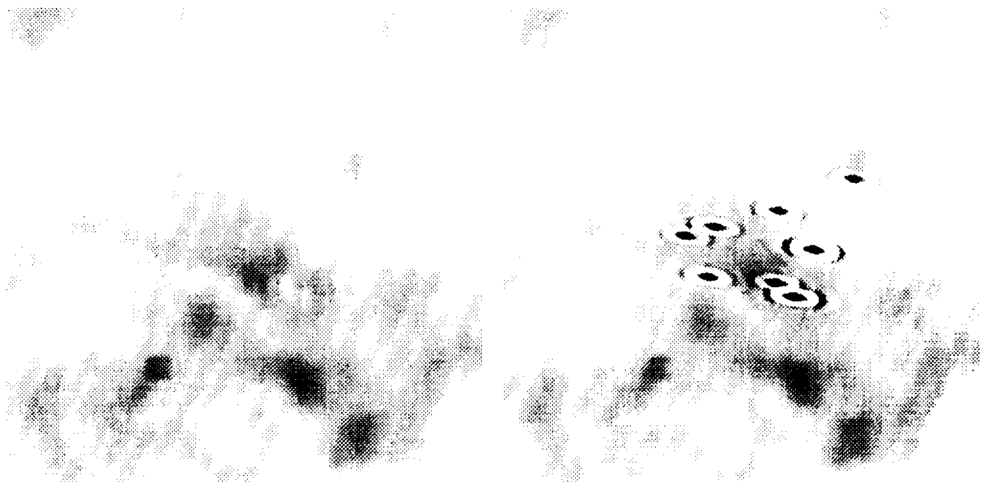

FIGURE 1 a) Spike model input image. Barely discernible spikes of the appropriate fluxes have been placed at the proper source locations, and added to a much smoothed version of the data. b) Spike model after HiRes processing.

The model images were meant to faithfully imitate the observed extended component of IRAS emission, while varying the treatment of the compact sources. The compact sources were alternatively treated as 1) unresolved spikes 2) Gaussians of various sizes and 3) a power-law distribution with intensity varying as θ^{-1} with angle.

The model for the extended component was based on the smoothed beam-sample model image that is normally produced during HiRes processing. The beam-sample model is a highly smoothed version of the 20th iteration HiRes image that has been further processed to exclude point sources found in the data. We further edited the smoothed images to remove any trace of pointlike sources which persisted.

The brightness of the stars in the original 60 and 100 μm maps were then measured, and the three types of compact models were placed on the smoothed maps at the known locations of the stars using the measured fluxes. The resulting maps were then processed using the IRAS simulator.

Figure 1a shows a model before processing, in this case a smoothed input map with barely discernible spikes at the position of the sources. Figure 1b shows the same map after HiRes processing at the 20th iteration. Comparison of the model image (Fig. 1b) with the actual HiRes data (Fig. 2b) shows the model indeed looks very similar to the data, down to the 'ringing' pattern seen around the compact sources.

Using Nearby Point Sources to Study Spatial Resolution

An alternative way to measure the effective spatial resolution achieved in the HiRes maps is to measure the spatial profile of a nearby point source. There are two cautions with this technique: first, the resolution depends on the local scan coverage, which can vary substantially over a degree particularly if there are gaps in the coverage, and second, it is not entirely clear how to identify which

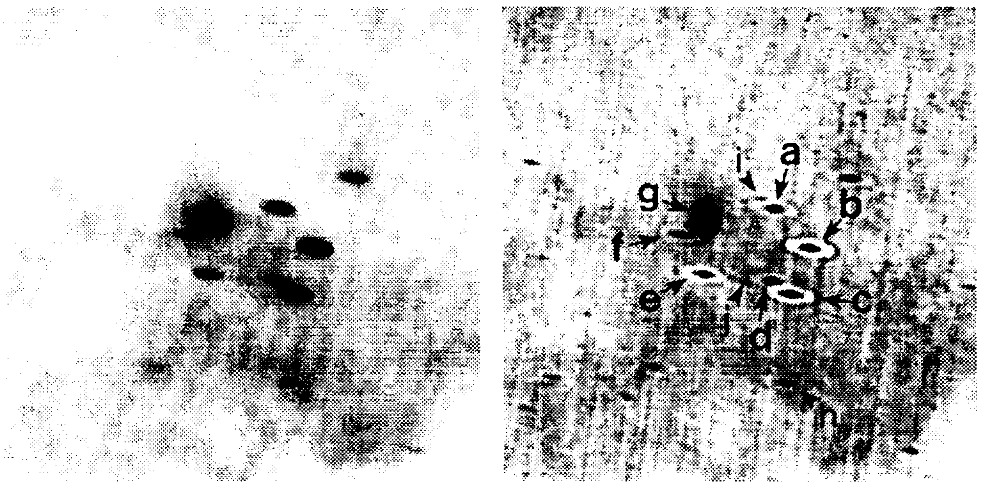

FIGURE 2 IRAS 60 μm image of the TMR embedded cluster. Images are 2 degrees on a side. a) Before HiRes Processing. b) The 20th iteration HiRes image.

sources are actually point sources.

We identified two likely point source candidates using the *IRAS Point Source Catalog, Version 2 (1988)*. The sources RVTau and IUTau have falling spectral energy distributions that suggest they should be unresolved, namely they are strong at 12 μm and weak at 100 μm. These two particular sources were chosen because they were the only sources strong enough at 60 μm to do meaningful comparisons and which were also close to the field of interest (within 3 degrees).

HIRES IMAGES OF THE TMR FAR-INFRARED CLUSTER

Figures 2a-b show the the TMR region at 60 μm before and after HiRes processing. The IRAS data show the far-infrared cluster as a ring of seven bright sources near the center, less than a degree across. The IRAS detectors are rectangular, resulting in an elliptically shaped beam. The 'ringing' pattern evident around the stronger sources is an artifact of the processing, and reflects the typical behavior of the HiRes algorithm to pointlike sources, particularly to sources lying on a nonzero background.

Stripes are also visible in the images and are a consequence of the one dimensional scanning pattern of the IRAS satellite. Small errors in the gain, and residual errors in the baseline determination are strongly amplified during the HiRes processing and typically appear as stripes.

Individual Sources

The identifications of the cluster sources, clockwise from the north, are L1527 (a), TMR1 (b), TMC1A (c), IC2087 (d), TMC1 (e), TMC1C (f), and HD 29647 (g) (also known as SAO 76704). More information on individual objects can be

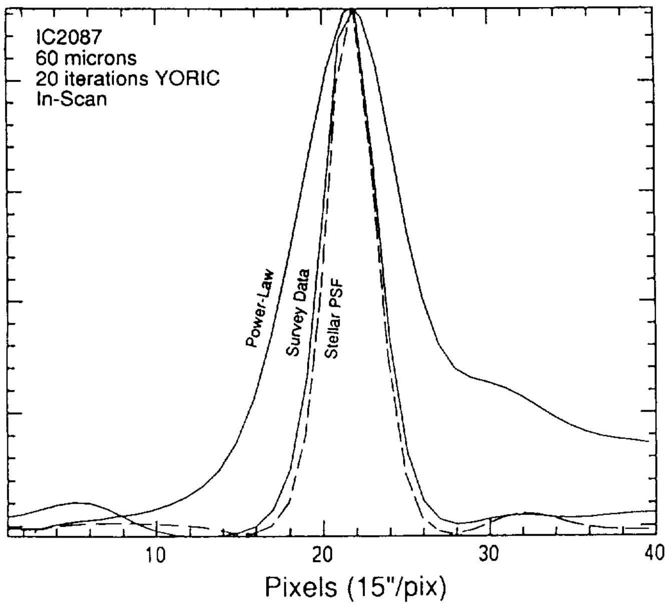

FIGURE 3 Sample one dimensional spatial profiles of the embedded source IC2087.

found in Crutcher (1984), Heyer, Snell, & Goldsmith (1987), and Terebey et al. (1989, 1990).

The lowest extinction is found in the north-east part of the ring containing TMC1C (f) and HD 29647 (g). In agreement with this general trend both sources are optically visible. TMC1C is a T Tauri star while HD 29647 is a bright star well known for its anomalous interstellar extinction properties. The IRAS data show HD 29647 is clearly extended.

IC2087 (d) has associated reflection nebulosity around it, suggesting it is moderately embedded. The other four objects are class I infrared sources and are thought to be protostars.

Molecular line mapping of the region indicates that several hundred solar masses of gas is concentrated around the embedded cluster and also extends to the south and south-east (Snell, Heyer, & Schloerb 1989).

SIZE DETERMINATION

Source size was examined in several ways. First the full-width at half-maximum (FWHM) sizes were estimated by fitting elliptical gaussians to the data. However the beam shape was not really gaussian enough to make this a good diagnostic. So instead, cuts were made along the major and minor axes. The data were averaged along this vector 3 pixels wide (45″) and the resulting one-dimensional profiles were graphically compared. For example Figure 3 displays several profiles for IC2087 along the minor axis. The stellar profile is seen to provide a good match to the data. As a measure of size we report the FWHM interpolated from the profiles.

It was found that the power–law models were, in every case, much more extended than the actual survey data. Typically, the FWHM of the power–law models (at 20 iterations) was 2.5 times that of the survey data.

We also attempted to fit the data against a sequence of radial gaussian models with varying sizes. However this approach was not successful because the gaussian models turned out to have beam shapes that were about 10 percent more elliptical than the actual data, so that different size gaussians were required to fit the major and minor axes.

This suggests that such model fits are too detailed given the imperfectly known IRAS detector response functions that enter into the IRAS simulator. The main result derived from the gaussian models was that the compact sources were most similar (to within $\sim 10''$) to the smallest sized model.

In the end we had two tools for assessing whether sources were resolved in the HiRes images. We used several candidate point sources found near our field to estimate an empirical point spread function. In addition we made extensive comparisons with the spike model. The input spikes had the same fluxes and locations as our compact sources, which allowed us to simulate the effects of source strength and local background level on the achieved resolution in the HiRes images.

Discussion of Measured Sizes

IC2087 was examined at all bands versus the two stars to look for extended flux. None was found. At all bands, both in-scan and cross-scan, it was found to have the same profile as the stars to within 1/3 pixel ($5''$) in-scan. Note that some uncertainty exists as the stars themselves did not have identical profiles. This is most pronounced in the cross-scan direction, as coverage variations are more pronounced and the sheer size of the profile leads to uncertainties as high as a full pixel ($15''$). The measured FWHM sizes are given in Table 1.

TABLE 1 Size of IC2087 at IRAS wavelengths.

Wavelength(μ m)	Flux(Jy)[a]	FWHM($'' \times ''$)[b]
12	5.0	48×34
25	6.8	72×35
60	7.3	113×54
100	18.2	210×150

---

[a] Fluxes from Point Source Catalog
[b] Cross-Scan by In-Scan direction

We then examined the other compact sources at 60 μm. The measured sizes are given in Table 2, starting with the two selected stars, RV Tau and IU Tau. The table shows roughly the expected behavior, that the achieved resolution is related to source strength. Weak sources, particularly those with significant local background have both lower signal to noise and take longer to converge than strong sources, which results in a lower achieved resolution.

As expected from the images, HD 29647 is found to be extended. However none of the other compact sources are extended compared with the pointlike stars. For example, TMC1C appears larger, but is weaker than other sources.

Examination of a source with the same flux and location in the spike model image indicates that the profile of TMC1C is consistent with that of a point source.

TABLE 2 Compact Source Sizes at 60 μm.

IRAS	Source	Flux(Jy)[a]	FWHM($'' \times ''$)[b]
04328+2824	IU Tau	3.5	98×51
04440+2605	RV Tau	6.5	82×49
04361+2547	TMR1	44.8	75×44
04365+2535	TMC1A	36.0	83×45
04368+2557	L1527	17.8	68×50
04369+2539	IC2087	7.3	113×54
04380+2553	HD 29647	11.0	274×112
04381+2540	TMC1	10.3	98×49
04385+2550	TMC1C	2.9	110×60

---

[a] Flux at 60 μm from Point Source Catalog

[b] Cross-Scan by In-Scan direction

NEW IRAS SOURCES IN THE HIRES IMAGES

We searched the HiRes Images for new compact infrared sources, in order to look for additional cluster members. In principle the PSC or FSC provide a list of all candidates. However in practice the two catalogs are not complete, while the FSC in particular suffers from reliability problems in confused regions. Incompleteness is important in star forming regions because it arises both for sources that sit inside dense cirrus emission, and for sources that that are confused with other nearby sources ($< 1'$).

As a first step we compared the HiRes images with a list of PSC sources. Figures 4a-d show the HiRes images at all four wavelengths. The positions of PSC sources are marked with circles. Only detections, not upperlimits, are marked in each band.

In general the PSC sources are easily detected by HiRes, except in the 100 μm images. At 100 μm, there are a number of 100 micron-only PSC sources that have no obvious or believable counterparts in the HiRes images. Since the image shows extensive cirrus emission throughout the field we suspect these PSC entries represent peaks in the cirrus distribution.

In the immediate vicinity of the cluster the 60 μm image shows seven likely members which define the TMR cluster. At 12 and 25 μm one easily identifies between two and four additional members of the cluster (which are also PSC sources), depending on where the cluster boundaries are drawn.

The 60 μm image also reveals a strong compact source (h, Fig. 2b) that is not found in the PSC, in the lower center of the image. This source has a counterpart in the 12 and 25 μm images, and also appears in the AO HiRes images. Therefore we judge this to be a new embedded source, although located outside the molecular ring and probably not a cluster member.

The 60 μm image also shows two new faint sources in the ring, one located

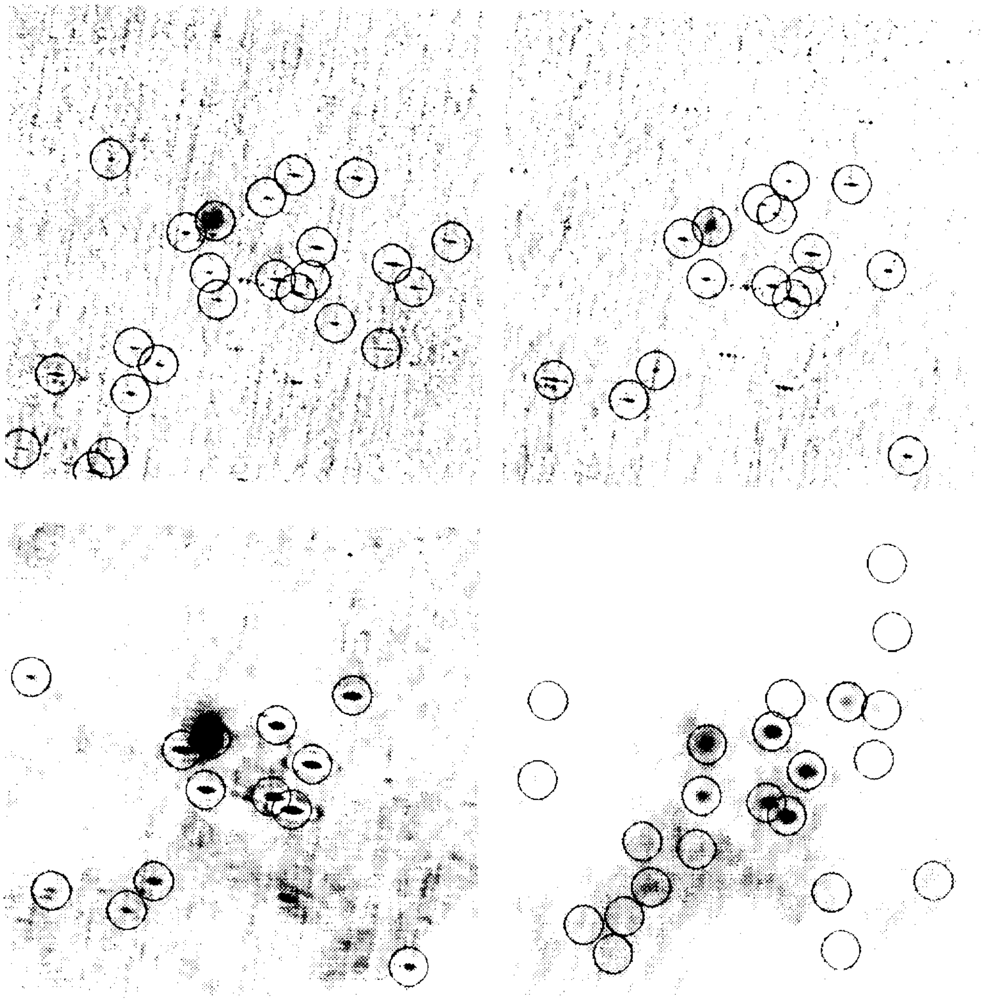

FIGURE 4 HiRes images of the TMR embedded cluster at all four wavelengths, 20th iteration. The positions of PSC sources are marked as circles. At each wavelength only PSC detections (not upperlimits) are shown. Nearly all PSC sources are obvious in the HiRes images. Exceptions are discussed in the text. a) Top-left 12 μm. b) Top-right 25 μm. c) Lower-left 60 μm. d) Lower-right 100 μm.

on the north (i), the other on the south (j). The northern source has a PSC counterpart in the 25 μm image, so in this case HiRes detects a PSC source at a wavelength that is given an upperlimit. The southern source in the ring is more problematic. Although it has a counterpart at 12 and 25 μm, it has no counterpart in the AO HiRes images. It is therefore either a variable source–a star, or bad data masquerading as a source. The case for bad data is strengthened by the fact that the source profile in the HiRes images looks very different from other compact sources.

Lastly, the AO HiRes images (not shown) reveal several new sources outside the ring that are fairly strong but are not visible in the survey data, and therefore are likely to be variable infrared sources (most likely stellar rather than embedded).

SUMMARY

We have examined the HiRes images in the vicinity of the Taurus Molecular Ring. The 60 μm image reveals an embedded cluster of seven strong infrared sources in a ring, which we suggest to be a low-density star cluster that is currently forming. Further investigation shows that the sources are unresolved at 60 μm at roughly one arcminute resolution in agreement with protostar models, with the exception of HD 29647.

Depending on how the boundaries of the cluster are drawn, at least two, and possibly four additional sources that are primarily seen at 12 and 25 μm are also likely to be members. Outside the cluster region the HiRes images reveal several new sources that are not found in the PSC. We conclude that the HiRes images are a powerful tool for studying infrared sources in star forming regions.

ACKNOWLEDGMENTS

This work was carried out at the Jet Propulsion Laboratory, California Institute of Technology, under a contract with the National Aeronautics and Space Administration. We thank Ron Beck, Diane Engler, and John Fowler for their efforts on behalf of HiRes.

REFERENCES

Aumann, H. H., Fowler, J. W., and Melnyk, M. 1990, *AJ*, **99**, 1674

Crutcher, R. M. 1984, *ApJ*, **288**, 604

Butner, H. M., Evans, N. J., Lester, D. F., Levreault, R. M., & Strom, S. E. 1991, *ApJ*, **376**, 636

Edwards, S., Jarrett, T., Strom, S., Snell, R., Strom, K., Beichman, C. A. 1986, *ApJ*, **307**, L65

Heyer, M. H., Snell, R. L., & Goldsmith, P. F. 1987, *ApJ*, **321**, 370

IPAC User's Guide, 1993, Edition 5, ed. D. Levine. (IPAC: Pasadena)

IRAS Point Source Catalog, Version 2. 1988, Joint *IRAS* Science Working Group (Washington DC: GPO)

Snell, R. L., Heyer, M. H., and Schloerb, F. P. 1989, *ApJ*, **337**, 739

Strom, K. M. & Strom, S. E. 1993, *ApJ*, **412**, 233

Surace, J., Mazzarella, J., Soifer, B.T., and Wehrle, A.E. 1993, *AJ*, **105**, 864

Terebey, S., Vogel, S. N., and Myers, P. C. 1989, *ApJ*, **340**, 472

Terebey, S., Beichman, C. A., Gautier, T. N. and Hester, J. J. 1990, *ApJ*, **362**, L63

HIRAS IMAGES OF FOSSIL DUST SHELLS AROUND AGB STARS

L.B.F.M. WATERS
Astronomical Institute 'Anton Pannekoek', University of Amsterdam, Kruislaan 403, 1098 SJ Amsterdam, The Netherlands SRON Laboratory for Space Research Groningen, P. O. Box 800,9700 AV Groningen, The Netherlands

D.J.M. KESTER, TJ.R. BONTEKOE AND C. LOUP
SRON Laboratory for Space Research Groningen, P. O. Box 800, 9700 AV Groningen, The Netherlands

ABSTRACT We present high resolution HIRAS 60 and 100 μm images of AGB stars surrounded by fossil dust shells. Resolving the extended emission of the circumstellar dust allows a determination of the mass loss history of the star. We show that the geometry of the 60 μm emission surrounding HR 3126 agrees well with that of the optical reflection nebula. The emission around the carbon star U Hya is resolved into a central point source and a ring of dust, and the mass loss rate in the detached shell is 70 times higher than the current mass loss rate.

INTRODUCTION

Stars on the Asymptotic Giant Branch (AGB) are known for their very high mass loss rates, with values that range between about 10^{-7} and 10^{-4} $M_\odot$ yr^{-1} and with outflow velocities of 5-30 km s^{-1}. In these dense, cool outflows dust can easily condense; AGB stars are often highly reddened by circumstellar dust and radiate their energy mainly in the (far)-infrared, and therefore can be studied best at such wavelengths.

The IRAS satellite has detected many AGB stars throughout our Galaxy and even in the Magellanic Clouds. These observations show that there is a large range in optical depth of the dust shells surrounding these stars, i.e. there is a large range in mass loss rates. A matter of debate is however if and how the mass loss changes with time for AGB stars of different chemical composition. The difficulty is that for most AGB stars the distance and thus the luminosity is not known, and therefore the effects of mass and luminosity on the mass loss rate cannot be disentangled. Knowledge of mass loss rates as a function of time is paramount for a better understanding of AGB evolution because mass loss determines evolutionary timescales for these stars.

Studies of the distribution of C and M stars in the IRAS color-color diagram led to the conclusion that mass loss in C stars, and to some extent also in M stars is not constant but varies strongly on relatively short timescales (e.g.,

S. Terebey and J. Mazzarella (eds.), *Science with High-Spatial Resolution Far Infrared Data*, 137–142, 1994, Jet Propulsion Laboratory, Pasadena, CA.

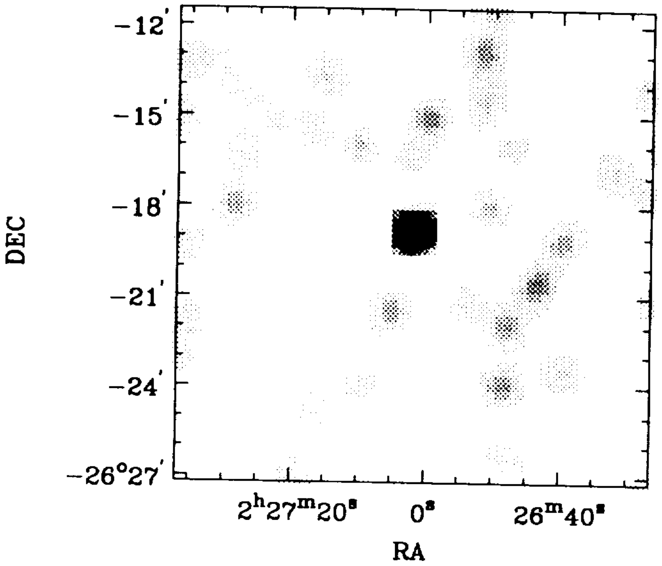

FIGURE 1 Grey-scale image of the 60 μm emission of R For. The source has no 60 μm excess and indeed is a point source. Image size is $16' \times 16^{prime}$ and pixel size is 15″

Willems & de Jong 1986,1988; Chan & Kwok 1988; Zijlstra et al., 1992). This conclusion is based on the fact that many C stars and some M stars show a large 60 and 100 μm excess due to a cool dust shell at large distance from the star. This dust shell probably was ejected some time ago when the mass loss rate was much higher than at present. Indeed some nearby C stars such as U Hydrae are associated with *IRAS Small Scale Structure Catalog* at 60 and 100 μm suggesting the presence of a fossil shell of dust.

Independent confirmation of the presence of fossil shells around AGB stars came from observations of extended CO emission in S Sct, U Ant and TT Cyg (Olofsson et al. 1990), clearly demonstrating the presence of a detached shell of molecular gas expanding at velocities between 13 and 22 km s^{-1}. The dust in this shell very likely causes the observed 60 and 100 μm excess.

HIRAS IMAGES OF FOSSIL DUST SHELLS

We have used the Groningen HIRAS system to produce high resolution 60 and 100 μm images of the extended emission around about 30 well studied AGB stars. For a description of the system we refer to Bontekoe et al. (1993). We used as input list the results obtained by Young et al. (1993) who used one dimensional co-adds of IRAS scans to determine whether or not the source is extended. In addition, we used the list of Loup (1991) containing AGB stars with high quality detections in the four IRAS bands. Here we report on the results obtained for three objects, R For, HR 3126 and U Hya.

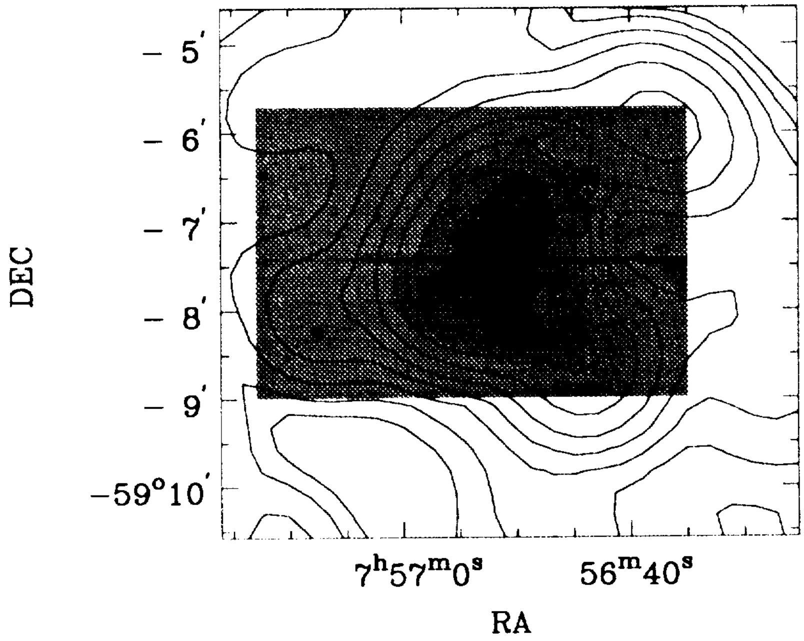

FIGURE 2 Grey-scale image of the continuum emission in the I-band of the reflection nebula around HR 3126. Superposed are the 60 μm contours, that closely follow the optical image

R FOR

Figure 1 gives the 60 μm image of the carbon star R For. The star has no 60 μm excess as deduced from the IRAS broad-band photometry (Loup 1991) and also the star is not associated with an extended source. The region around R For is relatively free of cirrus. As can be seen in Figure 1, the 60 μm image essentially shows a point source without any evidence for extended emission, which is as expected.

HR 3126

The MO III star HR 3126 is a peculiar M giant whose evolutionary status is not well understood. It is surrounded by a reflection nebula (IC 2220) which has a filamentary structure. Deep images taken by Dachs & Isserstedt (1973) and Witt & Rogers (1991) show the nebula is bipolar with filaments suggesting the geometry may be caused by magnetic fields. A recent detailed CO map by Nyman (1993) shows that the CO emission is also bipolar. A study of the IR spectrum of HR 3126 by Chiar et al. (1993) shows that the dust is oxygen-rich and has a very wide temperature distribution.

In Figure 2 we present a superposition of the I-band image published by Witt & Rogers (1991) (halftone) and the 60 μm HIRAS image (contours). The spikes in the image are due to the central star which is overexposed. The 60 μm emission is clearly extended and follows the emission of the reflection nebula, which proves that the dust radiating at 60 μm is also responsible for the optical reflection. The fact that the nebula is extended at 60 μm in combination with

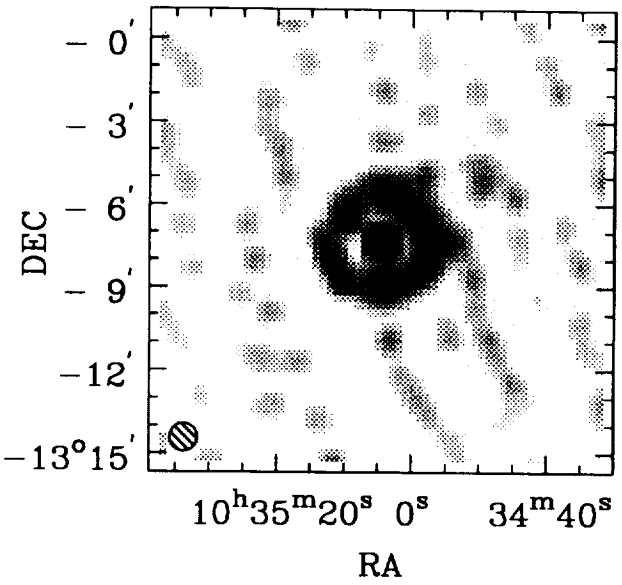

FIGURE 3 Half-tone image of the maximum entropy solution to the 60 μm brightness distribution for U Hydrae. Dimension of the image is 16′×16′ and the pixel size is 15″. The resolution at 60 μm is 1.0′.

the geometry strongly suggests that the mass loss of HR 3126 was much larger in the (recent) past than at present (2-4 10^{-7} $M_\odot$ yr^{-1}, Reimers 1977).

U HYDRAE

The carbon star U Hya is one of the brightest AGB stars in the visual, and therefore probably also one of the nearest carbon stars. The IRAS data on U Hya reveal the presence of a Small Extended Source as well as a point source. The star has CO (1-0) millimeter emission from which a present-day mass loss rate of 2 $10^{-7}M_\odot$ yr^{-1} is derived (Kastner 1990). In Figures 3 and 4 we present the 60 and 100 μm images of U Hya. At 60 μm the source is clearly resolved into a central point source and a detached ring of emission with a radius of about 1.75′. At 100 μm the reduced resolution of HIRAS (estimated to be 1.7′) does not allow the source to be resolved into a central star and detached ring. The overall distribution of intensity is consistent with that seen at 60 μm.

We have estimated the age of the shell using a distance to U Hya of 350 pc and an expansion velocity of 15 km s^{-1}, and find 12,000 years since the shell was ejected. With a simple optically thin dust model we find a mass loss rate of 1.4 $10^{-5}M_\odot$ yr^{-1}, which is a factor 70 higher than the present-day mass loss rate. Clearly the mass loss of carbon stars on the AGB is not constant but varies considerably on timescales of (at least) 10^4 years. Such timescales are in the same order of magnitude as the thermal pulse timescale for evolved AGB stars (Boothroyd & Sackmann 1988). A more detailed description will appear elsewhere (Waters et al., 1993).

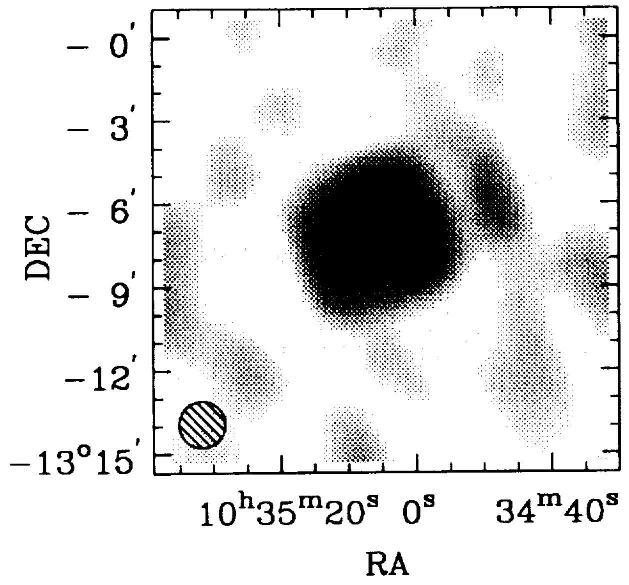

FIGURE 4 Same as Figure 3 but at 100 μm. The resolution of 1.7′does not allow the source to be resolved into a central star and ring.

ACKNOWLEDGMENTS

We thank Chris Rogers for providing the I band image of HR 3126. LBFMW acknowledges financial support from the Royal Dutch Academy of Arts and Sciences. The IRAS data were obtained using the IRAS data base server of the Space Research Organisation of the Netherlands (SRON) and the Dutch Expertise Centre for Astronomical Data Processing funded by the Netherlands Organisation for Scientific Research (NWO). The IRAS data base server project was also partly funded through the Air Force Office of Scientific Research, grants AFOSR 86-0140 and AFOSR 89-0320.

REFERENCES

Bontekoe, Tj. R. et al. 1993, submitted to *A&A*

Boothroyd, A.I. and Sackmann, I.-J. 1988a, *ApJ*, **328**, 641

Chan, S.J. and Kwok, S. 1988 *ApJ*, **334**, 362

Chiar, J.E., Whittet, D.C.B., Aitken. D.K., Roche, P.F., Smith, C.H., Walker, H.J., Whitelock, P.A., and Wright, C. 1993, *ApJ*, **409**, 404

Dachs, J. and Isserstedt, J. 1973, *A&A*, **23**, 241

IRAS Small Scale Structure Catalog. 1988, prepared by G. Helou and D. Walker (Washington, DC: GPO)

Kastner, J.H. 1990, Thesis, UCLA

Loup, C. 1991, Thesis, University of Grenoble

Nyman 1993, private communication

Olofsson, H., Carlstrom, U., Eriksson, K., Gustafsson, B., Willson, L.A. 1990, *A&A*, **230**, L13

Reimers, D. 1977, *A&A*, **54**, 485

Waters, L.B.F.M. et al. 1993, in preparation

Willems, F.J., and de Jong, T. 1986, *ApJ*, **309**, L39

Willems, F.J., and de Jong, T. 1988, *A&A*, **198**, 173

Witt, A.N., and Rogers, C. 1991, *PASP*, **103**, 415

Young, K., Phillips, T.G., and Knapp, G.R. 1993, *ApJ*, **409**, 725

Zijlstra, A.A., Loup, C., Waters, L.B.F.M., and de Jong, T. 1992, *A&A*, **285**, L5

N95- 21769 5

/ /3

WAVELET ANALYSIS APPLIED TO THE IRAS CIRRUS

WILLIAM D. LANGER
MS 169-506, Jet Propulsion Laboratory, Caltech, Pasadena, CA 91109

ROBERT W. WILSON
HOH-L239, AT&T Bell Laboratories, Holmdel, NJ 07733

CHARLES H. ANDERSON
Box 8108, Washington University School of Medicine,
St. Louis, MO 63110

ABSTRACT The structure of infrared cirrus clouds is analyzed with Laplacian pyramid transforms, a form of non-orthogonal wavelets. Pyramid and wavelet transforms provide a means to decompose images into their spatial frequency components such that all spatial scales are treated in an equivalent manner. The multiscale transform analysis is applied to IRAS 100 μm maps of cirrus emission in the north Galactic pole region to extract features on different scales. In the maps we identify filaments, fragments and clumps by separating all connected regions. These structures are analyzed with respect to their Hausdorff dimension for evidence of the scaling relationships in the cirrus clouds.

INTRODUCTION

In general, interstellar clouds appear inhomogeneous with features on different scale size depending on the spatial resolution of the telescope and the tracer used to probe the structure. This structure results from a fragmentation process that is not well understood and cannot be easily modeled because of the non-linear nature of the hydrodynamic equations which describe the cloud evolution. The formation and evolution of interstellar clouds is governed by a variety of forces including gravity, magnetic fields, rotation, thermal pressure, turbulence, and systematic motions. In addition discrete stellar sources inject energy into the clouds in the form of winds and shocks, producing systematic and turbulent motion. A highly "clumpy" or fragmented structure may reflect gravitational fragmentation or the presence of turbulence resulting from the cascade and redistribution of energy injected on different scales. In contrast, a highly filamentary structure might result from ordered magnetic fields.

To study the structure and dynamics of interstellar clouds observers have mapped them on different scales and to different degrees, mainly with the isotopes of CO, CS, and the 100 and 60 μm infrared dust emission, each of which traces a different aspect of the density and mass distribution. Interpreting these

S. Terebey and J. Mazzarella (eds.), *Science with High-Spatial Resolution Far Infrared Data*, 143–155, 1994, Jet Propulsion Laboratory, Pasadena, CA.

maps has proven to be more complicated because one does not know *a priori* what kind of features to extract and exactly how the distribution of features, their sizes and number, relate to the dynamics of the cloud.

To interpret the maps one needs some method to extract structural features and determine their number, size, distribution, mass, and energy content. Several approaches have been applied and discussed in the literature including a search for connected objects (Dickman, Horvath, and Margulis 1990; Falgarone, Phillips, and Walker 1991), the autocorrelation function, the structure function (Kleiner and Dickman 1984 and 1985), an iterative fitting procedure assuming Gaussian-shaped clumps (Stutzki and Gusten 1990) and structure tree analysis (Houlahan and Scalo 1990 and 1992). Recently we suggested that Laplacian pyramid (multiscale) transforms (LPT) are more suitable for determining the structure of interstellar clouds (Langer, Wilson, and Anderson 1993).

The best known example of the multiscale transform is the wavelet transform (Grossman and Morlet 1987; see also the reviews by Daubechies 1992; Farge 1992). Multiscale transforms provide a mathematically consistent way to extract structural components and map properties from astronomical images. The multiscale transform has been characterized as a generalization of the Fourier Transform which is capable of representing a function in terms of spatial and frequency localization. The localized structures at different scales are easier to identify in the transformed space than in the original (x, y) space. The wavelet transform is well suited to provide detailed information and deep insight into structure. Orthonormal wavelets have been used to extract particular features from complex astronomical data, including: galaxy counts (Slezak, Bijaoui, and Mars 1990; Martinez, Paredes, and Saar 1993); stellar photometry in globular clusters (Auriere and Coupinot 1989); ^{13}CO spectral data of the L1551 outflow (Gill and Henricksen 1990); and, photometric analysis of galaxies (Coupinot et al. 1992).

Here we apply a multiscale transform analysis of infrared cirrus clouds in the North Polar region using the IRAS Sky Survey Atlas (Wheelock et. al. 1994) plates and analyze the fractal structure and morphology of the clouds. Infrared 60 and 100 μm IRAS maps have been analyzed for scale-dependent morphology by a number of authors using algorithms to characterize the features which rely on connecting contours in the original (x, y) intensity maps. Bazell and Désert (1988) analyzed the fractal structure of interstellar cirrus using the Skyflux plates for three regions: one above and one below the plane ($b = +23°$ and $-14°$) and a third region at $b = -40°$ containing two well known high-latitude MBM clouds. Dickman, Horvath, and Margulis (1990) analyzed IRAS images of five molecular cloud complexes (including the well known regions of Chameleon, ρ Oph, and Taurus). Both studies found a highly fractal structure for the clouds and concluded that the clouds had a highly turbulent structure. However, they differ in the behavior of the scaling from region to region, which might not be surprising considering that one concentrates on molecular and the other diffuse regions. Our multiscale analysis of cirrus emission reveals a more complex structure than either of these previous studies.

MULTISCALE TRANSFORMS

First, we review the various multiscale transforms (Pyramids and Wavelets) and compare them to Fourier Transforms. Laplacian pyramid transforms preceded and spurred the recent interest by mathematicians in the more formalized orthogonal wavelets. In practice the orthogonal wavelets have proven useful primarily in image data compression, while the Laplacian pyramid has remained more useful for carrying out a variety of image analysis tasks.

Fourier Transform

A Fourier Transform decomposes a function $f(x)$ into a linear composition of Fourier vectors, whose basis functions are sines and cosines, defined by their Fourier coefficients,

$$\hat{f}(k) = (2\pi)^{-1/2} \int f(x) e^{ikx} dx. \tag{1}$$

Unfortunately e^{ikx} oscillates forever and the information content of $f(x)$ is delocalized among all the spectral coefficients $\hat{f}(k)$. Regions of $f(x)$ that vary sharply – for example a delta function – have their information spread among all of k space. Such transform properties are not very useful for real astronomical images which contain a great deal of structure.

One approach to achieve localization is to use a window to isolate the portion of the frequency or spatial scale of interest. Windowed transforms can also be applied sequentially to recover all of the function, however such transforms use fixed window size and thus do not analyze the function at all scales. An example of a windowed transform is the Gabor transform,

$$G^a(x) = (4\pi a)^{-1/2}\, e^{-x^2/4a} \tag{2}$$

which uses a Gaussian window. The real part of the transform of the Gabor function, ReG_ω is shown in Figure 1 for three values of ω; note that the Gabor transform has a fixed window size and that the transformed G oscillate within a fixed envelope.

Wavelet Transform

The wavelet transform localizes information in space and scale and the decomposition is done by translation and dilation of a single "Parent" function, the analyzing wavelet. The wavelet transform is defined by

$$T_g(a,b) = |a|^{-1/2} \int_{-\infty}^{\infty} f(x) g\{(x-b)/a\} dx \tag{3}$$

where the factor a covers different ranges in scale (frequency) and b moves the localization center (position or time). The wavelet transform separates data or functions into different spatial components and analyzes each component with a resolution to match its scale. The wavelet transform function must have the property that its mean is zero over x,

$$\int_{-\infty}^{\infty} g(x) dx = 0. \tag{4}$$

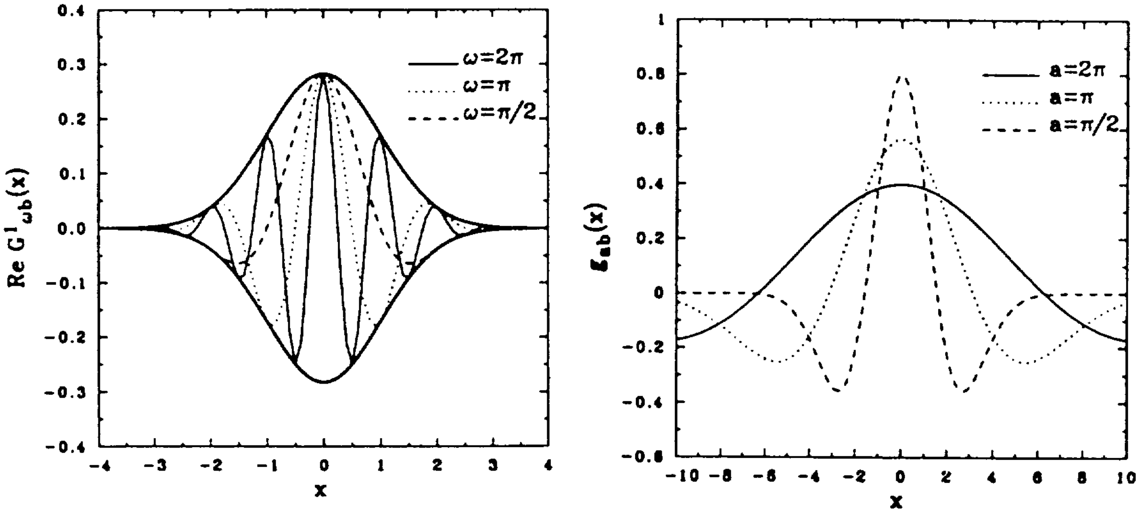

FIGURE 1 The functions g_{ab} and $ReG_{\omega b}$ for three values of a and ω ($b = 0$). The Gabor transform has a fixed window size in contrast to the wavelet transform's flexible window (Martinez et al. 1993).

One of the best known examples of a wavelet transform in astronomy is the Marr (or "Mexican Hat") wavelet, which in one dimension has the form,

$$g(z) = (1 - z^2)e^{-z^2/2}, \quad \text{where } z = (x - b)/a \tag{5}$$

The transformed function g_{ab} is shown in Figure 1 for three values of a (assuming $b = 0$) where one can see that the Marr wavelet has a flexible window size. Wavelets have the useful property that they preserve scaling behavior and are sensitive to signal variations but not to constant behavior. They also provide a useful description of turbulence because they retain information about the spatial structure of the flow (c.f. the review by Farge 1992).

Discrete Wavelet Transform

There is a discrete wavelet transform (DWT) analogous to the discrete Fourier transform (DFT), both of which are rotations in function space, but take an input space into different domains. For the DFT the basis functions are unit vectors or Dirac delta functions (in the continuum limit). For the DFT the domain has sine and cosine basis functions, while for the DWT they are localized in space. The best known examples of the DWT use the Daubechies basis functions (Daubechies 1992). We do not have space to review the DWT (see Press et al. 1993) but point out that the transform is a matrix whose odd and even rows perform different convolutions: the odd rows generate components of the data convolved with filter coefficients and perform a moving average with the smoothing filter H; the even rows perform a convolution with a filter L which represents the detailed information in the data. The DWT is applied hierarchically to the data vector (i.e., first to the full length data N, then to the "smooth" vector of length N/2, etc.) ultimately producing a set of wavelet coefficients that represent the smoothed information on the largest scale and

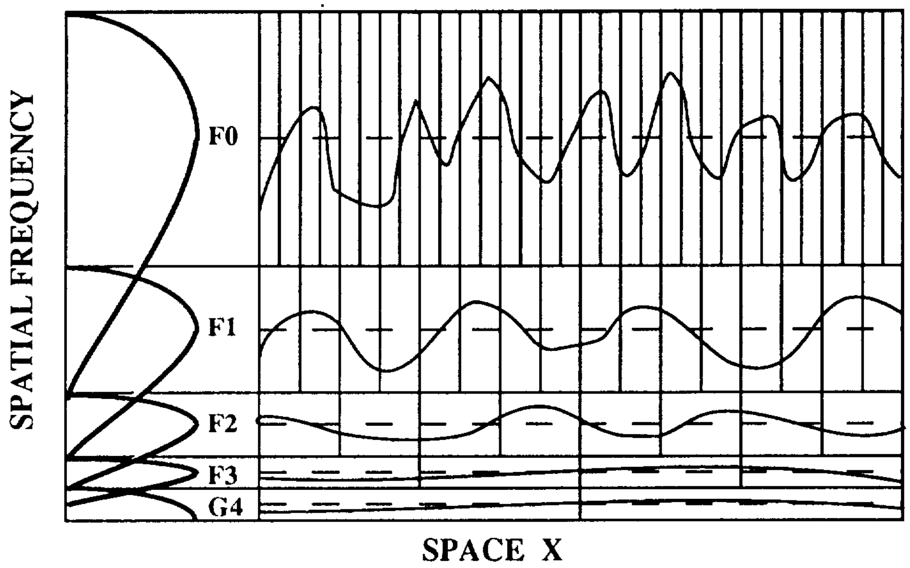

FIGURE 2 Scale invariant filter bank: Filter responses, $F_n(k) = F_0(2^n k)$, on the left.

detailed information on scales differing by factors of two. Specific examples are given by Daubechies (1992) and Press et al. (1993).

Pyramid Transforms

Pyramid transforms preceded and spurred the recent interest by mathematicians in the more formalized orthogonal wavelets. However, one of the major difficulties with the orthogonal wavelets is that, while their basis functions display shift and scale invariant properties, the coefficients in these expansions do not (see Strang 1989; Simoncelli et al. 1992). The fact that the power within a given scale is not invariant to translations of the input should be enough to make one wary. In addition, when implemented as separable filters, the orthogonal wavelet transform creates three highly anisotropic bandpass components at each scale, which have no simple relationship to underlying physical properties.

Pyramid transforms provide a means to decompose images into their spatial frequency components such that all spatial scales are treated in an equivalent manner. The concepts are equally applicable to data of any dimension, where each axis represents some continuous physical parameter such as spectral wavelength, time, or in the case of images vertical and horizontal lengths or angular displacements. An intuitive grasp of the idea can be obtained in one dimension by considering the illustration in Figure 2. The horizontal axis represents a parameter such as space and the vertical axis spatial frequency. If we consider a signal $S(x)$ that has been bandpass limited by a fixed amount, then it can represented by a uniform sequence of samples $S(x_i)$, as set by the Nyquist sampling theorem, with no loss of information. Now consider passing the signal through a bank of filters that are scaled copies of one another, such that $F_n(k) = F_0(2^n k)$, where the scaling by factors of two is chosen for convenience. The output of each filter treats the signal in a scale invariant fashion because of the scaling relationship between the filters. The outputs of each filter must be sampled at a rate that is proportional to the corresponding bandwidth, hence each band is sampled at a rate that differs from its neighbors by a factor of two, as illustrated in Figure 2. This method of signal decomposition is the basis of all scale invariant multiresolution representations such as Pyramids and Wavelets. The signal processing community have labeled them as a special class of subband encoding schemes.

The generality of this form of signal analysis is best illustrated by noting that the human visual and auditory systems utilize it. The scale invariant nature of many physical processes is what makes these representations important. The statistics of the signals and the forms of the structures produced by these filters provide measures of how underlying physical processes change with scale. The coefficients in these representations are much more statistically independent of one another than they are in the original data formats, which leads to a rich set of localized descriptors of images and better data compression for storage.

The number of such decompositions is large since there are many filter designs whose scaled filter banks will cover the frequency range of interest with sufficient density to prevent loss of information. This means there is a multitude of possible multiscale transforms unlike the Fourier transform. The choice of which filter to use is determined by factors such as efficiency of computation, signal-to-noise ratios, information storage and the type of data analysis one desires to perform. When one goes into higher dimensional spaces the choices for the shape of the filter become increasingly more flexible and hence increase the number of possible transforms. The orthonormal wavelets, which have recently received a lot of recognition, are a particular subset of the multiscale transforms. These provide critically sampled representations with minimal storage, as well as having some nice mathematical properties, but the constraint of orthogonality leads to filter designs that are not necessarily the best for many applications. There are a number of overcomplete transforms, such as the Laplacian pyramid, based on circularly symmetric filters, oriented pyramids, which have "wavelet"-like filters, and a recent new class with a property called "shiftability" (cf. Strang 1989, Simoncelli et al. 1992).

The Laplacian pyramids are best understood as the outputs of a bank of scaled circularly symmetric, bandpass spatial frequency filters, with center frequencies $k_n = k_0/2^n$ and roughly octave bandwidths. The simple variant used here is called an FSD (Filter, Subtract, and Decimate) pyramid (cf. Van der Wal 1991). Starting with the original image, designated as $G_0(x, y)$, the following rules are applied recursively to create a sequence of lowpass images (or Gaussian levels) $G_n(x, y)$ and bandpass (or Laplacian levels) $L_n(x, y)$:

$$\hat{G}_{n+1} = H * G_n \quad \{\textbf{Filter}\} \tag{6}$$

$$L_n = G_n - \hat{G}_{n+1} \quad \{\textbf{Subtract}\} \tag{7}$$

$$G_{n+1} = \{\textbf{Decimate}\} \quad \hat{G}_{n+1} \tag{8}$$

The filter operation $H * G_n$ involves convolving the image G_n with a lowpass filter H. A separable filter, $H(x, y) = h(x)h(y)$, was used in this work, where we adopted a five tap filter for $h(x)$ having the tap values 1/16, 1/4, 3/8, 1/4, 1/16, which produces an approximately circularly symmetric filter in the spatial frequency domain. The Laplacian components, L_n, are computed by subtracting the low pass version from the unblurred one at each scale. This operation is equivalent to filtering with a "Mexican hat" or difference of a Gaussian-like shaped kernal. The blurred version, G_n, is then subsampled by throwing away every other pixel and row, which is traditionally called "decimation." Decimation is justified because the lowpass filter reduces the spatial frequency content such that little aliasing is introduced by this process. Since this reduces the number of pixel values by four at each stage in a two-dimensional map, the computation of all the levels L_1 to L_N takes only one third the time and resources to compute L_0. Typically the final level N is set by stopping the process when the smallest dimension of the array $G_{n+1}(x, y)$ would be no smaller than eight. Mathematically, the set of values $L_n(x, y)$ for $n = 0$ to N plus G_{N+1}, constitute the components of an overcomplete non-orthogonal wavelet decomposition of the original image G_0. The bandpass components show less than two percent anisotropic response to spatial frequency orientation and less than five percent to translation of the input image. This operation is a computationally efficient, basic wavelet transform that has a relationship to some simple multiscale statistics. The G_n are mean values computed over regions that increase in size by factors of two and the L_n provide the local deviations from these multiscale mean values.

IRAS IMAGES OF THE NORTH POLAR CIRRUS

To analyze the structure of cirrus emission we have chosen a region in the north Galactic pole (declination 90° at map center) in order to minimize the line-of-sight confusion. We obtained 60 and 100 μm images of the North Polar Cirrus from the ISSA data measuring 5° on a side with pixels of $1.5' \times 1.5'$, although the actual resolution of the images is closer to $4'$ (the IRAS beam size at 100 μm). Figure 3 is a contour plot of the 100 μm image and shows the highly complex filamentary and globular nature of the emission. From the 100 and 60 μm images one can calculate a dust color temperature and opacity assuming a one component model of the dust grains (cf. Langer et al. 1989). The color temperature map is roughly uniform with a temperature of 25 K and the temperature drops in the regions of brightest emission where the opacity is a minimum. This behavior is well known for the 60 and 100 μm maps and is a result of using an overly simplified grain emission model. Therefore we decided to restrict our analysis to the 100 μm maps as the 100 μm emission arises from cooler dust, is optically thin, and thus more likely to arise uniformly from all the material along the line-of-sight. The 100 μm maps show a great deal of structure on all scales and the variation in emission is either due to increased column density, changing dust grain distribution, or variations in heating sources.

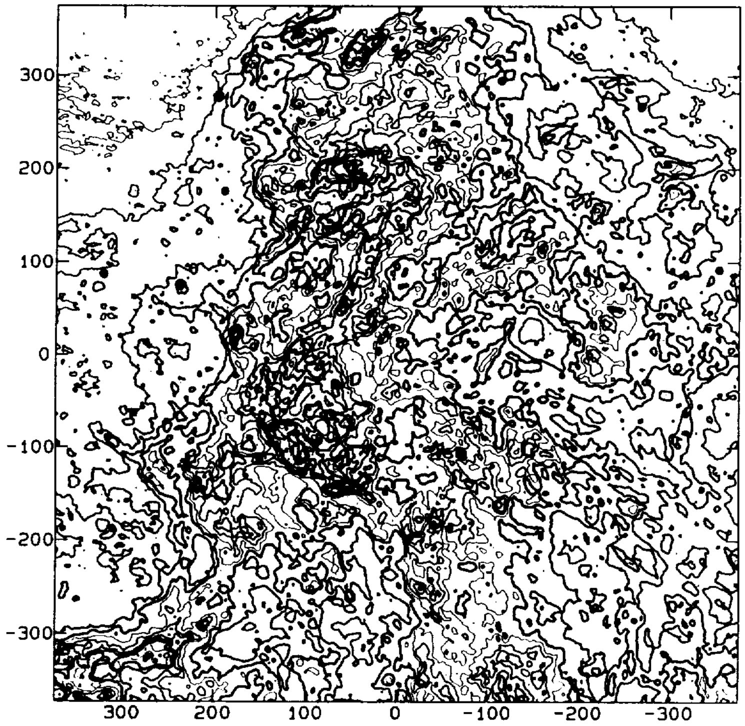

FIGURE 3 The 100 μm image of the North Polar Cirrus (dec = 90°, 0^h is at the top and RA goes counterclockwise with 6^h on the left); the axes are in arcmin with respect to the center. Intensity units range from 2 to 16 × 10^6.

RESULTS

The LPT applied to the 100 μm image of the North Polar Cirrus generates a set of amplitude maps for each of the basis functions, ranging from L_0 to L_5 covering the smallest to largest scales (1.5′ to 9′), and G_5 (the original image is labeled G_0). The G_n are mean values computed over regions that increase in size by factors of two and the L_n provide the local deviations from these multiscale values. The Ln images represent the detailed information and have equal positive and negative areas (average over the maps is zero). G_5, which has a resolution of 48′, is smooth and positive definite over the map. There is not room here to display the Laplacian images but examples of the transform maps for CO clouds can be seen in Langer et al. (1993).

To extract the structure in the map we assume that at each scale the features are embedded one within the other, or superimposed along the line-of-sight. We define a clump or filament as a connected region of positive amplitude, that is the zero contour boundary in the Laplacian maps. Bubbles or valleys would correspond to connected negative regions. (These maps are better for isolating features because of the separation of different scales and the preservation of locality in the transformed space.)

For each image we can determine the following properties of the connected positive or negative regions:

Perimeter = P,

Area = A,

Intensity = $\int \phi(x,y)dA$,

where $\phi(x,y)$ = amplitude of the wavelet basis function at (x,y),

Brightness = $[\int \phi(x,y)dA]/A$,

rms = $\int |\phi(x,y)|^2 dA$.

The major problem with this approach is that there are many features at small scale that correspond to noise in the maps or are on smaller scales than the beam resolution (the pixel area is 2.25 arcmin^2 while the IRAS beam is roughly $3'$ to $4'$). We avoid this problem by only considering features whose area, A, is greater than 16 arcmin^2). Table 1 summarizes the number of distinct features of positive amplitude for each of the Laplacian maps.

TABLE 1 Summary of Cirrus Features in Each LPT Basis Map

Order (l)	$(\Delta\lambda)^*$ $(')$	Number of Features
0	1.5	1423
1	3.0	684
2	6.0	252
3	12.0	81
4	24.0	28
5	48.0	11

* The wavelength of each band is approximated by the width, $\Delta\lambda$, of each high pass filter.

Here we concentrate on only one property of the structure analysis of the cirrus clouds, the scale-dependent morphology, or fractal structure. One widely used approach to measuring the morphology of the cloud structures is the Hausdorff dimension (Bazell and Désert 1988, Dickman et al. 1990) which is the fractal dimension of the objects in the cloud. The fractals are self-similar under scale changes and so a determination of the Hausdorff dimension, D, can help identify the scale-dependent morphology of the cloud. Ideally, the geometrical structures and the scale dependence provide information about the forces at work in the cloud. D is defined as

$$A^{1/2} = KP^{1/D} \tag{9}$$

where a plot of log perimeter versus log area yields a slope of $D/2$ and has an intercept equal to $-D(log K)$. Regular geometrical objects (circles, ellipses, squares, etc.) all have $D = 1$ (i.e., the same scaling) but different intercepts (i.e., K depends on shape). A value of $D \approx 4/3$ characterizes the relationship expected for Kolmogorov turbulence (incompressible, homogeneous, isotropic turbulence); see the discussion by Dickman et al. Filamentary structures that scale only with length, on the other hand, have $D \approx 2$, as would be characteristic of gas supported by magnetic fields in the radial direction. Figure 4 shows an example of the plot of log(P) versus log(A) for the $l = 1$ image ($\Delta\lambda \approx 3'$). Note that the fit is not particularly good for large areas ($A > 400$ arcmin^2). For the small wavelengths ($l = 0$ and 1) the fits are dominated by the many small features in the map (note each cross in Figure 4 can represent many clumps of the same area and perimeter). Figure 5a plots D as a function of the l value and shows relatively little variation with wavelength. The log(P)-log(A) fits for $l = 4$ and 5 do not have much area dependence and the average value for D in Figure 5 is about 1.45. Bazell and Désert found a rather different average value, $D \approx 1.25$, for the cirrus clouds, however, there was variation within each image (see their Figure 2). Dickman et al.'s study of 100 μm maps of molecular regions found D ranging from 1.2 to 1.3, similar to those found for cirrus clouds (remember that these results use a completely different method than that discussed here to determine the map features).

Determining the Hausdorff dimension as a function of area, in the sense of considering several ranges of area within an l map, yields somewhat different results. Figure 5b plots D for the $l = 1$ image divided up into four different ranges. For the smallest features the Hausdorff dimension is 1.25, similar to the result of Bazell and Désert, but it increases with area reaching a value about 2 for the largest objects in the image. As the $l = 1$ map corresponds to features that respond to a multiscale filter of about $3'$ (in at least one direction) the largest features resemble thin filamentary or web-like structures. This result suggests that the forces that control the structure at large and small scales in the cirrus map of the north pole region are different.

DISCUSSION

D for all the North Polar Cirrus features ranges from 1.35 to 1.5 with an average of 1.45 for all the Laplacian maps. These values are larger than the average value of 1.25 found by Bazell and Désert in three cirrus maps, their maximum value of 1.40 for plate 2, and the values for $D(\approx 1.18 - 1.28)$ for 100 μm IRAS maps of the molecular clouds studied by Dickman et al. It is not clear if the differences are due to the choice of objects or the method to extract the map features. We will analyze the Chameleon region in the near future to test the latter possibility. The fractal nature of the cloud B5 studied with CO maps (Langer et al.) has D ranging from 1.3 to 1.7. These differences may occur because CO emission probes the dense interior of the cloud where the dynamics are much more influenced by gravity and embedded sources. D for cirrus clouds is consistent with a turbulent gas (Kolmogorov turbulence including the effects of intermittency — see Falgarone et al.). However, the strong dependence of D on the area range (Figure 5b) shows that for $l = 1$ and 0 (the smallest scales) D increases with increasing area reaching values about 2. This dependence suggests that the smallest features obey a Kolmogorov scaling law (D is close to the Bazell and Désert value) while the largest feature at $l = 0$ and 1 are filamentary-like structures. Visual inspection shows these features to consist

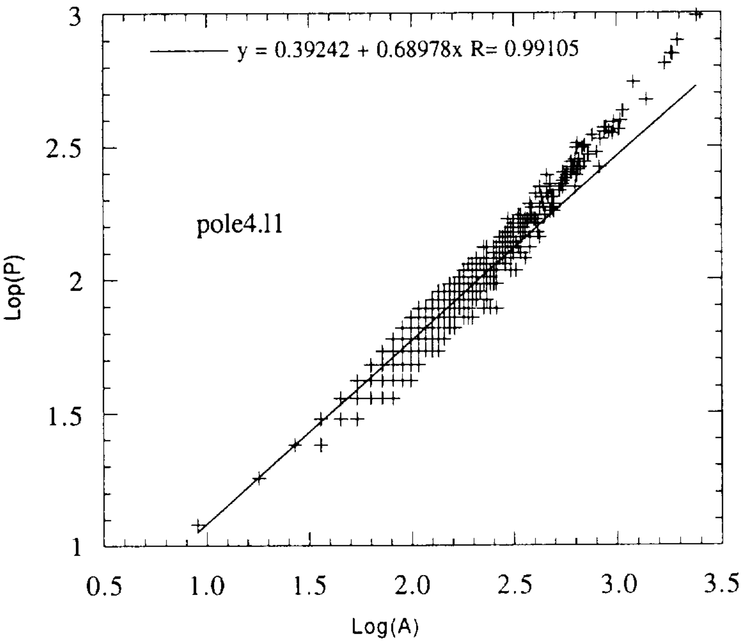

FIGURE 4 Determination of the Hausdorff dimension, D, and the shape factor, K, from plots of perimeter versus area for the $l = 1$ image. The fits are listed in the Figure.

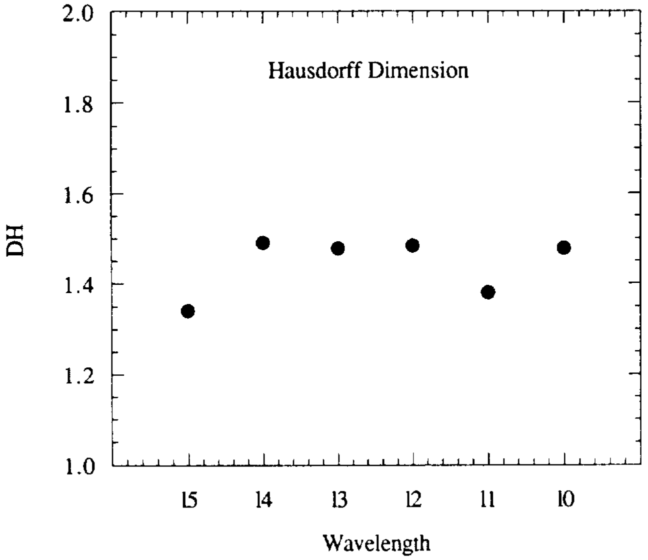

FIGURE 5a. Hausdorff dimension, D, versus l_n ($\approx$ wavelength, see Table 1) using all the features in each map.

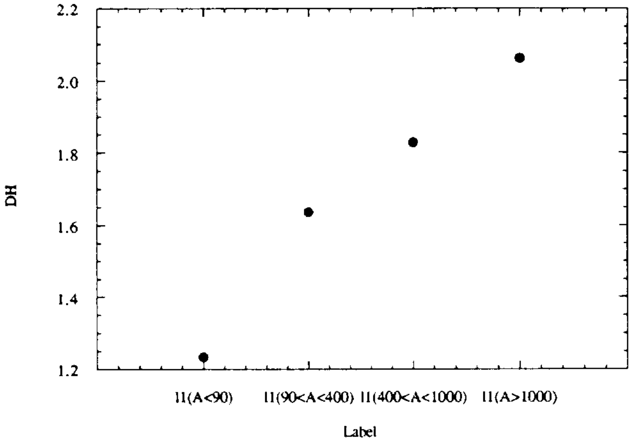

FIGURE 5b. Hausdorff dimension, D, versus different ranges in area for the $l = 1$ map.

of long single filaments and web-like structures. The latter are likely due to the overlap of separate features along the line of sight since the data have no velocity information and/or the merging of very many small scale features within the filters. Higher resolution 100 μm data is needed to test this hypothesis.

ACKNOWLEDGEMENTS

We thank Dr. T. N. Gautier for providing the IRAS images of the north polar cirrus used in this paper. RWW wishes to thank the Jet Propulsion Laboratory, California Institute of Technology, for hospitality and support as Distinguished Visiting Scientist. This work was carried out in part at the Jet Propulsion Laboratory, California Institute of Technology, under a contract with the National Aeronautics and Space Administration.

REFERENCES

Auriere, M. and Coupinot, G. 1989, *Proc. of the 1st ESO/ST-ECF Data Analysis Workshop*, eds. Grobs et al.

Bazell, D. and Désert, F. X. 1988, *ApJ*, **333**, 353

Coupinot, G., Hecquet, J., Auriere, M., and Fautaully, R. 1992, *A&A*, **259**, 701

Daubechies, I. 1992, *Ten Lectures on Wavelets*, CBMS-NSF Regional Conference Series in Applied Mathematics (Philadelphia: SIAM)

Dickman, R. L., Horvath, M. A., and Margulis, M. 1990, *ApJ*, **365**, 586

Falgarone, E., Phillips, T. G., and Walker, C. K., 1991, *ApJ*, **378**, 186

Farge, M. 1992, *Ann. Rev. Fluid Mech.*, **24**, 395

Gill, A. G. and Henriksen, R. N. 1990, *Ap. J. Letters*, **365**, L27

Grossman, A. and Morlet, J. 1987, *Mathematics and Physics, Lectures on Recent Results*, ed. L. Streit (World Scientific)

Houlahan, P. and Scalo, J. 1990, *Ap. J. Suppl.*, **72**, 133

Houlahan, P. and Scalo, J. 1992, *ApJ*, **393**, 172

Kleiner, S. C. and Dickman, R. L. 1984, *ApJ*, **286**, 255

Kleiner, S. C. and Dickman, R. L. 1985, *ApJ*, **295**, 466

Langer, W. D., Wilson, R. W., Goldsmith, P. F., and Beichman, C. A. 1989, *ApJ*, **337**, 355

Langer, W. D., Wilson, R. W., and Anderson, C. H. 1993, *ApJ*, **408**, L45

Martinez, V. J., Paredes, S., and Saar, E., 1993, *MNRAS*, **260**, 365

Press, W. H., Flannery, B. P., Teukolosky, S. A., and Vetterling, W. T. 1993, *Numerical Recipes 2nd Edition* (Cambridge University Press: Cambridge)

Simoncelli, E. P., Freeman, W. T., Adelson, E. H., and Heeger, D. J., 1992, *IEEE Trans., Info. Theory, Special Issue on Wavelets*, **38**, 587

Slezak, E., Bijaoui, A., and Mars, G. 1990, *A&A*, **227**, 301

Stutzki, J. and Gusten, R. 1990, *ApJ*, **356**, 513

Strang, G. T. 1989, *SIAM Review*, **31**, 614-627

Van der Wal, G. S. 1991, *The Sarnoff Pyramid Chip, Proc. Computer Architecture for Machine Perception*, (CAMP-91), Paris, p. 69

Wheelock, S. et al. 1994, *Explanatory Supplement to the IRAS Sky Survey Atlas*, (Pasadena:JPL), in press

p 7

A HIRES ANALYSIS OF THE FIR EMISSION OF SUPERNOVA REMNANTS

ZHONG WANG
Infrared Processing and Analysis Center, MS 100-22,
California Institute of Technology, Jet Propulsion Laboratory,
Pasadena, CA 91125

ABSTRACT The HiRes algorithm has been used to analyze the far-infrared emission of shocked gas and dust in supernova remnants. In the case of supernova remnant IC 443, we find a very good match between the resolved features in the deconvolved images and the emissions of shocked gas mapped in other wavelengths (lines of H_2, CO, HCO+, and HI). Dust emission is also found to be surrounding hot bubbles of supernova remnants which are seen in soft X-ray maps. Optical spectroscopy on the emission of the shocked gas suggests a close correlation between the FIR color and local shock speed, which is a strong function of the ambient (preshock) gas density. These provide a potentially effective way to identify regions of strong shock interaction, and thus facilitate studies of kinematics and energetics in the interstellar medium.

INTRODUCTION

Supernova remnants (SNRs) can be bright in the mid- and far-infrared either because of non-thermal radiative processes internally, or interactions with the interstellar medium (ISM) surrounding them. Several recent studies have surveyed a large number of Galactic SNRs in the IRAS All Sky Survey, and identified a substantial fraction of them as FIR sources despite considerable confusion problems due to the Galactic plane (Arendt 1989; Saken et. al. 1992). General correlations between IR and radio, and/or between IR and X-ray emissions are cited, even though the resolution that IRAS data provide is often insufficient to study the IR morphology. In addition, it is found on a statistical basis that older remnants are both colder and more massive. These results suggest that the emission measured by IRAS come mostly from shock interactions with dense gas and dust. However, the actual mechanism of interaction, and its dependence on local conditions largely remain to be explored.

An alternative approach to the statistical analysis is trying to better resolve the IR emission around a few extended SNRs, and compare the images in the four IRAS bands with the physical conditions in the surrounding medium studied in other wavelengths. In this way, one can hopefully address the origin of the infrared emission as well as the energy balance in the evolution of the remnants. The HiRes algorithm (Aumann et. al. 1990) becomes particularly useful in this regard, because it provides not only a much better linear resolution, but also a convenient way to examine infrared color variation through *beam matching*.

S. Terebey and J. Mazzarella (eds.), *Science with High-Spatial Resolution Far Infrared Data*, 157–163, 1994, Jet Propulsion Laboratory, Pasadena, CA.

In this contribution, I present the preliminary results of a HiRes analysis to illustrate some of the possibilities that this approach can provide.

DATA ANALYSIS

The FIR emission of supernova remnant IC 443 is detected in all four IRAS bands and its ring-like structure has been well identified (Huang et. al. 1986; Braun & Strom 1986; Arendt 1989). However, since the angular scale of the entire region is about 20′, the ~ 4′ resolution of the coadded images is inadequate to analyze the infrared morphology. As a result, only the integrated fluxes have been measured in the previous studies.

Since both the absolute flux level and the signal-to-nise ratio in the 60 and 100 μm images of SNRs are higher than that in 12 and 25 μm, it is justified to perform more HiRes iterations on the longer wavelength images. In practice, I used the survey data as input, and adopted the HiRes 12, 25, 60 and 100 μm images at 5, 5, 10, and 20 iterations, respectively. Although these do not provide the best possible resolution at all four bands, they do give more comparable beam sizes. More importantly, they are physically meaningful because of the different signal-to-noise ratios in the four bands. The region selected to perform the deconvolution is a 2° field centered on IC 443.

The variation of the beam from the field center to the sides is rather small in this case, so I adopted measurements of simulated beam at the image center to be the representative one. The next step was to examine the resolution maps at each band, and try to match the resolution based on the "least common denominator". Four different two-dimensional smoothing kernels were used to *convolve* the maps into nearly identical beam sizes and shapes, while preserving the best possible resolution. The parameters of the kernel used, and the measurements of input and output beams are listed in Table 1. These measurements were based on 2-D least-square Gaussian fits.

Table 1. Beam measurements[a]

	Before Convolution[b]		Gaussian Kernel[c]		After Convolution[b]	
Band(i)[d]	a(maj)	a(min)	sa	ar	a(maj)	a(min)
b1(5)	6.58	2.11	1.65	0.920	7.55	4.45
b2(5)	7.16	2.22	1.62	0.573	7.56	4.45
b3(10)	5.34	3.12	2.25	0.589	7.54	4.45
b4(20)	5.33	3.97	2.25	0.367	7.55	4.46

[a] all measurements are in unit of pixel, 1 pixel = 15″;
[b] a(maj), a(min) are half width along the major and minor axes, respectively;
[c] sa, ar are the semi-major axis and axis ratio of the 2-D Gaussian;
[d] bn(i): where n represents band id, and i is the number of iterations used.

From Table 1, we see that the beams in the four IRAS bands are well matched after convolution with the selected kernel, with a relatively minor penalty of a ~ 30% increase in beamwidth. The beam matching of the actual images was confirmed by comparing a few stellar sources present in the same field. Figure 1 compares the *beam-matched* 60 and 100 μm images with the unprocessed ones. The resolution of the HiRes images is about $1.9' \times 1.1'$, a significant improvement over the $\sim 4' \times 3'$ beam in pre-HiRes images. The biggest advantage of having beam-matched maps in all four bands, however, is to make infrared color maps that would be physically meaningful. One can then easily compare colors of different regions, provided that the sizes of regions over which the flux integrations are made is larger than the beam size.

COMPARISON WITH OTHER OBSERVATIONS

Before trying to interpret the physical meaning of the HiRes images and color maps, it is necessary to assess the reliability of the enhanced features seen in the HiRes deconvolution. In IC 443, this can be best shown in comparisons with observations of the same region made in other wavelengths.

Using millimeter-wave radio telescopes, Dickman et. al. (1992, see also Huang et. al. 1986) mapped the broad CO and HCO+ line emission in the surrounding areas of IC 443. These molecular lines, typically as broad as 60 km s^{-1}, are often identified as the shock interface with nearby molecular clouds. Overlapping the CO and HCO+ maps with the deconvolved IRAS images, we find that all broad molecular line regions also have strong FIR emission. These regions are located mainly along the ω-shaped ring structure in the middle and southern parts of the SNR. Some of the previously unresolved FIR features, such as the one corresponding to "position F" (Dickman et. al. 1992) near the geometric center of IC 443, are clearly isolated FIR emission peaks, similar to their counterparts in the molecular line survey.

Burton et. al. (1988, 1993) made extensive maps of the (1–0) S(1) line emission of molecular hydrogen covering the entire region of IC 443. The near-infrared line represents shocked molecular gas at a warm (~ 2000 K) temperature. Although the H_2 map is at a much higher resolution, the overall correspondence with the deconvolved IRAS images is striking. This suggests that the mid- and far-infrared emission detected by IRAS is mainly from heated dust associated with the shocked molecular gas traced by the H_2 line emission. This comparison serves two purposes: on the one hand, some emission regions with structures poorly resolved in the HiRes images can be studied by referring to the NIR image; conversely, the FIR color information extracted from comparing different IRAS bands can be used to help interpret the significant variations of H_2 emission around this SNR (see below).

Wang et. al. (1994) mapped the 21 cm neutral hydrogen line emission of IC 443 with relatively high resolution ($15''$ as compared to the $50''$ resolution in previous studies). Again, the regions with strong infrared and molecular line emission also show up prominently with broad-line H I. Detailed comparisons indicate that the detected H I is mainly the diffuse gas resulting from shock dissociation of molecules as the SNR interacts with the surrounding dense clouds. However, the kinematic information from HI is incomplete due to the foreground

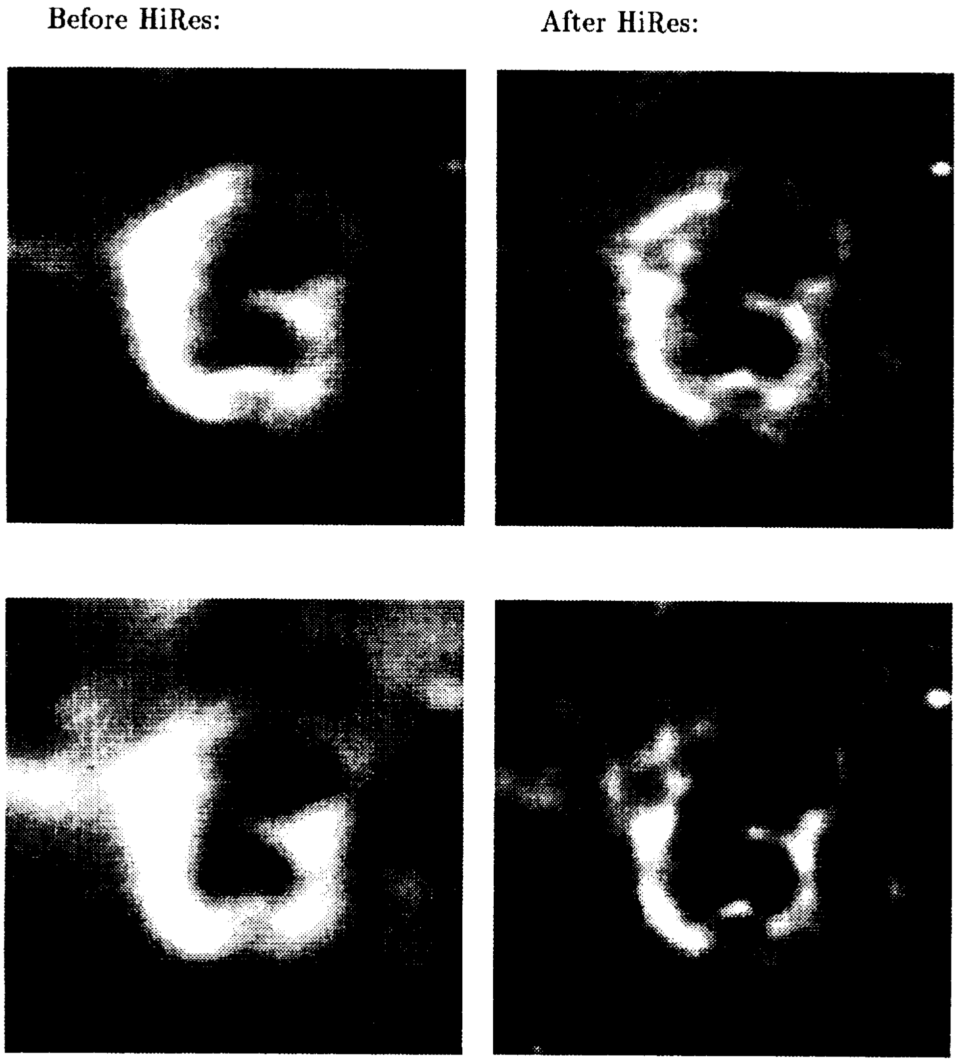

FIGURE 1 Greyscale maps of the IRAS 60 (upper) and 100 μm (lower) images of IC 443 before and after HiRes processing. This is a one-degree field centered on the supernova remnant; north is at top, and east is to the left. Grey levels are linear. Some of the vertical stripes seen in the processed images are due to artifacts of the deconvolution algorithm. The HiRes images are "beam matched", such that the effective resolutions are very similar (see text).

absorption within the Galactic plane.

Finally, the IPC aboard Einstein and, more recently, the PSPC aboard ROSAT both made large-scale diffuse X-ray emission maps of IC 443 in the 0.1–3 KeV energy range (Petre et. al. 1988; Rho & Petre 1993). Comparison between the infrared and soft X-ray maps is intriguing because the higher energy photons are emitted by the hot interior of the SNR bubble (e.g., Arendt et. al. 1991). Indeed, their positional coincidence with the rim of X-ray emitting regions provides independent confirmation that much of the faint structures seen in the HiRes images, especially in the NW region of IC 443, are actual SNR shock fronts.

In summary, the HiRes images with much improved resolution clearly demonstrate the relationship between the mid- and far-infrared emission and the SNR shock interactions in the ISM.

INFRARED COLOR VARIATION

As pointed out above, one of the great advantages for having beam-matched IRAS images is to construct color maps of infrared emission, which are important to the studies of shock interactions.

In the case of IC 443, we find that the FIR color changes drastically from one part of the SNR shell to the other, presumably tracing the density variation in the ambient medium. In the NE part of the SNR where the optical filaments are prominent, there is a low S(12)/S(25) and a high S(60)/S(100) flux density ratio as compared to the rest of the FIR bright regions (SE and SW), where molecular line emissions are the strongest.

Theoretically, the energy spectrum of the dust emission in interstellar shocks depends critically on the average preshock density, n_0. Where n_0 is low, the shock speed is high and so is the heating rate. The corresponding FIR (60 and 100 μm) color then reflects a higher dust temperature. Conversely, lower dust temperatures are found where the preshock density is high. In IC 443, the latter case is typically regions dominated by molecular gas.

We have also obtained spectroscopic (echelle) data of the optical filaments at a velocity resolution of about 8 km s^{-1}. Since the curvature of the shock front always tends to broaden the observed linewidth, it can be shown that the FWHP (full-width at zero power) of the emission lines of any particular region is a direct indicator of the shock speed at that position. And it is so regardless of the actual angle between the shock velocity vector and the line of sight (Dopita 1979). Adopting this assumption, we find in the NE where the S(60)/S(100) color ratio is high, the shock speed is about twice that of the SE and SW regions (120 km s^{-1} versus 60 km s^{-1}). The optical data thus confirm the idea that the SNR has encountered very dense gas in the southern part, resulting in faster cooling and a dramatic slow-down in the shock propagation.

The detailed morphology of the regions with different FIR colors can also be quite different. Referring to the high resolution H_2 line images, we find that the NE region shows thin, multi-layered filamentary structures; while the SE and SW regions show more pronounced, ripple-like features (Burton et. al. 1993). These difference could be due to the changing characteristics of the shock as its speed drops substantially (e.g., Wang & Scoville 1992).

DISCUSSION

One other thing that is clear from the color maps is that an enhanced ratio of S(60)/S(100) is usually accompanied by a decreased S(12)/S(25). This is also true for integrated fluxes of a large sample of SNRs (e.g., Arendt 1989). It reminds one of a similar trend among galaxies (Helou 1986), which is accounted for in terms of changing conditions in the ionizing radiation (Désert 1986). In the case of SNR shocks, however, the explanation maybe somewhat different. It is likely that the color ratio change among different shocked regions in a SNR is directly related to the amount of very small grains (VSG) that survive at the shock front. Faster shocks in the diffuse gas (with warmer 60–100 μm emission) tend to destroy most of the VSGs which are responsible for the emission at the shortest (12 μm) wavelength, resulting in a lower S(12)/S(25) ratio.

For interstellar shocks in dense gas, line emissions could potentially alter the colors measured using IRAS flux density ratios. Burton et. al. (1990) detected a strong [OI]λ 63 μm line at one of the molecular emission peaks in IC 443, and estimated that it may contribute substantially to the local broad-band 60 μm flux density. If this is generally the case, then the IRAS data, even with the beam-matched images, cannot be used to derive effective dust temperatures directly. More FIR spectroscopic observations are therefore needed to help better address the real properties of dust emission in the shocked ISM.

ACKNOWLEDGMENTS

I thank the staff at IPAC for providing technical support for the HiRes processing, and I am grateful to Dr. M. G. Burton for his help in analyzing the data discussed in this contribution. This work was carried out in part at the Jet Propulsion Laboratory, California Institute of Technology, under a contract with the National Aeronautics and Space Administration.

REFERENCES

Arendt, R.G. 1989, *Ap. J. Suppl. Ser.*, **70**, 182

Arendt, R.G., Dwek, E., & Petre, R. 1991, *ApJ*, **368**, 474

Aumann, H.H., Fowler, J.W., & Melnyk, M. 1990, *A.J.*, **99**, 1674

Braun, R. & Strom, R. 1986, *A&A*, **164**, 193

Burton, M.G., Geballe, T.R., Brand, P.W.J. T., & Webster, A.S. 1988, *MNRAS*, **231**, 617

Burton, M.G., Hollenbach, D.J., Hass, M.R., & Erickson, E.F. 1990, *ApJ*, **355**, 197

Burton, M.G., Spyromilio, J. & Wang, Z. 1993, *in preparation*

Désert 1986, F.X., in *Light on Dark Matter*, ed. F.P. Israel, 213

Dickman, R.L., Snell, R.L., Ziurys, L.M., & Huang, Y.L., 1992, *ApJ*, **400**, 203

Dopita, M. 1979, *Ap. J. Suppl. Ser.*, **40**, 455

Helou, G. 1986, *Ap.J. Lett.*, **311**, L33

Huang, Y.L., Dickman, R.L., & Snell, R.L. 1986, *ApJ*, **302**, L63

Petre, R., Szymkowiak, A.E., Seward, F.D., & Willingale, R. 1988, *ApJ*, **335**, 215

Rho, J. & Petre, R. 1993, in *IAU Colloq. 145: Supernova and Supernova Remnants*, eds. R. McCray and Z.R. Wang (Cambridge), *in press*

Saken, J.M., Fesen, R.A., & Shull, M. 1992, *Ap.J. Suppl. Ser.*, **81**, 715

Wang, Z. & Scoville, N.Z. 1992, *apj*, **386**, 158

Wang, Z., Scoville, N.Z., Burton, M.G., & Kenney, J.P. 1994, *in preparation*

2

7

ARCMINUTE SCALE HI AND IRAS OBSERVATIONS TOWARD HIGH LATITUDE CLOUD G86.5+59.6

P. G. MARTIN
Canadian Institute for Theoretical Astrophysics, University of Toronto, Toronto, ON, Canada M5S 1A7; Visiting Associate, Theoretical Astrophysics and IPAC, California Institute of Technology, Pasadena, CA 91106

C. ROGERS
Dominion Radio Astrophysical Observatory, Herzberg Institute of Astrophysics, National Research Council, P.O. Box 248, Penticton, BC, Canada V2A 6K3

W. T. REACH
NASA/GSFC, Lab for Astronomy and Solar Physics, Code 685, Greenbelt, MD 20771

P. E. DEWDNEY
Dominion Radio Astrophysical Observatory, Herzberg Institute of Astrophysics, National Research Council, P.O. Box 248, Penticton, BC, Canada V2A 6K3

C. E. HEILES
Astronomy Department, University of California at Berkeley, Berkeley, CA 94720

ABSTRACT

G86.5+59.6 is a degree-sized high latitude cloud originally selected for investigation by Heiles, Reach, & Koo (1988) on the basis of its appearance on the IRAS Skyflux images at 60 and 100 μm. Because of the interesting possibility that this is an intermediate velocity cloud colliding with HI in the Galactic plane, we have examined this region further, both at low resolution over an extended field to provide some context and at higher (arcminute) resolution within the cloud.

INTRODUCTION

IRAS images of infrared cirrus present an all-sky picture of an interstellar environment made up of extended regions each comprising smaller scale substructure. HI 21-cm emission and infrared emission by interstellar dust are correlated over large angular scales (Boulanger & Pérault 1988), and on the finer scale afforded by IRAS images too (Joncas, Dewdney, & Boulanger 1992). There is

S. Terebey and J. Mazzarella (eds.), *Science with High-Spatial Resolution Far Infrared Data*, 165–171, 1994, Jet Propulsion Laboratory, Pasadena, CA.

PAGE 164

some cosmic scatter, perhaps the result of variations in grain emissivity, illumination, the dust-to-gas ratio, and unaccounted-for molecular, ionized, or atomic gas. Thus HI and infrared emission provide complementary information to address many interesting questions like: How does the degree of HI – infrared correlation change with angular resolution? How well mixed is the interstellar environment, particularly dust and gas? Do interstellar environments approach homogeneity at some large angular scale?

G86.5+59.6 is a degree-sized high latitude cloud originally selected for investigation by Heiles, Reach, & Koo (1988; hereafter HRK) on the basis of its appearance on the IRAS Skyflux images at 60 and 100 μm. Such regions of bright infrared cirrus might be the result of superposition of unrelated structures separated along the line of sight. However, in the position-velocity plots of the Heiles & Habing (1974) HI survey, HRK found G86.5+59.6 to be a relatively isolated feature in intermediate velocity gas (IVG: ~ -40 km s^{-1}) along with significant "local" low velocity gas (LVG: ~ 0 km s^{-1}) and a connection by a fainter "bridge" (BVG), suggesting that the IVG and LVG components are interacting.

The velocity information available for the gas can be used to "deproject" the effects of superposition implicit in the infrared cirrus; i.e., morphological comparison of observations of dust and gas at sufficient angular resolution might establish the association of dust with particular velocity components of the gas. Interpretation of infrared or HI features seemingly isolated in space and/or velocity can also benefit from the wider context of extensive angular and velocity coverage. Our study illustrates and addresses some of these issues.

STEPPING BACK: THE BIG PICTURE

To provide some context for the G86.5+59.6 degree-sized feature, we have examined a 25° surrounding region using cirrus mosaics of infrared surface brightness (I_{60} and I_{100}) based on the 5′resolution IRAS Sky Survey Atlas (ISSA; Wheelock et al. 1994). G86.5+59.6 is a relatively bright central feature (still, $I_{100} < 5$ MJy sr^{-1}), superimposed on more extensive IRAS cirrus of even lower surface brightness. We also made a data cube from the Heiles & Habing HI survey (beam sampled at 36′) for the same field and projection, and more recently resurveyed (fully sampled) a 16° field with the DRAO 26-m telescope. The integrated column density, $N_{\rm HI}$, is also not very large, typically a few times 10^{20} cm^{-2}.

Integrated Column Density

The cirrus mosaics were degraded to the same resolution as the HI surveys. A plot comparing I and $N_{\rm HI}$ pixel by pixel shows an obvious linearity (e.g., $I_{100} = 0.85 N_{\rm HI} - 1.4$) whose slope is typical of this relationship at high latitudes (Boulanger & Pérault 1988). This correlation was used to create consistent "colour tables" with which to display the cirrus and $N_{\rm HI}$ images, making the morphological correspondence between infrared brightness and $N_{\rm HI}$ all the more striking. In addition to the central G86.5+59.6 feature, many "arm" and "ring" features appear in each with identical "colours". Below we shall investigate whether there is as good (or better) correspondence at higher resolution.

Radial Velocity Slabs from the Survey Data

To seek an association of the infrared cirrus with particular velocity systems (deprojection), we made images from the HI survey data cubes integrated over three velocity slabs (IVG, -70 to -29 km s^{-1}; BVG, -29 to -13 km s^{-1}; and LVG, -13 to 35 km s^{-1}). The colour representation was kept identical to show correctly the relative importance of different features.

G86.5+59.6 is clearly the brightest (largest column density) feature in the IVG, but it is not totally isolated; there are other IVG features with clear counterparts in the infrared cirrus, for example the NW part of the ring to the E and several arms to the W.

The LVG is much more widespread, as might be expected for the "local" material, and is actually brighter at positions other than G86.5+59.6. It too has structure seen in the cirrus, for example, defining the S part of the cirrus ring with extensions to the SE. There is a slight brightening at G86.5+59.6, but perhaps a more interesting feature is a ridge of emission running to the NE. This ridge lies parallel to bright IVG which lies just to its NW.

The BVG is the least spectacular component, but very interesting. Because the division into three slabs is rather arbitrary, it naturally blends in some regions with features of the IVG and in others with the LVG. In particular, it contributes to the N and S of the cirrus ring. At G86.5+59.6, however, it is less bright than in other parts of the ring, and therefore seems less likely to be the result of an interaction.

The BVG also helps illustrate the effects of superposition on the perception of features in the infrared cirrus (or total $N_{\rm HI}$). Although the features in the BVG are generally weak they can be identified in the cirrus; this is because they add to any smooth pedestal present from other velocity components; in particular, a bright patch of cirrus to the SE of the ring is created by BVG on a much smoother background of LVG. In this context, it is interesting that G86.5+59.6 is situated near the conjunction of three arms in the IVG. Thus in addition to the LVG contribution (pedestal), the G86.5+59.6 bright feature that stands out might be the result of superposition of different systems within the IVG. This can be investigated at higher (arcminute) resolution.

60/100 μm Brightness Ratio

HRK measured the overall 60/100 μm brightness ratio to be about 0.3, higher than (0.2) for most of the other clouds in their study; this diagnostic suggested that grains in this line of sight have been modified by shocks. From the mosaics we found that although there is some range in the ratio in the larger field (0.25 – 0.34) quite similar ratios occur for dust associated with IVG and LVG. The ratio at G86.5+59.6, near 0.32 overall, is not unusual in comparison to its surroundings. This value 0.32 is like the Galactic average for atomic gas (Deul 1988) and that found on a large scale in the northern Galactic cap (Boulanger & Pérault 1988; $b > 50°$, which encompasses G86.5+59.6). There are regions in the Galaxy where the brightness ratio is lower (closer to 0.20), including much of the HRK sample, but this ratio is more typical of molecular clouds (Deul 1988). While there is no persuasive evidence from this broad perspective that indicates that G86.5+59.6 is a special region of interaction, there are suggestions of local colour changes near G86.5+59.6 related to different velocity components. The sense of these appears to be a somewhat lower ratio for LVG and higher ratio for IVG; whether this distinction is generally true is still being investigated.

ZOOMING IN ON G86.5+59.6 WITH DRAO ST AND HIRES

To pursue the issue of interaction a 2° field has been observed with the DRAO Synthesis Telescope, with velocity resolution 0.8 km s^{-1} and with angular resolution $1'$. This angular resolution is about 35 times better than in the survey data and about 5 times that in the ISSA plates. We have reprocessed the IRAS data with the IPAC HiRes software, to enhance the resolution to as small as $1'$ (as measured on test data and actual point sources in this field).

Integrated Column Density

As mentioned above, the column density and infrared surface brightness at G86.5+59.6 are quite low, and so this is an interesting test of observational and processing capabilities in *faint* diffuse fields. By simple inspection of Figure 1, it can be seen that the morphological similarity of the cirrus and integrated $N_{\rm HI}$ images down to about $2'$ is quite remarkable. *At this finest scale yet achieved, this agreement is quite quantitative.* There is a good pixel by pixel correlation between I and $N_{\rm HI}$ and the slope of this linear relationship is similar to that found in the above and other studies at larger angular scales. This suggests that there is dust associated with each of the two major velocity components (even without velocity slicing of the cube) and that there is a general absence of H_2. Emission in CO has not been detected at positions within G86.5+59.6 (HRK; W. Reach, private communication).

Radial Velocity Slabs from the DRAO ST Data

To investigate the association of velocity structure in HI with cirrus morphology on this finer scale, the DRAO ST data have been integrated over the same velocity ranges as defined for the survey data radial velocity slabs. The HI images were displayed for comparison with the HiRes images, again using a consistent colour table.

A striking discovery is that the IVG provides most of the detailed morphological structure seen in this infrared cirrus. *This deprojection analysis therefore shows definitively that there is dust in the IVG component*, of note because the dust has either survived the acceleration to −40 km s^{-1} or more or has reformed since (dust destruction is predicted in shocks of sufficiently high velocity).

As in the survey data, the LVG is more diffuse; but it has a hook-like feature (with NE spur) which can be located in the cirrus too. This hook and spur do not align exactly with a similar pattern in the IVG. Nor does the LVG appear at the ends of the SE-NW bar in the IVG.

The BVG has weak features that perhaps correlate (with modest lateral displacement) most with the IVG. Again, the division between velocity slabs is somewhat arbitrary. There are no obvious bridges between common features in both the IVG and LVG as would provide circumstantial evidence for interaction.

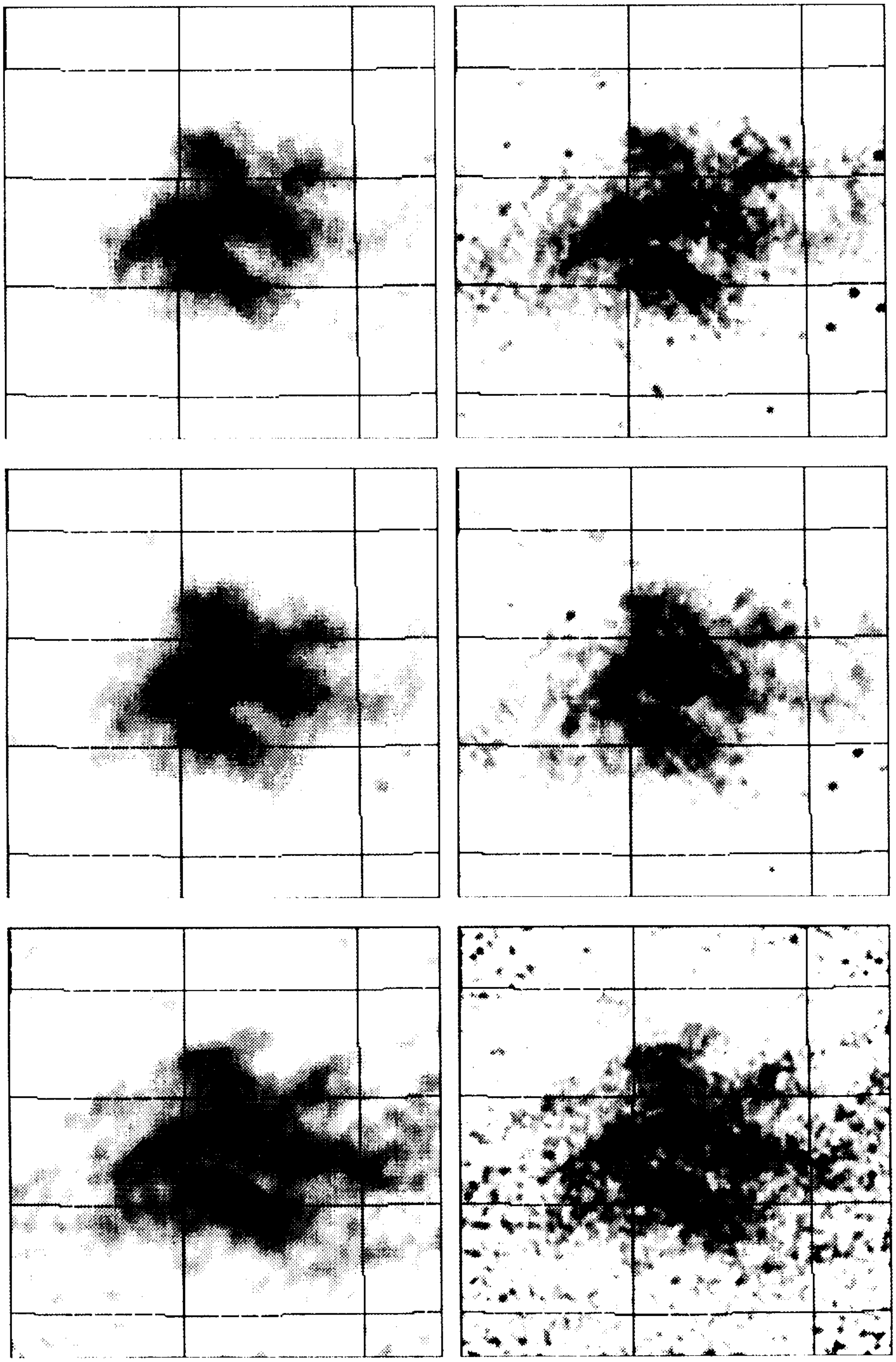

FIGURE 1 2° images of G86.5+59.6. Top row, 60 μm; middle, 100 μm; bottom, N_{HI}. Left column, ISSA resolution ~4.5′; right, resolution improved to ~2.3′. Images printed with consistent grey scales to assess the correspondence in morphology.

EXAMINATION OF THE HI DATA CUBES

The detailed relationships between HI and infared cirrus are arguably best studied by examining the images of individual velocity channels. This work is still in progress on both the survey data and ST data and no final conclusions will be presented. An unresolved question is whether the three velocity components are interacting now or whether they interacted in the past. Because the relative velocity vector would not necessarily be lined up along our line of sight, then potential connections between the morphologies in the different velocity components need not be exactly superimposed. Instead, the patterns in each slab might be translated versions of one another (translating the LVG pattern to the W does seem to line up the structures better with the IVG) or one pattern could be embedded in another. Investigation of velocity gradients and fine velocity structure in the cube is important.

Volume Rendering

One analysis tool with which we are working is volume rendering of the HI data cube. In the ST cube the tapering by the 9-m primary beam pattern is not removed so that noise near the cube edges is not amplified. While this permits a clear view of the interior of the cube, it does tend to heighten the perception of central concentration in all velocity ranges. The 26-m cube emphasizes how the LVG is more widely distributed while the IVG is concentrated. Near G86.5+59.6 the LVG and IVG components of $N_{\rm HI}$ appear as clearly separated components (whether there is spatial separation is another question). These renderings also reveal that there are different morphological features in the different velocity components, as was described above using the three coarse velocity slabs. Here one has the potential of observing the "three-dimensional" structure, including any systematic velocity gradients. This approach can in principle be used to deproject, or at least interpret, the infrared cirrus image. For example, the relatively sharp NE boundary in the infrared cirrus image of G86.5+59.6 reflects that of the IVG; to the SW the IVG boundary is itself less sharp and in the integrated cirrus it is even less apparent because of the underlying diffuse LVG.

Animation

We have also found it instructive to make an animation showing successive velocity slices of the data cubes (0.8 km s^{-1} per slice). The directional orientation of the velocity gradients near G86.5+59.6 within the LVG and IVG components can be noted: toward negative radial velocities, LVG runs from the NE to the SW, while IVG appears (in broad brush) to have subcomponents running from NE and SE to the W. We also have experimented with a false-colour animation in which the LVG and IVG components appear simultaneously against a background image of I_{100}. This is an effective means of intercomparing the morphologies of the different velocity components and infrared emission at small angular scales and with better velocity resolution than in the broad velocity slabs. *The animation shows several striking correspondences of features in the infrared image with features in HI which appear over only a few velocity channels* (thus these features have small line widths). Also the LVG slice with maximum column density (peak in the integrated line profile toward G86.5+59.6) appears to bisect and fill in a spatial gap present in the IVG slice at its peak velocity; the opportunity to investigate such potentially interesting interrelationships is washed out in the radial velocity slabs.

REFERENCES

Boulanger, F., & Pérault, M. 1988, *ApJ*, **330**, 964

Deul, E. 1988, Ph.D. thesis, Leiden

Heiles, C., & Habing, H. 1974, *A&AS*, **14**, 1

Heiles, C., Reach, W.T., & Koo, B-C. 1988, *ApJ*, **332**, 313 (HRK)

Joncas, G., Dewdney, P.E., & Boulanger, F. 1992, *ApJ*, **397**, 165

Wheelock, S., et al., 1994, *Explanatory Supplement to the IRAS Sky Survey Atlas*, (Pasadena:JPL), in press

93

p 4

APPLICATION OF MCM IMAGE CONSTRUCTION TO IRAS COMET OBSERVATIONS

MARTIN F. SCHLAPFER AND RUSSELL G. WALKER
Jamieson Science & Engineering, Inc., 5321 Scotts Valley Drive #204, Scotts Valley, CA 95066

ABSTRACT There is a wealth of IRAS comet data, obtained in both the survey and pointed observations modes. However, these measurements have remained largely untouched due to difficulties in removing instrumental effects from the data. We have developed a version of the Maximum Correlation Method for Image Construction algorithm (MCM) (Aumann, Fowler, and Melnyk, 1990, Astron. J. 99, 1674-1681) which operates in the moving coordinate system of the comet and properly treats both real cometary motion and apparent motion due to spacecraft parallax. This algorithm has been implemented on a 486/33 PC in FORTRAN and IDL codes. Preprocessing of the IRAS CRDD includes baseline removal, deglitching, and removal of long tails due to dielectric time constants of the detectors. The resulting images are virtually free from instrumental effects and have the highest possible spatial resolution consistent with the data sampling. We present examples of high resolution IRAS images constructed from survey observations of Comets P/Tempel 1 and P/Tempel 2, and pointed observations of IRAS-Araki-Alcock.

BACKGROUND

The study of comets is of great importance to our understanding of the solar system and its origin, as well as other astrophysical environments such as the interstellar and circumstellar media. Comets are believed to contain the most primitive material in the solar system. Because of their small masses and orbital parameters, comets have probably undergone relatively little processing since their formation (e.g. Weissman and Stern 1990), and thus contain important clues to the conditions in the early solar nebula.

Comets are also known to be a source of interplanetary dust, hence, the determination of their contribution is essential to a detailed modeling of the zodiacal cloud. The understanding of interplanetary dust is relevant not only to solar system studies, but also to studies of most types of astrophysical objects. The proper characterization and subtraction of the foreground light from the zodiacal cloud is a necessary step in many studies of extra-solar system objects ranging from stars to clusters of galaxies.

The detection by the Infrared Astronomical Satellite (IRAS) of comet IRAS-Araki-Alcock on April 26, 1983 marked the first observation from space of a comet in the far-infrared and the first discovery of a comet using a systematic satellite search for fast moving objects. Post mission analysis (Walker et al, 1987) revealed that the IRAS survey produced 122 highly reliable detections of 24 comets. The IRAS observations of comets are by far the largest potential set of infrared comet images ever obtained.

APPROACH

Our method for the production of comet images uses a computer algorithm based on the Maximum Correlation Method (MCM) for Image Construction (Aumann, Fowler, and Melnyk, 1990) and closely parallels the HiRes Processing performed at IPAC (Melnyk and Rice, 1991). The major departure from the IPAC scheme occurs in the Comet Image Preprocessor, where the coordinates of each detector footprint (data sample) are transformed to a moving sun-referenced coordinate system with the comet at the origin.

Preprocessing

A precursor to image construction envolves preprocessing of the IRAS survey or AO CRDD scans. The Comet Image Preprocessor performs three major functions:

1. Remove data artifacts, such as baseline, tails, and radiation hits,
2. Transform the coordinates of the data samples to a coordinate system that moves

S. Terebey and J. Mazzarella (eds.), *Science with High-Spatial Resolution Far Infrared Data*, 173–176, 1994, Jet Propulsion Laboratory, Pasadena, CA.

with the comet, and

3. Associate each data sample with the specific pixels in the map covered by the response function and their weights in the observed response. This information is stored in an array and is later looked up by the Comet Image Processor.

Typical outputs from several stages of the preprocessor are shown in figures 1-4. Figure 5 shows a first iteration 25μm image of P/Tempel 1 with the detailng algorithm turned off. Compare this image with the image in figure 6c.

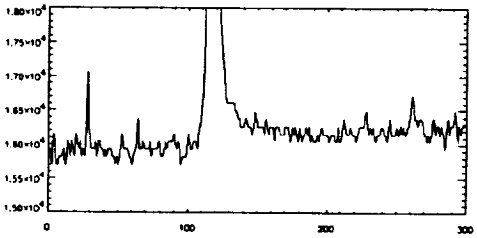

Figure 1. A 20 second snip of a 12μm CRDD survey scan of P/Tempel 2 before any pre-processing.

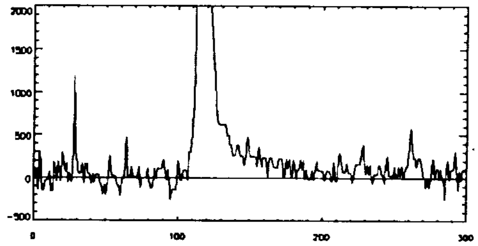

Figure 2. A 20 second snip of a 12μm CRDD survey scan of P/Tempel 2 after baseline removal.

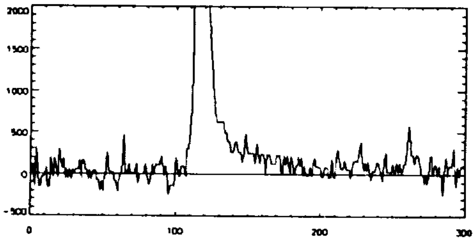

Figure 3. A 20 second snip of a 12μm CRDD survey scan of P/Tempel 2 after noise spike removal (deglitching).

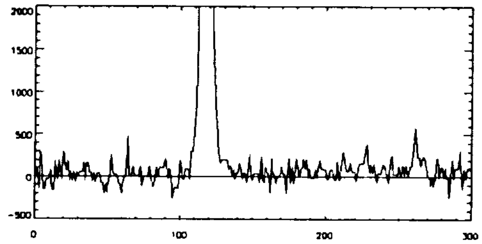

Figure 4. A 20 second snip of a 12μm CRDD survey scan of P/Tempel 2 after detailing.

Image Construction (MCM)

Image construction begins with a map of uniform low level radiance, and builds an image by scanning an analytical version of the IRAS focal plane over the map, simulating the IRAS data taking process. The analytical data samples are compared to the CRDD data samples and pixel correction factors determined. Details of this process are given by Aumann, et al (1990) and Melnyk and Rice (1991). Building the map is an iterative process, wherein each subsequent iteration begins with the most recent estimate of the map radiance. Statistics relating to pixel noise and convergence are generated at each iteration. The actual resolution achieved by the MCM depends upon the density of coverage, the range of scan angles across the field, and the signal to noise ratio of the measured flux. Rice (1993) has successfully used MCM image construction to produce high resolution IRAS maps of nearby galaxies.

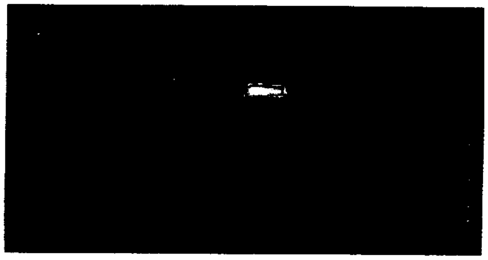

Figure 5. P/Tempel 1 first iteration 25μm image from the Comet Image Processor with the detailing algorithm turned off. Compare this image of P/Tempel 1 with that in figure 6c.

Data Products

Intensity Maps

The intensity map is the surface brightness image produced by the Comet Image Processor. Two intensity maps are produced. The first is the map resulting from from the first iteration (equivalent to the IPAC FRESCO image) and the second is the high resolution image produced at the final iteration. Figure 6 shows images of comets IRAS-Araki-Alcock, P/Tempel 1, and P/Tempel 2. The image contours begin at 3σ and each succeeding contour is twice the previous.

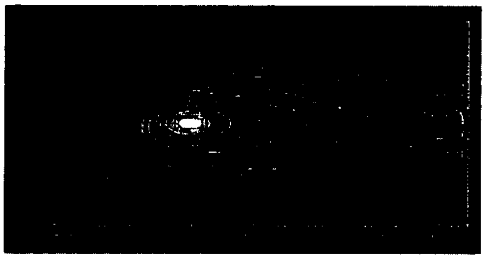

Figure 6a. 60μm first iteration image of IRAS-Araki-Alcock.

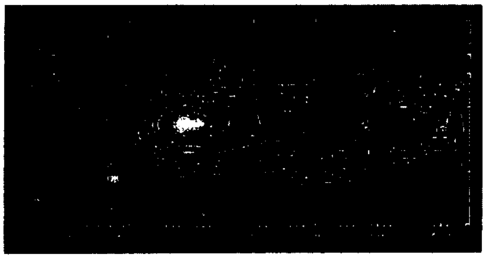

Figure 6b. 60μm tenth iteration image of IRAS-Araki-Alcock.

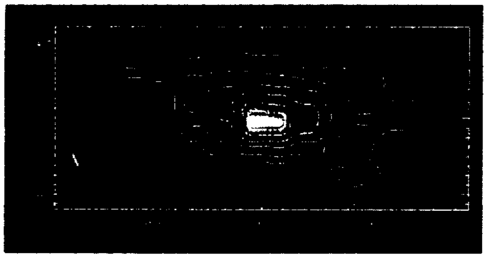

Figure 6c. 25μm first iteration image of P/Tempel 1.

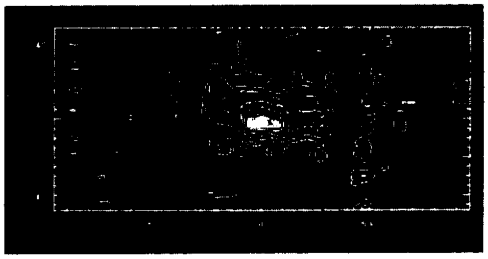

Figure 6d. 25μm 15th iteration image of P/Tempel 1.

Figure 6e. 12μm first iteration image of P/Tempel 2.

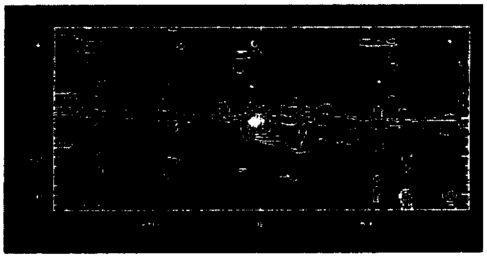

Figure 6f. 12μm 15th iteration image of P/Tempel 2.

The Comet Image Processor also produces several ancilary maps that aid interpretation.

Coverage Map
The coverage map is a measure of the uniformity of coverage of the scanned field. It is computed by summing the relative response of each detector to that pixel for all the times the pixel was sampled. Non-uniformities in coverage are functions of both the detector spatial response and the density of scans. This map is used in an aid to understanding the reliability of features appearing in the intensity maps.

Photometric Noise Map
This is a map of the internal photometric uncertainty of the flux in a pixel as a result of averaging overlapping detector samples. The photometric noise map may be used to estimate the error in aperture photometry of the comet, photometric profiles, and flux ratios.

Resolution Map
The resolution map estimates the spatial resolution and its variation across the field. An array of point sources is constructed along the top and bottom of the field using the analytical model of the IRAS focal plane. Scans of the point sources are summed with CRDD to produce new CRDD that contains all the information and noise of the original plus the array of point sources. This new CRDD is processed by the Comet Imaging Processor to the same number of iterationss that converged the intensity map. The in-scan and cross-scan resolutions are estimated from the widths of the reconstructed point sources.

Convergence Map
This is a map showing which pixels within the image have met the convergence criteria. This map is a simple tool to exclude non-converged, and therefore incorrect, pixel flux

values from further analysis.

Background Map

The true distribution of comet radiance is distorted by the presence of background stars, asteroids, galaxies, and small extended structures. The background map is produced as an aid to estimate the impact of background features on the comet image. This image is built from all the IRAS survey scans that fell within the field of interest during those times when the comet was not present. It is produced in both fixed celestial coordinates, and in the moving comet-referenced system.

PSC 2 and Asteroid Overlay

The PSC 2 and asteroid overlay is produced as a further aid to understanding the features within a comet image. This is the final intensity map overlaid with the positions of all the IRAS PSC 2 sources and numbered asteroids in that field at the time of observation. With the overlay is a listing of the sources and their fluxes on the four spectral bands.

Photometric Profiles

Photometric profiles are generated as an aid to image validation, quality assesment, and image analysis. These include:

1. Aperture photometry centered on the comet and extending to large radii,
2. Intensity profile along the sun-comet direction and passing through the brightest pixel of the intensity map, and
3. Intensity profile normal to the sun-comet direction and passing through the brightest pixel of the intensity map.

REFERENCES

Aumann, H. H., Fowler, J. W., Melnyk, M., 1990, "A Maximum Correlation Method for Image Construction of IRAS Data", Astron. J. 99, 1674-1681.

Melnyk, M., 1990, "Technical Reference to the Full Resolution Survey Coadder (FRESCO):, IPAC User's Guide, Ed. 4, Part V, California Institute of Technology.

Melnyk, M. and Rice, W., 1991, "High Resolution Processing", IPAC User's Guide, Ed. 4, Part VI, Californis Institute of Technology.

Rice, W., 1993, "An Atlas of High-Resolution IRAS Maps of Nearby Galaxies", Astron. J. Vol 105, pp 67-96.

Walker, R. G., Matson, D. L., and Veeder, G. L., 1987, "IRAS Observations of Comets", Advances in Space Research, Vol. 6, no. 57, p. 57.

Weissman, P. R. and Stern, S. A. (1990) Physical Processing of Cometary Nuclei. In Proc. of Workshop on Analysis of Return Comet Nucleus Samples.

LUMINOUS RADIO-QUIET SOURCES IN THE W3(MAIN) CLOUD CORE

C. G. WYNN-WILLIAMS, E. F. LADD, J. R. DEANE, AND D. B. SANDERS
Institute for Astronomy, University of Hawaii, 2680 Woodlawn Drive, Honolulu, HI 96822

ABSTRACT We have resolved 450μm and 800μm emission from the W3(Main) star forming region into three major peaks, using 8″ – 14″ beams with the James Clerk Maxwell Telescope on the summit of Mauna Kea. One of the submillimeter sources is identified with W3 – IRS5, a well-known candidate protostar. However, to our suprise, we find that none of the submillimeter peaks coincides with any of the prominent compact HII regions in the area. We estimate that the three submillimeter sources together contribute 30 – 50% of the total bolometric luminosity of the region, and speculate that the contribution of luminous radio-quiet sources to the total luminosity of HII region/molecular cloud complexes may be larger than is often assumed.

INTRODUCTION

The spectral energy distributions of HII region/molecular cloud complexes indicate that the bulk of their luminosity is emitted in the far infrared and that this far infrared and submillimeter emission is generated by cool (T = 30–60 K) dust (see e.g. Wynn-Williams & Becklin 1974; Chini, Krugel, & Wargau 1987). Because of the large beam sizes typically used for far-infrared and submillimeter continuum observations, it has been difficult to determine whether the OB stars ionizing the HII regions are the sources of the luminosity, or whether this luminosity is generated independently within the nearby molecular material. We present new submillimeter continuum observations of the W3(Main) region with high spatial resolution ($<$ 0.1 pc). These new observations show that the distribution of submillimeter flux is not similar to the distribution of radio continuum emission, and suggest that the total luminosity generated by HII region/molecular cloud complexes is not dominated by the O and B stars which generate the observed HII regions.

OBSERVATIONS

Submillimeter observations of the W3(Main) region were made with the 15 m JCMT in 1992 November. The continuum maps were obtained using the facility UKT-14 bolometer system with passbands centered at approximately 450 μm and 800 μm. Our results are shown in Figure 1, along with maps of 20 μm

S. Terebey and J. Mazzarella (eds.), *Science with High-Spatial Resolution Far Infrared Data*, 177–181, 1994, Jet Propulsion Laboratory, Pasadena, CA.

(Wynn-Williams et al. 1972) and a 5 GHz radio continuum emission (Harris & Wynn-Williams 1976). The submillimeter continuum emission breaks up into three main emission centers—one in the east, and two in the west. We designate the sources SMS 1, 2, and 3 from E to W in order of decreasing right ascension.

DISCUSSION

SMS 1 is resolved and nearly circular at half power, with low flux level extensions to the east in the direction of IRS 3/W3B and north in the direction of IRS 1/W3A (see Figure 2a). The 450 μm and 800 μm centroid positions are consistent with the 20 μm position of IRS 5 (Wynn-Williams et al. 1972), several H_2O maser groupings (Genzel et al. 1987), and the radio continuum source W3(M) (Colley 1980).

SMS 2 lies close to the 20 μm source IRS 4 (Wynn-Williams et al. 1972), and near to the compact HII region W3(C) (Wynn-Williams 1971; see Figure 2b). We find that the position of SMS 2 lies 7.5″ from the center of W3(C). The size of the positional discrepancy is sufficiently large that we are confident that SMS 2 is not associated with W3(C). IRS 4 lies 4″ from the centers of both W3(C) and SMS 2, nearly on a line between these two sources. Therefore we conclude that there are are least two distinct major sources of emission in this area (W3(C) and SMS 2), and quite likely an additional unrelated infrared source (IRS 4).

SMS 3 is more extended than the other two submillimeter sources, with FWHM size of $30'' \times 16''$ ($\alpha \times \delta$). No 20 μm emission was detected in this region to a point source detection threshold of 150 Jy (Wynn-Williams et al. 1972), nor was radio continuum emission detected greater than 6 mJy/2″ beam (Harris & Wynn-Williams 1976).

Combining our data with infrared results (Wynn-Williams et al. 1972; Werner et al. 1980), we have estimated the 20–800 μm luminosities for these three sources, as well as for IRS 1 (which was not detected as a distinct source in our submillimeter maps) and the entire region. The total luminosity for the region is estimated to be 5.2×10^5 $L_\odot$. IRS 1 and IRS 5 each account for about 30% of the total. SMS 1 and SMS 2 account for an additional 6% each. However, it should be noted that the luminosity of SMS 2 may contain some additional contribution from either IRS 4 or the source associated with W3(C), and therefore this luminosity should be regarded as an upper limit to the luminosity of SMS 2.

IRS 5 has long been recognized as a candidate high-mass protostar, based on its high luminosity, infrared energy distribution, and relatively weak radio continuum emission (see e.g. Wynn-Williams et al. 1972; Hackwell et al. 1978; Werner et al. 1980; Wynn-Williams 1982). We have found two more sources in the W3(Main) cloud that exhibit behavior similar to that of IRS 5. While both have luminosities about a factor of 5 lower than that of IRS 5, they are not associated with detected radio continuum emission. These radio-quiet sources account for at least 35% (SMS 1/IRS 5 + SMS 3) and up to 50% (SMS 1/IRS 5 + SMS 2 + SMS 3) of the total luminosity generated in the W3(Main) core. With the addition of extended emission probably generated by lower-luminosity, non-ionizing sources, the luminosity from W3(Main) could be roughly equally

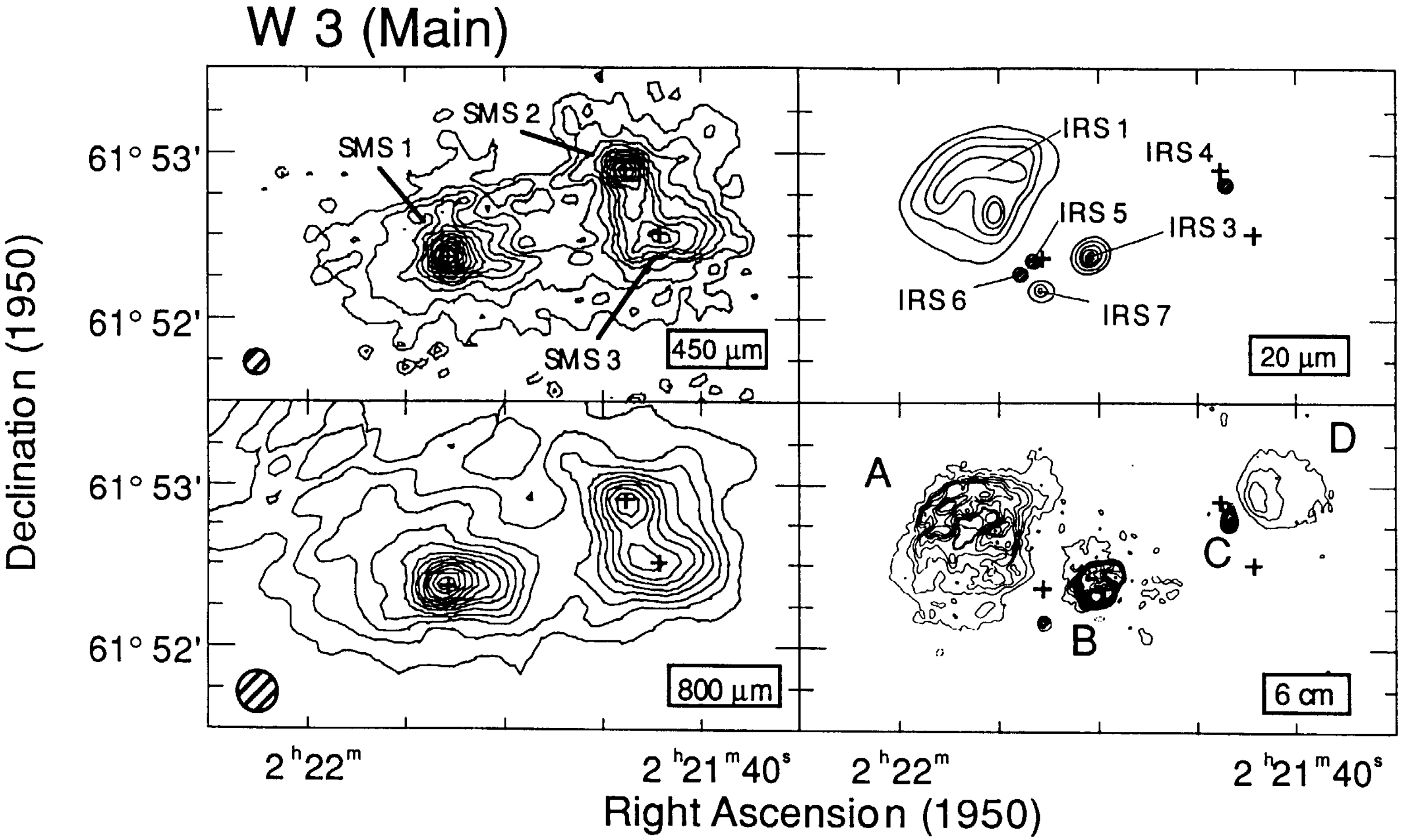

Fig. 1 Submillimeter images of the W3 (Main) region at 450 µm (**top left**) and 800 µm (**bottom left**) compared with the 20 µm map from Wynn-Williams et al. (1972; **top right**) and the 5 GHz contours from Harris & Wynn-Williams (1976; **bottom right**). The submillimeter beam sizes are shown in the lower left of each relevant panel. Contours for the 450 µm map begin at 15 Jy / 8" beam and increment by 15 Jy / 8" beam. Contours for the 800 µm map begin at 1 Jy / 14" beam and increment by 1 Jy / 14" beam.

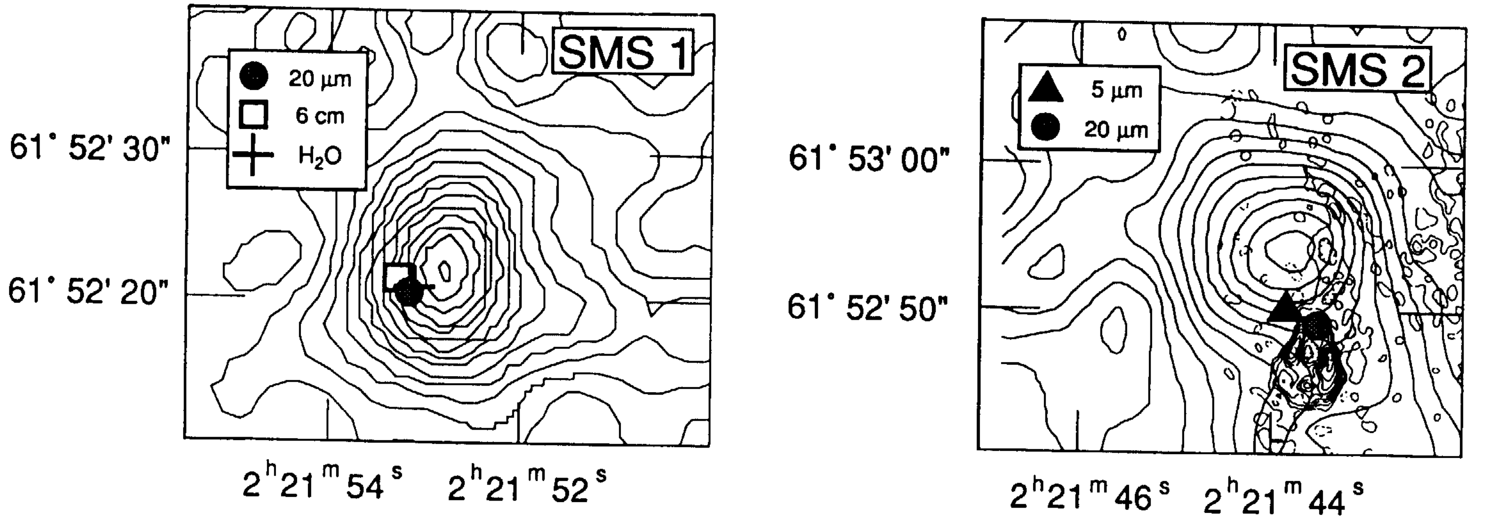

Fig. 2 **a)** Contours of the 450 μm emission near IRS 5. The 450 μm contours begin at 5 Jy / 8" beam and increment by 5 Jy / 8" beam. The positions of the 20 μm source, the radio continuum source W3 (M) and the H_2O maser centers are indicated by a circle, box and cross respectively. **b)** Comparison of our 450 μm contours with the 15 GHz emission from Colley (1980) toward the SMS 2 / IRS 4 / W3 (C) region. The 450 μm contours begin at 5 Jy / 8" beam and increment by 5 Jy / 8" beam. The position of the 20 μm and 5 μm sources are indicated by a circle and a triangle respectively.

divided between sources associated with HII regions and sources which have little or no ionized environs.

ACKNOWLEDGMENTS

We thank the operators of the JCMT for their assistance in obtaining the submillimeter continuum data. C. G. W.-W. acknowledges support from NSF grant AST89-19563. E. F. L. was supported by the James Clerk Maxwell Telescope Fellowship.

REFERENCES

Chini, R., Krugel, E., & Wargau, W. 1987, A&A, 181,378

Colley, D. 1980, MNRAS, 193,495

Genzel, R. Downes, D., Moran, J. M., Johnston, K. J., Spencer, J. H., Walker, R. C., Haschick, A., Matveyenko, L. I., Kogan, L. R., Kostenko, V. I., Rönnäng, B., Rydbeck, O. E. H., & Moiseev, I. G. 1978, A&A, 66,13

Hackwell, J. A., Gehrz, R. D., Smith, J. R., & Briotta, D. A. 1978, ApJ, 221,797

Harris, S., & Wynn-Williams, C. G. 1976, MNRAS, 174,649

Werner, M. W., Becklin, E. E., Gatley, I., Neugebauer, G., Sellgren, K., Thronson, H. A., Harper, D. A., Loewenstein, R., & Moseley, S. H. 1980, ApJ, 242,601

Wynn-Williams, C. G. 1982, ARA&A, 20,587

Wynn-Williams, C. G. 1971, MNRAS, 151,397

Wynn-Williams, C. G., & Becklin, E. E. 1974, PASP, 86,5

Wynn-Williams, C. G., Becklin, E. E., & Neugebauer, G. 1972, MNRAS, 160,1

Science with High Spatial Resolution Far-Infrared Data

LIST OF AUTHORS

182

Science with High Spatial Resolution Far-Infrared Data

LIST OF ATTENDEES

George Aumann
California Institute of Technology
Infrared Processing and Analysis Center
MS 100-22
Pasadena, CA 91125

Jean-Phillipe Bernard
California Institute of Technology
Infrared Processing and Analysis Center
MS 100-22
Pasadena, CA 91125

T. Romke Bontekoe
European Space Agency
Astrophysics Division
Postbus 299
2200 AG Noordwijk
THE NETHERLANDS

Yu Cao
California Institute of Technology
MS 103-33
Pasadena, CA 91125

Thomas Chester
California Institute of Technology
Infrared Processing and Analysis Center
MS 100-22
Pasadena, CA 91125

James Deane
Inst. for Astronomy
2680 Woodlawn Drive
Honolulu, HI 96822

N. Devereux
New Mexico State University
Dept. of Astronomy
Box 30001 - Dept 4500
Las Cruces, NM 88003

Rhodri Evans
University of Toledo
Dept. of Physics and Astronomy
Toledo, OH 43606

John Fowler
California Institute of Technology
Infrared Processing and Analysis Center
MS 100-22
Pasadena, CA 91125

W. Gong
Queen Mary College
Dept. of Physics
Miles End Road
London E1 4NS
UNITED KINGDOM

John Hackwell
The Aerospace Corp.
P.O. Box 92957
M2-266
Los Angeles, CA 90009

Bryant Heikkila
New Mexico State University
Dept. of Astronomy
Las Cruces, NM 88003

George Helou
California Institute of Technology
Infrared Processing and Analysis Center
MS 100-22
Pasadena, CA 91125

Do Kester
University of Groningen
Space Research Dept
WSN Gebouw
P.O. Box 800
9700 Av Groningen
THE NETHERLANDS

Ned Ladd
University of Hawaii
Institute for Astronomy
2680 Woodlawn Drive
Honolulu, HI 96822

William Langer
Jet Propulsion Laboratory
MS 169-506
4900 Oak Grove Drive
Pasadena, CA 91109

Joanna F. Lees
University of Chicago
Dept. of Astronomy
5640S. Ellis Ave
Chicago, IL 60637

Daniel Lester
University of Texas
Dept. of Astronomy
RLM Hall
Austin, TX 78712

Debbie Levine
California Institute of Technology
Infrared Processing and Analysis Center
MS 100-22
Pasadena, CA 91125

Steve Lord
California Institute of Technology
Infrared Processing and Analysis Center
MS 100-22
Pasadena, CA 91125

Kenneth Marsh
Jet Propulsion Laboratory
MS 163-327
4900 Oak Grove Drive
Pasadena, CA 91109

A.P. Marston
Drake University
Dept. of Physics and Astronomy
Des Moines, IA 50311

Peter Martin
University of Toronto
Canadian Inst. Theor. Astrophysics
Toronto, ON, M5S 1A7 CANADA

Joseph M. Mazzarella
California Institute of Technology
Infrared Processing and Analysis Center
MS 100-22
Pasadena, CA 91125

Mehrdad Moshir
California Institute of Technology
Infrared Processing and Analysis Center
MS 100-22
Pasadena, CA 91125

Stephan D. Price
Phillips Laboratory
Optical Physics Division
Hanscom AFB, MA 01731-5000

Thomas Prince
California Institute of Technology
MS 220-47
Pasadena, CA 91125

Richard Puetter
University of California, San Diego
CASS
Code C-011
LaJolla, CA 92093

Michael P. Rupen
National Radio Astron.Obs.
P.O. Box O
Socorro, NM 87801

Martin Schlapfer
Jamieson Science and Engineering
Suite 204
5321 Scotts Valley Drive
Scotts Valley, CA 95066

James Schombert
California Institute of Technology
Infrared Processing and Analysis Center
MS 100-22
Pasadena, CA 91125

Jason Surace
Institute for Astronomy
University of Hawaii
2680 Woodlawn Drive
Honolulu, HI 96822

Susan Terebey
California Institute of Technology
Infrared Processing and Analysis Center
MS 100-22
Pasadena, CA 91125

R.P Verma
Tata Institute of Fundamental Research
Homi Bhabha Road
Bombay 400005
INDIA

Z. Wang
Center for Astrophysics
MS 66
60 Garden Street
Cambridge, MA 02138

L.B.F.M. Waters
Laboratory for Space Research
P.O. Box 800
9700 Av Groningen
THE NETHERLANDS

Michael Werner
Jet Propulsion Laboratory
MS 233-303
4900 Oak Grove Drive
Pasadena, CA 91109

William Webber
New Mexico State University
Dept. of Astronomy
Las Cruces, NM 88003

Gareth Wynn-Williams
University of Hawaii
Institute for Astronomy
2680 Woodlawn Drive
Honolulu, HI 96822

Cong Xu
Max-Plank-Inst fur Kernphysik
Astrophysics Group
Postfach 103980
D-6900 Heidelberg 1
GERMANY

Erick Young
University of Arizona
Steward Observatory
Tucson, AZ 85721

Ann Wehrle
California Institute of Technology
Infrared Processing and Analysis Center
MS 100-22
Pasadena, CA 91125